ELECTROCHEMICAL AND ADSORPTION STUDIES OF GLYCEROL BASED CARBONS AND ITS COMPOSITES WITH Fe-MnO_X AND OMS-2

A THESIS

Submitted to

GOA UNIVERSITY

For the degree of

DOCTOR OF PHILOSOPHY

In

CHEMISTRY

By

Ms. APURVA A. NARVEKAR

SCHOOL OF CHEMICAL SCIENCES

GOA UNIVERSITY

TALEIGAO PLATEAU, GOA – 403 206, INDIA

FEBRUARY 2020

STATEMENT

I hereby state that this thesis entitled, "**Electrochemical and adsorption studies of glycerol based carbons and its composites with Fe-MnO_x and OMS-2**" is my original work and it has not previously formed the basis for the award of any degree, diploma, associateship, fellowship or any other similar titles to the best of my knowledge.

Apurva A. Narvekar
(Candidate)

Prof. J. B. Fernandes
(Research Guide)
School of Chemical Sciences,
Goa University.

Prof. S. G. Tilve
(Co-guide)
School of Chemical Sciences,
Goa University.

CERTIFICATE

As required under the University ordinance, I certify that the thesis entitled, "ELECTROCHEMICAL AND ADSORPTION STUDIES OF GLYCEROL BASED CARBONS AND ITS COMPOSITES WITH Fe-MnO_X AND OMS-2" submitted by **Miss Apurva A. Narvekar** for the award of Doctor of Philosophy in Chemistry is a record of research work done by the candidate during the period of study and it has not previously formed the basis for the award of any degree, diploma, associateship, fellowship or any other similar titles.

Prof. J. B. Fernandes
(Research Guide)
School of Chemical Sciences,
Goa University.

Prof. S. G. Tilve
(Co-guide)
School of Chemical Sciences,
Goa University.

ACKNOWLEDGEMENTS

Firstly, I would like to express my gratitude to my research guide **Prof. J. B. Fernandes** for providing me an opportunity to pursue my doctoral studies under his guidance. I am thankful to sir for the invaluable guidance, fruitful discussions, constructive criticism, patience and timely help provided all through my research work. Your teachings helped in all the time of research and writing this thesis. Thank you sir, for always motivating and encouraging me.

I wish to express sincere thanks to co-guide **Prof. S. G. Tilve**, Vice Dean (Research), School of Chemical Sciences, for his all-important suggestions, kind help, necessary facilities and for being always co-operative throughout the course of this investigation.

I sincerely thank **Prof. V. S. Nadkarni**, Dean, School of Chemical Sciences, Goa University, **Prof. B. R. Srinivasan**, Vice Dean (Academic), School of Chemical Sciences, **Prof. A. V. Salker**, **Prof. R. N. Shirsat**, **Prof. V. M. S. Verenkar**, **Dr. S. N. Dhuri and Dr. Mahesh Majik** for providing useful suggestions and assessment of research work during annual FRC presentations.

I extend my thanks to Prof. **V. Sahni**, Vice-chancellor, Goa University, **Prof. Y. V. Reddy,** Registrar**, Prof. S. Shetye**, former Vice-Chancellor and **Prof. V. P. Kamat** former registrar for allowing to work in the university and for providing necessary facilities.

I would like to acknowledge Mr. Girish Prabhu, **NIO-Goa** for helping in characterization of samples by XRD, **SAIF-IIT Madras** for FT-Raman and SEM analysis and **SAIF-IIT Bombay** for TEM and ICP-AES analysis.

I am grateful to my teacher **Dr. Purnakala Samant**, Principal, Govt. College of Arts, Science and Commerce, Khandola, Marcela-Goa, for always believing in me. Thank you madam, for your encouragement, support and love. I will forever remain indebted to you.

I am thankful to **Dr. Sajo Naik** for his valuable help and suggestions.

My heartfelt thanks to my dear friend **Dr. Anjani Nagvenkar,** Post doctoral researcher at Technion-Israel Institute of Technology, Israel for her unconditional help and for positively affecting my life all these years.

I can never thank enough to my teacher **Mr. Daniel Coutinho** for his help in learning to use various instruments when i had just begun my research work.

I wish to thank **Dr. Kiran**, **Dr. Mithil**, **Dr. Dattaprasad**, **Dr. Sudarshana**, **Mr. Chandan**, **Mr. Pratik**, **Mr. Rahul**, **Ms. Luann** and **Mr. Sarvesh** for the help rendered to me to carry out different analysis. My sincere thanks also go to research scholars **Mr. Johnross**, **Ms. Prajyoti**, **Ms. Madhavi, Ms. Amarja**, **Mr. Sudesh**, **Mr. Abhijeet**, **Mr. Ketan**, **Mr. Shashank**, **Ms. Pooja**, **Ms. Neha**, **Ms. Mangala**, **Ms. Lima** and **Mr. Ratan** for their constant encouragement.

I thank the non teaching staff of School of Chemical Sciences, Goa University library and office for their help as and when needed.

My heartiest thanks to my friends **Mr. Amol Gaonkar, Mr. Sangam Tari and Ms. Maria Fernandes** for all positive talks, chai & coffee times and source of help whenever needed during the course of this study.

Above all, I am indebted to my mother **Smt. Asmita** for her love, prayers, sacrifices and blessings. I am also grateful to my brother **Mr. Shrikrishna** for being supportive and loving.

Finally, **Thank you GOD** for the countless blessings.

Apurva A. Narvekar

INDEX

CONTENTS **Page No.**

List of Figures v
List of Tables xi
List of Schemes xiv

CHAPTER I – General Introduction

Overview 1
1.1 Activated Carbon 3
1.1.1 KOH activation 4
1.1.2 $ZnCl_2$ activation 7
1.2 Carbon materials from glycerol 9
1.3 OMS-2 and Fe-Mn oxides 11
1.4 Fuel Cell 13
1.4.1 Mechanism of electro-oxidation of methanol 15
1.4.2 Electrocatalytic oxidation of ethanol 20
1.5 Supercapacitors 24
References 26

CHAPTER II – Synthesis and adsorption behavior of glycerol based carbons

Introduction 45
2.1 Synthesis of glycerol based carbon 50
2.2 Adsorption studies 51
2.3 Results and discussion 53
2.3.1 XRD and Thermal analysis 53

2.3.2 Infrared spectral analysis 55
2.3.3 Surface area, porosity and SEM 57
2.4 General adsorption behavior 60
2.4.1 Effect of adsorbent dosage 61
2.4.2 Effect of initial pH 62
2.4.3 Effect of initial methylene blue concentration 63
2.4.4 Effect of contact time and determination of adsorption equilibrium 64
2.5 Adsorption isotherm 65
2.6 Thermodynamic studies 68
2.7 Adsorption behavior of GBC-350 71
2.8 Kinetics of adsorption 75
Summary & Conclusions 78
References 80

CHAPTER III – Activation of glycerol based carbons

Introduction 85
3.1 Chemical activation of glycerol based carbon 88
3.2 Characterization of activated glycerol based carbon materials 89
3.2.1 Structural properties of activated glycerol based carbons GBC_K and GBC_Z – XRD studies 89
3.2.2 Extent of order/disorder in the carbon structure - Raman scattering studies. 90
3.2.3 Surface functional groups of the activated glycerol based carbons: FTIR spectroscopy 93
3.2.4 Evaluation of thermal stability of activated carbons GBC_K and GBC_Z –TG-DTA analysis 97
3.2.5 Textural properties of activated glycerol based carbons (GBC_K and GBC_Z) – BET analysis 99
3.2.6 Morphology of activated glycerol based carbons – SEM analysis 102
3.3 Surfactant induced activation of glycerol based carbons 105
3.4 Characterization of the surfactant activated glycerol based carbons 106

3.4.1 Structural properties of GBC_{S1} and GBC_{S2} – XRD and Raman studies 106
3.4.2 Surface functional groups on GBC_{S1} and GBC_{S2} - FTIR spectra 107
3.4.3 Textural properties of glycerol based carbons GBC_{S1} and GBC_{S2} – BET sorptometry and SEM analysis 110
3.5 Adsorption of methylene blue on glycerol based carbons (GBC_K, GBC_Z, GBC_{S1} and GBC_{S2}) 114
3.6 General adsorption behavior of the activated carbons GBC_K and GBC_Z 116
3.6.1 Experimental 116
3.6.2 Results and discussion 117
3.6.2.1 Effect of initial pH on adsorption efficiency 117
3.6.2.2 Effect of contact time and adsorption equilibrium 117
3.6.2.3 Adsorption isotherms 118
3.6.2.4 Kinetics of Adsorption 123
Summary & conclusions 124
References 126

CHAPTER IV – Synthesis and characterization of Fe-Mn oxides and Mn OMS-2

Introduction 131
4.1. α-Fe_2O_3 132
4.1.1 Investigation towards synthesis of doped α-Fe_2O_3 132
4.1.2 Thermal and XRD analysis of the Fe-Mn oxides 133
4.1.3 TEM in relation to XRD analysis 136
4.1.4 Transformation of Fe-Mn oxide in Mn-doped α-Fe_2O_3. 139
4.1.5 Surface area and porosity 141
4.1.6 Magnetic behavior 144
4.1.7 Catalytic activity 145
4.2 α-MnO_2 (OMS-2) and Fe-OMS-2 147
4.2.1 Synthesis of OMS-2and Fe-OMS-2 147

4.2.2 Characterization 148
Summary & conclusions 157
References 158

CHAPTER V – Electrochemical properties of glycerol based carbons and their nanocomposites

General introduction 162
5.1 Supercapacitance behavior of glycerol based carbons and its composites 163
5.2 Electrocatalysis of Methanol oxidation reaction (MOR) 178
5.3 Electrocatalysis of ethanol oxidation reaction (EOR) 191
Summary & conclusions 203
References 205

List of publications 209

List of Figures

Figure		Page No.
Figure 1.1:	Schematic representation of a fuel cell	14
Figure 2.1:	XRD profiles of the glycerol based carbons obtained by treatment of the as prepared carbons at 120 ^{o}C and 350 ^{o}C.	53
Figure 2.2:	(a) TG-DTA plot of GBC-120 in nitrogen atmosphere and (b) Comparison of TG/DTG profiles (N_2 atmosphere, heating rate of 10 ^{o}C min^{-1}).	54
Figure 2.3:	Infrared spectra of GBC carbons (a) spectrum of GBC-120 (b) spectra of various GBC carbons heat treated between 200 - 800 ^{o}C.	57
Figure 2.4:	Pore size distribution and N_2 adsorption-desorption isotherm (inset) for the carbon samples (a) GBC-120 and (b) GBC-350.	59
Figure 2.5:	SEM images of (A) GBC-120 (B) GBC-350.	60
Figure 2.6:	Effect of amount of adsorbent on adsorption efficiency.	61
Figure 2.7:	Relative adsorption efficiency of GBC-120 carbon at different pH values.	62
Figure 2.8:	Effect of initial concentration of methylene blue on adsorption efficiency.	63
Figure 2.9:	Kinetic plots obtained when GBC-120 carbon samples were equilibrated with methylene blue solution at pH = 4.7 and 7.0	64
Figure 2.10:	(a) General adsorption Isotherm and (b-d) Applicability of various adsorption models for adsorption of methylene blue on GBC-120 at 25 ^{o}C and pH=7 .	66
Figure 2.11:	Summary of the adsorption mechanism discussed in the section 2.5.	68
Figure 2.12:	Plot of ln K_L v/s 1/T for adsorption of methylene blue on GBC-120 at various temperatures between 289 – 323 K.	69

	Figure	Page No.
Figure 2.13:	(a) General adsorption Isotherm and (b-d) Applicability of various adsorption models for adsorption of methylene blue on GBC-350 at 25 ^{o}C.	71
Figure 2.14:	Comparative investigation of adsorption-time behavior of the glycerol based carbons at 25 ^{o}C (a) GBC-120 and (b) GBC-350.	73
Figure 2.15:	Application of pseudo first and pseudo second order kinetic models during equilibriation of methylene blue on the GBC samples. GBC-350(I) is initial stage of adsorption and GBC-350(II) is second stage of adsorption.	76
Figure 3.1:	X-ray diffractogram of (a) activated glycerol based carbons GBC_K and GBC_Z in relation to the un-activated carbon GBC-120.	90
Figure 3.2:	Raman spectra of the activated carbons GBC_K and GBC_Z in relation to the corresponding un-activated carbon GBC-120.	91
Figure 3.3:	Raman spectra representing comparative Raman Intensities of GBC_K, GBC_Z, GBC-800 and Vulcan XC72R.	92
Figure 3.4:	FT-IR spectra of (a) the KOH activated carbon GBC_K and (b) infrared absorptions of the activated carbon GBC_K in relation to the un-activated carbon GBC-120	95
	(c) FT-IR spectra of $ZnCl_2$ activated glycerol based carbon GBC_Z.	96
Figure 3.5:	TG-DTA-DTG profiles of the KOH and $ZnCl_2$ activated glycerol based carbons in N_2 atmosphere of (a) GBC_K and (b) GBC_Z.	97
Figure 3.6:	N_2 adsorption desorption isotherms (inset) and pore size distribution profiles of the activated glycerol based carbons (a) GBC_K and (b) GBC_Z.	100

	Figure	Page No.
Figure 3.7:	SEM images of activated glycerol based carbons (a) GBC_K and (b) GBC_Z in comparison to (c) GBC-800 and (d) commercial carbon Vulcan XC 72R.	104
Figure 3.8:	X-ray diffraction patterns of the glycerol based carbons GBC_{S1} andGBC_{S2}.	106
Figure 3.9:	Raman spectra of glycerol based carbons GBC_{S1} and GBC_{S2}.	107
Figure 3.10:	Infrared spectra of glycerol based carbons (a) GBC_{S1} and (b) GBC_{S2}.	109
Figure 3.11:	Pore size distribution (BJH) and N_2 adsorption desorption isotherms of carbons (a) GBC_{S1} and (b) $GBC_{S2.}$	111
Figure 3.12:	SEM images of GBC_{S1} at a magnification of (a) 10000x, (b) 60000x and GBC_{S2} at a magnification of (c) 10000x (d) 60000x.	113
Figure 3.13:	Comparative kinetic plots of adsorption of methylene blue on glycerol based carbon samples. (Volume of adsorbate: 200 mL, Dosage of adsorbent: 20 mg, Temperature: 299 K, Contact time: 20 hours, Initial concentration = 50 µg mL).	114
Figure 3.14:	Adsorption efficiency of (a) GBC_K and (b) GBC_Z carbon at different initial pH values.	118
Figure 3.15:	General adsorption isotherm profiles for the glycerol based carbons (a) GBC_K and (b) $GBC_{Z.}$	119
Figure 3.16:	Langmuir isotherm and Freundlich isotherm for adsorption of Methylene blue on GBC_K and GBC_Z.	120
Figure 3.17:	Pseudo first and second order kinetic plots for adsorption of methylene blue on GBC_K and GBC_Z.	123
Figure 4.1.	(a) TG-DTA-DTG curves of the synthesized Fe-Mn oxide (MF1) obtained in air atmosphere in the temperature range of 30 ^oC to 1000 ^oC. (b) Corresponding thermal analysis profiles of iron oxide sample (F1).	134

	Figure	Page No.
Figure 4.2.	X-ray powder diffraction pattern of Fe-Mn oxides (a) as Fe-Mn oxide mixed phase (MF1) gets transformed to MF7 which is Mn doped α-Fe_2O_3 (b) synthesized iron oxides in absence of Mn wherein α-FeOOH (F1) gets transformed to α-Fe_2O_3 (F6 and F8).	136
Figure 4.3.	Fig. 4.3: (a) TEM images of the Mn containing iron oxide samples. MF1 was a mixed oxide obtained by co-precipitation from Fe(III) and Mn(II) salts followed by drying the product at 100 ^oC. MF6 was obtained by calcination of MF1 at 600 ^oC. MF7 was prepared by heating MF1 in air at 750 ^oC. (b) The iron oxide F1 was prepared by precipitation from Fe(III) salt, and drying at 100 ^oC. F6 was obtained by calcination of F1 at 600 ^oC. F8 was prepared by heating F1 in air at 800 ^oC.	137
Figure 4.4.	(a) N_2 adsorption desorption isotherms and pore size distribution profiles of the synthesized samples**.** (b) Pore size distribution plots of the synthesized samples where MF1 is (α-FeOOH+ $MnFe_2O_4$); MF6 is Mn^{2+}(α-Fe_2O_3) ; F1 is α-FeOOH and F6 is undoped α-Fe_2O_3.	142
Figure 4.5.	Room temperature magnetization curves of the synthesized Fe-Mn and iron oxide samples where MF1 is (α-FeOOH+ $MnFe_2O_4$); MF6 or MF7 were Mn^{2+}(α-Fe_2O_3) ; F1 is α-FeOOH and F6 is undoped α-Fe_2O_3	144
Figure 4.6.	Catalytic activity of the Mn doped α-Fe_2O_3 samples MF6 and MF7 in relation to the corresponding undoped iron oxide, for decomposition of H_2O_2 in presence and absence of sunlight.	145
Figure 4.7.	TG-DTA profile of OMS-2 in oxygen atmosphere.	149
Figure 4.8.	TG profile of OMS-2 and Fe-OMS-2 in oxygen atmosphere.	150
Figure 4.9.	Infrared spectra of OMS-2 and Fe doped OMS-2.	151

	Figure	Page No.
Figure 4.10.	X-ray diffraction patterns of undoped OMS-2 and Fe doped OMS-2.	152
Figure 4.11.	N_2 adsorption desorption and pore size distribution profiles (inset) of (a) OMS-2 (b) 0.3% Fe-OMS-2.	153
Figure 4.12.	N_2 adsorption desorption and pore size distribution profiles (inset) of (a) 2.5% Fe-OMS-2 (b) 3.5% Fe-OMS-2.	154
Figure 4.13.	TEM images of (A) OMS-2 (B) 0.3% Fe-OMS-2 (C) 2.5% Fe-OMS-2 (D) 3.5% Fe-OMS-2.	156
Figure 5.1:	Cyclic voltammetry profiles of carbons at different scan rate recorded in 0.5 M Na_2SO_4 (a) GBC_K (b) GBC_Z at different scan rates.	166
Figure 5.2:	Cyclic voltammetry profiles of glycerol based carbons at different scan rate recorded in 0.5 M Na_2SO_4 (a) GBC_{S1} (synthesized using surfactant CTAB) (b) GBC_{S2} (synthesized using surfactant SDS).	167
Figure 5.3:	Cyclic voltammetry profiles of commercially available carbons at different scan rates recorded in 0.5 M Na_2SO_4 (a) SWCNT (b) VulcanXC72R.	171
Figure 5.4:	Plot of capacitance as a function of scan rate.	172
Figure 5.5:	Cyclic voltammograms of OMS-2 and Fe-OMS-2 in 0.5 M Na_2SO_4 at a scan rate of 2 mV s^{-1}.	173
Figure 5.6:	Cyclic voltammetry profile of OMS-2 and GBC_Z composites at a scan rate of 2 mV s^{-1}.	175
Figure 5.7:	Plot of capacitance versus % OMS-2 in OMS-2-GBC_Z composites. (a) decrease in capacitance as % MnO2 increase (b) determination of optimum composition to get maximum capacitance for the composite.	176
Figure 5.8:	X-ray diffraction patterns of GBC_K and $Ru_{GBCK.}$	180
Figure 5.9:	N_2 adsorption desorption isotherm and pore size distribution profiles (a) Ru/GBC_K (b) Ru/GBC_Z	181

	Figure	Page No.
Figure 5.10:	N_2 adsorption desorption isotherm and pore size distribution profiles (a) Ru/GBC_{S1} (b) Ru/GBC_{S2}.	182
Figure 5.11:	FE-SEM (a) Ru/GBC_K (b) Ru/GBC_Z (c) Ru/GBC_{S1} (d) Ru/GBC_{S2}.	184
Figure 5.12:	Tafel polarization studies for methanol oxidation reaction in 0.5 M H_2SO_4 on GBC supported Ruthenium catalyst.	186
Figure 5.13:	Tafel plots of bimetallic composites studied for methanol electro-oxidation reaction in 0.5 M H_2SO_4.	187
Figure 5.14:	The cyclic voltammetry profiles of the bimetallic catalyst composites in 0.5 M H_2SO_4 solution and 1 M methanol at a scan rate of 2 mV s^{-1}. (a) Pt_C - Ru_C (b) Pt_C - Ru_{GBCK} (c) Pt_C - Ru_{GBCZ} electrodes.	188
Figure 5.15:	Tafel polarization studies for ethanol oxidation reaction using Ru on various samples in acidic medium.	192
Figure 5.16:	The CV profiles of Pt_C and Pt_C - Ru_{GBCK} electrodes in 0.5 M H_2SO_4 solution and 1 M ethanol at a scan rate of 2 mV s^{-1}.	195
Figure 5.17:	The CV profile of Pt_C - Ru_{GBCK} electrode shown in relation to the Pt_C-Ru_C electrocatalyst in 0.5 M H_2SO_4 solution and 1 M ethanol at a scan rate of 2 mV s^{-1}.	195
Figure 5.18:	Tafel plots for ethanol electro-oxidation on the synthesized composite catalysts.	197
Figure 5.19:	Tafel plots of different catalysts for ethanol oxidation; the electrolyte was 1M ethanol and 0.5 M H_2SO_4.	197
Figure 5.20:	XRD pattern of Pt/C, Ru/C, Mn OMS-2 and the composite Pt-Ru-MnOMS-2/C.	200
Figure 5.21:	Cyclic voltammogram for ethanol oxidation reaction in 0.5M H_2SO_4 for Pt_C-Ru_C-Mn-OMS-2 in relation to OMS-2 and Pt_C-Ru_C catalysts.	202

List of Tables

	Table	Page No.
Table 1.1:	Properties of some literature reported activated carbon synthesized from natural sources.	8
Table 2.1:	Review of some adsorption and kinetic models.	49
Table 2.2:	The assignments corresponding to different frequencies observed in the infra-red spectra of glycerol based carbons.	56
Table 2.3:	The values of surface area, pore volume and pore size of GBC-120 and GBC-350 from BET analysis.	58
Table 2.4:	Values of various adsorption isotherm parameters during adsorption of methylene blue on GBC-120.	66
Table 2.5:	Evaluation of thermodynamic parameters during adsorption of methylene blue on GBC-120 at various temperatures.	70
Table 2.6:	Kinetic parameters obtained from application of pseudo first and pseudo second order kinetic models for adsorption of MB on GBC carbons.	77
Table 3.1:	Parameters obtained from Raman spectra of activated glycerol based carbons and commercial carbon Vulcan XC72R.	93
Table 3.2:	The assignments corresponding to different frequencies observed in the infrared spectra of the activated glycerol based carbon.	96
Table 3.3:	Textural properties obtained from BET analysis of glycerol based carbons GBC_K, GBC_Z and GBC-800.	101
Table 3.4:	Elemental analysis data obtained from EDS analysis of glycerol based carbons.	103
Table 3.5:	Textural properties obtained from BET analysis of glycerol based carbons GBC_{S1} and GBC_{S2}.	112

	Table	Page No.
Table 3.6:	Values of Langmuir adsorption isotherm and Freundlich adsorption isotherm parameters during adsorption of methylene blue on activated glycerol based carbons GBC_K and GBC_Z.	120
Table 3.7:	Kinetic parameters obtained from application of Pseudo First order and second order kinetic models.	123
Table 4.1:	Synthesis, XRD and TEM characteristics of the Fe-Mn oxide samples.	138
Table 4.2:	Synthesis and catalytic activity of the samples in relation to surface area, porosity and magnetic characteristics.	143
Table 4.3:	% Fe and % Mn in Fe doped OMS-2 obtained from ICP-AES analysis.	148
Table 4.4:	Thermal analysis of pure and Fe doped OMS-2 samples.	150
Table 4.5:	The estimated values of surface area, porosity and Scherrer crystallite sizes of OMS-2 and Fe doped OMS-2.	155
Table 5.1:	Surface characteristics and capacitance (mF cm^{-2}) of carbon materials.	169
Table 5.2:	BET surface area and Specific capacitance of OMS-2 and Fe doped OMS-2.	173
Table 5.3:	Enhancement in capacitance of the GBC carbons when made into a composite with 1% OMS-2.	177
Table 5.4:	Surface area, porosity data of synthesized Ru/GBCs samples.	183
Table 5.5:	Current produced i_{100} in µ amps, at overpotential of 100 millivolts for Ru/Cs and its composites with Pt/C catalysts.	186
Table 5.6:	Parameters from cyclic voltammograms of methanol electro-oxidation reaction on the bimetallic catalysts investigated.	188
Table 5.7:	Current produced in µ amps, at overpotential of 100 mV for different catalysts for ethanol oxidation reaction.	192
Table 5.8:	Current produced i_{100} in µ amps, at overpotential of 100 millivolts for various catalysts composition.	198

Table 5.9: Tafel slopes reported in literature for EOR [17, 18] 200

List of Schemes

	Scheme	Page No.
Scheme 1.1.	Dual pathway for ethanol electro-oxidation reaction in acidic medium on Pt catalyst	21
Scheme 2.1.	Flow chart for synthesis of the glycerol based carbons (GBC-120 and GBC-350).	50
Scheme 3.1.	Synthesis and activation of glycerol based carbons.	87
Scheme 4.1.	Structural transformation of the 'as prepared' sample MF1 into a Mn^{2+} doped α-Fe_2O_3 (MF7); ccp and hcp in the illustration is indicative of structures formed by cubic and hexagonal close packing of O^{2-} ions respectively.	140
Scheme 4.2.	Mechanism of decomposition of hydrogen peroxide	146

Electrochemical and Adsorption studies of Glycerol based carbons and its composites with Fe-MnO_x and OMS-2

CHAPTER I

GENERAL INTRODUCTION

Overview

There is abundant glycerol generated as a byproduct during transesterification process in bio-diesel industry.

Reaction: Triglyceride + methanol ⟶ Mixture of fatty esters + glycerol

Recently glycerol is utilized in synthesis of carbon material as a solid acid catalyst in organic transformations.

Conventionally activated carbon is produced from coal and biomass. In the present investigation glycerol based activated carbons are being developed as alternative carbon materials to address concern related to environmental issues and energy.

The work of the thesis therefore deals with

- Conversion of glycerol into activated carbons by adopting suitable synthetic strategies
- Evaluation of adsorption capabilities of the glycerol based carbons or GBC^s
- Synthesis of suitable metal oxides to make composites with GBC^s
- Evaluation of catalytic/electrochemical activity of the synthesized materials

In view of the above, the present introductory chapter concerns understanding required and the literature status in relation to

- Activated carbons
- Pure and modified manganese oxides such as
    - i α-MnO_2 also known as Mn OMS-2
    - ii Fe modified manganese oxides
- Electrochemical properties
    - i Capacitance and
    - ii Electrocatalysis related to direct alcohol fuel cells

In recent times there is increasing awareness for the need to conserve the depleting energy resources as well as environmental protection. Thus material research is focused on developing materials for environmental application, for energy conversion systems like fuel cells and energy storage technologies like batteries, supercapacitors etc. Energy research is significant due to increasing demand for cleaner energy as planet is facing after effects of fossil fuel energy production process. Although considerable amount of work has been done in producing renewable energy and the possibility of renewable energy linking demand and energy supply has been stated. However the upfront cost of technologies to be used to generate energy from renewable sources is skyscraping. Also renewable energy sources have geographic limitation in addition to storage issue and intermittent nature of renewable energy sources. Thus a need for alternative energy source arises. Energy policy of every nation takes into account three important factors which are energy security, safeguarding the environment and the economic growth.

Carbon materials are class of distinctive materials and synthesis conditions can be optimized to design it for a specific application. Activated carbons are traditionally used for adsorption of pollutants. Their adsorption ability is determined by properties such as high surface area, porosity and surface functionalities. The presence of functional groups like –OH, -COOH etc makes carbon hydrophilic. Carbons are also studied as a solid acid catalyst for different organic transformation and its use as a catalysts support in fuel cell is well known.

1.1 Activated carbon

Activated carbons can be defined as porous amorphous materials with disorganized graphitic sheets. Graphite is a 3D structure consisting of several hexagonal layers of sp^2 carbons, held by Van der Waals forces. A single 2D layer of graphite is graphene. Activated carbons are generally obtained by carbonization of biomass followed by physical or chemical activation. Thus carbonization and activation are two main steps involved in the synthesis of activated carbon.

Carbonization is at first carried out by converting the initial carbonaceous raw matter to carbon by removing its non carbon components. The process involves either through

(i) Chemical treatment or

(ii) Thermal treatment in limited supply of air or in inert atmosphere

Carbonization generally results in obtaining carbon with low surface area and poorly developed pore structure. Porosity can be enhanced as well as can be tuned by employing suitable activation methods. The properties of the activated carbon produced depend on

(i) Type of raw material

(ii) Activating agent and

(iii) Activation conditions

Physical activation processes involves treating a carbonized material at high temperature between 600 – 1100 ^oC in inert atmosphere like N_2 or Ar, air atmosphere, CO_2 or steam. Steam activated carbon obtained from olive bagasses showed maximum surface area of 1106 $m^2\ g^{-1}$ at activation temperature of 900 ^oC [1]. It was also observed during the comparative study of chemical and physical activation of coconut shell carbon that pore size distribution in coconut shell carbon could be more precisely tuned

by physical activation method [2]. But physical activation also leads to low degree of compactness in carbon structure.

Chemical activation methods include use of different chemical activating agents like H_2SO_4, H_3PO_4, KOH, $ZnCl_2$ etc. During activation the raw material is saturated with the chosen chemical activating agent and the mixture is further treated at temperature between 400-800 ^oC in inert atmosphere. The chemically activated carbon often shows higher surface area along with improved porosity. The degree of initial saturation with activating agent mostly decides pore size distribution. Another advantage is that the product obtained is in high yield and the synthesis is carried out at considerably lower activation temperature and requires less activation time. This makes chemical activation method preferable over physical activation methods. The commercially available activated carbons are often reported to have a surface area in the range of 800 – 1500 $m^2 g^{-1}$ with considerable microporosity. The most commonly preferred chemical activating agents in literature are KOH and $ZnCl_2$ which are discussed here.

1.1.1 KOH activation

Among different chemical activating agents investigated, activation of carbon using KOH has gained wide attention as it produces carbons with high surface area (1500 – 3200 $m^2 g^{-1}$) and evolved porosity. Activating process involves impregnation of the raw material with excess aqueous KOH followed by treatment at a temperature between 500 – 900 ^oC. KOH activated carbon find application in water purification [3], energy storage [4] and supercapacitors [5]. KOH activation is considered to be effective method to create micropores as well as mesopores within the carbon framework.

KOH activated carbon having high surface area (1500-4000 m^2 g^{-1}) and ~ 90 % microporosity has been synthesized from coal or coke [6, 7]. Microwave induced KOH activation has also been carried out. Theses microporous carbons are reported to show high adsorption for methylene blue [8]. Carbon from gulfweed prepared by KOH activation were reported to shows good performance as supercapacitor with value as high as 395 F g^{-1} [9]. KOH has also been used for reactivation of carbons. Thus commercial activated carbon having surface area of 1460 m^2 g^{-1} when re-activated with KOH showed remarkable increase in surface area close to 3000 m^2 g^{-1} and also increase in pore volume from 1.66 to 2.70 cm^3 cm^{-3} [10].

Mechanism of KOH activation

Mechanism of KOH activation has not been well understood as too many variables are involved in the experimental procedures implemented. It is generally assumed that during activation, carbon and KOH undergo redox process wherein KOH is reduced to metallic K and carbon is oxidized to carbon dioxide, carbon monoxide and carbonates. Otowa et al. [11] proposed an activation mechanism according to which initial heating at a temperature of 400 ^oC could lead to dehydration of KOH to form K_2O and H_2O.

$$KOH_{(s)} \longrightarrow K_2O_{(s)} + H_2O_{(g)} \quad (1)$$

At temperature ~ 400 ^oC water is in gaseous form. It will react with carbon as per the water gas reaction. It leads to the formation of water gas (H_2 and CO).

$$C_{(s)} + H_2O_{(g)} \longrightarrow H_{2(g)} + CO_{(g)} \quad (2)$$

This reaction is followed by water gas shift reaction which converts poisonous CO to CO_2 by producing flammable H_2 gas

$$CO_{(g)} + H_2O_{(g)} \longrightarrow H_{2(g)} + CO_{2(g)} \quad (3)$$

Further the dehydration of KOH to K_2O take place at a temperature of about 400 ^oC and CO_2 may react with K_2O to give potassium carbonate.

$$CO_2 + K_2O \longleftrightarrow K_2CO_3 \quad (4)$$

During activation process, at a temperature of about 600 ^oC all of the KOH is consumed. At a temperature higher than 700 ^oC, K_2O was reduced to K. The possible reactions include

$$C + K_2O \longrightarrow 2K + CO \quad (5)$$

$$H_2 + K_2O \longrightarrow 2K + H_2O \quad (6)$$

The conversion of carbon into gaseous CO and CO_2 leads to the development of pores in carbon. At a temperature of ~ 800 ^oC, there is complete decomposition of K_2CO_3.

$$K_2CO_3 + 2C \longrightarrow 2K + 3CO \quad (7)$$

Intercalation of potassium metal into carbon structure leads to widening of carbon atomic layers thereby inducing porosity.

Lozano-Castelló et al. [12] observed evolution of CO, CO_2 and H_2 gas by TPR/He and TPR/H_2 studies and the most probable reaction during chemical activation by KOH is represented as

$$6KOH + 2C \longrightarrow 2K + 3H_2 + 2K_2CO_3 \quad (8)$$

1.1.2 $ZnCl_2$ activation

Chemical activation using $ZnCl_2$ activating agent is also well investigated as it produces activated carbon with appreciable surface area and microporosity. Activation process has been exploited to prepare activated carbon using different carbon precursors. It is observed that the impregnation step during activation is a key, as the impregnation ratio have significant effect on microporosity of the final activated carbon. Several research groups highlighted the importance of $ZnCl_2$ activated carbon in adsorption of dyes [13-16], capacitors [17-18] and for removal of polluting species such as nitrates [19], 2-Chlorophenol [20], sulfates [21] and heavy metal ions such as Cr(VI) [22]. Further $ZnCl_2$ activated carbon from almond shells, gave a better yield of the final product [22]. Surface areas in the range 600 - 2500 m^2 g^{-1} have been reported following $ZnCl_2$ activation as summarized in Table 1.1.

Table 1.1: Properties of some literature reported activated carbons synthesized from natural sources.

Carbon precursor	**Textural properties**		**References**
	Surface area ($m^2 g^{-1}$)	**Porosity/pore volume ($cm^3 g^{-1}$)**	
Glucose	~ 2500	1.37	[17]
Coconut coir pith	910	0.363	[20]
Cellulose	916	0.133	[22]
Rise husk	1136	--	[23]
Kraft lignin	1800	~1.8	[24]
Oil palm shell	1429 – 1134	0.74 – 0.62	[25]
Peat	1000	0.5	[26]
Peanut shell	1642	0.42	[27]
Tobacco stem	1347	0.41	[28]
Coffee residue	915	1.00	[29]
Sugar beet bagasse	1697	--	[30]
Tectona grandis sawdust	~600	0.44	[31]
Tamarind wood	1322	1.042	[32]
Cherry stones	1971	0.74	[33]
Tomato processing solid waste	1093	1.569	[34]

1.2 Carbon materials from glycerol

For generating newer carbon materials, source of carbon or raw material used for synthesis is one of the most considered factors considering the cost and quality of the final product. Research in this field is captivating as properties of carbon materials can be tuned by modifying the synthesis conditions. Carbon materials find application in many areas which makes them invaluable. In literature, considerable amount of work has been reported on synthesis and applications of different carbon forms like activated carbon, carbon nanotubes, carbon nanofibers, carbon xerogels, carbon aerogels, graphene oxide, graphene etc. The present investigation is focused on synthesis of carbon materials from glycerol, as glycerol is one of the byproducts produced in huge amounts in bio-diesel industry. The overproduction of glycerol makes it our responsibility to transform it into a suitable material of interest.

Catalytic activity of glycerol based carbon as solid acid catalysts was examined for various organic transformations. SO_3H group on the surface of glycerol based carbon makes it highly efficient and reusable solid acid catalyst with its reusability compared to mineral acid catalysts like H_2SO_4.

Devi et al. [35] prepared glycerol based carbon by insitu partial carbonization and sulphonation of glycerol for its utilization as a solid acid catalyst for esterification reaction. 99% conversion was observed for esterification of palmitic acid with methanol using 10% weight of glycerol based carbon catalyst. Further study on glycerol based carbon catalyzed acetylation of alcohol, phenol and amines has been reported [36]. The catalyst showed good activity and reusability with yield of 92 – 89 % after 5 cycles. Glycerol based carbon catalyst was also investigated for its activity towards chemoselective synthesis of pentaerythritol (PE) diacetals in methanol at reflux

temperature and recovered catalyst showed good activity for 5 cycles with pre-treatment [37]. Its applicability as a catalyst for wet peroxide oxidation (WPO) by tuning its textural properties via calcining at different temperature [38]. It was reported that when as prepared glycerol based carbon was thermally treated in air at a temperature of 300 ^{o}C ($GBCM_{300}$), it leads to remarkable increase in surface area and microporosity. This sample was potent catalyst for degradation of 2-nitrophenol showing up to 80% conversion. $GBCM_{300}$ was employed for catalytic wet oxidation process and was observed that activity of the catalyst can be recovered by regenerating through thermal treatment in air at 300 ^{o}C for 2 hours.

Further glycerol based carbons were explored for their application in adsorption. Alvarez-Torrellas et al. [39] examined various glycerol-based carbons for removal of flumequine and tetracycline by adsorption. Synthesis of glycerol based carbons using different acids like H_2SO_4, H_3PO_4, HCl and CH_3COOH were investigated. Synthesized carbons were further physically activated at different temperature in N_2 atmosphere and employed for adsorption of volatile organic compounds and Cr (VI) removal [40]. Glycerol based activated carbons were observed to outperform commercial ACs in adsorption. Impact of different dehydration acid, its concentration and activation environment on textural and surface properties gives information to prepare tailored activated carbons.

1.3 OMS-2 and Fe-Mn Oxides

(i) Mn OMS-2 or α-MnO_2

Molecular sieves are porous materials with small pores of molecular dimensions and having uniform shape and size. These materials are attractive due to their wide applicability in diverse areas. Zeolites are known as molecular sieves which are basically aluminosilicates build by assembly of Si and Al tetrahedra. Zeolites find application in different area like as catalysts in chemical industry [41], in oil refining [42], as adsorbent [43], ion exchanger [44] and for H_2 storage [45].

In manganese oxides, Mn occurs in +2, +3 and +4 oxidation states and naturally occurring manganese oxide/ hydroxides are involved in the environmental geochemistry [46].

In all manganese oxides the basic unit is distorted octahedral of O^{2-} and/or OH^- coordination such as [MnO_6] or [$Mn(O,OH)_6$]. The sharing of these octahedra either by linking via corner or edges leads to different structural features in manganese oxides. The common polymorphic form of manganese dioxide (Mn in +4 oxidation state), are known as α, β or γ-MnO_2. Of these α-MnO_2 also known as Mn(OMS-2) is being investigated here to make composites with the synthesized carbons. α-MnO_2 structure is made up series of tunnels formed due to corner sharing of edge shared [MnO_6] octahedra which extend along c-axis of tetragonal unit cell. The tunnels have dimensions of the type [2×2]. During catalysis these tunnels [2×2] enable the ions or the intermediates to diffuse. Naturally occurring α-MnO_2 samples like *hollandite* normally contain big cation Ba^{+2} in majority along with other elements (eg. K^+) in minor quantity. Foreign ion or considerable amount of water is known to give stability to the structure of α-MnO_2.

(ii) Fe-Mn oxides & α-Fe_2O_3

Iron oxides are interesting as they have tunable properties such as optical, electrical, magnetic, electrochemical and catalytic. Among different polymorphic forms of ferric oxide, the most widely investigated includes α-Fe_2O_3 (hematite) and γ-Fe_2O_3 (maghemite) [49-50]. Further, α-Fe_2O_3 is antiferromagnetic below Morin temperature (260 K) and shows a very weak ferromagnetic behavior (< 1 emu g^{-1}) between 260 K and the Neel temperature (950 K). The enhanced magnetic behavior is seen following doping of transition metal ion like Mn^{2+}, Cu^{2+} etc. [49]. The various properties and applications of α-Fe_2O_3 have been recently reviewed [50]. Several methods have also been adopted for synthesis of iron – manganese oxides and manganese ferrites to obtain materials of higher magnetism and catalytic activity [47-52]. Thus Yuping et al., reported formation of a mixture of α-Fe_2O_3 and $MnFe_2O_4$ phases produced from a Fe-Mn containing slurry whose magnetic properties could be of interest as catalysts or as catalyst support material [53]. Iron-manganese mixed oxide catalysts were also studied for catalytic combustion of ethanol and the catalytic activity was found to be greatly influenced by the Fe:Mn ratio of the mixed oxide formed [54] and several other catalytic processes [55-56]. Fe (III) oxides are well known to show high activity for catalytic decomposition of H_2O_2 [57-58]; the activity being dependent on surface area and particle sizes [59-60]. Several synthetic strategies have been adopted to obtain hematite of high reactivity; methods such as surfactant assisted synthesis [58], combustion synthesis [61-62], sol-gel method [63-64], co-precipitation method [65] etc. These methods have to be chosen considering their cost effectiveness and methods that would avoid or minimize emission of hazardous gases. The recent trend is to adopt

simple aqueous solution methods of co-precipitation to obtain α-Fe_2O_3, as that affords better control over synthesis conditions, product morphology and particle sizes [65-66].

1.4 Fuel cell

A fuel cell is an electrochemical cell in which electrical energy is generated by a chemical reaction of a fuel at anode and oxidant at cathode. A common fuel used includes either hydrogen or methanol or ethanol and the oxidant is generally air or oxygen. The products of oxidation are mainly H_2O and CO_2 in case of alcohol fuel cells. Thus fuel cell technology is cleaner and therefore most widely researched. Fuel cells generally have practical energy efficiency between 40 - 60 % making it attractive in energy sectors. Fuel cells basically consist of anode, cathode and an electrolyte. Thus classification of fuel cells is mostly based on type of electrolyte used or the temperature. Based on the operating temperature they are classified as high and low temperature fuel cells. Most widely studied fuel cells are hydrogen-oxygen fuel cells and direct methanol fuel cells based on polymer membrane electrolytes. A direct methanol fuel cell has advantage with respect to availability of methanol fuel and its ease of handling. Fig. 1.1 depicts simple fuel cell.

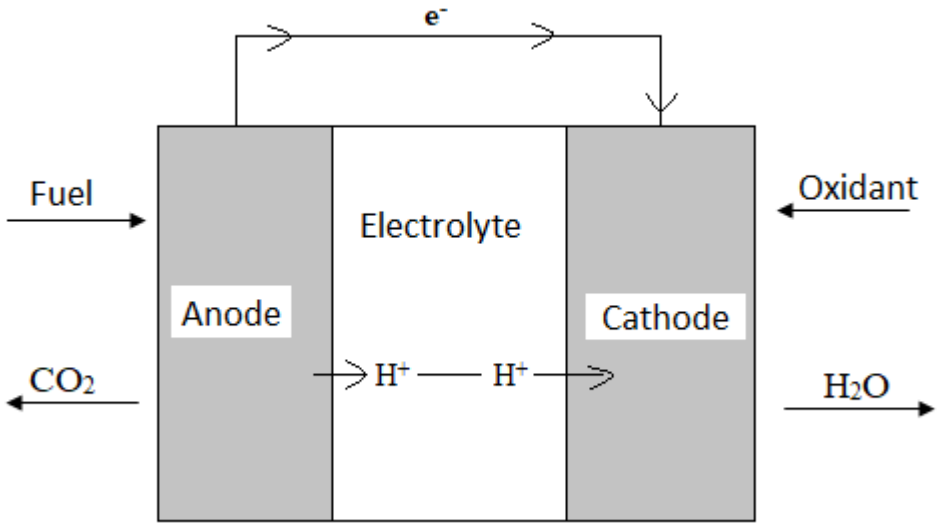

Fig. 1.1: Schematic representation of a fuel cell.

The fuel is oxidized at the anode and the released species (H^+ and e^-) move to the cathode side and get reduced to H_2O by reaction with the oxidant O_2 and thus generate energy. The efficiency of oxidation and reduction reactions at two electrodes is directly determined by the activity of the electrocatalysts. Noble metal catalysts like Pt, Ru are still the most effective electrocatalysts and therefore are studied extensively. But Pt is a very costly metal and thus becomes expensive part in the total cost of fuel cell operation. Additionally Pt is highly sensitive to the intermediate oxidation product CO and further oxidation of CO to CO_2 is a crucial step. The operating temperature range for direct methanol fuel cell (DMFC) is 60-90 ^oC with power up to 100 W. The overall electrode reactions for methanol or ethanol fuel are given below

For methanol oxidation reaction

At anode: $CH_3OH + H_2O \longrightarrow CO_2 + 6\ H^+ + 6\ e^-$

At cathode: $3/2\ O_2 + 6\ H^+ + 6\ e^- \longrightarrow 3\ H_2O$

Overall reaction: $CH_3OH + 3/2\ O_2 \longrightarrow CO_2 + 2\ H_2O$

For ethanol oxidation reaction

At anode: $CH_3CH_2OH + 3\ H_2O \longrightarrow 2\ CO_2 + 12\ H^+ + 12\ e^-$

At cathode: $3\ O_2 + 12\ H^+ + 12\ e^- \longrightarrow 6\ H_2O$

Overall reaction: $CH_3CH_2OH + 3\ O_2 \longrightarrow 2\ CO_2 + 3\ H_2O$

1.4.1 Mechanism of electro-oxidation of methanol

Extensive study to understand electro-oxidation of methanol has been done. Pt is known to show highest activity for methanol electro-oxidation in DMFC. Not all the electrode materials are active adsorbents for adsorption of methanol. Only Pt and Pt based electrocatalysts have been found to exhibit activity as well as stability [67]. During oxidation of methanol to CO_2, 6 electrons are involved and thus it must include many steps with various intermediates [68]. Bagotzky and Vassilyer [69] said that methanol chemisorptions on Pt occurs following dehydrogenation by the reaction,

$$CH_3OH \longrightarrow C\text{-}OH + 3H_{ads}$$

And water discharge in acidic solution occurs at positive potentials giving OH_{ads} species

$$H_2O \longrightarrow OH_{ads} + H^+ + e^-$$

Intermediates such as HCOOH and H_2CO were detected when oxidation process was monitored with mass spectroscopy [70]. Measurements done using gas chromatography also showed the species HCOOH, H_2CO, $HCOOCH_3$ and CO_2 [71]. Similar results were confirmed by HPLC analysis [72]. It was further proposed that H_2CO can react to produce CO_2 or HCOOH [73]. Oxidation of formic acid was investigated but no definite mechanism was proposed [74]. The intermediate CO produced during oxidation was strongly bonded to the Pt electrocatalyst surface and therefore oxidation of this intermediate was considered as rate determining step for complete oxidation to CO_2.

Additionally, oxide formation on Pt surface could also facilitate oxidation of CO to CO_2 as the platinum oxide occurs at the potential at which CO oxidation also takes place [75]. From XPS studies carried out by Goodenough et al [76] three Pt oxides were observed after the oxidation of methanol on Pt surface whereas before oxidation only two Pt oxides were noticed. This indicates that a unstable form of Pt oxide may oxidize CO, but subsequent investigation with Ag and Au metal catalyst couldn't confirm the mechanism [77].

Chen et al. reported formation of $HCOO^-$ intermediate for the first time during methanol oxidation on Pt electrode in acidic solution and it was observed to be reactive and responsible for oxidation to CO_2 [78]. They further used in-situ surface enhanced IR absorption spectra (SEIRAS) simultaneously with cyclic voltammetry to study the nature of intermediates adsorbed on the surface of the catalyst. IR bands associated with CO linearly and bridge bonded to Pt catalyst surface was observed. Decrease in the intensity of band due to CO decreased rapidly at more positive potential.

Parsons and Vandernoot (1988) also investigated mechanism of methanol electro-oxidation on Pt electrocatalyst in 1988 [79]. Methanol oxidation on Pt surface is believed to occur in order as follows:

$$CH_3OH + Pt_{(s)} \longrightarrow Pt\text{-}CH_2\text{-}OH + H^+ + e^- \quad (1)$$

$$Pt\text{-}CH_2\text{-}OH + Pt_{(s)} \longrightarrow Pt_2\text{-}CH\text{-}OH + H^+ + e^- \quad (2)$$

$$Pt_2\text{-}CH\text{-}OH + Pt_{(s)} \longrightarrow Pt_3\text{-}C\text{-}OH + H^+ + e^- \quad (3)$$

$$Pt_3\text{-}C\text{-}OH \longrightarrow Pt\text{-}CO + 2Pt_{(s)} + H^+ + e^- \quad (4)$$

$$Pt(s) + H_2O \longrightarrow Pt\text{-}OH + H^+ + e^- \quad (5)$$

$$Pt\text{-}OH + Pt\text{-}CO \longrightarrow Pt\text{-}COOH \quad (6a)$$

OR

$$Pt\text{-}CO + H_2O \longrightarrow Pt\text{-}COOH + H^+ + e^- \quad (6b)$$

$$Pt\text{-}COOH \longrightarrow Pt_{(s)} + CO_2 + H^+ + e^- \quad (7)$$

Based on the intermediates detected additional reactions that could occur includes

$$Pt\text{-}CH_2\text{-}OH \longrightarrow Pt_{(s)} + HCHO + H^+ + e^- \quad (8)$$

$$Pt_2\text{-}CH\text{-}OH + Pt\text{-}OH \longrightarrow 3Pt + HCOOH + H^+ + e^- \quad (9)$$

OR

$$Pt_2\text{-}CH\text{-}OH + H_2O \longrightarrow 2Pt_{(s)} + HCOOH + H^+ + e^- \quad (10)$$

$$Pt_3C\text{-}OH + Pt\text{-}OH \longrightarrow 3Pt_{(s)} + Pt\text{-}COOH + H^+ + e^- \quad (11a)$$

$$Pt_3C\text{-}OH + H_2O \longrightarrow 2Pt_{(s)} + Pt\text{-}COOH + H^+ + e^- \quad (11b)$$

Although Pt is widely investigated for electrocatalytic oxidation of methanol it creates a economic limitation for commercializing fuel cells. Therefore investigations have been carried out to explore alternative catalytic materials. Thus when Ir was studied, it showed much less activity compared to Pt and did not possess significant economic advantage [80]. Alloys of Pt with other metals were also examined for electrocatalytic activity. The choice of other metal was such that it could form surface oxide in the potential range of oxidation of methanol. Ru among others studied showed highest activity whereas when Pt alloyed with Ir and Os were observed to act as promoters [81]. FTIR study using Pt-Ru electrocatalyst [82] showed that during methanol electro-oxidation CO_{ads} on electrode surface was decreased at any given potential. However the frequency corresponding to bound CO increased. The effect was related to decreased π

bonding effect from Pt to CO. This make carbon electron deficient and thus nucleophilic attack of water on carbon further promotes CO oxidation at lower potential.

Analysis using ternary metal catalyst system with Pt-Ru has been investigated. Recently attention has turned to use of Pt and metal oxide composite catalyst. Pt deposited on hydrous WO_{3-X} was identified as a active catalysts for electro-oxidation of methanol [83]. Several studies with Pt incorporated oxides have also been carried out [84].

For more than three decades now the best electrocatalyst known for methanol oxidation is Pt-Ru alloy [85] and it has been employed for approx. 25 years in DMFC. These electrocatalysts are supported on carbon materials for better dispersion of catalysts particles. This can enhance the active surface area for catalysis and thus the amount of noble catalyst required is reduced. Catalyst support can not only affect morphology but also electronic conductivity during oxidation, mass transport as well as stability of metal nanoparticles. Therefore optimizing the quantity of carbon support for improved efficiency of fuel cell becomes important. Considering these aspects, different type of carbon supports have been investigated for dispersion of metal nanoparticles namely carbon nanotubes [86], mesoporous carbons [87], graphene [88], graphene-MWCNT hybrid support [89] etc. Zeng et al investigated hybrid support i.e. WO_3 doped ordered mesoporous carbon [90]. It was observed that hybrid support improves catalytic activity by mutual effect promoting mass-specific activity of the catalyst. Studies done using graphene or reduced graphene oxide supports showed that oxygen groups present on the surface of graphene or rGO can assist oxidation of adsorbed CO on Pt sites. Small Pt-based alloy nanoparticles well dispersed on graphene such as Pt-Ru/GNs, Pt-Pd/GNs, Pt-Ni/GNs, Pt-Fe/GNs, Pt-Sn/GNs etc. displayed superior electrocatalytic activity for methanol oxidation [91]. The oxygenated groups on graphene oxide acts as binding sites

for metal nanoparticles by improving their stability and also makes its very hydrophilic resulting in improved electrocatalytic activity. However facile synthesis route to prepare Pt on rGO is still a challenge.

Among various oxides investigated for their activity towards methanol electro-oxidation manganese dioxide is one of the good choices considering its properties like its good electrochemical behavior, proton electron intercalation properties and low cost. Additionally it is also well known chemical oxidation catalysts. Presence of MnO_2 on the surface of CNTs was observed to show improved proton conductivity of the catalysts and this further enhanced performance of the catalysts during oxidation of methanol [92]. Composite of Pt and MnO_2 showed better performance as MnO_2 was assisting in CO oxidation by producing OH_{ads} species [93] by a following reaction

$$H_2O_{ads} + MnO_2 \longrightarrow MnOOH + OH_{ads} + e^-$$

Such activity can be related to the presence of Mn^{+4}/Mn^{+3} redox couple.

Further studies using MnO_2 reported that the presence of MnO_2 in $Pt/MnO_2/CNTs$ composite catalyst presents higher electrochemical active surface area and superior methanol electro-oxidation activity [94]. Manganese octahedral molecular sieves found to be active for methanol electro-oxidation. For a composite of OMS-2 and 5% Ru it was concluded that Ru can act as nucleating centre for CO clustering within the framework of OMS-2 and promotes CO oxidation to CO_2 thereby enhancing its activity [95].

1.4.2 Electrocatalytic-oxidation of ethanol

Ethanol is an important and attractive fuel for direct alcohol fuel cell as it has advantages over methanol in terms of safety and ease of availability. It is a renewable bio-fuel and is relatively less toxic. It is produced in considerable amounts from sugar containing raw materials by fermentation [96]. It offers high energy density (8.01 kWh kg^{-1}) which is close to that of gasoline [97]. But major barrier in development of direct ethanol fuel cells (DEFCs) is slow reaction kinetics of ethanol electro-oxidation [98]. Thus detailed study on understanding reaction mechanism and structural parameters of active catalysts is important. Several instrumental techniques are adopted to elucidate the mechanism [99 - 105].

These studies have also shown that just as in case of methanol Pt or Pt based materials are better catalysts for electro-oxidation of ethanol [106]. A few mg cm^{-2} of Pt is found inevitable to obtain considerable activity for the electro-oxidation of alcohols in fuel cells [105]. Much study therefore has been also focused on introducing bimetallic catalysts thereby reducing Pt loading [107] along with developing catalysts support with high surface area which can promote catalysis [108].

Further studies on EOR suggested that ethanol could in principle be completely oxidized to CO_2 and water [109]. However Behm et al. studied EOR by combining cyclic voltammetry technique and potential step measurements of reaction transients observed that % selectivity range of oxidation of ethanol to CO_2 was only 0.5-7.5 % [110]. Thus practically ethanol does not react fully and is only partially oxidized to ethanol and probable redox reactions are as given below [109]

Thus

$C_2H_5OH \longrightarrow CH_3CHO + 2H^+ + 2e^-$

$½\ O_2 + 2H^+ + 2\ e^- \longrightarrow H_2O$

occurs at anode and cathode of fuel cell

Generally accepted dual-pathway mechanism for ethanol electro-oxidation on Pt based catalysts can be given as [111-116]:

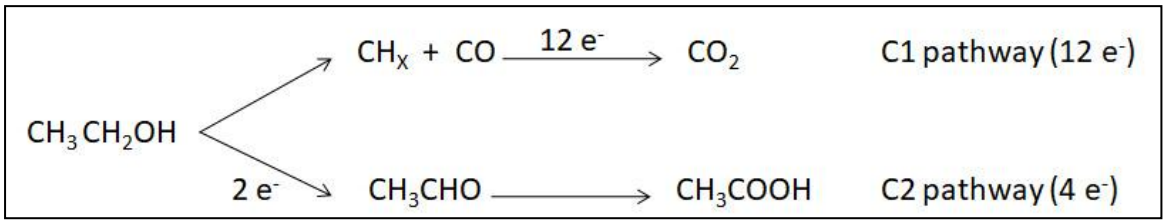

Scheme 1.1 Dual pathway for ethanol electro-oxidation reaction in acidic medium on Pt catalyst.

C1 pathway involves oxidation of ethanol to CO_2 by producing CO_{ads} intermediate and the process involves 12 electrons. On the other hand C2 pathway represents incomplete oxidation of ethanol to ethanal by giving two electrons followed by formation of ethanoic acid (acetic acid) by delivering four electrons without cleavage of C-C bond.

C1 and C2 pathway can be further elaborated as follows:

C1 pathway

$CH_3CH_2OH + 3H_2O \longrightarrow 2CO_2 + 12H^+ + 12\ e^-$

$CH_3CH_2OH + 5H_2O \longrightarrow 2HCO_3^- + 14H^+ + 12\ e^-$

$CH_3CH_2OH + 5H_2O \longrightarrow 2CO_3^{2-} + 16H^+ + 12\ e^-$

C2 pathway

$$CH_3CH_2OH + H_2O \longrightarrow CH_3COOH + 4H^+ + 4e^-$$

$$CH_3CH_2OH \longrightarrow CH_3CHO + 2H^+ + 2\,e^-$$

However ethanol electro-oxidation is a complex process where parallel reactions are occurring during oxidation thereby producing more than 40 possible intermediates [113].

The major intermediate formed on Pt catalyst has been identified as CO_{ads} while CH_3COOH and CH_3CHO have been detected [111-112]. In 1989, Iwasita et al., detected only linearly adsorbed CO during electro-oxidation of ethanol in $HClO_4$ on Pt [114]. It was further concluded that CO_2 and CH_3COOH were produced at high concentration of ethanol along with CH_3CHO as the main product [115].

Thus after several such investigations [99, 110, 115-117] it can be concluded that C2 pathway is dominant for EOR on Pt based electro-catalyst giving CH_3CHO and CH_3COOH as main products [118-119]. In strong alkaline medium first step is a cleavage of O-H bond of ethanol whereas in acidic medium it is cleavage of C_α-H bond [120-121].

Thus the possible reactions for electro-oxidation of ethanol on Pt surface can be given as follows

$$CH_3CH_2OH + Pt_{(s)} \longrightarrow Pt\text{-}O\text{-}CH_2\text{-}CH_3 + H^+ + e^- \qquad (1a)$$

OR

$$CH_3CH_2OH + Pt_{(s)} \longrightarrow Pt\text{-}CHOHCH_3 + H^+ + e^- \qquad (1b)$$

followed by any of the following three possibilities

$$Pt\text{-}CHOHCH_3 \longrightarrow Pt + CH_3CHO + H^+ + e^- \quad (2a)$$

OR

$$Pt\text{-}CHOHCH_3 + Pt \longrightarrow Pt_2\text{-}COHCH_3 + H^+ + e^- \quad (2b)$$

OR

$$Pt\text{-}CHOHCH_3 + Pt_{100}(H) \longrightarrow Pt\text{-}CO + CH_4 + 2H^+ + 2e^- \quad (2c)$$

Pt-based materials are still the best for ethanol electro-oxidation irrespective of the electrolyte media [122]. Other metals investigated for EOR includes Pd, Ru, Rh, Ni, Sn, Bi, Ir, Au, Ce, Fe, Au and Ni [123]. PtRu [123] and PtSn [124] are found to be efficient for EOR by bi-functional performance. These alloys promote CO oxidation to CO_2 but decreases in Pt content lowers C-C bond activation and therefore lowers the production of CO_2 [124]. Different metal oxides like RuO_2, CeO_2, ZrO_2 have also been analyzed and are known to enhance the activity [125]. Adzic and co-workers studied Pt-Rh-SnO_2/C for EOR in acidic medium, where high activity was obtained and it was related to effective cleavage of C-C bond for a composition of Pt:Rh:Sn is 3:1:4 [126].

1.5 Supercapacitors

Supercapacitors are electrochemical devices which can store energy by accumulation of charges at the electrode-electrolyte interfaces or by surface reversible redox reactions. However based on the storage mechanism and the type of material, supercapacitors can be classified as [127-128]

i Electrical double layer capacitors (EDLC)
ii Pseudo-capacitors
iii A combination of both EDLC and Pseudo-capacitors

In practical supercapacitors, charge storage occurs through both the mechanisms simultaneously [129].

Electrical double layer capacitor stores and deliver energy by adsorption and desorption of ions at the surface of the electrode in the electrochemical double layer [130–140]. In the electrochemical cell, double layer is created when the potential is applied to the electrode which causes ions of the electrolyte to diffuse towards the charged electrode surface [141-142]. In order to achieve high energy storage capacity, supercapacitor electrode should have high surface area and well developed porosity [143]. Thus activated carbons which are porous with considerably high specific surface area and good electrical conductivity are widely studied for supercapacitor applications [144]. The size and geometry of the pores in carbon materials are considered to be important factors in addition to its surface area [140]. Today activated carbon obtained from coconut shell is used as active material employed in almost all supercapacitor devices. Due to the economical factor, use of coconut shell activated carbon for supercapacitor applications still prevails. However in recent times, attention is being focused on graphene based electrode materials for supercapacitors. Pseudo-capacitors store energy faradaically. Thus redox reactions occur on the electrode generating charges which

transfer across the electrical double layer. An electrochemically active material for pseudocapacitance include transition metal oxides and conducting polymers. Transition metal oxides which are on the forefront of supercapacitance research include oxides such as RuO_2, MnO_2, NiO, Co_3O_4 etc which show variable oxidation states [145-148]. RuO_2 exhibit highest capacitance but its high cost limits its extensive application [149]. Thus much research is focused on MnO_2 which is inexpensive, environmentally friendly and also possesses high energy density. However in absence of conductive additives it shows poor electrical conductivity [150]. Thus composite of MnO_2 with a good conductive materials like activated carbons were expected to show enhanced electrochemical capacitance. Deng et al. [151] investigated MnO_2/graphene composite electrode and maximum specific capacitance of 218 F g^{-1} was reported. The composite electrode of MnO_2 and reduced graphene oxide synthesized via different methods showed enhanced supercapacitance performance with a specific capacitance in the range 170-500 F g^{-1} [152-154]. The composite electrode materials consisting of carbon and metal oxides, offer enhanced specific capacitance, high energy density and better rate capability [154]. Thus developing a good supercapacitor material should focus on developing suitable electrode composites to make hybrid capacitors, involving sustainable materials. Different factors to be considered for developing metal oxide-carbon composite electrodes include

- Optimization of pore structure of carbon
- Electrical conductivity of carbon
- Controlling thickness of metal oxide in the composite electrode
- Extending carbon-oxide interfacial area

References

[1] H. Demiral, İ. Demiral, B. Karabacakoğlu, F. Tümsek, *Production of activated carbon from olive bagasse by physical activation*, Chem. Eng. Res. Des. 89 (2011) 206-213.

[2] M. J. Prauchner, F. Rodríguez-Reinoso, *Chemical versus physical activation of coconut shell: A comparative study*, Micropor. Mesopor. Mat. 152 (2012) 163-171.

[3] T. Otowa, Y. Nojima and T. Miyazaki, *Development of KOH activated high surface Area carbon and its application to drinking water purification*, Carbon 35 (1997) 1315-1319.

[4] J. Wang, S. Kaskel, *KOH activation of carbon-based materials for energy storage*, J. Mater. Chem. 22 (2012) 23710-23725.

[5] E. Frackowiak (2007) *Carbon materials for supercapacitor application*, Phys. Chem. Chem. Phys. 9 (2007) 1774-1785.

[6] A. N. Weunerberg, T. M. O'Grady, U. S. Patent 4, 082, 694 Apr. 4, 1978.

[7] F. Kraehenbuehl, H. F. Stoeckli, *The use of immersion calorimetry in the determination of micropore distribution Of carbons in the course of activation*, Carbon 24 (1986) 483-488.

[8] A. Khasri, O. S. Bello, M. A. Ahmad, *Mesoporous activated carbon from Pentace species sawdust via microwave-induced KOH activation: optimization and methylene blue adsorption*, Res. Chem. Intermed. 44 (2018) 5737-5757.

[9] S. Li, K. Han, P. Si, J. Li, C. Lu, *High–performance Activated Carbons Prepared by KOH Activation of Gulfweed for Supercapacitors*, Int. J. Electrochem. Sci. 13 (2018) 1728 – 1743.

[10] B. Buczek, *Preparation of active carbon by additional activation with potassium hydroxide and characterization of their properties*, Adv. Mater Sci Eng. (2016) 1-4, Article ID 5819208.

[11] T. Otowa, R. Tanibata, M. ltoh, *Production and adsorption characteristics of MAXSORB: high-surface-area active carbon*, Gas Sep. Purif. 7 (1993) 241-245.

[12] D. Lozano-Castello, J. M. Calo, D. Cazorla-Amorós, *A. Linares-Solano, Carbon activation with KOH as explored by temperature programmed techniques and the effects of hydrogen*, Carbon 45 (2007) 2529-2536.

[13] Y. Ma, *Comparison of Activated Carbons Prepared from Wheat Straw via ZnCl2 and KOH Activation*, Waste Biomass Valori. 8 (2017) 549-559.

[14] D. Das, D. P. Samal, B. C. Meikap, *Preparation of Activated Carbon from Green Coconut Shell and its Characterization* J. Chem. Eng. Process Technol. 6 (2015) 1-7.

[15] K. Karthick, C. Dinesh, C. Namasivayam, *Utilization of $ZnCl_2$ activated Jatropha husk carbon for the removal of reactive and basic dyes: Adsorption equilibrium and kinetic studies*, Sustain. Environ. Res. 24 (2014) 139-148.

[16] M. Khodaie, N. Ghasemi, B. Moradi, M. Rahimi, *Removal of methylene blue from wastewater by adsorption onto $ZnCl_2$ activated corn husk carbon equilibrium studies*, (2013) 1-6, Article ID 383985.

[17] B. Chang, Y. Wang, K. Pei, S. Yang, X. Dong, *$ZnCl_2$-activated porous carbon spheres with high surface area and superior mesoporous structure as an efficient supercapacitor electrode*, RSC Adv. 4 (2014) 40546-40552.

[18] X. J. He, R. C. Li, J. F. Han, M. X. Yu, M. B. Wu, *Facile preparation of mesoporous carbons for supercapacitors by one-step microwave assisted $ZnCl_2$ activation*, Mater. Lett. 94 (2013) 158-160.

[19] C. Namasivayan, D. Sangeetha, *Removal and recovery of nitrate from water by ZnCl2 activated carbon from coconut coir pith, an agricultural waste*, Indian J. Chem. Technol. 12 (2005) 513-521.

[20] R. Subha, C. Namasivayam, *$ZnCl_2$-Modified Activated Carbon from Biomass Coir Pith for the Removal of 2-Chlorophenol by adsorption Process*, Bioremediat. J. 14 (2010) 1-9.

[21] C. Namasivayam, D. Sangeetha, *Application of coconut coir pith for the removal of sulfate and other anions from water*, Desalination 219 (2008) 1–13.

[22] X. Luo, Y. Cai, L. Liu, J. Zeng, *Cr(VI) adsorption performance and mechanism of an effective activated carbon prepared from bagasse with a one-step pyrolysis and $ZnCl_2$ activation method*, Cellulose 26 (2019) 4921–4934

[23] T. H. Usmani, T. W. Ahmad, A. H. K. Yousufzai, *Preparation and liquid-phase characterization of granular activated-carbon from rice husk*, Bioresour. Technol. 48 (1994) 31-35.

[24] E. Gonzalez-Serrano, T. Cordero, J. Rodríguez-Mirasol, J. J. Rodríguez, *Development of porosity upon chemical activation of kraft lignin with $ZnCl_2$*, Ind. Eng. Chem. Res. 36 (1997) 4832-4838.

[25] A. B. M. N. Allwar, M. A. B. M. Nawi, *Textural Characteristics of Activated Carbons Prepared from Oil Palm Shells Activated with $ZnCl_2$ and pyrolysis under nitrogen and carbondioxide*, J. Phys. Sci. 19 (2008) 93–104.

[26] T. Varila, D. Bergna, R. Lahti, H. Romar, T. Hu, U. Lassi, *Activated carbon production from peat using $ZnCl_2$: Characterization and applications*, Bioresources 12 (2017) 8078-8092.

[27] H. Shang, Y. Lu, F. Zhao, C. Chao, B. Zhang, H. Zhang, *Preparation of high surface area porous carbon from biomass by carbonization in molten salt medium*, RSC adv. 5 (2015) 75728-75734.

[28] R. Chen, L. Li, Z. Liu, M. Lu, C. Wang, H. Li, W. Ma, S. Wang, *Preparation and Characterization of Activated Carbons from Tobacco Stem by Chemical Activation*, J. Air Waste Manag. Assoc. 67 (2017) 713-724.

[29] V. Boonamnuayvitayaa, S. Sae-ungb, W. Tanthapanichakoonc, *Preparation of activated carbons from coffee residue for the adsorption of formaldehyde*, Sep. Purif. Technol. 42 (2005) 159-168.

[30] Y. Önal, C. Akmil-Başar, C. Sarıcı-Özdemir, S. Erdoğan, *Textural development of sugar beet bagasse activated with $ZnCl_2$*, J. Hazard. Mater. 142 (2007) 138-143.

[31] K. Mohantya, D. Dasb, M.N. Biswas, *Adsorption of phenol from aqueous solutions using activated carbons prepared from Tectona grandis sawdust by $ZnCl_2$ activation*, Chem. Eng. J. 115 (2005) 121-131.

[32] J. Acharyaa, J.N. Sahub, B.K. Sahoob, C.R. Mohantyc, B.C. Meikap, *Removal of chromium(VI) from wastewater by activated carbon developed from Tamarind wood activated with zinc chloride*, Chem. Eng. J. 150 (2009) 25-39.

[33] M. Olivares-María, C. Fernández-Gonza´lez, A. Macías-García V. Gómez-Serrano, *Preparation of activated carbon from cherry stones by chemical activation with $ZnCl_2$*, Appl. Surf. Sci. 252 (2006) 5967-5971.

[34] H. Sayğili, F. Güzel, *High surface area mesoporous activated carbon from tomato processing solid waste by zinc chloride activation: process optimization, characterization and dye adsorption*, J. Clean. Prod. 113 (2016) 995-1004.

[35] B. L. A. Prabhavathi Devi, K. N. Gangadhar, P. S. Sai Prasad, B. Jagannadh and R. B. N. Prasad, *A Glycerol-based Carbon Catalysts for the Preparation of Biod*iesel, ChemsusChem 2 (2009) 617-620.

[36] K. N. Gangadhar, M. Vijay, R. B. N. Prasad, B. L. A. Prabhavathi Devi, *Glycerol-Based Carbon-SO_3H Catalyzed Benign Synthetic Protocol for the Acetylation of Alcohols, Phenols and Amines under Solvent-Free Conditions*, Green Sustain. Chem. 3 (2013) 122-128.

[37] C. Ummadisetti, B. N. P. Rachapudi, B. L. A. Prabhavathi Devi, *Glycerol-based SO_3H-Carbon Catalyst: A green recyclable catalyst for the chemoselective synthesis of pentaerythritoldiacetals*, Eur. J. Chem. 5 (3) (2014) 536-540.

[38] R. S. Ribeiro, A. M. T. Silva, M. T. Pinho, J. L. Figueiredo, J. L. Faria, H. T. Gomesa, *Development of glycerol-based metal-free carbon materials for environmental catalytic applications*, Catalysis Today 240 (2015) 61–66.

[39] S. Álvarez-Torrellas, R. S. Ribeiro, H. T. Gomes, G. Ovejero, J. García, *Removal of antibiotic compounds by adsorption using glycerol-based carbon materials*, Chem. Eng. J. 296 (2016) 277–288.

[40] Y. Cui, J. D. Atkinson, *Tailored activated carbon from glycerol: role of acid dehydrator on physiochemical characteristics and adsorption performance*, J. Mater. Chem. A 5 (2017) 16812-16821.

[41] B. Yilmaz U. Müller, *Catalytic applications of zeolites in chemical industry*, Top Catal. 52 (2009) 888–895.

[42] A. Primo, H. Garcia, *Zeolites as catalysts in oil refining*, Chem Soc Rev. (2014) DOI:10.1039/c3cs60394f

[43] S. Wanga, Y. Peng, *Natural zeolites as effective adsorbents in water and wastewater treatment*, Chem. Eng. J. 156 (2010) 11–24.

[44] L. Ćurković, Š. Cerjan-Stefanović, T. Filipan, *Metal ion exchange by natural and modified zeolites*, Wat. Res. 31 (1997) 1379-1382.

[45] M. Armandi, B. Bonelli, I. Bottero, C. Otero Areán, E. Garrone, *Synthesis and characterization of ordered porous carbons with potential applications as hydrogen storage media*, Micropor. Mesopor. Mater. 103 (2007) 150-157.

[46] J. E. Post, *Manganese oxide minerals: Crystal structures and economic and environmental significance*, Proc. Natl. Acad. Sci. 96 (1999) 3447-3454.

[47] R. A. Bepari, P. Bharali, B. K. Das, *Controlled synthesis of α- and γ-Fe_2O_3 nanoparticles via thermolysis of PVA gels and studies on α-Fe_2O_3 catalyzed styrene*, J. Saudi Chem. Soc. 21 (2017) 170-178.

[48] S. Sakurai, A. Namai, K. Hashimoto, S. Ohkoshi, *First Observation of Phase Transformation of All Four Fe_2O_3 Phases ($\gamma \rightarrow \varepsilon \rightarrow \beta \rightarrow \alpha$-Phase)*. J. Am. Chem. Soc. 51 (2009) 18299-18303.

[49] S. I. Ramya, C. K. Mahadevan, *Preparation and structural, optical, magnetic and electrical characterization of $Mn^{2+}/Co^{2+}/Cu^{2+}$ doped hematite nanocrystals*, J. Solid State Chem. 211 (2014) 37-50.

[50] D. A. Wheeler, G. Wang, Y. Ling, Y. Li, J. Z. Zhang, *Nanostructured hematite: synthesis, characterization, charge carrier dynamics and photoelectrochemical properties*, Energy Environ Sci. 5 (2012) 6682-6702.

[51] N. M. Deraz, A. Alarifi, *Controlled synthesis, physicochemical and magnetic*

properties of nanocrystalline and Mn ferrite system, Int. J. Electrochem. Sci. 7 (2012) 5534-5543.

[52] K. Zipare, J. Dhumal, S. Bandgar, V. Mathe, G. Shahane, *Superparamagnetic Manganese ferrite nanoparticles: Synthesis and Magnetic Properties*, J. Nanosci. Nanoengg. 1 (2015) 178-82.

[53] Y. Feng, J. Fornell, H. Zhang, P. Solsona, M. D. Baró, S. Suriñach, E. Pellicer, J. Sort, *Synthesis of α-Fe_2O_3 and Fe-Mn Oxide Foams with Highly Tunable Magnetic Properties by the Replication Method from Polyurethane Templates*, Materials. 11 (2018) 280-287.

[54] F. G. Durán, L. E. Cadús, B. P. Barbero, *Iron-Manganese Mixed Oxide Catalysts For Ethanol Combustion. Influence Of The Fe:Mn Atomic Ratio and the Calcination Temperature,* Lat. Am. Appl. Res. 42 (2012) 217-21.

[55] T. Herranz, S. Rojas, M. Ojeda, F. J. Pérez-Alonsa, P. Terreros, K. Pirota, J. L. G. Fierro, *Synthesis, Structural Features, and Reactivity of Fe−Mn Mixed Oxides Prepared by Microemulsion*, Chem. Mater. 18 (2006) 2364-2375.

[56] W. Sun, X. Li, Q. Zhao, J. Mu, J. Chen, *Fe–Mn Mixed Oxide Catalysts Synthesized by One-Step Urea-Precipitation Method for the Selective Catalytic Reduction of NO_x with NH_3 at Low Temperatures,* Catal. Lett. 148 (2018) 227-234.

[57] Y-H. Jo, Y. W. Chung, S-H. Do, *Simple preparation of Mn-Fe_2O_3 composite: Identification and evaluation as an activator in Fenton like oxidation*, 2nd Ann. Int. Conf. (SEES 2013) http://doi: 10.5176/2251-189X_SEES13.23.

[58] M. Hermanek, R. Zboril, I. Medrik, J. Pechousek, C. Gregor, *Catalytic Efficiency of Iron(III) Oxides in Decomposition of Hydrogen Peroxide: Competition between*

the Surface Area and Crystallinity of Nanoparticles, J. Am. Chem. Soc. 129 (2007) 10929-10936.

[59] F. V. F. Araujo, L. Yokoyama, L. A. C. Teixeira, J. C. Campos, *Heterogeneous Fenton process using the mineral hematite for discoloration of a reactive dye solution*, Brazilian J. Chem. Engg. 28 (2011) 605-616.

[60] J. Liu, B. Wang, Z. Li, Z. Wu, K. Zhu, J. Zhuang, Q. Xi, Y. Hou, J. Chen, M. Cong, J. Li, G. Qian, Z. Lin, *Photo-Fenton reaction and H_2O_2 enhanced photocatalytic activity of α-Fe_2O_3 nanoparticles obtained by a simple decomposition route*, J. Alloy Compd. 771 (2019) 398-405.

[61] R. Ianos, A. Takulescu, C. Pacurariu, I. Lazau, *Solution combustion synthesis and characterization of magnetite nanopowders*, J. Am. Ceram. Soc. 98 (2012) 2236-2240.

[62] G. Mihoc, R. Ianos, C. Pacurariu, I. Lazau, *Combustion synthesis of some iron oxides used as adsorbents for removal of phenol and p-chlorophenol from waste water*, J. Therm. Anal. Calorim. 112 (2013) 391-397.

[63] K. Raja, M. M. Jaculine, M. Jose, S. Verma, A. A. M. Prince, K. Ilangovan, S. J. Das, *Sol–gel synthesis and characterization of α-Fe_2O_3 nanoparticles*, Superlattice. Microst. 86 (2015) 306-312.

[64] S. Sundar, G. Venkatachalam, S. J. Kwon, Sol-*Gel Mediated Greener Synthesis of γ-Fe_2O_3 Nanostructures for the Selective and Sensitive Determination of Uric Acid and Dopamine*, Catalysts (2018) http://doi:10.3390/catal8110512.

[65] A. Lassoued, B. Dkhil, A. Gadri, S. Ammar, *Control of the shape and size of iron oxide (α-Fe_2O_3) nanoparticles synthesized through the chemical precipitation method*, Results. Phys. 7 (2017) 3007-3015.

[66] H. Mansour, R. Bargougui, C. Autret-Lambert, A. Gadri, S. Ammar, *Co-precipitation synthesis and characterization of tin-doped α-Fe_2O_3 nanoparticles with enhanced photocatalytic activities*, J. Phys. Chem. Solids. 114 (2018) 1-7.

[67] A. Hamnett, *Mechanism and electrocatalysis in the direct methanol fuel cell*, Catal. Today 38 (1997) 445-457.

[68] C. Lamy, *Electrocatalytic oxidation of organic compounds on noble metals in aqueous solution*, Electrochim. Acta 29 (1984) 1581-1588.

[69] V. S. Bagotzky, Y. B. Vassilyev, *Mechanism of Electro-oxidation of Methanol on the platinum electrode*, Electrochim. Acta. 12 (1967) 1323-1343.

[70] T. Iwasita, W. Vielstich, E. Santos, *Identification of the adsorbate during methanol oxidation*, J. Electroanal. Chem. 229 (1987) 367-376.

[71] K. Ota, Y. Nakagawa, M. Takahashi, *Reaction products of anodic oxidation of methanol in sulfuric acid solution*, J. Electroanal. Chem. 179 (1984) 179-186.

[72] E. M. Belgsir, H. Huser, J. M. Leger, C. Lamy, *A kinetic analysis of the oxidation of methanol at platinum-based electrodes by quantitative determination of the reaction products using liquid chromatography*, J. Electroanal. Chem. 225 (1987) 281-286

[73] S. Motoo, M. Shibata, *Electrocatalysis by ad-atoms: Part IX. A fast parallel path for formaldehyde oxidation on a platinum electrode by oxygen adsorbing ad-atoms*, J. Electroanal Chem. 139 (1982) 119-130.

[74] O. Wolter, J. Willsau, J. Heitbaum, *Reaction Pathways of the Anodic Oxidation of Formic Acid on Pt Evidenced by 180 Labeling A DEMS Study*, J. Electrochem. Sot. 132 (1985) 1635-1638.

[75] K. Kunimatsu, *Adsorption of Carbon Monoxide on a Smooth Palladium Electrode: An in-Situ Infrared Spectroscopic Study*, J. Phys. Chem. 88 (1984) 2195-2200.

[76] J. B. Goodenough, L. A. Hamne'it, B. J. Kennedy, R. Manoharan, S. A. Weeks, *Methanol oxidation on unsupported and carbon supported Pt + Ru anodes*, J. Electroanal. Chem. 240 (1988) 133-145.

[77] M. Beltowska-Brzezinska, *Electrochemical oxidation of formaldehyde on gold and silver*, Electrochim. Acta, 30 (1985) 1193-1198.

[78] X. Y. Chen, A. Miki, S. Ye, H. Sakai, M. Osaka, *Formate, an active intermediate for direct oxidation of methanol on Pt electrode*, J. Am. Chem. Soc. 125 (2003) 3680-3681.

[79] R. Parsons, T. VanderNoot, *The oxidation of small organic molecules A survey of recent fuel cell related research*, J. Electroanal. Chem. 257 (1988) 9-45.

[80] M.S. Ureta-Zanarm, P. Bravo, J. H. Zagal, *Methnaol oxidation on modified iridium electrodes*, J. Electroanal. Chem. 337 (1992) 241-251.

[81] A. Hamnett, B. J. Kennedy, *Bimetallic carbon supported anodes for the direct methanol – air fuel cell*, Electrochim. Acta, 33 (1988) 1613-1618.

[82] J. Munk, P. A. Christensen, A. Hamnett, E. Skou, *The electrochemical oxidation of methanol on platinum and platinum+ruthenium particulate electrodes studied by insitu FTIR spectroscopy and electrochemical mass spectrometry*, J. Electroanal. Chem. 401 (1996) 215-222.

[83] A. K. Shukla, M. K. Ravikumar, A. S. Arico, G. Candiano, V. Antonucce, N. Giordano, A. Hamnett, *Methanol electro-oxidation on carbon-supported Pt-WO_{3-x} electrodes in sulphuric acid electrolyte*, J. Appl. Electrochem. 25 (1995) 528-532.

[84] J. H. White, A. F. Sammells, *Perovskite Anode Electrocatalysis for Direct Methanol Fuel Cells,* J. Electrochem. Soc. 140 (1993) 2167-2177.

[85] F. A. Viva, M. M. Bruno, M. Jobbágy, H. R. Corti, *Electrochemical characterization of Pt-Ru nanoparticles supported on mesoporous carbon for methanol electro-oxidation,* J. Phys. Chem. C 116 (2012) 4097-4104.

[86] C. Luo, H. Xie, Q.Wang, G. Luo, C. Liu, *A Review of the Application and Performance of Carbon Nanotubes in Fuel Cells,* J. Nanomater. (2015) 1-10. http://dx.doi.org/10.1155/2015/560392.

[87] C. Alegre, M. E. Gálvez, E. Baquedano, R. Moliner, E. Postor, M. J. Lázaro, *Oxygen-functionalized highly mesoporous carbon xerogel based catalysts for direct methanol fuel cell anodes,* J. Phys. Chem. C 117 (2013) 13045-13058.

[88] M. Liu, R. Zhang, W. Chen, *Graphene supported nanoelectrocatalysts for fuel cells: Synthesis, properties and application,* Chem. Rev. 114 (2014) 5117-5160.

[89] N. Jha, R. I. Jafri, N. Rajalakshmi, S. Ramaprabhu, *Graphene - multi walled carbon nanotube hybrid electrocatalyst support material for direct methanol fuel cell,* Int. J. Hydrogen energ. 36 (2011) 7284-7290.

[90] J. Zheng, C. Francia, C. Gerbaldi, V. Baglio, S. Specchia, A. S. Aricò, P. Spinelli, *Hybrid ordered mesoporous carbons doped with tungsten trioxide as supports for Pt electrocatalysts for methanol oxidation reaction,* Electrochim. Acta 94 (2013) 80-91.

[91] H. Lin, C. Song, L. Zhang, J. Zhang, H. Wang, D. P. Wilkinson, *A review of anode catalysis in the direct methanol fuel cell,* J. Power Sources 155 (2006) 95-110.

[92] Y. Zhao, L. Zhan, J. Tian, S. Nie, Z. Niug, *MnO_2 modified multi-walled carbon nanotubes supported Pd nanoparticles for methanol electro-oxidation in alkaline medium,* Int. J. Hydrogen energ. 35 (2010) 10522-105226.

[93] G-Y. Zhao, H-L Li, *Electrochemical oxidation of methanol on Pt nanoparticle composited MnO_2 nanowire arrayed electrode,* Appl. Surf. Sci. 254 (2008) 3232-3235.

[94] C. Zhou, H. Wang, F. Peng, J. Liang, H. Yu, J. Yang, *MnO_2/CNT supported Pt and PtRu nanocatalysts for direct methanol fuel cells,* Langmuir 25 (2009) 7711-7717.

[95] J. S. Rebello, P. V. Samant, J. L. Figueiredo, J. B. Fernandes, *Enhanced electrocatalytic activity of carbon-supported MnOx/Ru catalysts for methanol oxidation in fuel cells,* J. Power Sources 153 (2006) 36-40.

[96] S. S. Gupta, J. Datta, *An investigation into the electro-oxidation of ethanol and 2-propanol for application in direct alcohol fuel cells (DAFCs),* J. Chem. Sci. 117 (2005) 337-344.

[97] M. Li, A. Kowal, K. Sasaki, N. Marinkovic, D. Su, E. Korach, P. Liu, R. R. Adzic, *Ethanol oxidation on the ternary Pt–Rh–SnO_2/C electrocatalysts with varied Pt:Rh:Sn ratios,* Electrochim. Acta 55 (2010) 4331-4338.

[98] E. Antolini, *Catalysts for direct ethanol fuel cells,* J. Power Sources 170 (2007) 1-12.

[99] H. Wang, Z. Jusys, R. J. Behm, *Ethanol electrooxidation on a carbon-supported Pt catalyst: Reaction kinetics and product yields,* J. Phys. Chem. B 108 (2004) 19413-9424.

[100] D. M. Anjos, F. Hahn, J. M. Leger, K. B. Kokoh, G. Tremiliosi, *In situ FTIRS studies of the electrocatalytic oxidation of ethanol on Pt alloy electrodes*, J. Solid State Electrochem. 11 (2007) 1567-1573.

[101] F. Vigier, C. Coutanceau, F. Hahn, E. Belgsir, C. Lamy, *On the mechanism of ethanol electro-oxidation on Pt and PtSn catalysts: Electrochemical and in situ IR reflectance spectroscopy studies*, J. Electroanal. Chem. 563 (2004) 81-89.

[102] S. C. S. Lai, S. E. F. Kleijn, F. T. Z. Ozturk, V. C. V. Vellinga, J. Koning, P. Rodriguez, M. T. M. Koper, *Effects of electrolyte pH and composition on the ethanol electro-oxidation reaction*, Catal. Today 154 (2010) 92-104.

[103] L. Huang, E. Sorte, S.-G. Sun, Y.Y.J. Tong, *A straightforward implementation of in situ solution electrochemical 13C NMR spectroscopy for studying reactions on commercial electrocatalysts: Ethanol oxidation*, Chem. Commun. 51 (2015) 8086-8088.

[104] H. Hitmi, E. Belgsir, J.-M. Léger, C. Lamy,R. Lezna, *A kinetic analysis of the electro-oxidation of ethanol at a platinum electrode in acid medium*, Electrochim. Acta 39 (1994) 407-415.

[105] D. J. Tarnowski, C. Korzeniewski, *Effects of surface step density on the electrochemical oxidation of ethanol to acetic acid*, J. Phys. Chem. B 101 (1997) 253-258.

[106] H. Hoster, T. Iwasita, H. Baumgärtner, W. Vielstich, *Pt–Ru model catalysts for anodic methanol oxidation: Influence of structure and composition on the reactivity*, Phys. Chem. Chem. Phys. 3 (2001) 337-346.

[107] O. A. Khazova, A. A. Mikhailova, A. M. Skundin, E. K. Tuseeva, A. Havránek, K. Wippermann, *Kinetics of methanol oxidation supported and unsupported Pt/Ru catalysts bonded to PEM fuel cell*, 2 (2002) 100-108.

[108] S. S. Gupta, S.S. Mahapatra, J. Datta, *A potential anode material for the direct alcohol fuel cell*, Journal of Power Sources 131 (2004) 169-174.

[109] S. Srinivasan, B. B. Dave, K. A. Murugesamoorthi, A. Parthasarathy, A. J. Appleby, *Overview of Fuel Cell Technology. In Fuel cell Systems*, Plenum Press: New York, NY, USA, 1993.

[110] H. Wang, Z. Jusys, R. Behm, *Ethanol electro-oxidation on carbon-supported Pt, PtRu and Pt_3Sn catalysts: A quantitative DEMS study*, J. Power Sources 154 (2006) 351-359.

[111] L. W. H. Leung, S. C. Chang, M. J. Weaver, *Real-time FTIR spectroscopy as an electrochemical mechanistic probe—Electrooxidation of ethanol and related species on well-defined Pt(111) surfaces,* J. Electroanal. Chem. 266 (1989) 317-336.

[112] L. Colmenares, H. Wang, Z. Jusys, L. Jiang, S. Yan, G. Q. Sun, R. J. Behm, *Ethanol oxidation on novel, carbon supported Pt alloy catalysts-model studies under defined diffusion conditions,* Electrochim. Acta 52 (2006) 221-233.

[113] H. F. Wang, Z. P. Liu, *Comprehensive mechanism and structure-sensitivity of ethanol oxidation on platinum: New transition-state searching method for resolving the complex reaction network*, J. Am. Chem. Soc. 130 (2008) 10996-11004.

[114] T. Iwasita, B. Rasch, E. Cattaneo, W. Vielstich, *A sniftirs study of ethanol oxidation on platinum,* Electrochim. Acta 34 (1989) 1073-1079.

[115] M. E. Paulino, L. M. Nunes, E. R. Gonzalez, G. Tremiliosi-Filho, *In situ FTIR spectroscopic study of ethanol oxidation on Pt (111)/Rh/Sn surface: The anion effect*, Electrochem. Commun. 52 (2015) 85-88.

[116] L. W. H. Leung, S. C. Chang, M. J. Weaver, *Real-time FTIR spectroscopy as an electrochemical mechanistic probe-Electrooxidation of ethanol and related species on well-defined Pt(111) surfaces,* J. Electroanal. Chem. 266 (1989) 317-336.

[117] G. A. Camara, T. Iwasita, *Parallel pathways of ethanol oxidation: The effect of ethanol concentration,* J. Electroanal. Chem. 578 (2005) 315-321.

[118] X. Teng, *Anodic Catalyst Design for the Ethanol Oxidation Fuel Cell*, (2015) http://www.formatex.info/energymaterialsbook/book/473-484.pdf

[119] S. Sun, M. C. Halseid, M. Heinen, Z. Jusys, R. J. Behm, *Ethanol electrooxidation on a carbon-supported Pt catalyst at elevated temperature and pressure: A high-temperature/high-pressure DEMS study*, J. Power Sources 190 (2009) 2-13.

[120] P. A. Christensen, S. W. M. Jones, A. Hamnett, *In situ FTIR studies of ethanol oxidation at polycrystalline Pt in alkaline solution,* J. Phys. Chem. C 116 (2012) 26109-26109.

[121] H. F. Wang, Z. P. Liu, *Comprehensive mechanism and structure-sensitivity of ethanol oxidation on platinum: New transition-state searching method for resolving the complex reaction network,* J. Am. Chem. Soc. 130 (2008) 10996-11004.

[122] Y. Wang, S. Zou, W.-B. Cai, *Recent advances on electro-oxidation of ethanol on Pt- and Pd-based catalysts: from reaction mechanisms to catalytic materials,* Catalysts 5 (2015) 1507-1534.

[123] L. Colmenares, H. Wang, Z. Jusys, L. Jiang, S. Yan, G. Q. Sun, R. J. Behm, *Ethanol oxidation on novel, carbon supported Pt alloy catalysts-model studies under defined diffusion conditions,* Electrochim. Acta 52 (2006) 221-233.

[124] Q. Wang, G. Q. Sun, L. H. Jiang, Q. Xin, S. G. Sun, Y. X. Jiang, S. P. Chen, Z. Jusys, R. J. Behm, *Adsorption and oxidation of ethanol on colloid-based Pt/C, PtRu/C and Pt_3Sn/C catalysts: In situ FTIR spectroscopy and on-line DEMS studies,* Phys. Chem. Chem. Phys. 9 (2007) 2686–2696.

[125] H. B. Suffredini, G. R. Salazar-Banda, L. A. Avaca, *Enhanced ethanol oxidation on PbOx-containing electrode materials for fuel cell applications,* J. Power Sources 171 (2007) 355-362.

[126] A. Kowal, M. Li, M. Shao, K. Sasaki, M. Vukmirovic, J. Zhang, N. Marinkovic, P. Liu, A. Frenkel, R. Adzic, *Ternary Pt/Rh/SnO_2 electrocatalysts for oxidizing ethanol to CO_2,* Nat. Mater. 8 (2009) 325-330.

[127] J. Hou, Y. Shao, M. W. Ellis, R. B. Moored, B. Yie, *Graphene-based electrochemical energy conversion and storage: fuel cells, supercapacitors and lithium ion batteries,* Phys. Chem. Chem. Phys. 13 (2011) 15384-15402.

[128] Y. Huang, J. Liang, Y. Chen, *An Overview of the Applications of Graphene-Based Materials in Supercapacitors,* small 8 (2012) 1805-1834

[129] L. L. Zhang, R. Zhou, X. S. Zhao, *Graphene-based materials as supercapacitor electrodes,* J. Mater. Chem. 20 (2010) 5983 – 5992.

[130] J. Liu, J. Wang, C. Xu, H. Jiang, C. Li, L. Zhang, J. Lin, Z. X. Shen, *Advanced energy storage devices: Basic principles, analytical methods and rational materials design,* Adv. Sci. 5 (2018) 1700322-1700340.

[131] Y. Zhang, S. Yu, G. Lou, Y. Shen, H. Chen, Z. Shen, S. Zhao, J. Zhang, S. Chai, Q. Zou, *Review of macroporous materials as electrochemical supercapacitor electrodes*, J. Mater. Sci. 52 (2017) 11201-11228.

[132] F. Wang, X. Wu, X. Yuan, Z. Liu, Y. Zhang, L. Fu, Y. Zhu, Q. Zhou, Y. Wu and W. Huang, *Latest advances in supercapacitors: from new electrode materials to novel device designs*, Chem. Soc. Rev. 46 (2017) 6816-6854.

[133] E. Frackowiak, Q. Abbas, F. Béguin, *Carbon/carbon supercapacitors*, J. Energy Chem. 22 (2013) 226-240.

[134] M. Sevilla, R. Mokaya, *Energy storage applications of activated carbons: supercapacitors and hydrogen storage*, Energy Environ. Sci. 7 (2014) 1250-1280.

[135] W. Gu, G. Yushin, *Review of nanostructured carbon materials for electrochemical capacitor applications: advantages and limitations of activated carbon, carbide-derived carbon, zeolite-templated carbon, carbon aerogels, carbon nanotubes, onion-like carbon and graphene*, Wiley Interdiscip. Rev.: Energy Environ. 3 (2013) 424-473.

[136] E. Frackowiak, *Carbon materials for supercapacitor applications*, Phys. Chem. Chem. Phys. 9 (2007) 1774–1785.

[137] A. Burke, *R & D considerations for the performance and application of electrochemical capacitors*, Electrochim. Acta 53 (2007) 1083-1091.

[138] W. G. Pell, B. E. Conway, *Analysis of power limitations at porous supercapacitor electrodes under cyclic voltammetry modulation and dc charge*, J. Power Sources 96 (2001) 57-67.

[139] W. Li, J. Liu, D. Zhao, *Mesoporous materials for energy conversion and storage devices*, Nat. Rev. Mater. 1 (2016) 16023-16039.

[140] R. Heimböckel, F. Hoffmann, M. Fröba, *Insights into the influence of the pore size and surface area of activated carbons on the energy storage of electric double layer capacitors with a new potentially universally applicable capacitor model*, Phys. Chem. Chem. Phys. 21 (2019) 3122-3133.

[141] A. Burke, *Ultracapacitors: why, how and where is the technology*, J. Power Sources 91 (2000) 37-50.

[142] R. Kötz, M. Carlen, *Principles and applications of electrochemical capacitors*, Electrochim. Acta 45 (2000) 2483-2498.

[143] N. Jäckel, P. Simon, Y. Gogotsi, V. Presser, *Increase in capacitance by subnanometer pores in carbon*, ACS Energy Lett. 1 (2016) 1262-1265.

[144] C. Li, X. Zhang, K. Wang, X. Sun, Y. Ma, *High-power lithium ion hybrid supercapacitor enabled by holey carbon nanolayers with targeted porosity*, J. Power Sources 400 (2018) 468-477.

[145] V. D. Patake, C. D. Lokhande, O. S. Joo, *Electrodeposited ruthenium oxide thin films for supercapacitor: Effect of surface treatments*, 255 (2009) 4192-4196.

[146] D. Yan, Z. Guo, G. Zhu, Z. Yu, H. Xu, A. Yu, *MnO_2 film with three-dimensional structure prepared by hydrothermal process for supercapacitor*, 199 (2012) 409-412.

[147] U. M. Patil, R. R. Salunkhe, K.V. Gurav, C. D. Lokhande, *Chemically deposited nanocrystalline NiO thin films for supercapacitor application*, Appl. Surf. Sci. 255 (2008) 2603-2607.

[148] B. R. Duan, Q. Cao, *Hierarchically porous Co_3O_4 film prepared by hydrothermal synthesis method based on colloidal crystal template for supercapacitor application*, Electrochim. Acta 64 (2012) 154-161.

[149] J. P. Zheng, P. J. Cygan, T. R. Jow, *Hydrous ruthenium oxide as an electrode material for electrochemical capacitors*, J. Electrochem. Soc. 142 (1995) 2699-2703.

[150] H. Y. Lee, S. W. Kim, H. Y. Lee, *Expansion of active site area and improvement of kinetic reversibility in electrochemical pseudocapacitor electrode*, Electrochem. Solid-State Lett. 4 (2001) A19-A22.

[151] S. Deng, D. Sun, C. Wu, H. Wang, J. Liu, Y. Sun, H. Yan, *Synthesis and electrochemical properties of MnO_2 nanorods/graphene composites for supercapacitor applications*, Electrochim. Acta 111 (2013) 707-712.

[152] R. Jiang, T. Huang, J. Liu, J. Zhuang, A. Yu, *A novel method to prepare nanostructured manganese dioxide and its electrochemical properties as a supercapacitor electrode*, Electrochim. Acta 54 (2009) 3047-3052.

[153] S. Chen, J. Zhu, X. Wu, Q. Han, X. Wang, *Graphene oxide-MnO_2 nanocomposites for supercapacitors*, ACS Nano 4 (2010) 2822-2830.

[154] M. Zhi, C. Xiang, J. Li, M. Li, N. Wu, *Nanostructured carbon-metal oxide composite electrodes for supercapacitors: a review*, Nanoscale 5 (2013) 72-88.

CHAPTER II

SYNTHESIS AND ADSORPTION BEHAVIOR OF GLYCEROL BASED CARBONS

Introduction

There is a continuing interest in developing newer methods of synthesis of carbon materials as adsorbents and catalysts. In recent times, increasing attention is given to develop functionalized carbon materials that could both act as excellent catalysts and also have improved adsorption characteristics [1]. Carbon catalysts with acid functionalities are finding increasing use in organic transformations. A glycerol based carbon (GBC) was recently synthesized by partial carbonization of glycerol using sulfuric acid. This carbon was found to be an effective solid acid catalyst in organic transformations including chemo selective synthesis [2-5]**.** This was due to the presence of acidic functionalities such as SO_3H on its surface. Thus the GBC carbon was found to be advantageous over other carbon catalysts owing to its ease of synthesis, efficiency and comparative stability.

On the other hand activated carbons obtained from different natural sources including nutshells, wood, coconut husk etc. often need appropriate chemical or physical activation in order to get efficient activity. However glycerol as a carbon source is readily available as a byproduct of biodiesel production industry and is thus cost effective. In addition to being used as a catalyst, a glycerol based carbon was also recently synthesized for adsorptive removal of antibiotics from their aqueous solutions [6, 7].

Apart from being used as adsorbents and catalysts, carbons are also required as supports for noble metal catalysts such as electrocatalysts in fuel cell reactions. The catalysts used in fuel cells are often platinised carbons such as Pt-C or Pt-Ru/C etc. These carbon supports need to be very pure carbon materials free from any metallic impurities as well as free from any residual chloride or sulphur. Since glycerol is readily available in a

pure form, it is amenable towards appropriate synthesis of pure carbon materials of desired properties. Depending upon synthesis conditions, it should also be possible to use glycerol as a raw material to synthesize pure microporous carbon or mesoporous carbon with desired surface functionalities. A series of investigations would thus be required to selectively develop various forms of carbon starting from glycerol as a raw material and then tailor its properties to make it useful either as an adsorbent or as a catalyst or as a catalyst support or having combination of these characteristics. In the present investigation, a glycerol based carbon is synthesized and examined for its adsorption behavior towards removal of methylene blue dye. The knowledge gained here is expected to be a background information when further studies are undertaken in development of suitable glycerol based carbon materials. Since methylene blue is also a well known pollutant associated with effluents from textile industry, the present investigation is expected to throw light not only on surface characteristics of the glycerol based carbon but also on its efficacy in mitigating pollutants by adsorption.

The activated carbons play a crucial role in mitigating pollutants such as dyes, pharmaceuticals, surfactants, heavy metal ions etc. by adsorption from industrial waste waters [8-12]. The dyeing process in the textile industry leads to release of approximately 10 – 15 % dyes into the environment. The effluents from these industries thus carry a large number of dyes and other additives which are added during the coloring process [13]. Due to their high water solubility they get readily transferred through water bodies. They may also undergo degradation to form products that are highly toxic [14]. Thus removal of dyes from the water bodies is important as they are harmful for living beings. A widely used cationic dye in different industries is methylene blue which is also known to be carcinogenic.

Adsorption by activated carbons is an important process for removal of pollutants particularly dyes and metal ions from industrial waste waters. Adsorption is a very effective separation technique in terms of initial cost, simplicity of design, ease of operation and insensitive to toxic substances. It is a tertiary technology during waste water treatment for adsorption of micropollutants, as well as to remove colour and odor [15]. The efficiency of removal by adsorption from solution depends upon the nature of dyes (cationic or anionic dyes), pH of adsorbate solution, pzc of the adsorbent and its surface functionalities, as well as surface area and porosity of the adsorbent. The use of different adsorbents like clay, silica materials, zeolite and activated carbons for removal of methylene blue (MB) have been extensively studied and is recently reviewed [16]. A variety of adsorbents have been designed depending upon the type of adsorbates to be removed. Activated carbons are generally more effective adsorbents for removal of high molecular weight compounds particularly those with low water solubility. However activated carbons with surface functionalities are efficient for adsorbing a wider range of organic pollutants such as dyes and pharmaceuticals.

The nature of interaction between the adsorbate molecules and the adsorbent can be understood from the adsorption isotherms. An adsorption isotherm is a plot which relates the amount of substance adsorbed to the equilibrium concentration of the adsorbate molecules in the solution at a specified temperature. The amount adsorbed depends on the nature of adsorbate and adsorbent which in turn affect the shape of adsorption isotherm profile. The data is usually investigated in terms of different adsorption isotherm models which include, Langmuir, Freundlich, Frumkin adsorption isotherms. These are considered in the present investigation. The Langmuir Isotherm assumes that adsorption is of monolayer and all the active sites on the adsorbent surface

are equivalent in energy. Freundlich adsorption isotherm explains the multilayer adsorption behavior. For understanding the interaction between adsorbed molecules, the applicability of Frumkin adsorption isotherm is generally investigated. The description of adsorption isotherms and kinetic models [17-22] used in this work are briefly summarized in Table 2.1.

Table 2.1: Review of some adsorption and kinetic models

Sr. No.	Adsorption Isotherm	Parameters and their significance
1.	Langmuir adsorption isotherm $x = \frac{x_m K c}{1 + Kc}$ $\frac{1}{x} = \frac{1}{x_m K} . \frac{1}{c} + \frac{1}{x_m}$	x = Amount of methylene blue adsorbed per unit mass of carbon (mg g^{-1}). x_m = Maximum adsorption capacity with complete monolayer coverage on the surface of carbon (mg g^{-1}). c = Concentration of methylene blue in the solution which is in equilibrium with the carbon. K = Langmuir adsorption constant which is related to energy of adsorption
2.	Freundlich adsorption isotherm $x = k\, c^{\frac{1}{n}}$ $\log x = \log k + \frac{1}{n} \log c$	k = Freundlich adsorption constant which is indicative of maximum adsorption capacity. 1/n = Measure of intensity of adsorption. (1/n = 0 - 1)
3.	Frumkin adsorption isotherm $\frac{\Theta}{(1-\Theta)} e^{-2\alpha\Theta} = \frac{\beta}{55.55} c$ $\log\left(\frac{\theta}{(1-\theta)c}\right) = \log\frac{\beta}{55.55} + \frac{2\alpha\theta}{2.303}$ $Where\ \theta = \frac{M}{M_{ads}}$	α = adsorbate interaction parameter β = Adsorption-desorption equilibrium constant. θ = Amount of adsorbate adsorbed at equilibrium. M = Concentration of the dye adsorbed at equilibrium. M_{ads} = Maximum amount of dye adsorbed at equilibrium.
	Kinetic models (expressions in linear form)	Parameters and their significance
1. 2.	Pseudo first order kinetic model $\log(q_e - q_t) = \log q_e - \frac{K_1}{2.303}\, t$ Pseudo second order kinetic model $\frac{t}{q_t} = \frac{t}{q_e} + \frac{1}{K_2 {q_e}^2}$	K_1 and K_2 are first and second order rate constants. q_e is the amounts of dye adsorbed at equilibrium and q_t is the amounts of dye adsorbed at time t.

2.1 Synthesis of glycerol based carbon

The sulphonated glycerol based carbon was synthesized by dehydration of glycerol using sulphuric acid in the molar ratio (*1*: *4*) [2, 6]. Thus 25 mL (Density = 1.84 g mL^{-1}) of sulphuric acid was added drop wise to 10 g of glycerol under continuous stirring over a period of 25 min (approximately at the rate of 1 mL min^{-1}). During the process, glycerol was taken in a 500 mL beaker and kept on hot plate magnetic stirrer. The sulphuric acid was added from a overhead reservoir. As the temperature was increased from ambient temperature to 180 ^{o}C, the clear solution gradually became a brown viscous mass. The temperature of the product was continued to be maintained at 180 ^{o}C for another 20 minutes until the evolution of the gases was completed. The black mass was then filtered and washed with hot water until the washings were neutral. The product was designated as GBC-120. The yield of GBC-120 (carbon-SO_3H) was 0.467 gram per gram of glycerol used. The details of preparing GBC-120 and GBC-350 are summarized in Scheme 2.1.

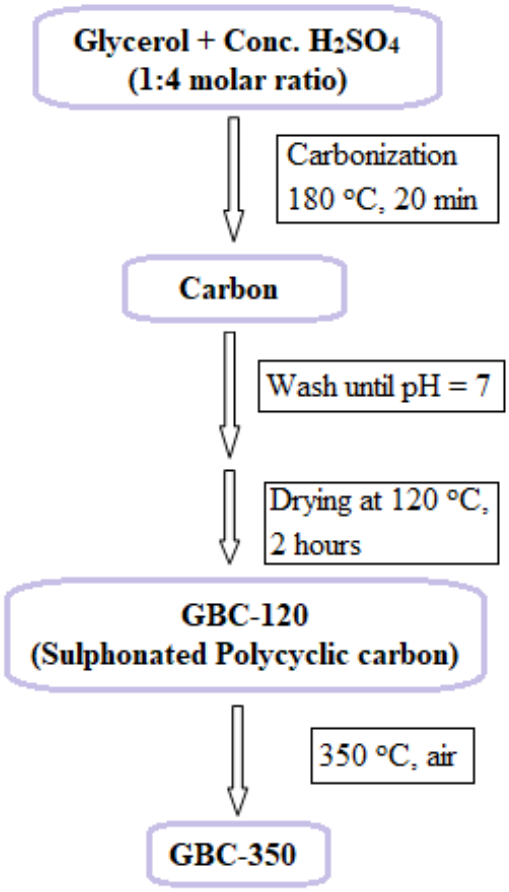

Scheme 2.1. Flow chart for synthesis of the glycerol based carbons (GBC-120 and GBC-350)

2.2 Adsorption studies

2.2.1 Effect of adsorbent dosage

2, 4, 6, 8, 10 mg of GBC-120 were each taken in conical flasks containing 100 mL of 5 µg mL^{-1} solution of methylene blue. The adsorption was carried out at pH 4.7. The flasks were kept for shaking overnight (~15 hours) and the amount adsorbed in each case was determined.

2.2.2 Effect of initial Methylene blue concentration

The dye concentrations were varied from 10-50 µg mL^{-1}. The adsorption was carried out using 2 mg of GBC-120. The adsorption was allowed to take place overnight (~15 hours). The adsorption was carried out at pH 4.7.

2.2.3 Effect of initial pH

2 mg of GBC-120 was contacted with 50 mL of 50 µg mL^{-1} of methylene blue at different pH (2.6-9.6). The flasks were kept for shaking for 2 hours and then the amount of methylene blue adsorbed was determined.

2.2.4 Effect of contact time and determination of adsorption equilibrium

The time required to establish equilibrium between the concentration of methylene blue adsorbed and its concentration in the solution was determined. Thus 20 mg of the previously dried carbon sample was added to known concentration (50 µg mL^{-1}) of methylene blue (pH=7). The progress of adsorption was monitored by taking out 1.0 mL aliquots of the solution at various predetermined time intervals until the equilibrium is reached. The data was interpreted in terms of relevant kinetic models.

2.2.5 Adsorption Isotherms

The adsorption isotherms of GBC-120 and GBC-350 carbons were determined at ambient temperature by equilibriating various concentrations of methylene blue with a know amount of the carbons (~ 2 mg). All the solutions were allowed to equilibriate at 25 ^{o}C at predetermined equilibriation times. The equilibrium concentrations were calculated by measuring the absorbance of methylene blue solution in each case. The data was then fitted in various adsorption isotherm and kinetic models.

2.3 Results and Discussion

2.3.1 XRD and Thermal analysis

The synthesized glycerol based carbon was characterized by XRD, thermal analysis and infra-red spectroscopy. Fig. 2.1 gives the XRD profiles of the samples GBC-120 and GBC-350.

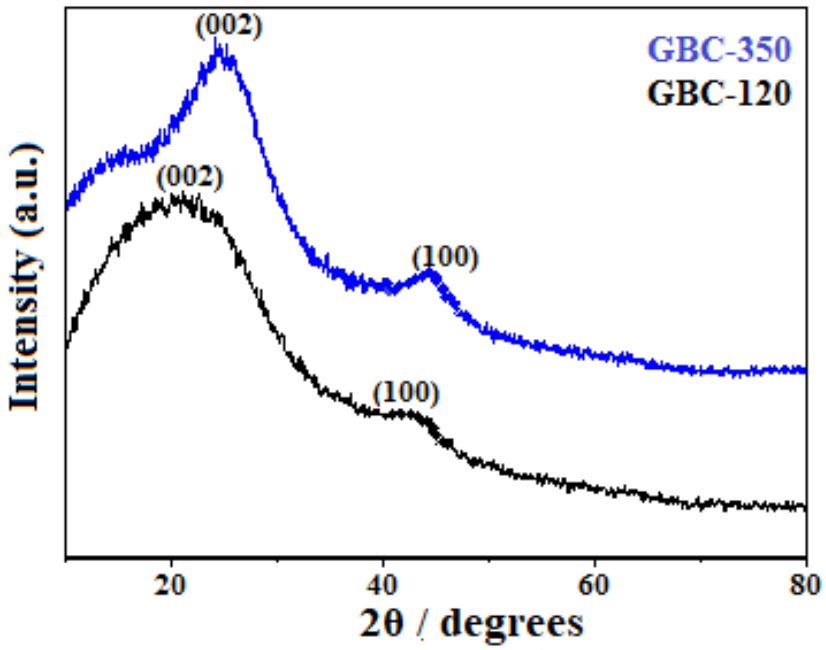

Fig. 2.1: XRD profiles of the glycerol based carbons obtained by treatment of the as prepared carbons at 120 ^{o}C and 350 ^{o}C.

Both the samples showed the expected two broad peaks at 2θ around 20 - 24^{o} and 43^{o} which correspond to reflection planes of (002) and (100) respectively [23]. It was observed that the peak at 43^{o} was diffuse for the as prepared GBC-120 sample, due to its comparatively amorphous nature.

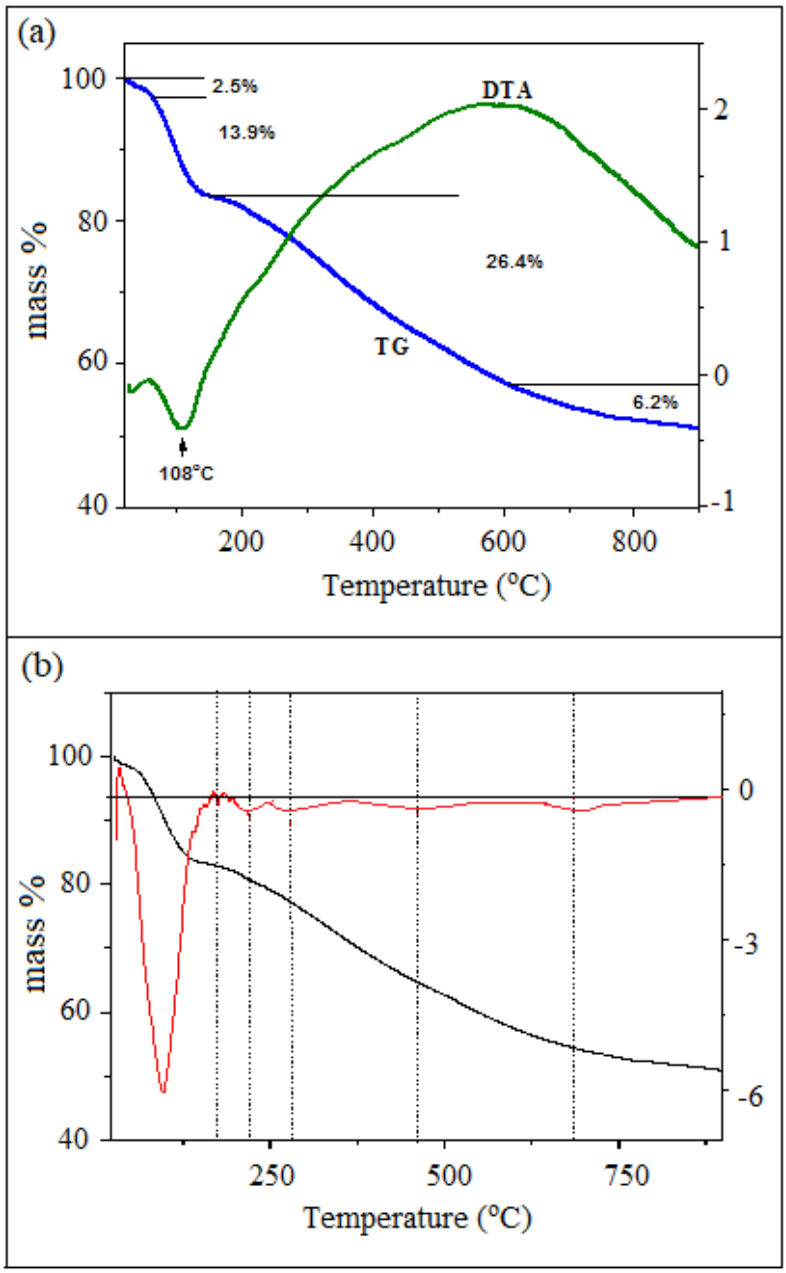

Fig. 2.2: (a) TG-DTA plot of GBC-120 in nitrogen atmosphere and (b) Comparison of TG/DTG profiles (N_2 atmosphere, heating rate of 10 ^oC min^{-1}).

Fig. 2.2 gives thermal analysis profiles of GBC-120 carried out in N_2 atmosphere. The TGA profile in Fig. 2.2(a), shows an initial mass loss of ~ 16.4 % up to 108 ^oC, due to loss of physisorbed and hydrogen bonded water. Further mass loss continues till about 800 ^oC due to gradual loss of the surface functional groups. The DTA shows a broad

endothermic profile in this temperature range with a maximum around 600 ^{o}C. This suggested that the loss of surface functionalities was accompanied with structural rearrangement, resulting in development of porosity in the carbon structure. It can be seen from Fig. 2.2 (b) that the TG-DTG profile of GBC-120 exhibits a mass loss between 180 - 700 ^{o}C. This broad range shows three distinct regions. The peak at 220 ^{o}C is considered as characteristic for decomposition of –SO_3H and –COOH groups. A large broad peak between 280 to 460 ^{o}C is due to decomposition of lactones and phenolic groups. And the similar broad peak from 460 to 700 ^{o}C is due to decomposition of carbonyl group. These results are in agreement with a recent report on a similarly prepared carbon based catalyst [24].

2.3.2 Infrared spectral analysis

Fig. 2.3 gives the infrared spectra of GBC-120 carbon and the spectra recorded after subjecting it to various heat treatments between 200 - 800 ^{o}C.

The glycerol based carbon which is known to have -SO_3H groups attached to polycyclic cluster of graphitic rings, shows characteristic absorptions in the infrared region of 1720 – 900 cm^{-1}. This is in agreement with literature reports [25-29]. The corresponding assignments are given in Table 2.2.

From Fig. 2.3 (b), it can be observed that when GBC-120 was heated at varying temperatures above 120 ^{o}C, the intensity of -SO_3H peak at 1044 cm^{-1} decrease. This peak vanished by 300 ^{o}C while the other peaks at 1208 cm^{-1} and 1355 cm^{-1} which are also due to -SO_3H functionality were still present. Thus the thermal treatment at 300 ^{o}C resulted in partial decomposition of -SO_3H due to dehydroxylation of the adjacent sulphonyl groups. The other peaks at 1593 and 1721 cm^{-1} were due to C = C and C = O

groups respectively. The carbonyl peak is a composite peak due to –CHO and –COOH and in agreement with the ir spectra reported earlier [30]. A –CHO functionality was expected as it is known that glycerol in presence of sulphuric acid decomposed via an acrolein type intermediate which has a –CHO group [31]. The peak at 1721 cm^{-1} was present till 700 ^{o}C. It eventually disappeared for the GBC-800 sample when the carbonyl functionalities were finally decomposed. This is supported by the evidence from the thermal analysis profile (Fig. 2.2) that decomposition of the surface functionalities gets completed around 800 ^{o}C.

Table 2.2: The assignments corresponding to different frequencies observed in the infra-red spectra of glycerol based carbons.

Frequencies (cm^{-1})	**Functional groups**
1721	C = O stretch of COOH and carbonyl group
1593	C = C stretch of graphitic rings
1355	O = S = O stretch of SO_3H
1208	(i) Symmetric S = O stretch (ii) C - OH stretching of phenolic group
1044	Asymmetric stretching of SO_3H

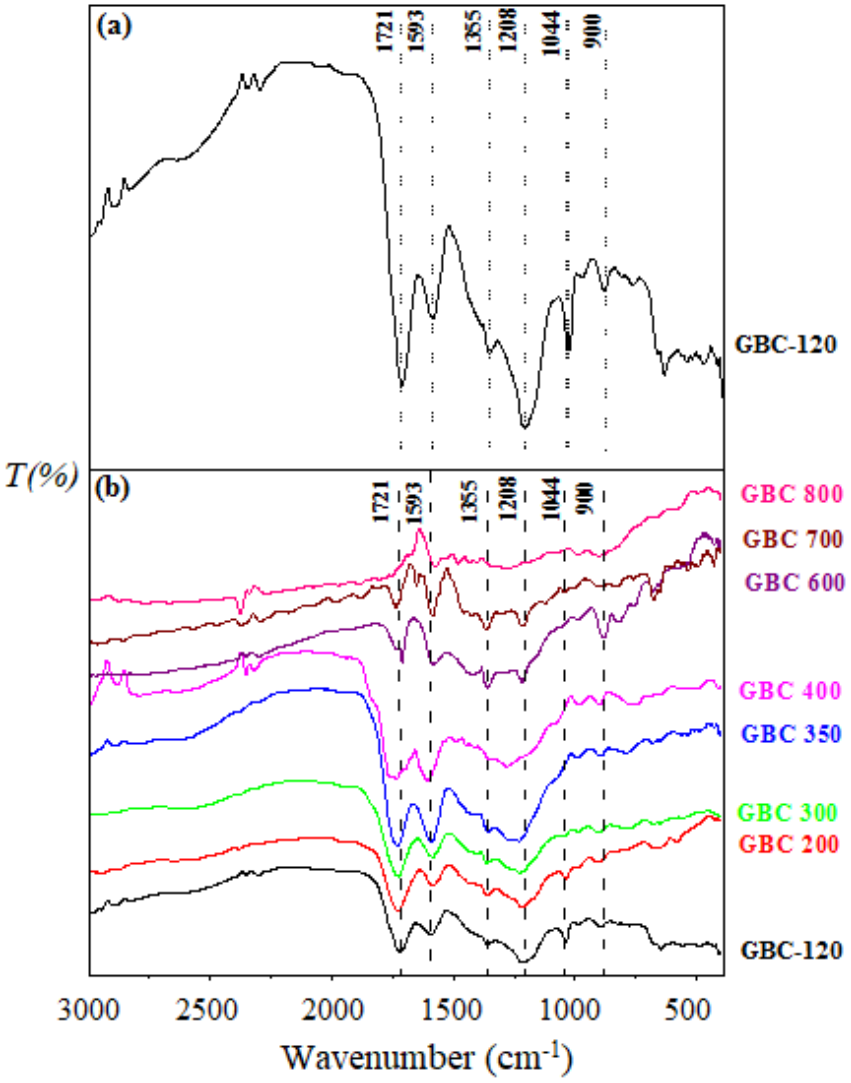

Fig. 2.3: Infrared spectra of GBC carbons (a) spectrum of GBC-120 (b) spectra of various GBC carbons heat treated between 200 - 800 ^{o}C.

2.3.3 Surface area, porosity and SEM

Fig. 2.4 gives the N_2 adsorption desorption isotherms along with pore size distribution profiles for GBC-120 and GBC-350. A clear hysteresis loop was observed for both the samples. The surface area and porosity values are presented in Table 2.3 along with SEM data.

It can be seen from Table 2.3 that GBC-120 with its associated SO_3H functionalities showed a relatively small surface area of about 21 $m^2 g^{-1}$. On the other hand GBC-350 showed much larger surface area of 464 $m^2 g^{-1}$. This suggested that the partial decomposition of SO_3H greatly enhances the surface area of the carbon due to greater dispersion of the GBC-350 particles. This is supported by the respective SEM images (Fig. 2.5) wherein GBC-120 shows larger agglomerates as compared to GBC-350. Further, the increased surface area of GBC-350 exposes its surface porosity resulting in its having much larger pore volume. Thus the pore volume of GBC-350 was 0.10 $cm^3 g^{-1}$ as compared to 0.065 $cm^3 g^{-1}$ for GBC-120 even though both the samples have similar pore radii of around 18.3 Å.

Table 2.3: The values of surface area, pore volume and pore size of GBC-120 and GBC-350 from BET analysis.

Sample	**Surface Area** ($m^2 g^{-1}$)	**Pore volume** (cc g^{-1})	**Pore radius** (Å)	SEM/ EDAX Analysis Wt (%) of the elements		
				C	O	S
GBC-120	21.00	0.06	18.38	82.45	15.82	1.74
GBC-350	464.00	0.10	18.27	87.55	12.09	0.36

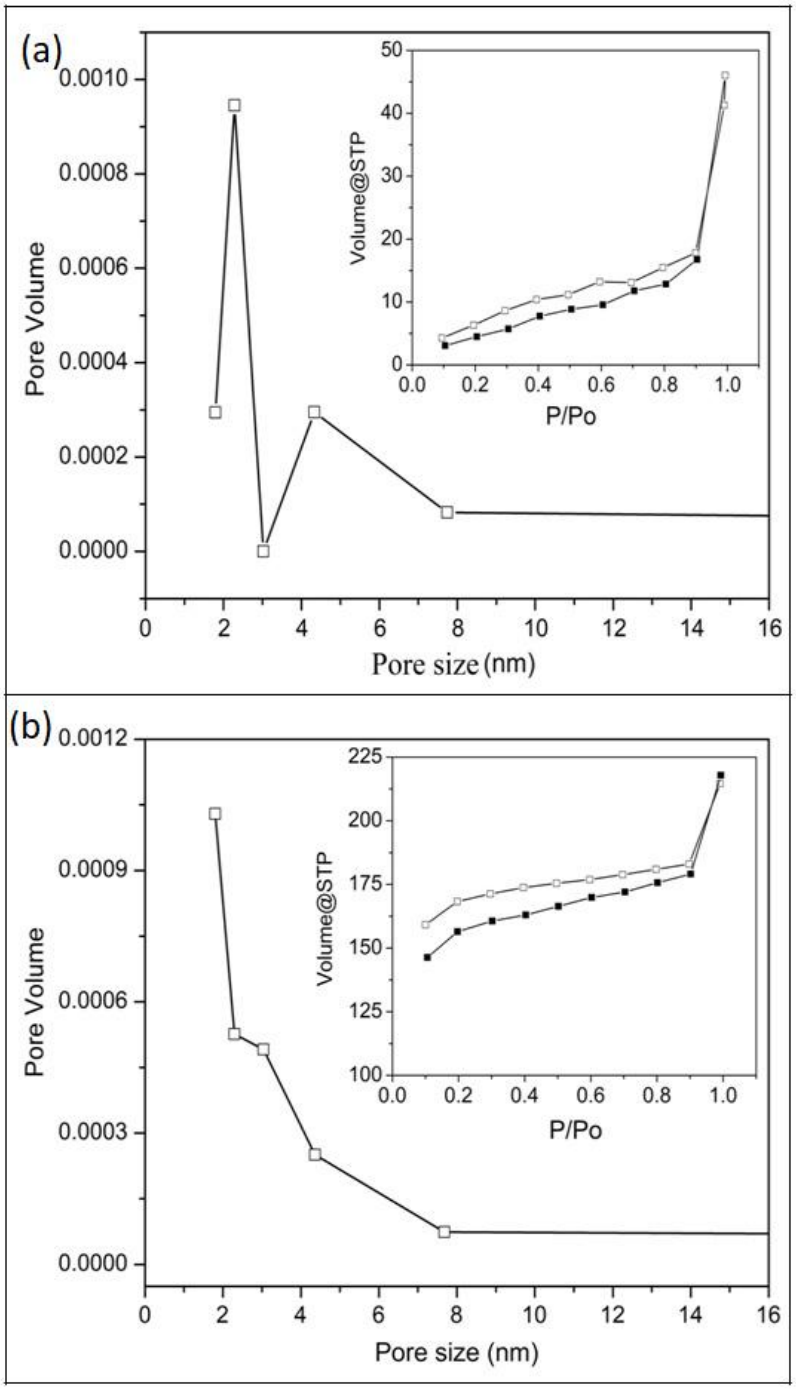

Fig. 2.4: Pore size distribution and N_2 adsorption-desorption isotherm (inset) for the carbon samples (a) GBC-120 and (b) GBC-350.

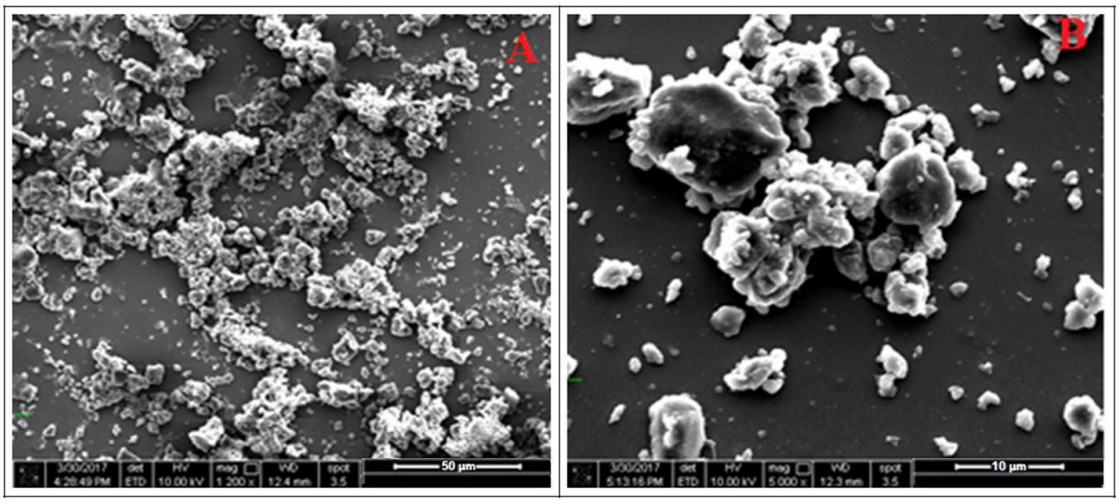

Fig. 2.5: SEM images of (A) GBC-120 (B) GBC-350

2.4 General adsorption behavior

The adsorption studies were carried out to investigate the influence of SO_3H groups on the carbon surfaces. The removal efficiency of the methylene blue dye from the solution was calculated using the relation

$$Removal\ (\%) = \frac{C_i\ - C_e}{C_i} \times 100 \qquad (1)$$

and equilibrium adsorption was determined using the equation:

$$q_e = \frac{C_i - C_e}{W} \times\ V \qquad (2)$$

C_i and C_e are the initial and equilibrium concentrations of the dye in µg mL^{-1} respectively, W is the weight of carbon in g and V is volume of the dye solution in litres.

2.4.1 Effect of adsorbent dosage

The effect of adsorbent dosage was studied by taking methylene blue solution of 25 µg mL^{-1}. 100 mL aliquots of the above solution were equilibrated by stirring with varying quantities of the adsorbents for 15 hours. The resulting adsorption behavior is shown in Fig. 2.6. It can be seen that the relative percent removal of the dye gradually increased and the adsorption efficiency was nearly 100 % with 8-10 mg of the carbon. The adsorption capacity or q_e thus obtained using equation 3.2 was around 300 mg g^{-1} of the carbon. This investigation was carried out at pH 4.7. This was the unadjusted pH value when GBC-120 carbon was stirred in methylene blue solution. Further studies were carried out to investigate the effect of pH on probable enhancement in adsorption.

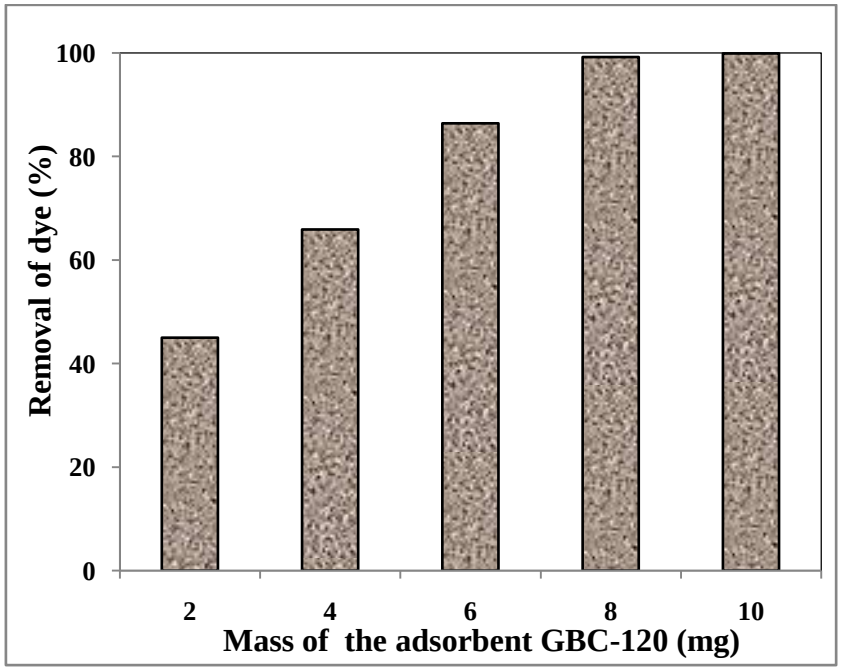

Fig. 2.6: Effect of amount of adsorbent on adsorption efficiency

2.4.2 Effect of initial pH

2 mg of GBC-120 carbon was stirred for 2 hours with 50 mL of methylene blue solution having concentration of 50 µg mL^{-1}. The pH of the solutions was adjusted in the range 2.6-9.6 using either HCl or NaOH. Fig. 2.7 shows the percent efficiency of methylene blue at various pH values. It can be seen from the figure that there is low adsorption efficiency at lower pH values and the adsorption tends towards maximum in the pH range 7-9. Therefore the subsequent adsorption studies were carried out at pH around 7. The adsorption capacity at pH 7 using equation 2 was 428 mg g^{-1}.

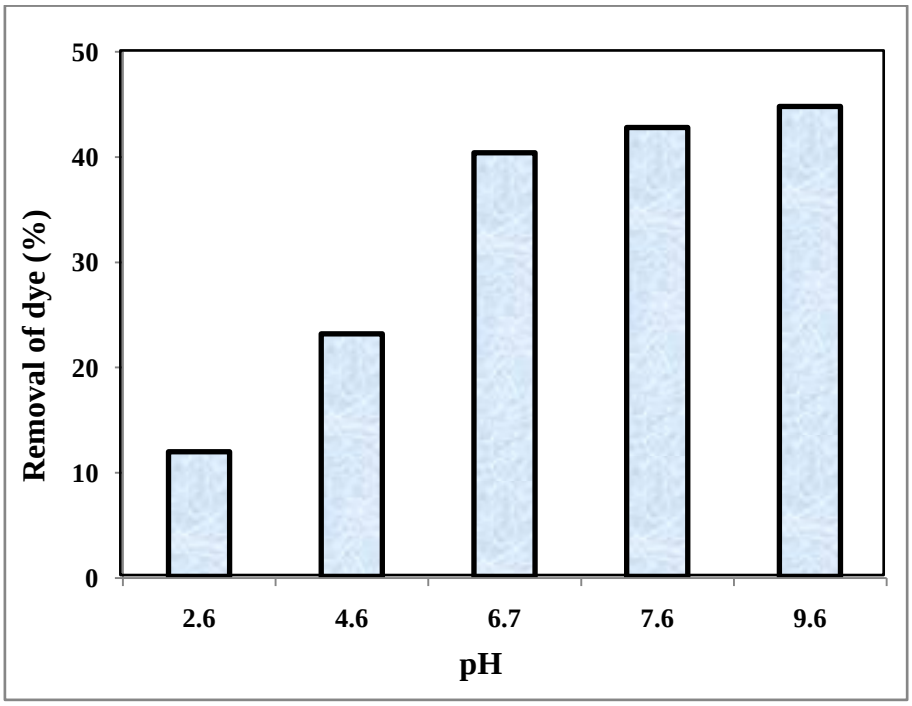

Fig. 2.7: Relative adsorption efficiency of GBC-120 carbon at different pH values.

Adsorption following regeneration: GBC-120 was regenerated by treatment with small amount of concentrated H_2SO_4. Further, 10 mg of the regenerated carbon was treated with 20 mL of methylene blue solution of concentration 50 µg $mL^{-1}$and the pH was adjusted to 7. The adsorption was carried out for 2 hours using the original and

regenerated carbons. The amount adsorbed in both the cases was found to be around 419 mg g^{-1}. Thus GBC-120 carbon could be easily regenerated and reused.

2.4.3 Effect of initial methylene blue concentration

Adsorption studies were carried out by equilibriating 2 mg of GBC-120 carbon using 100 mL methylene blue solution having initial concentrations of 10, 20, 30, 40, 50 µg mL^{-1}. The pH of each solution was adjusted to 7. The results are presented in Fig 2.8. It can be seen from the figure that the mass of 2 mg carbon could completely remove methylene blue solution from its initial concentration of 10 µg mL^{-1}. This was equivalent to an adsorption capacity of 500 mg g^{-1}.

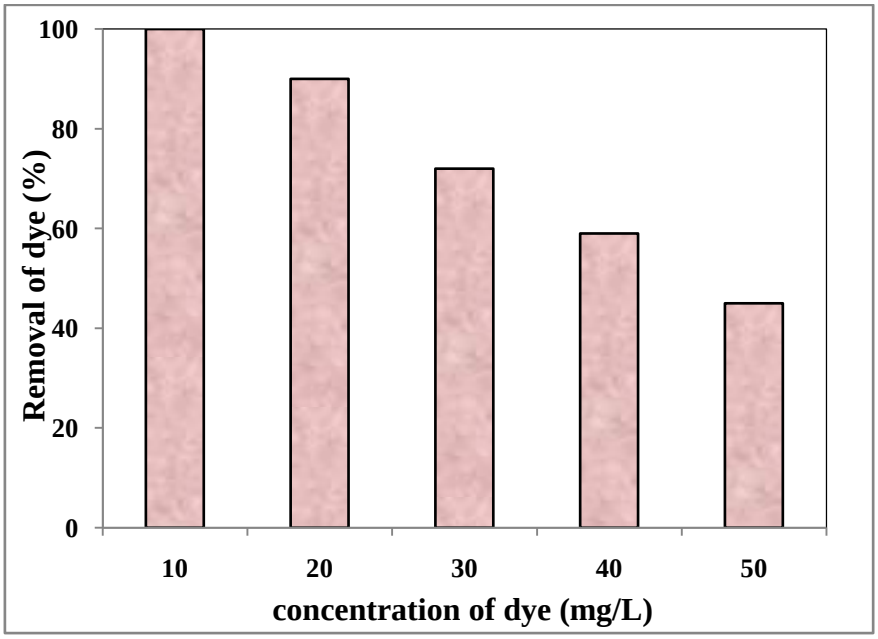

Fig. 2.8: Effect of initial concentration of methylene blue on adsorption efficiency.

2.4.4 Effect of contact time and determination of adsorption equilibrium

The adsorption was studied by equilibriating 20 mg of carbon with methylene blue solution of concentration 50 µg mL^{-1}. The adsorption was studied in two separate experiments in which the pH of the methylene blue solution was adjusted to 4.7 and 7.0 respectively. The adsorption was carried out for about 15-20 hours until no further adsorption occurred as evident from constant absorbance of the supernatant solution. The resulting adsorption time profiles are given in Fig. 2.9.

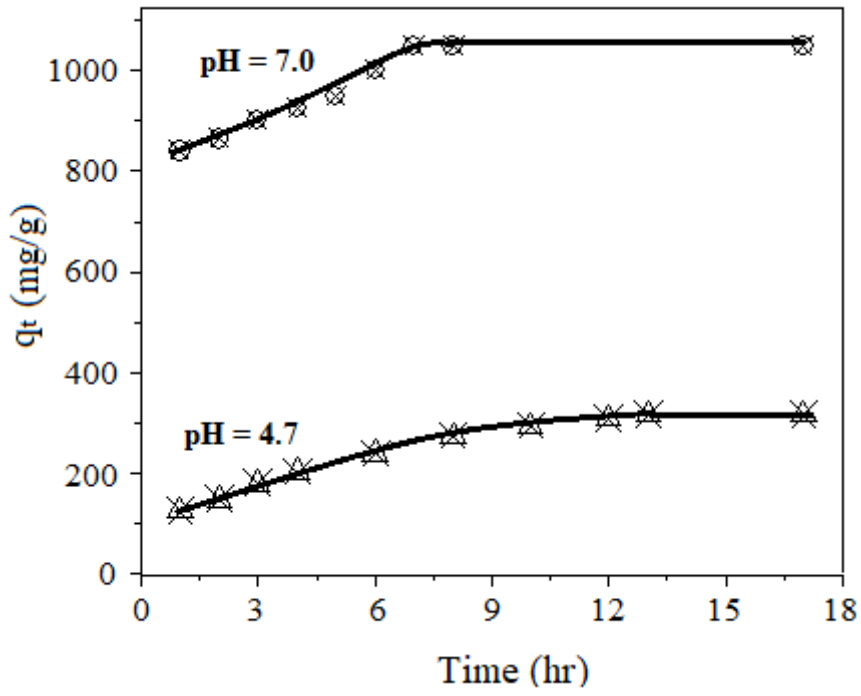

Fig. 2.9: Kinetic plots obtained when GBC-120 carbon samples were equilibrated with methylene blue solution at pH = 4.7 and 7.0.

At pH 4.7, the amount adsorbed gradually increased and became maximum (about 300 mg g^{-1}) after about 13 hours. It is seen in the previous section that adsorption increases with pH. Hence adsorption equilibrium-time profile was also investigated at pH 7.0. It was seen that adsorption increased at relatively faster rate and equilibrium was reached

within 7 hours. The amount adsorbed under this condition reached a high value of about 1050 mg g^{-1}. This is noteworthy since the recent literature suggest that maximum adsorption capacity of methylene blue on activated carbon is upto about 580 mg g^{-1} . This enhanced adsorption capacity of GBC-120 is mainly due to its SO_3H functionality. It is shown that when surface functional groups are affected by thermal treatment at 350 ^oC the adsorption capacity significantly drops to 130 mg g^{-1}.

2.5 Adsorption isotherm

An adsorption isotherm is a plot of amount of substance adsorbed per unit mass of adsorbent as a function of various equilibrium concentrations at a specified temperature. Typically an adsorption isotherm falls in one of the six specified categories [32]. Accordingly the plots are classified into Type I, Type II etc. The nature of these plots depends on nature of adsorbate and adsorbent. Further the adsorption is influenced by the surface area, porosity and nature of surface functionalities of the adsorbent. Various mathematical expressions are available to describe the nature of adsorption as described in Table 2.1. Typical adsorption behavior involves Langmuir adsorption. It corresponds to rapid rise in adsorption as concentration increases, and ends up with a plateau region due to saturation of surface adsorption sites. The Freundlich adsorption isotherm extends to further adsorption beyond saturation due to formation of multilayers.

Fig. 2.10 (a) gives the general adsorption isotherm profile observed in this work for adsorption of MB on GBC-120. It showed Type I adsorption behavior in the lower concentration range. Such a behavior is expected for Langmuir adsorption isotherm. However at higher concentration above 10 μg mL^{-1} of the adsorbate, adsorption suddenly increased suggesting an overall Freundlich type of adsorption behavior.

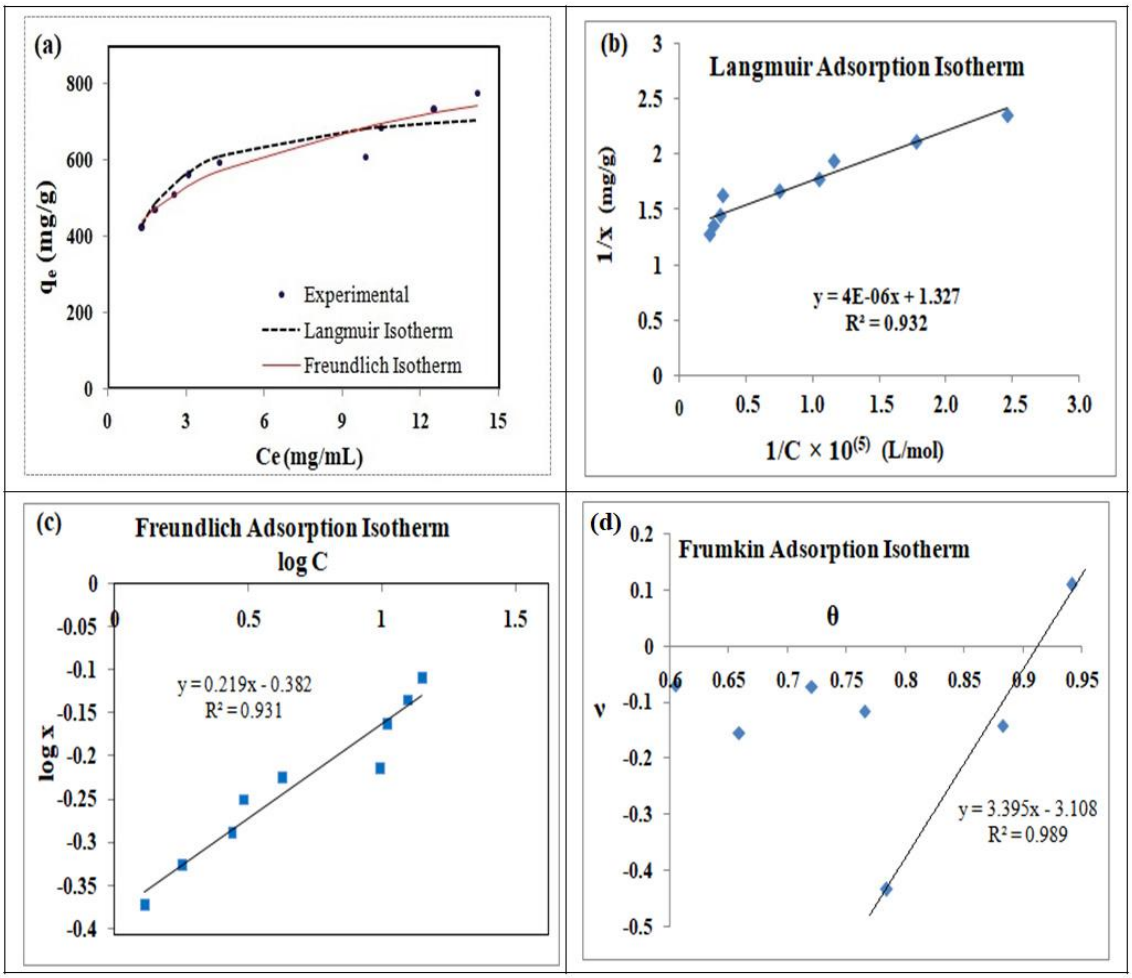

Fig. 2.10: (a) General adsorption Isotherm and (b-d) Applicability of various adsorption models for adsorption of methylene blue on GBC-120 at 25 ^{o}C and pH=7 .

Table 2.4: Values of various adsorption isotherm parameters during adsorption of methylene blue on GBC-120.

Langmuir		**Freundlich**		**Frumkin**	
X_m (mg/g)	754.00	k (mg/g)	415.00	α (µg/mL)	3.90
K (L/mg)	1.00	1/n	0.22	β (µg/mL)	-172.00
R^2 (Linear)	0.93	R^2 (Linear)	0.93	R^2	0.99
R^2 (Non Linear)	0.84	R^2 (Non Linear)	0.97	--	--

The general adsorption behavior represented above in Fig. 2.10 (a), the experimental points can be fitted in one or more mathematical descriptions of adsorption isotherm models such as those reviewed in Table 2.1. Fig. 2.10 (b-d) gives corresponding plots. The data extracted from these plots is presented in Table 2.4.

It is clear from Fig. 2.10 (b) that the data fitted well for Langmuir adsorption isotherm with coefficient of determination R^2 value of 0.93 and value of Xm obtained from the graph was close to the observed value around 750 mg g^{-1}. The low value of Langmuir adsorption constant K is indicative of predominantly Van der Waals type of adsorption. On the other hand Freundlich adsorption 1/n was about 0.22. 1/n which represents intensity of adsorption usually have values between 0 to 1. From the q_e versus C plot as in Fig. 2.10 (a) it is seen that the overall fit is better for Freundlich adsorption isotherm across the full concentration range studied.

However it is seen from Fig. 2.10 (d) that the Frumkin adsorption isotherm fits the experimental data well at higher concentration with coefficient of determination R^2 value of 0.99 with a positive interaction parameter α having a value of 3.9 $\mu g\ mL^{-1}$. This is due to multiple adhesive interactions between the surface SO_3H groups and MB molecules as well as the cohesive attractive interaction between the adsorbed MB multilayers. Evidence for such interactions during adsorption of MB on smectites was reported earlier [33]. Further the high value of α equal to 3.9 is also indicative of lateral interaction between the adsorbate molecules in adjacent layers resulting in greater tendency for desorption or breakdown of the multilayers. This is supported by negative value of β.

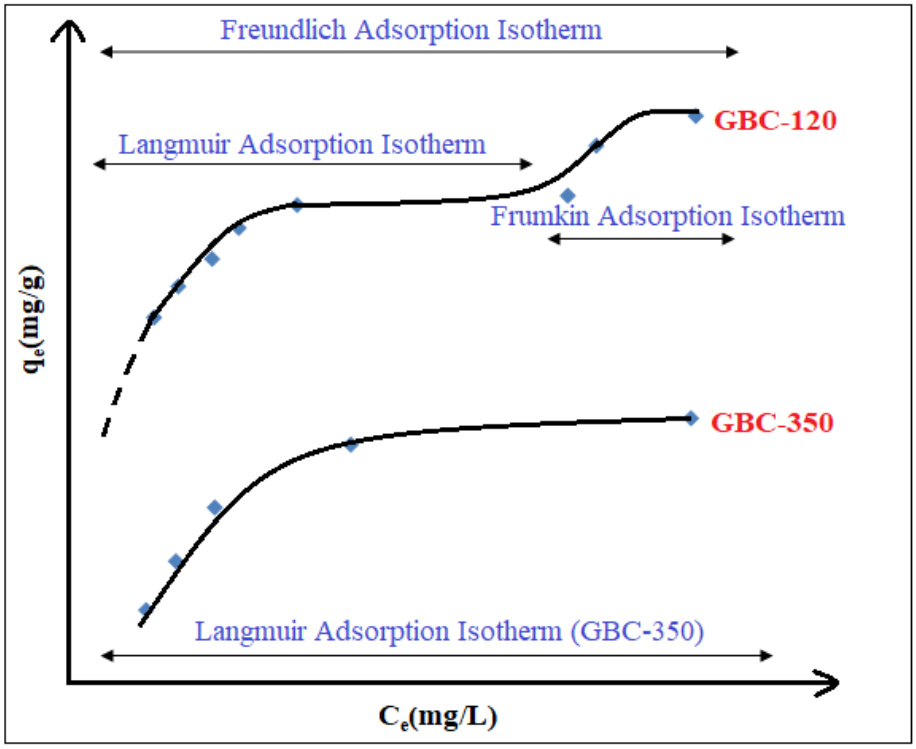

Fig. 2.11: Summary of the adsorption mechanism discussed in the section 2.5

2.6 Thermodynamic Studies

The evaluation of thermodynamic parameters following adsorption studies have been recently reviewed [34-37]. Thus the free energy change for the adsorption process and the corresponding Langmuir adsorption constant K_L can be shown to be related by the equation [38, 34]

$$\Delta G^o = -RTlnK_L \qquad (3)$$

The Langmuir isotherm with the following form has been commonly used for description of adsorption data at equilibrium [34]

$$q_e = q_{max} \frac{C_e K_L}{C_e K_L + 1} \qquad (4)$$

in which q_e and q_{max} are the adsorption capacity of adsorbent at equilibrium (mg g^{-1}) and its maximum value, C_e, is the equilibrium concentration of adsorbate in solution (moles L^{-1}),

K_L can be calculated using the equation (4) [34]:

$$K_L = \frac{\theta_e}{(1-\theta_e)C_e} \text{ where } \theta_e = \frac{q_e}{q_{max}} \qquad (5)$$

Since $\Delta G^o = \Delta H^o - T\Delta S^o$,

it follows that the enthalpy of activation and entropy of activation can be evaluated by using the equation

$$lnK_L = -\frac{\Delta H^o}{R}\frac{1}{T} + \frac{\Delta S^o}{R} \qquad (6)$$

Where R is the universal gas constant (8.314 J mol^{-1} K^{-1}) and T is temperature in Kelvin at which adsorption is carried out. Fig. 2.12 gives a plot of ln K_L v/s 1/T from which the activation parameters are calculated and are given in Table 2.5.

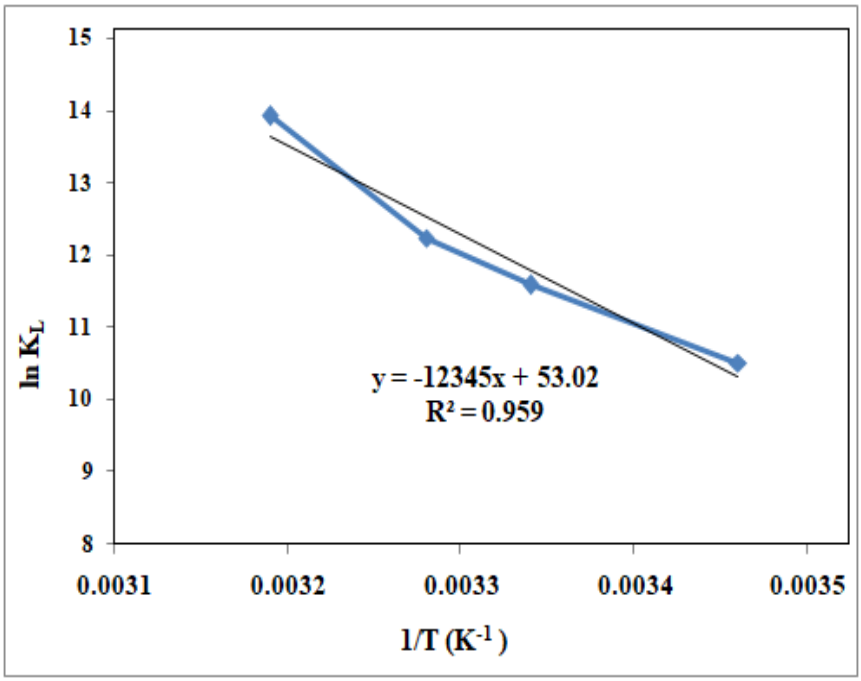

Fig. 2.12: Plot of ln K_L v/s 1/T for adsorption of methylene blue on GBC-120 at various temperatures between 289 – 323 K.

Table 2.5: Evaluation of thermodynamic parameters during adsorption of methylene blue on GBC-120 at various temperatures.

T (K)	**q_e (mg g^{-1})**	**C_e (µg mL^{-1})**	**θ_e**	**K_L (L mg^{-1})**	**K_L (L mol^{-1}) × 10^5**	**ln K_L**	**1/T × 10^3**	**ΔG (KJ mol^{-1})**	**ΔH^o (KJ mol^{-1})**	**ΔS^o (KJ mol^{-1})**
289	265	11.70	0.57	0.12	0.37	10.51	3.46	-26.05	102	0.44
299	338	8.10	0.73	0.33	1.08	11.58	3.34	-28.70		
304	372	6.40	0.80	0.65	2.07	12.24	3.28	-30.33		
313	427.80	3.60	0.92	3.48	11.1	13.92	3.19	-34.49		
323	461.90	1.90	1.00	--	--	--	3.09	--		

It is clear from these values that the free energy change becomes progressively more negative suggesting increasing spontaneity in adsorption as the temperature was increased from 289 K to 323 K. The enthalpy of activation for the adsorption process as calculated from the ln K v/s 1/T plot, was 102 KJ mol^{-1}. This confirmed that the formation of the activated complex during adsorption is an endothermic process.

2.7 Adsorption behavior of GBC-350

GBC-350 is formed by partial decomposition of SO_3H groups from GBC-120. When GBC-350 was stirred in methylene blue solution its pH remained close to 6.5. Fig. 2.13 (a-d) gives the general adsorption isotherm profile and its applicability to various adsorption isotherm models. It showed comparatively low adsorption (~130 mg g^{-1}) which was about 10 times less than that observed for GBC-120.

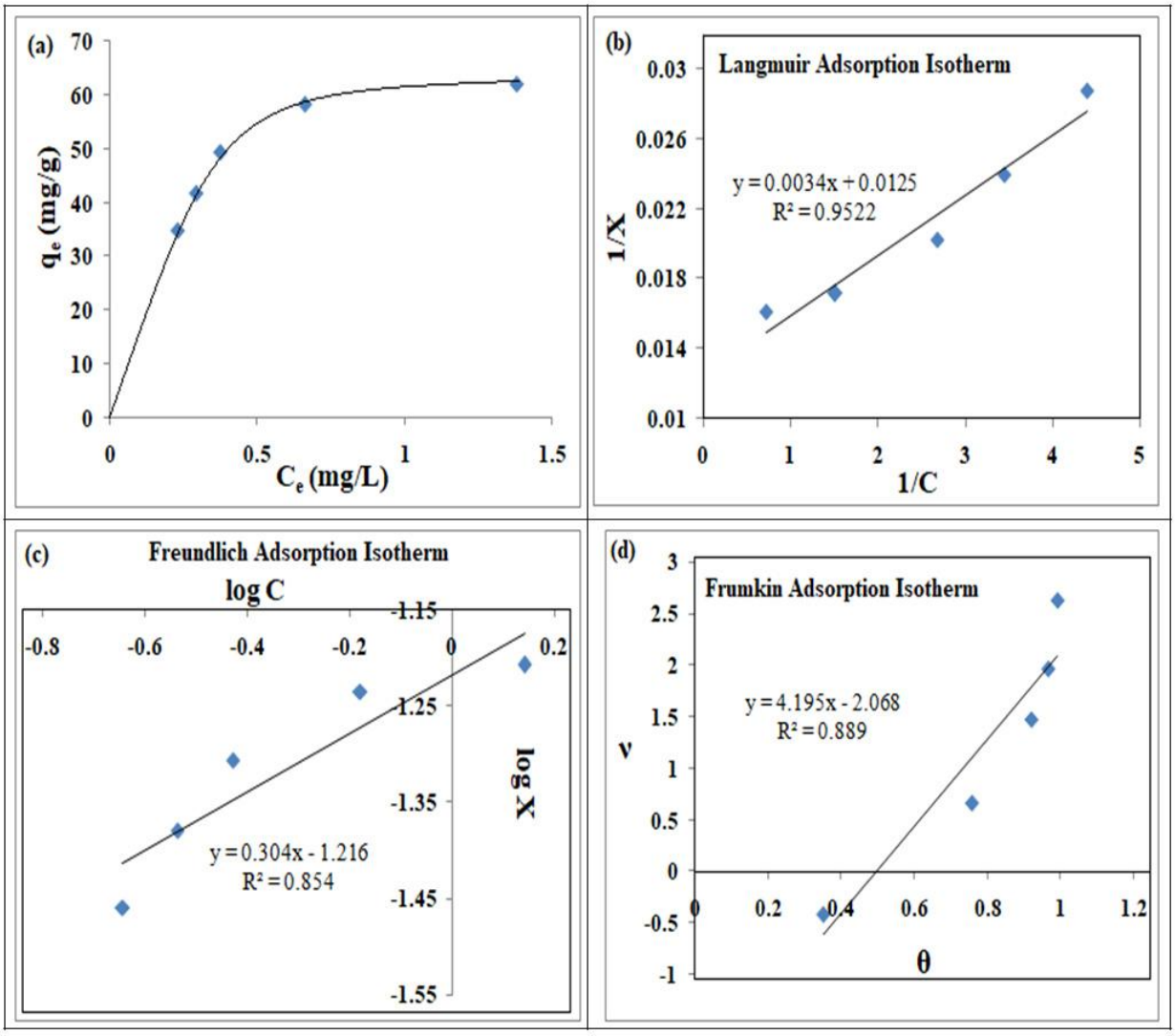

Fig. 2.13. (a) General adsorption Isotherm and (b-d) Applicability of various adsorption models for adsorption of methylene blue on GBC-350 at 25 ^oC.

It can be seen from the Fig. 2.13 (a) that there was initial rapid rise in adsorption. This was followed by decrease in adsorption till there was saturation of adsorption. Such a behavior is generally observed during monolayer formation. As expected the Langmuir adsorption model fitted the data more appropriately with R^2 value of 0.95 as compared when other adsorption models, Freundlich and Frumkin were used wherein the R^2 values were found to be generally less than 0.9.

Fig. 2.14 describes the comparative adsorption behavior of GBC-120 and GBC-350. The corresponding equilibriation times in relation to rate of adsorption are given in Table 2.6.

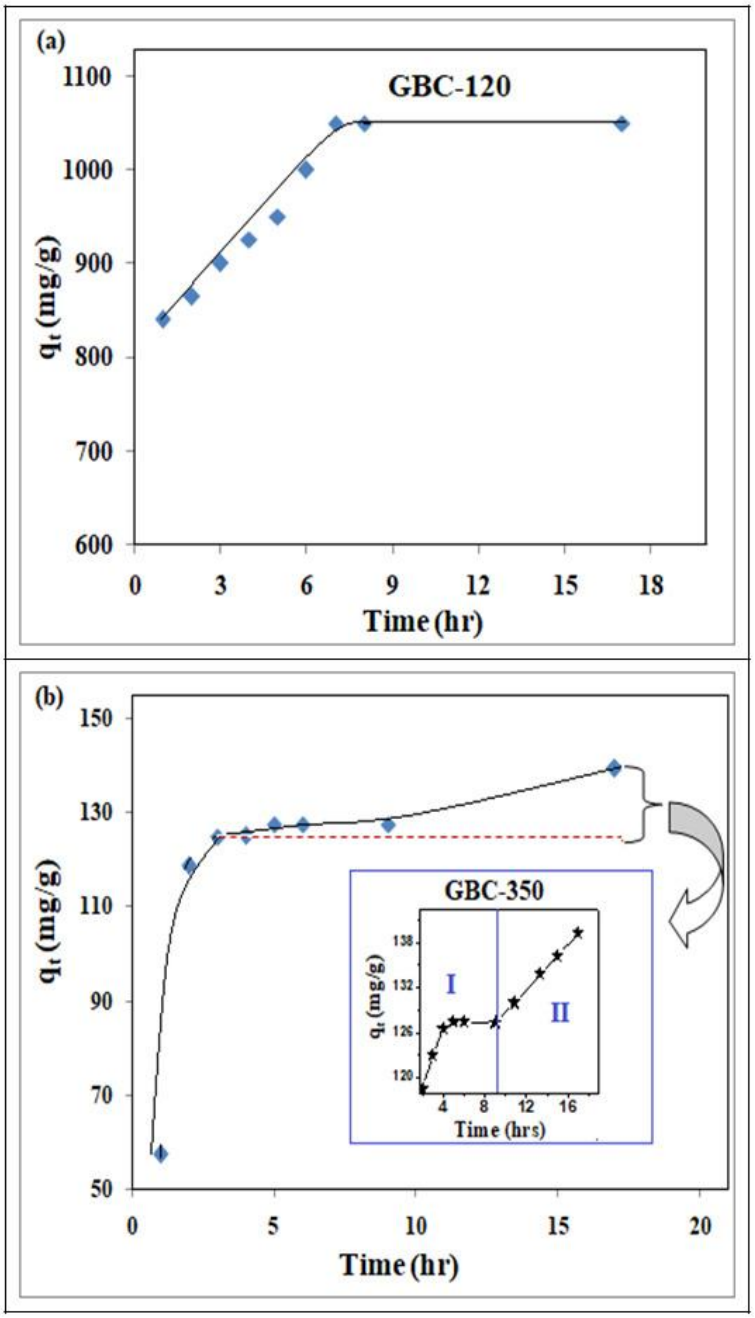

Fig. 2.14: Comparative investigation of adsorption-time behavior of the glycerol based carbons at 25 ^{o}C (a) GBC-120 and (b) GBC-350.

It can be seen from the above Figure that GBC-120 showed rapid adsorption in the beginning till it reached equilibrium at the end of 7 hours. On the other hand, GBC-350, although showed much lower adsorption, its initial rate of adsorption was much higher

as evident from the initial slope of 61 mg g^{-1} hr^{-1} as compared to GBC-120 whose initial slope was only 28 mg g^{-1} hr^{-1}. The higher equilibrium adsorption of 1050 mg g^{-1} on GBC-120 was due to presence of large amount of $–SO_3H$ as compared to GBC-350, where some surface functionalities were lost upon the thermal treatment.

The adsorption in GBC-350 was to a large extent completed after about 5 hrs. However complete equilibriation was not reached as there was very small amount of adsorption which occurred very slowly in the time interval of 5-17 hrs. Hence in GBC-350, it can be considered as a two stage adsorption process (i) initial equilibrium due to high surface area (ii) the second slow equilibrium, due to tendency of MB to diffuse into the micropores that were developed in the sample after heating it at 350 ^oC as discussed earlier in 2.3. Accordingly, to evaluate the kinetic parameters, the GBC-350 sample is referred to as GBC-350(I) and GBC-350(II). The corresponding adsorption profile is shown resolved in Fig. 2.14 (inset)

Further GBC-120 showed relatively low pzc value of 2.0 as compared to that of GBC-350 (3.5). Therefore it is expected that the cationic dye MB will be preferentially adsorbed on GBC-120 having large number of highly acidic sulphonyl groups generally in a dissociated form. The high adsorption in GBC-120 is due to hydrogen bonding between H of $–SO_3H$ functionality on GBC-120 surface and N of the methylene blue dye. A similar hydrogen bonded interaction was proposed during adsorption of methylene blue on iron oxide surface [39]. Further enhanced adsorption is also due to interaction of the cationic dye with the dissociated sulphonyl groups.

2.8 Kinetics of adsorption

The adsorption process from solution generally involves diffusion of the dyes (i) from the bulk solution to near the surface of the adsorbent followed by (ii) diffusion at the boundary layer.

The boundary layer is composed of the surface functionalities of the adsorbent and the pre-adsorbed layer of the adsorbate (MB) as well as the layer of water dipoles. Therefore the boundary layer can offer resistance to diffusion of the adsorbate before the actual adsorption interaction occurs on the available surface sites. (iii) The adsorbate molecules may further diffuse inside the pores of the adsorbent depending upon the nature of adsorbate, adsorbent and equilibriation time [20].

The kinetic data obtained on the GBC samples in the present investigation (Fig. 2.15) was then fitted in various available kinetic models (Table 2.1).

3.6.1. Applicability of pseudo first and pseudo second order kinetic models for GBC-120 and GBC-350.

Fig. 2.15. gives the pseudo first and pseudo second order kinetic plots for GBC-120, GBC-350(I) and GBC-350(II). The resulting kinetic parameters are summarized in Table 2.7.

Sample	Pseudo First order kinetics	Pseudo Second order kinetics
GBC-120	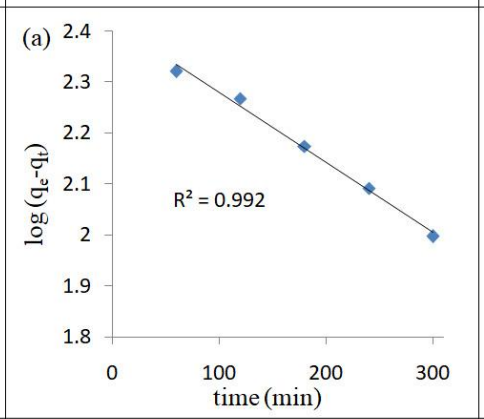	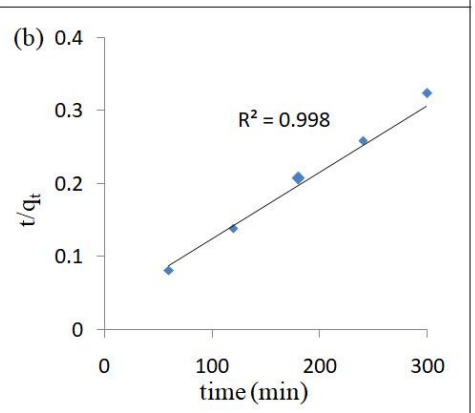
GBC-350(I)	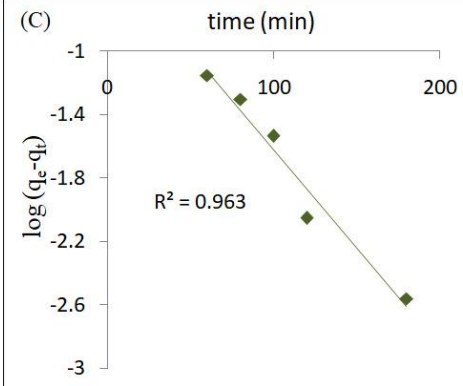	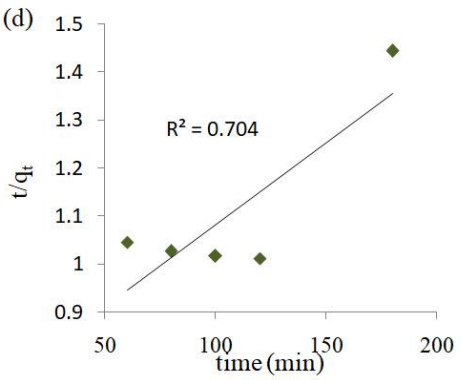
GBC-350(II)	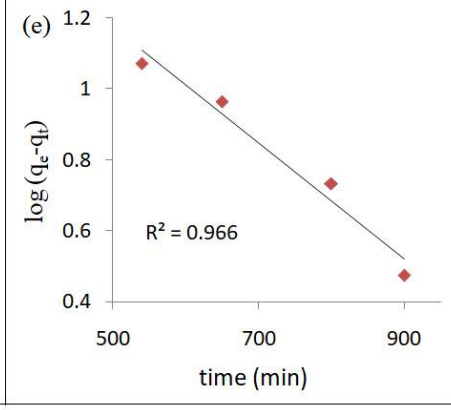	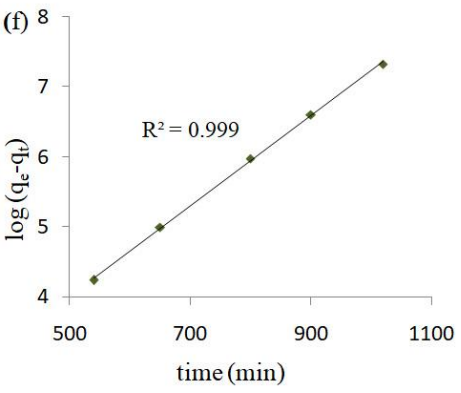

Fig. 2.15: Application of pseudo first and pseudo second order kinetic models during equilibriation of methylene blue on the GBC samples. GBC-350(I) is initial stage of adsorption and GBC-350(II) is second stage of adsorption.

Table 2.6: Kinetic parameters obtained from application of pseudo first and pseudo second order kinetic models for adsorption of MB on GBC carbons.

Carbon samples	**Pseudo first order kinetic model**			**Pseudo second order kinetic model**			q_e calculated (mg g^{-1})
	R^2	K_1 (min^{-1})	q_e observed (mg g^{-1})	R^2	K_2 (g mg^{-1} min^{-1})	q_e observed (mg g^{-1})	
GBC-120	0.91	0.0046	385	0.99	$4.17*10^{(-5)}$	865	1050
GBC-350 I	0.96	0.0286	408	0.70	$1.56\times10^{(-5)}$	029	130
GBC-350 II	0.97	0.0036	098	0.99	$5.14\times10^{(-5)}$	156	139

It can be seen from the R^2 values that the GBC-120 (Table 2.6) showed a relatively better fit for pseudo second order kinetics. This is confirmed by the fact that the value of q_e observed is more closer to the calculated value for all the initial concentrations. On the other hand for GBC-350(I), the R^2 values as well as the observed and calculated q_e values differed widely, 29 and 130 mg g^{-1} respectively for pseudo second order kinetic model. Thus the adsorption process did not follow first as well as pseudo second order kinetics. However GBC-350(II) showed a good fit for pseudo second order adsorption process (R^2 = 0.999) as the observed and calculated values of q_e (156 and 139 mg g^{-1}) were quite close.

Summary & Conclusions

i A glycerol based carbon (GBC) was synthesized by partial carbonization of glycerol using con H_2SO_4 in the molar ratio 1:4. The carbonized material was further treated at 120 ^oC and 350 ^oC to obtain the carbons GBC-120 and GBC-350 respectively.

ii The samples were characterized by XRD, ir, thermal analysis (TG-DTG-DTA) and pzc measurements. The TGA showed a gradual weight loss up to about 800 ^oC. The ir spectra of the GBC-120 showed characteristic absorptions due to $–SO_3H$ groups. The ir spectra were also recorded of GBC samples heat treated at various higher temperatures. All the peaks due to surface functionalities were eventually disappeared for the GBC-800 sample, in agreement with thermal analysis wherein the decomposition was complete around this temperature (800 ^oC). The BET surface area of GBC-120 was 21 $m^2 g^{-1}$ while GBC-350 showed much larger surface area of about 464 $m^2 g^{-1}$.

iii The adsorption studies were carried out using methylene blue as a model adsorbate. The GBC-120 gave maximum adsorption capacity of 1050 mg g^{-1}. The adsorption efficiency was observed to be dependent on initial concentration of the dye. There was nearly 100 % dye removal efficiency using 8-10 milligrams of the adsorbent powder, when the dye concentration was 25 μg mL^{-1}.

iv The GBC-120 showed Type-I adsorption isotherm profile at lower concentration range which obeyed conventional Langmuir adsorption isotherm models. However at higher equilibrium concentration above 10 μg mL^{-1}, the data fits better in Frumkin adsorption model with R^2 value of 0.989 due to large

interaction between the adsorbate molecules. The adsorption generally increased with temperature and showed a favorable free energy change. The GBC-350 showed comparatively less adsorption in spite of its much larger surface area due to loss of SO_3H functionalities.

v The adsorption data could be fitted in Langmuir adsorption isotherm profile. Investigation of adsorption kinetics revealed better fit with pseudo second order kinetic model for GBC-120 while GBC-350 showed a unique two stage adsorption profile and the data could be better fitted into pseudo second order kinetic model.

This investigation is expected to be an important contribution for further development of glycerol based carbon as an adsorbent, catalyst as well as catalysts support such as in electrocatalysis related to fuel cell where very pure carbon is necessary.

References

[1] K. V. Raghavan, B. M. Reddy (Eds), *Industrial Catalysis and Separations: Innovations for Process Intensification,* CRC Press (2014).

[2] B. L. A. Prabhavathi Devi, K. N. Gangadhar, P. S. Sai Prasad, B. Jagannadh and R. B. N. Prasad, *A Glycerol-based Carbon Catalysts for the Preparation of Biodiesel,* ChemsusChem 2 (2009) 617-620.

[3] K. Ramesh, S. N. Murthy, K. Karnakar, K. H. Reddy, Y. V. D. Nageswar, M. Vijay, B. L. A. Prabhavathi Devi, R. B. N. Prasad, *A mild and expeditious synthesis of amides from aldehydes using bio-glycerol-based carbon as a recyclable catalyst*, Tetrahedron Lett. 53 (2012) 2636–2638.

[4] K. N. Gangadhar, M. Vijay, R. B. N. Prasad, B. L. A. Prabhavathi Devi, *Glycerol-Based Carbon-SO_3H Catalyzed Benign Synthetic Protocol for the Acetylation of Alcohols, Phenols and Amines under Solvent-Free Conditions*, Green and Sust. Chem. 3 (2013) 122-128.

[5] C. Ummadisetti, B. N. P. Rachapudi, B. L. A. Prabhavathi Devi, *Glycerol-based SO_3H-Carbon Catalyst: A green recyclable catalyst for the chemoselective synthesis of pentaerythritoldiacetals,* Eur J Chem 5 (2014) 536-540.

[6] R. S. Ribeiro, A. M. T. Silva, M. T. Pinho, J. L. Figueiredo, J. L. Faria, H. T. Gomesa, *Development of glycerol-based metal-free carbon materials for environmental catalytic applications,* Catal. Today 240 (2015) 61–66.

[7] S. Álvarez-Torrellas, R. S. Ribeiro, H. T. Gomes, G. Ovejero, J. García, *Removal of antibiotic compounds by adsorption using glycerol-based carbon materials,* Chem. Eng. J. 296 (2016) 277–288.

[8] Tawfik A. Saleh, Ihsan Budi Rachman, Shaikh A. Ali, *Tailoring hydrophobic branch in polyzwitterionic resin for simultaneous capturing of Hg(II) and methylene blue with response surface optimization,* Sci. Rep. (2017) DOI:10.1038/s41598-017-04624-6.

[9] Tawfik A. Saleh, *Nanocomposites of carbon nanotubes/silica nanoparticles and their use for adsorption of Pb(II): from surface properties to sorption mechanism, Desalination and Water Treatment,* (2015) 1-15.

[10] Tawfik A. Saleh, *Mercury sorption by silica/carbon nanotubes and silica/activated carbon: a comparison study,* Journal of Water Supply: Research and Technology-AQUA, (2015) 892-903.

[11] Tawfik A. Saleh, Mustafa Tuzen, Ahmet Sari, *Magnetic activated carbon loaded with tungsten oxide nanoparticles for aluminum removal from waters,* J. Environ. Chem. Eng. 5 (2017) 2853-2860.

[12] Tawfik A. Saleh, Ahmet Sari, Mustafa Tuzen, *Optimization of parameters with experimental design for the adsorption of mercury using polyethylenimine modified-activated carbon,* J. Environ. Chem. Eng. 5 (2017) 1079-1088.

[13] Ratna, B. S. Padhi, *Pollution due to synthetic dyes toxicity & carcinogenicity studies and remediation,* Int. J. Environ. Sci. 3 (2012) 940-955.

[14] E. Rindle, W. J. Troll, *Metabolic reduction of benzidine azo dyes to benzidine in the Rhesus monkey,* J. Natl. Cancer Inst. 55 (1975) 181-182.

[15] Saleh, M.A.M., Mahmoud, D.K., Karim, W.A.W.A., Idris, A., *Cationic and anionic dye adsorption by agricultural solid wastes: a comprehensive review*, Desalination 280 (2011) 1–13.

[16] M. A. Mohammed, A. Shitu, A. Ibrahim, *Removal of Methylene Blue Using Low Cost Adsorbent: A Review,* Res. J. Chem. Sci. 4 (2014) 91-102.

[17] J. H. Potgieter, *Adsorption of Methylene blue on activated carbon,* J. Chem. Educ. 68 (1991) 349-350.

[18] M. Santhi, P. E. Kumar, *Adsorption of basic dye, methylene blue by a novel activated carbon prepared from Typha Angustata,* Chem. Sci. Trans. 4 (2015) 389-400.

[19] S. M. Yakout, E. Elsherif, *Batch kinetics, isotherm and thermodynamics studies of adsorption of strontium from aqueous solution into low cost rice-straw based carbons,* Carbon – Sci. and Tech. (2010) 144-153.

[20] Y. Önal, *Kinetics of adsorption of dyes from aqueous solutions using activated carbon prepared from the waste apricot,* J. Hazard. Mater. B 137 (2006) 1719-1728.

[21] V. Srivastava, P. Maydannik, Y. C. Sharma, M. Sillanppa, *Synthesis and applications of polypyrrole coated tenorite nanoparticles (PPy@TN) for the removal of anionic food dye 'tartrazine' and divalent metallic ions viz Pb(II), Cd(II), Zn(II), Co(II), Mn(II) from synthetic wastewater,* RSC advances 5 (2015) 80829-80846.

[22] Y. Li, Q. Du, X. Wang, P. Zhang, D. Wang, Z. Wang, Y. Xia, *Removal of Lead from aqueous solution by activated carbon prepared from Entermorpha Prolifera by zinc chloride activation,* J. Hazard. Mater. 183 (2010) 583-589.

[23] L. Wang, X. Li, J. Ma, Q. Wu, X. Duan, *Non-activated, N, S-co-doped Biochar Derived from Banana with Superior Capacitive Properties,* Sustain. Energy 2 (2014) 39-43.

[24] M. Gonçalves, R. Rodrigues, T. S. Galhardo, W. A. Carvalho, *Highly selective acetalization of glycerol with acetone to solketal over acidic carbon-based catalysts from biodiesel waste*, Fuel 181 (2016) 46-54.

[25] J. L. Figueiredo, M. F. R. Pereira, M. M. A. Freitas, J. J. M. Órfão, *Modification of surface chemistry of activated carbon*, Carbon 37 (1999) 1379 –1389.

[26] R. Fareghi-Alamdari, M. Golestanzadeh, N. Zekri, Z. Mavedatpoor, *Multi SO_3H supported on carbon nanotubes: a practical, reusable, and regioselective catalysts for the tert-butylation of p-cresol under solvent-free conditions,* J Iran Chem Soc 12 (2015) 12537–549.

[27] P. A. Russo, M. M. Antunes, P. Neves, P. V. Wiper, E. Fazio, F. Neri, F. Barreca, L. Mafra, M. Pillinger, N. Pinna, A. A. Valente, *Mesoporous carbon–silica solid acid catalysts for producing useful bio-products within the sugar-platform of biorefineries,* Green Chem.16 (2014) 4292–4305.

[28] H. Guo, Y. Lian, L. Yan, X. Qi, R. L. Smith, *Cellulose-derived superparamagnetic carbonaceous solid acid catalyst for cellulose hydrolysis in an ionic liquid or aqueous reaction system,* Green Chem.15 (2013) 2167-2174.

[29] J. Wang, W. Xu, J. Ren, X. Liu, G. Lu, Y. Wang, *Efficient catalytic conversion of fructose into hydroxyethylfurfural by a novel carbon based solid acid*, Green Chem.13 (2011) 2678-2681.

[30] L. Na, Z. Jian, Z. Qing-Fang, *Quantitative and Qualitative Analyses of Oxygen-containing Surface Functional Groups on Activated Carbon*, Chem. J. Chinese U 3 (2012) 548-554.

[31] H. Park, Y. S. Yun, T. Y. Kim, K. R. Lee, J. Baek, J. Yi, *Kinetics of the dehydration of glycerol over acid catalysts with an investigation of deactivation mechanism by coke,* Appl Catal. B 176–177 (2015) 1–10.

[32] S. Brunauer, L.S. Deming, W.S. Deming, E. Teller, *Classification of Adsorption Isotherms,* J. Am. Chem. Soc. 62 (1940).

[33] J. Bujdák, M. Janek, J. Madeiová, P. Komadel, *Methylene blue interaction with reduced-charged smectites,* Clays Clay Miner. 49 (2001) 244-254.

[34] Yu Liu, *Is the Free Energy Change of Adsorption Correctly Calculated?* J. Chem. Eng. Data 54 (2009) 1981-1985.

[35] Yu Liu, Ya-Juan Liu, *Review Biosorption isotherms, kinetics and thermodynamics,* Separation and Purification Technology 61 (2008) 229–242.

[36] Yu Liu, Hui Xu, *Equilibrium, thermodynamics and mechanisms of* Ni^{2+} *biosorption by aerobic granules,* Biochemical Engineering Journal 35 (2007) 174–182.

[37] E. C. Lima, M. A. Adebayo, F. M. Machado, *Chapter 3- Kinetics and Equilibrium Models of Adsorption in Carbon Nanomaterials as Adsorbents for Environmental and Biological Applications, C. P. Bergmann, F. M. Machado editors*, ISBN 978-3-319-1887-4, Springer (2015) 33-69.

[38] A. S. Özcan, A. Özcan, *Adsorption of acid dyes from aqueous solutions onto acid-activated bentonite,* J. Colloid Interface Sci. 276 (2004) 39-46.

[39] F. Li, X. Wu, S. Ma, Z. Xu, W. Liu, F. Liu, *Adsorption and desorption mechanism of methylene blue removal with Iron-oxide coated porous ceramic filter,* J Water Resource Prot 1 (2009) 1-57.

CHAPTER III

ACTIVATION OF GLYCEROL BASED CARBONS

3.1: Chemical activation

3.2: Surfactant mediated activation

3.3: Adsorption studies

Introduction

Activated carbon materials are characterized with large surface area, often having variable pore structures. Their properties can be tuned depending upon the desired applications, by suitably modifying the synthesis and activation strategy. Activated carbons are generally prepared from biomass such as coconut shells, seeds, rice husk, coir, wood waste etc. Preparation of activated carbons generally consist of two fundamental steps (i) carbonization of the raw materials and (ii) activation of the carbonized material at elevated temperatures (often 500^{o}C or above). This involves either physical or chemical activation leading to enhancement in porosity and surface area of the resulting carbon. Thus, activated carbons exhibit high adsorption capacity that makes them indispensable in various industrial applications. They are widely used in water purification processes due to their excellent adsorption property for heavy metal ions and dyes. Similarly activated carbons find application in pharmaceutical and food industry to remove color and also in gas masks to adsorb harmful gases.

It is often observed that chemical activation was more effective than the method of physical activation to obtain carbons having porous structure [1]. H_3PO_4, $ZnCl_2$ and KOH are the most widely used chemical activating agents for producing activated carbons [2, 3]. The carbon activation is often carried out in the temperature range 500 – 800 ^{o}C. It is generally observed that increase in temperature results in enhancement of surface area and porosity and decrease in surface functional groups. Surface areas in excess of 1500 m^2g^{-1} have been reported [3-5]. These chemical activating agents influence the surface area enhancement to different extents depending upon the carbon source such as coal, palm kernel, nutshells etc. [6-8] or whether it is a reactivated commercial carbon [9].

In the present investigation glycerol based activated carbon is being developed, with a view to finding their application in adsorption, supercapacitance and as electrocatalytic support. Glycerol is one of the byproducts produced in huge amount in biodiesel industry during the transesterification process. Thus its overstock makes it imperative to transform it into suitable value added products. The enhanced adsorption behavior and catalytic applications of glycerol based carbons has been recently reported with regards to dyes and pharmaceuticals [10, 11] as well as for catalyzed organic transformations [12-16].

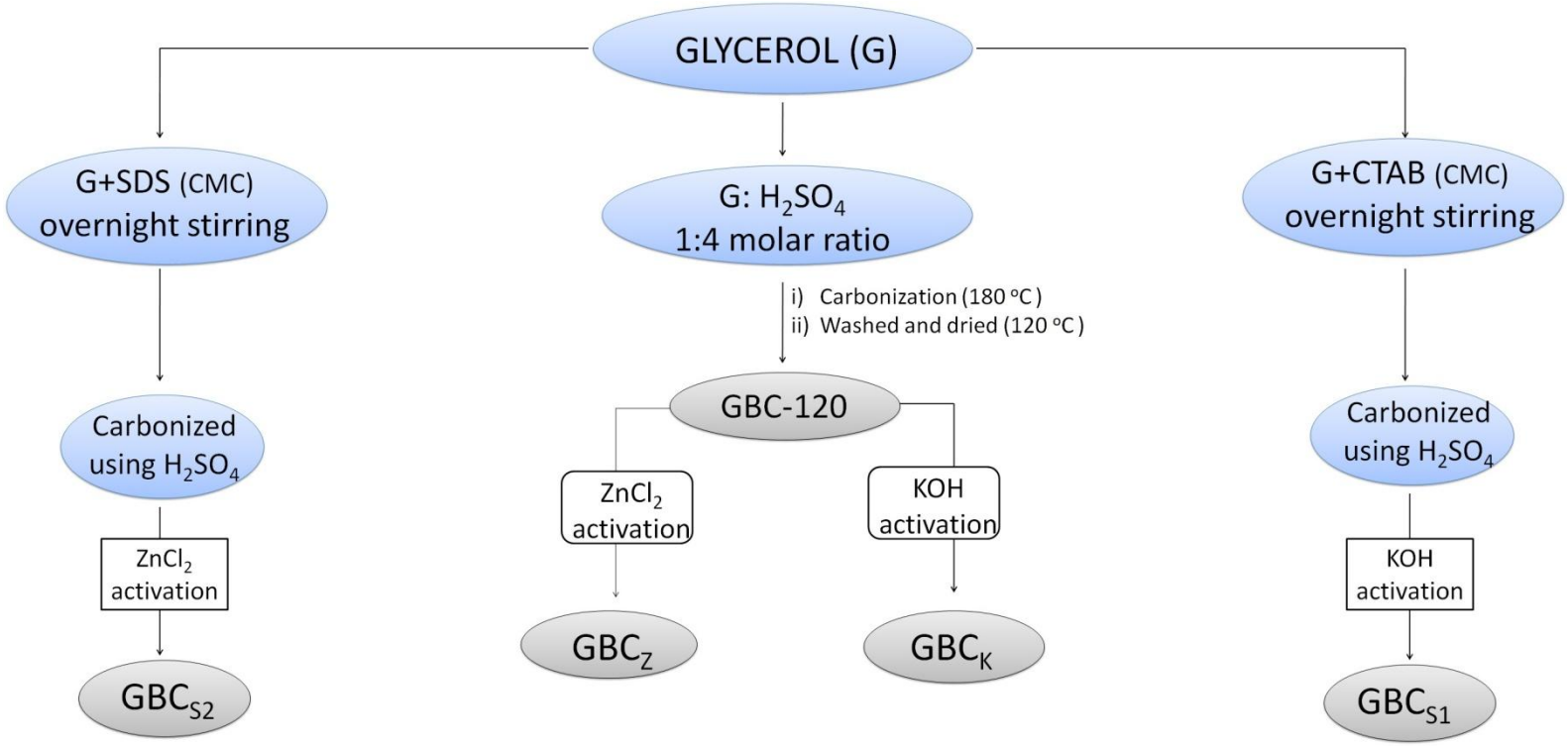

Scheme 3.1: Synthesis and activation of glycerol based carbons

3.1 Chemical activation of glycerol based carbon

Glycerol based carbon (GBC-120) was synthesized by dehydration of glycerol as discussed in Chapter I. It was further activated chemically by using KOH and $ZnCl_2$. The overall scheme of synthesis is illustrated in scheme 3.1.

3.1.1 Preparation of activated carbon using KOH

To activate GBC-120 using KOH as activating agent, ~ 2 g of GBC-120 carbon powder was soaked for 2 hours into 4 mL of aqueous KOH solution (250 mg/mL). The amount of KOH dissolved was ~1 g which was 50% by weight of the carbon powder taken. The carbon/KOH mixture was dried at 150 ^{o}C in an air oven. The dried mixture was further heated in N_2 atmosphere at 800 ^{o}C for 2 hours. The product was cooled and stirred in a small amount of concentrated nitric acid and further washed with distilled water until the washings were neutral. The KOH activated carbon thus obtained was dried at 110 ^{o}C and labeled as GBC_K.

3.1.2 Preparation of activated carbon using $ZnCl_2$ as activated agent

During activation of GBC-120 using $ZnCl_2$, mechanical mixing of $ZnCl_2$ and GBC-120 was carried out in 2:1 weight ratio. The mixture was then heated to 800 ^{o}C in N_2 atm for 8 hrs. The carbon material thus obtained after activation was treated with conc. HCl to remove traces of metallic impurities resulted during decomposition of $ZnCl_2$. It was further washed with excess of distilled water, filtered and dried. The product obtained is denoted as GBC_Z.

3.2 Characterization of activated glycerol based carbon materials

Investigation of structure, surface functionalities, texture and morphology of activated glycerol based carbons produced by KOH activation (GBC_K) and $ZnCl_2$ activation (GBC_Z) was carried out using XRD, Raman spectroscopy, infrared spectroscopy, sorptometric and SEM studies.

3.2.1 Structural properties of activated glycerol based carbons GBC_K and GBC_Z – XRD studies

Fig. 3.1 gives the X-Ray diffraction patterns of activated glycerol based carbons GBC_K and GBC_Z in relation to un-activated carbon GBC-120. The un-activated glycerol based carbon GBC-120 shows a broad peak centered at ~ 22^o and a small peak at $2\theta \sim 43^o$. These peaks were indexed to reflections from (002) and (100) planes respectively. However activated carbons show an additional broad peak at $2\theta \sim 14^o$ in the GBC_K and GBC_Z carbons. A peak around this value of 2θ is generally attributed to formation of graphite oxide. Thus, this broad peak in GBC_K is an indication of amorphous carbon tending towards forming better developed graphitic structure with organic functionalities. The structure of activated carbon is considered to be disorganized form of graphite. It shows a broad peak in the 2θ range of 10^o to 30^o. The peak at $2\theta \sim 13\text{-}14^o$ is a characteristic peak of graphite oxide [17]. The broad peaks in carbon materials centered at 2θ values of ~ 25^o and ~ 44^o suggests more effective alignment of layers in carbon structure and enhanced regularity in the structure [18]. The interlayer spacing'd' is obtained from Bragg's equation: $d = n \lambda / 2 \sin\theta$, where $\lambda = 1.54$ Å and θ is the diffraction angle for the peak position. d_{002} obtained for GBC_K and GBC_Z are 0.378 and

0.361 nm respectively. Whereas for a pure graphitic carbon, a typical interlayer spacing value d_{002} is 0.335 nm.

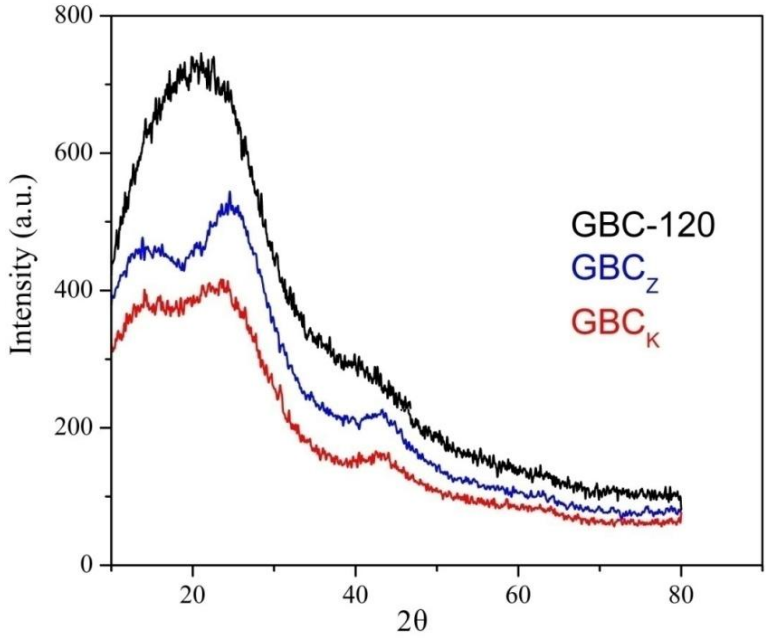

Fig. 3.1: X-ray diffractogram of (a) activated glycerol based carbons GBC_K and GBC_Z in relation to the un-activated carbon GBC-120.

3.2.2 Extent of order/disorder in the carbon structure - Raman scattering studies

Raman spectroscopic studies can be used to analyze extent of disorder in the graphitic structure of the activated carbon produced. The carbon materials such as graphite, graphite oxide, graphene, activated carbons etc., are known to show characteristic Raman absorptions in the region of 1000 cm^{-1} to 3000 cm^{-1}. They correspond to D, G and 2D peaks. The D peak is observed in the range of 1300 - 1400 cm^{-1} and the G peak is located in the range of 1550 - 1600 cm^{-1} [17]. The G band is due to C=C bond stretch of all sp^2 atoms in rings as well as chains [19]. The D band is assigned to structural defects or disorder in the graphitic rings [20, 21]. It is due to out-of-plane vibration of the carbons associated with formation of sp^3 bonds when the carbons at the surface get

oxidized. The ratio I_D/I_G gives a measure of degree of disorder in the carbon structure [20, 22]. Fig. 3.2 gives the Raman spectrum of the GBC_K and GBC_Z sample in relation to the un-activated carbon GBC-120.

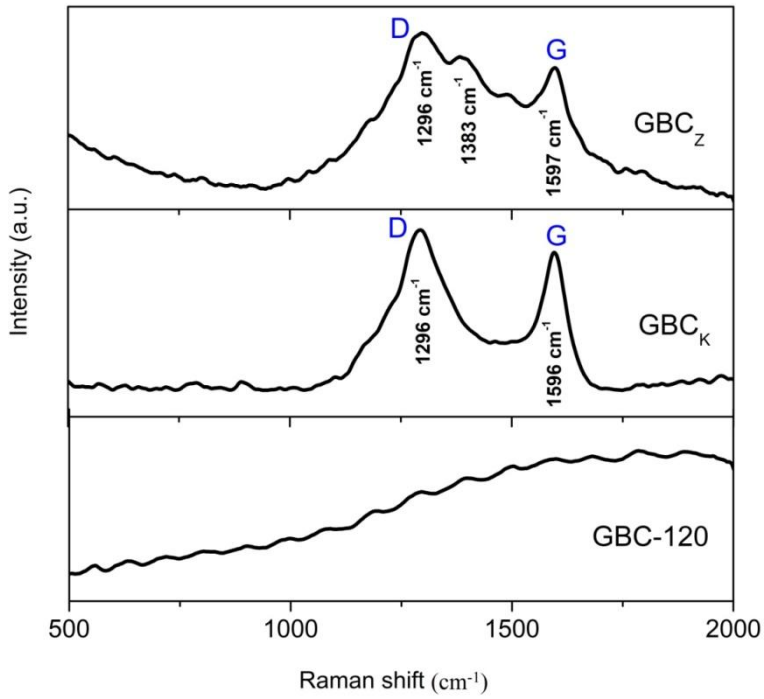

Fig.3.2: Raman spectra of the activated carbons GBC_K and GBC_Z in relation to the corresponding un-activated carbon GBC-120.

It can be seen that the activated carbons GBC_K and GBC_Z show two distinct peaks at Raman shift values of 1296 cm^{-1} and 1596 cm^{-1}. These correspond to D and G bands respectively. They are associated with vibrations of sp^2 carbons in the graphitic rings and are called first order Raman peaks. The ratio I_D/I_G observed for GBC_K and GBC_Z respectively were 1.13 and 1.21 (Table 3.1). This indicates disorder in the graphitic rings. Such disorder is generally expected for functionalized activated carbons due to various orientations of the functional groups. It may be noted that for pure graphite oxide, the I_D/I_G ratio is < 1 and it tends to zero for pure graphene. On the other hand, the Raman spectrum of the un-activated carbon GBC-120, did not show the D and G bands.

It is due to incomplete graphitization of its carbon structure. This is also in accordance with the results obtained from infra red absorption data wherein the graphitic C=C peak at 1625 cm^{-1} was much more intense for GBC_K as compared to the same peak for GBC-120 (Fig. 3.3). The crystallite size along a axis 'L_a' can be deduced from Raman spectra and is directly related to frequency of D band. With increase in the frequency of D band the crystallite size L_a decreases (Table 3.1). Comparative Raman spectra of GBC_K, GBC_Z and GBC-800 with commercial carbon Vulcan XC72R is given in Fig. 3.3. The parameters extracted from these Raman spectra are presented in Table 3.1. It is seen that the sample GBC_K had the lowest I_D/I_G ratio ~ 1.15 among the four investigated carbons. This indicated that the KOH activated carbon yielded comparatively more ordered structure and better graphitization. Its D and G bands were also more intense and better resolved.

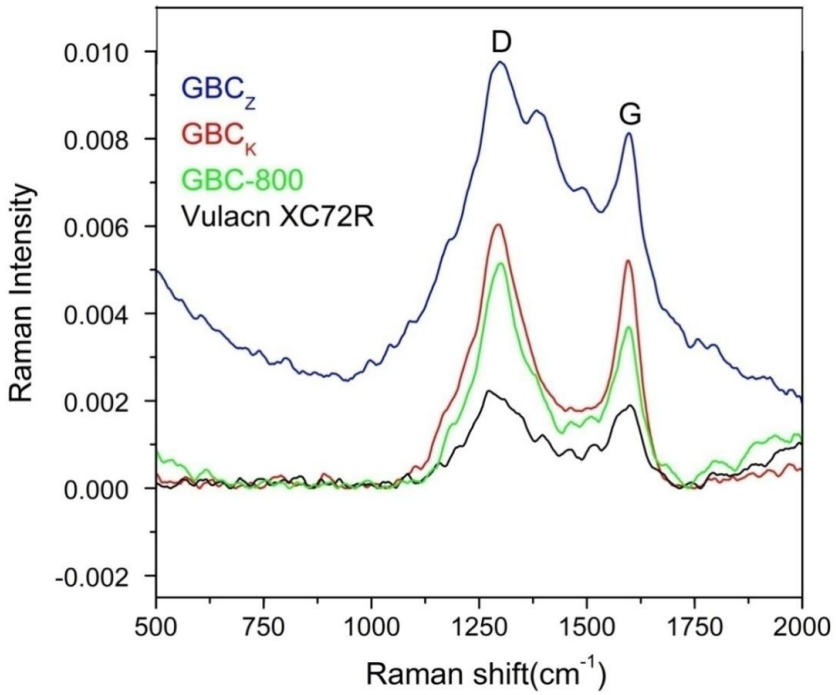

Fig 3.3: Raman spectra representing comparative Raman Intensities of GBC_K, GBC_Z, GBC-800 and Vulcan XC72R.

Table 3.1: Parameters obtained from Raman spectra of activated glycerol based carbons and commercial carbon Vulcan XC72R (Fig. 3.3).

Sr. No.	**Carbon samples**	**Intensity of the peaks (cm^{-1})**		**$R = I_D/I_G$**	**L_a (nm) = 4.4 R**
		D band	G band		
1	GBC_K	1296	1596	1.15	3.81
2	GBC_Z	1298	1596	1.21	3.64
3	GBC-800	1299	1597	1.41	3.12
4	Vulcan XC72R	1270	1602	1.16	3.79

3.2.3 Surface functional groups of the activated glycerol based carbons: *FTIR spectroscopy*

Applications of carbon materials are mainly determined by its specific surface area, porosity and surface functionalities [23, 24]. Variation in physicochemical properties of the carbon materials can be directly related to surface functional groups anchored on the carbon surface or within the carbon [25-27]. Infrared spectroscopy is widely used to identify surface functionalities of the carbon materials. It is a qualitative technique for the assessment of chemical structure.

Activated carbons show characteristic IR absorptions in the range of 4000 – 500 cm^{-1} [5, 28-30] indicating presence of various functionalities on its surface. The major band assignments observed in the glycerol based activated carbons are presented in Table 3.2. Fig. 3.4 (b) is a comparative display of the infrared spectra before activation (GBC-120) and after KOH activation (GBC_K). To begin with it is pertinent to note here that the peak at 1625 cm^{-1} is due to C=C stretch of the aromatic rings and the peak at ~1073 cm^{-1} is due to the SO_3H surface functionality [10].

The effect of activation process on the IR spectra of the synthesized carbons can be understood by simultaneously comparing the relative intensities of these two bands due to C=C and SO_3H. Thus the C=C band intensity in GBC_K is greatly increased with concomitant decrease in SO_3H band intensity as shown in Fig. 3.4 (b). On the other hand, in the un-activated carbon GBC-120, the C=C band intensity is much less while the corresponding SO_3H band is highly intense. The C=C stretching vibration in activated carbon structures is known to be associated with presence of polycylic cluster of graphitic rings. Thus, the KOH activation process caused high degree of aromatization with simultaneous decomposition of sulphonyl groups. Further, the activation process is also accompanied by large increase in the C=O (1710 cm^{-1}) and O–H (3441 cm^{-1}) band intensities due to additional generation of –COOH groups. Another distinguishing feature between the two carbons is the appearance of a distinct band at 2100 cm^{-1} in the GBC_K spectrum. It is due to increased graphitization of the carbon structure and partial ring opening to generate –C≡C moiety which can occur during the activation process in N_2 atmosphere [31].

The infrared spectra of $ZnCl_2$ activated glycerol based carbon GBC_Z was similar to GBC_K. However the relative intensity of the band at 1630 cm^{-1} due to C=C was much less. This implied lower amount of graphitization occurs when GBC-120 is activated with $ZnCl_2$. It thus showed relatively less ordered structure as was also evident from its Raman spectrum and the corresponding I_D/I_G value. These values for GBC_Z and GBC_K were 1.21 and 1.15 respectively (Table 3.1)

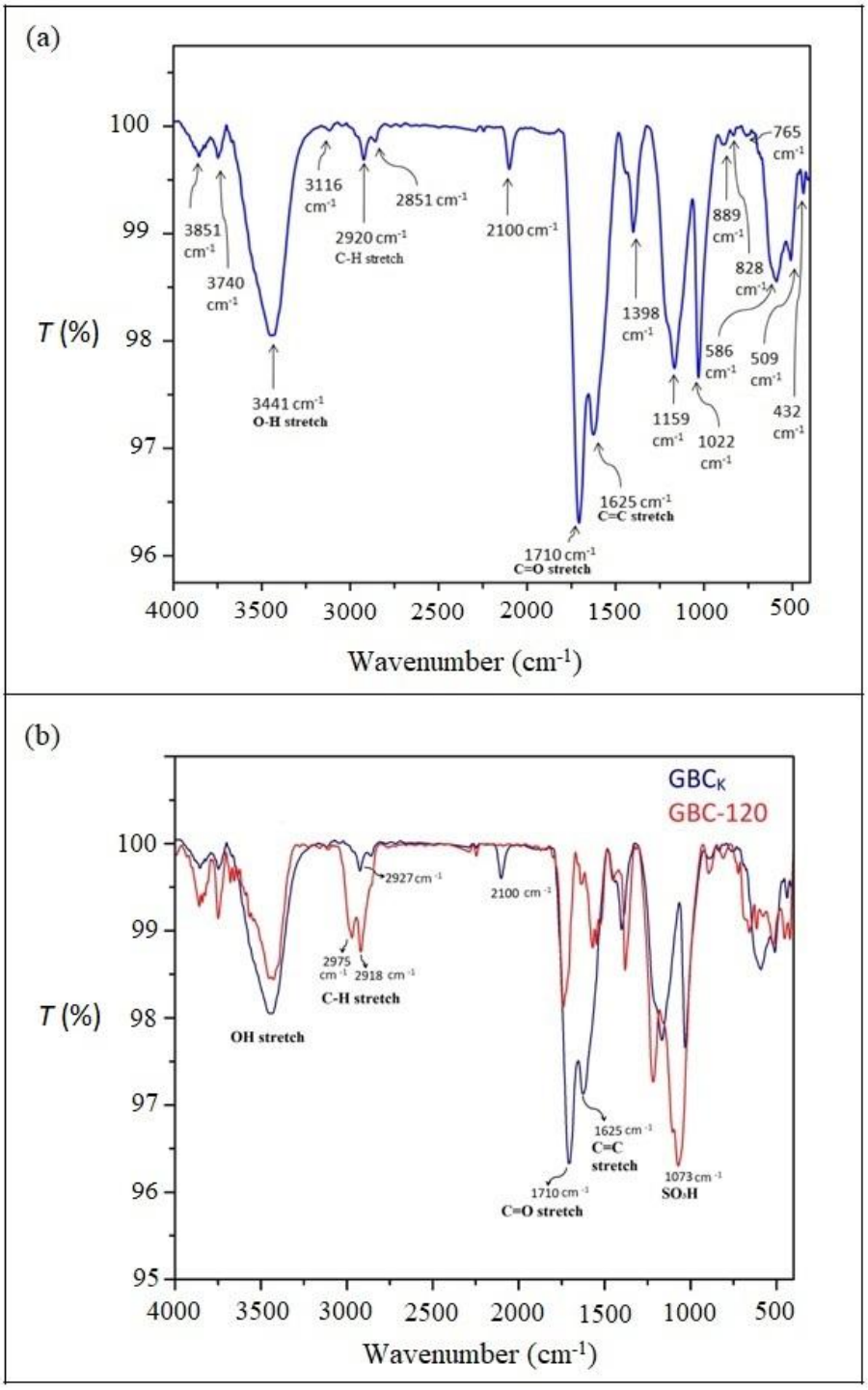

Fig. 3.4: FT-IR spectra of (a) the KOH activated carbon GBC_K and (b) infrared absorptions of the activated carbon GBC_K in relation to the un-activated carbon GBC-120.

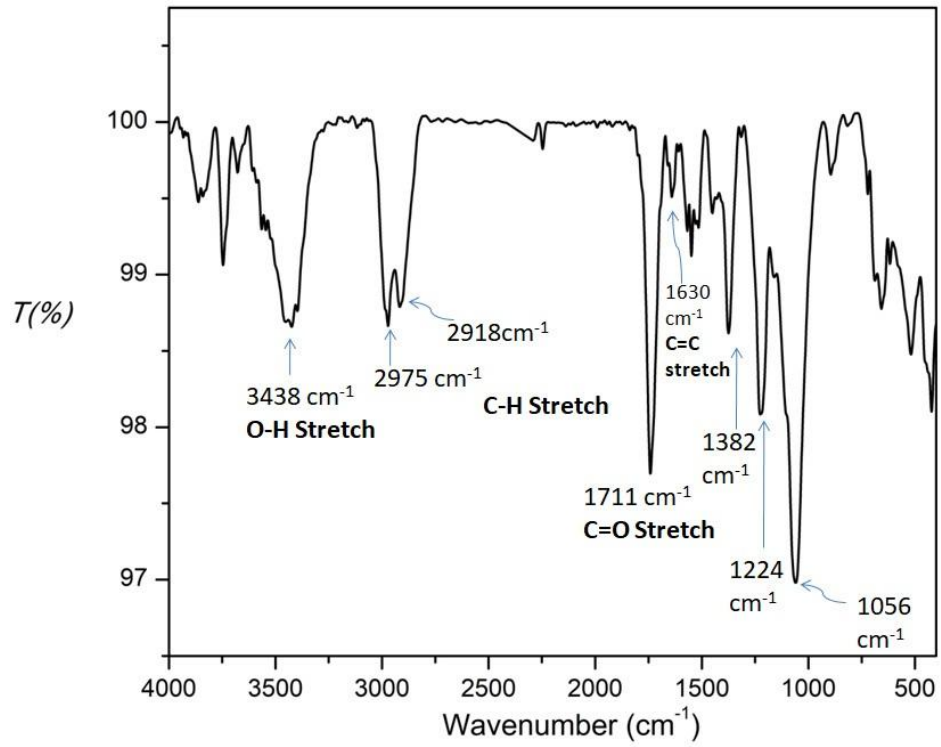

Fig. 3.4 (c): FT-IR spectra of $ZnCl_2$ activated glycerol based carbon GBC_Z.

Table 3.2: The assignments corresponding to different frequencies observed in the infrared spectra of the activated glycerol based carbon.

Frequencies (cm^{-1})	**Carbon surface functionality**
3851, 3740	O – H stretch associated with alcohol and phenolic groups
3440	O – H stretch when hydrogen bonding is involved
3116	= C – H stretch
2920, 2927	– C – H stretch
2851	– C – H stretch
2100	C ≡ C stretch
1710, 1741	C = O stretch of COOH and carbonyl group
1620, 1635	C = C stretch of graphitic rings
1398	O = S = O stretch of SO_3H
1160	(i) Symmetric S = O stretch (ii) C – OH stretching of phenolic group
1020-1080	asymmetric stretching of SO_3H

3.2.4 Evaluation of thermal stability of activated carbons GBC_K and GBC_Z –TG-DTA analysis

Thermal analysis was carried out from ambient temperature to 1000 ^{o}C and the corresponding profiles are presented in Fig. 3.5.

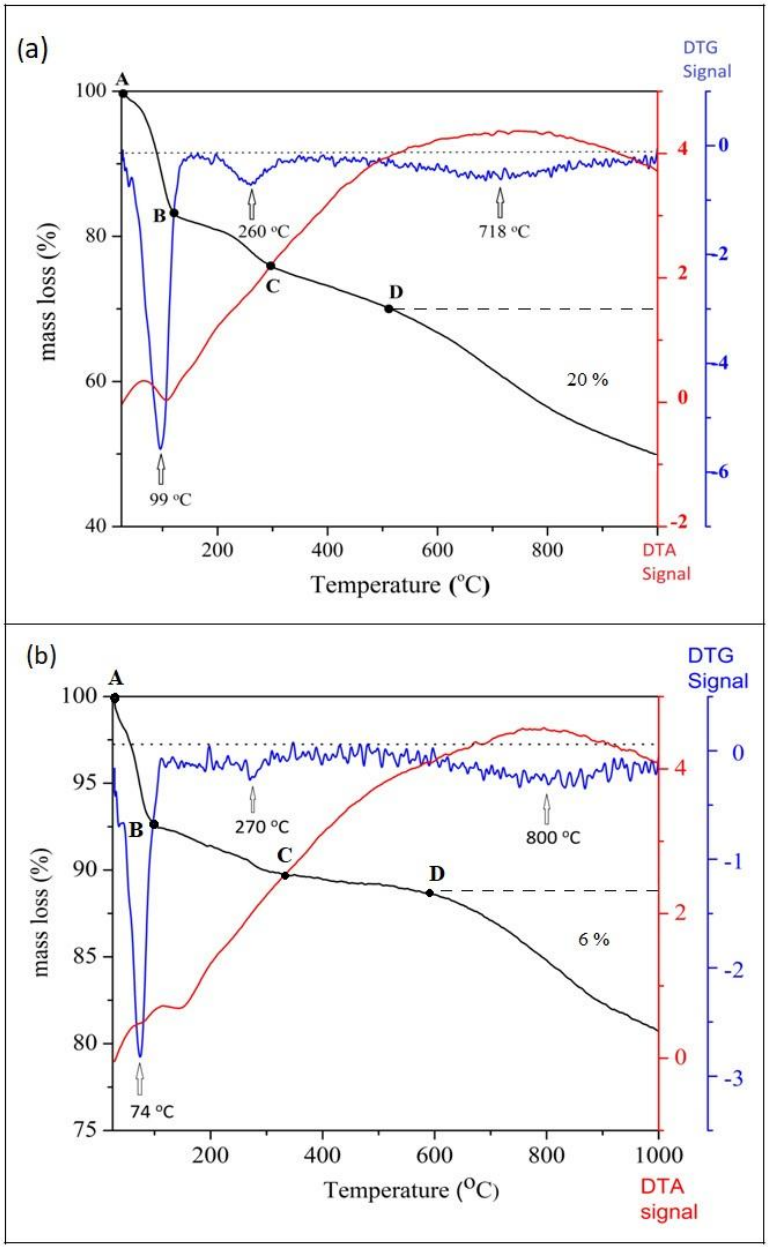

Fig. 3.5 TG-DTA-DTG profiles of the KOH and $ZnCl_2$ activated glycerol based carbons in N_2 atmosphere of (a) GBC_K and (b) GBC_Z.

The TG pattern of GBC_K can be divided into four broad stages:

(i) Region AB in the temperature range up to 120 ^oC with its DTG peak centered at 99 ^oC. It corresponds to a mass loss of ~ 18 % due to loss of physisorbed water and some hydrogen bonded water.

(ii) Second distinct stage (region BC), is due to mass loss in the temperature range 120 ^oC to 280 ^oC with its DTG peak centered at ~ 260 ^oC. It corresponds to mass loss associated with decomposition of –COOH and $–SO_3H$ groups.

(iii) The region on TG profile, identified as CD between temperatures 300-500 ^oC. In this region the carbon material absorbs thermal energy essentially to initiate the structural reorganization associated with the activation process. It can be identified alongside the rapidly rising portion on DTA curve at the above temperature.

(iv) Beyond 500 ^oC, the rise in DTA profile abruptly slows down and it peaks at ~ 718 ^oC. It is symmetrically disposed alongside the broad DTG peak in the temperature range 500 - 950 ^oC. This temperature range corresponds to structural reorganization and porosity development that occurs during the activation process. During this step, a mass loss of ~ 20 % was observed partly due to carbon burn off and partly due to further loss of some functional groups such as loss of surface carbonyls [32].

TG-DTA profile of GBC_Z as in Fig 3.5(b) shows similar mass loss pattern except the percentage of total mass loss which was ~50% for GBC_K and 18 % for GBC_Z carbon. Further the TGA profile of GBCZ was much less sloping. Thus the mass loss for GBC_K and GBC_Z, post temperature at D which is after 500 ^oC was 20 % and

6 % respectively. This is a region indicative of porosity development associated with carbon burn off. This would seem to further indicate higher thermal stability of $ZnCl_2$ activated glycerol based carbon and lower pore size and pore volume for GBC_Z.

3.2.5 Textural properties of activated glycerol based carbons (GBC_K and GBC_Z) – BET analysis

The physical properties of the carbons alter during chemical activation as the activating agents like KOH, $ZnCl_2$ generate porosity in carbon structure. The KOH activation process involves intermediate formation of K_2CO_3 and accompanied by evolution of carbonaceous volatiles [33]. Fig. 3.6 gives N_2 adsorption-desorption plots along with pore size distribution profile of GBC_K and GBC_Z. The adsorption isotherm of GBC_K showed a distinct hysteresis profile with characteristics of H2 type loop. The adsorption profile was more close to type IIb and IVb according to IUPAC classification as well as the classification given by Roquerol et al [34]. It involved gradual filling of pores upto a relative pressure of p/p_o ~ 0.7. This was followed by rapid rise in adsorption upto near saturation pressure, due to multilayer adsorption. The initial desorption branch showed a gradual slope upto a relative pressure p/p_o of ~ 0.55 followed by a steep desorption branch as was expected for an H2 type loop. The pore structure in such H2 type materials is known to be complex and is generally associated with interconnected network of pores of different size and shapes. Pore size distribution profile (Fig. 3.6a) indicates that the pore dimension of GBC_K is in the range of 2 - 4 nm. This suggests mesoporous nature of the activated carbon. The average pore size is in fact 2.1 nm as is evident from the sharp peak at around this value.

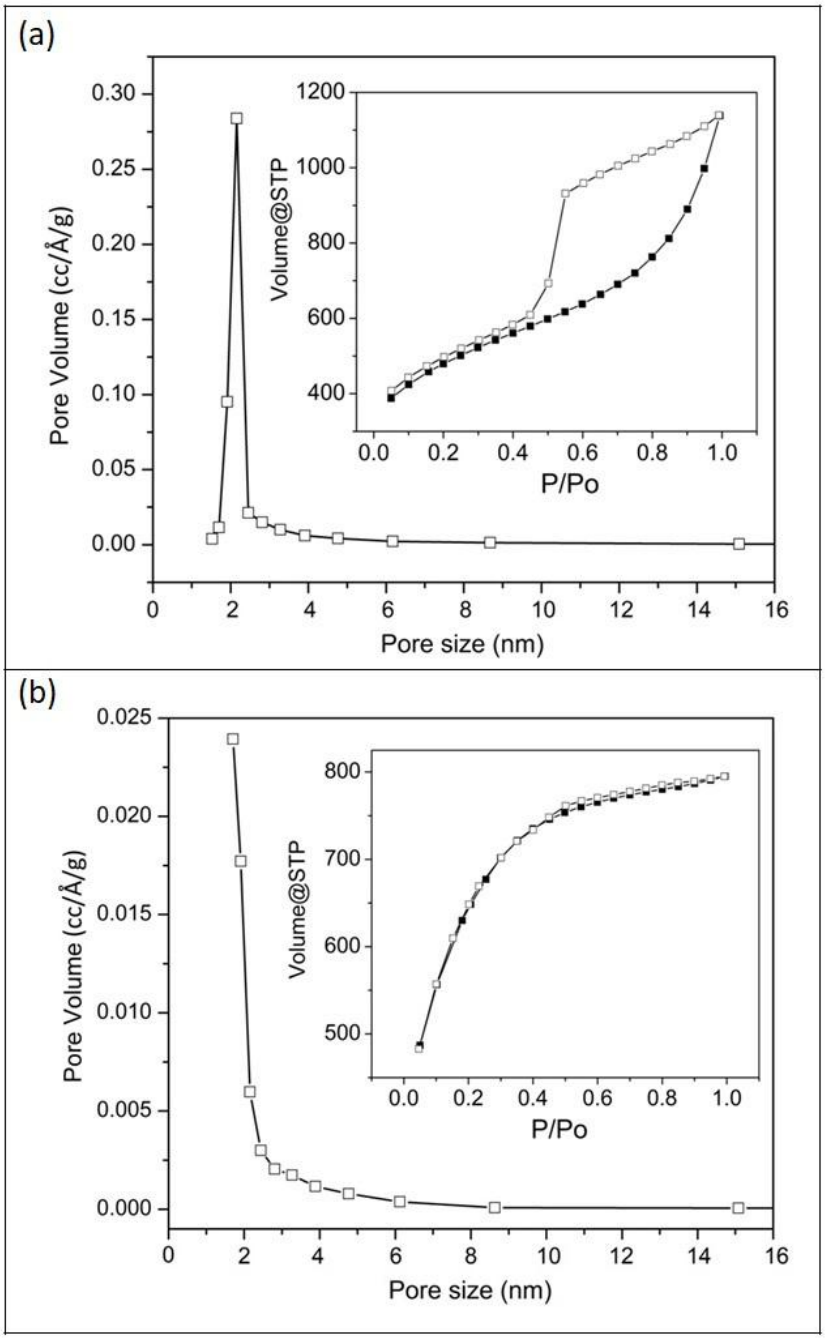

Fig. 3.6: N_2 adsorption desorption isotherms (inset) and pore size distribution profiles of the activated glycerol based carbons (a) GBC_K and (b) GBC_Z.

Table 3.3: Textural properties obtained from BET analysis of glycerol based carbons GBC_K, GBC_Z and GBC-800.

Sample	**S_{BET} ($m^2\ g^{-1}$)**	**V_{Total} ($cm^3\ g^{-1}$)**	**$V_{Micropore}$ ($cm^3\ g^{-1}$)**	**$V_{Mesopore}$ ($cm^3\ g^{-1}$)**	**Average pore radius (nm)**
GBC_K	1653	1.76	0.43	1.20	2.13
GBC_Z	1577	1.23	0.77	0.50	1.12
GBC-120	21	0.06	--	--	0.18
GBC-800	425	0.22	0.18	0.01	1.04

The adsorption isotherm of GBC_Z exhibit type I isotherm which is indicative of microporosity in the carbon materials as per IUPAC classification. From Fig. 3.6 it can be seen that there is sharp increase in the volume of gas adsorbed upto relative pressure of 0.40. Beyond this, with increase in relative pressure the isotherm seems to approach a plateau due to much reduced adsorption at higher pressure. Depending upon the sharpness of the approach to saturation pressure the type I isotherm is further subdivided into Ia and Ib. GBC_Z shows isotherm of type Ib possessing both narrow and wider micropores. At higher relative pressure adsorption adsorption desorption profile of GBC_Z was almost coincidental with minimal hysteresis. It can be seen that both the activated samples GBC_K and GBC_Z showed large values of surface area which was around 1600 $m^2\ g^{-1}$. In comparison the surface area of un-activated carbon GBC-120 was merely 21 $m^2\ g^{-1}$. Thus the activation process showed ~ 80 times enhancement in surface areas. Also before activation the pore volume was negligible (~ 0.06 $cm^3\ g^{-1}$). There was nearly 30 times increase in pore volume following activation. Thus GBC_K showed a pore volume of 1.76 $cm^3\ g^{-1}$.

A comparison between the two activated carbons revealed that KOH activated carbon showed an average pore radius of 2.13 nm. On the other hand GBCZ not only showed lower pore volume, its average pore radius of 1.12 nm was half that of GBC_K. This higher porosity in GBC_K is in agreement with the comparative thermal analysis elaborated in the previous section wherein the mass loss for GBC_K in the temperature range > 500 ^oC was significantly higher than it was for GBC_Z.

Further analysis of porosity indicated that in GBC_K, volume was occupied by mesopores. The mesopore volumes for GBC_K and GBC_Z were 1.20 and 0.50 $cm^3\ g^{-1}$ respectively, indicating enhanced mesoporosity was caused following KOH activation. In comparison GBC_Z was largely microporous. For further comparison, a sample designated as GBC-800 was also prepared by thermal treatment of GBC-120 at 800 ^oC but without any chemical activating agent. This sample did not show such enhancement in surface area and porosity. Its surface area and pore volume showed only a marginal increase. The corresponding values were merely 425 $m^2\ g^{-1}$ and 0.22 $cm^3\ g^{-1}$ respectively. This observation thus underlined the importance of chemical activation of the glycerol based carbons.

3.2.6 Morphology of activated glycerol based carbons – SEM analysis

Scanning electron microscopy (SEM) studies were done to understand the surface morphology of the glycerol based carbons GBC_K and GBC_Z. For comparison SEM analysis of GBC-800 and commercial carbon Vulcan XC72R were also carried out. These are shown in Fig. 3.7. The images reveal development of porosity in the activated carbons in comparison to that of un-activated GBC-120 shown earlier (Fig.2.6). KOH activated carbon GBC_K showed presence of larger pores whereas in case of GBC_Z,

comparatively smaller and non uniform pores were observed. This observation was in agreement with textural data presented in Table 3.3.

Elemental analysis of the carbons was carried out using energy dispersive spectroscopy (EDS) analysis. Table 3.4 presents At % of elements in the carbon materials.

Table 3.4: Elemental analysis data obtained from EDS analysis of glycerol based carbons.

Sample	**SEM/EDS analysis (At %) of the elements**			
	C	**O**	**S**	**K**
GBC-120	82.5	15.8	1.7	--
GBC_K	92.6	6.3	0.8	0.35
GBC_Z	95	3.3	1.6	--
Vulcan XC72R	92.3	7.7	--	--

It can be seen that the GBC^S show significant amount of sulphur content. It is due to the presence of SO_3H surface groups as revealed in their IR spectra (Fig. 3.4). The % S in GBC-120 and GBC_Z is almost same (~ 16 %). This is also evident from similar intensity of SO_3H peaks in these two samples. In comparison GBC_K showed only 0.8 % S and as expected SO_3H peak intensity is greatly diminished. The carbon content in the un-activated GBC-120 was much less ~ 82 % due to simultaneous presence of large amount of oxygen. This sample has larger amount of oxygen functionalities –COOH and –OH as shown earlier in its thermal analysis and IR spectral data. These functionalities decompose during activation which is carried out at elevated temperature (~ 800 ^oC). Hence the activated samples show relatively lower values of carbon and oxygen.

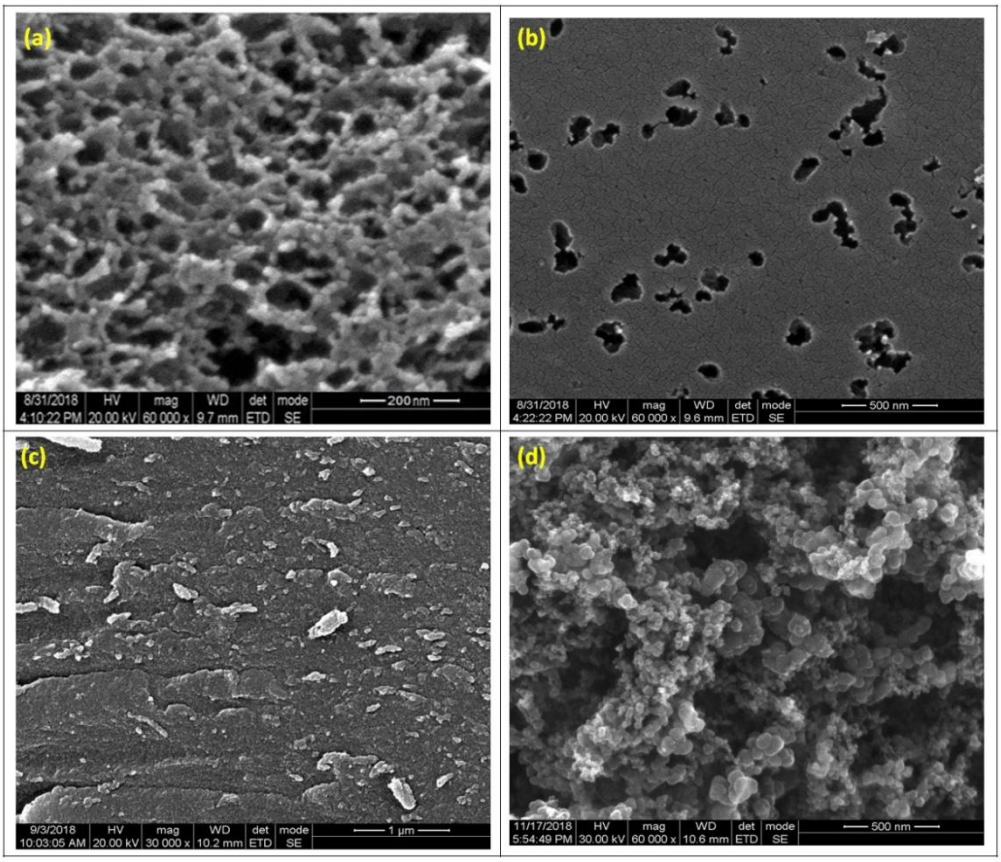

Fig. 3.7: SEM images of activated glycerol based carbons (a) GBC_K and (b) GBC_Z in comparison to (c) GBC-800 and (d) commercial carbon Vulcan XC 72R

3.3 Surfactant induced activation of glycerol based carbons

3.3.1 CTAB activated glycerol based carbon

In a typical synthesis, mixture of glycerol (10 g) and CTAB (1 mM) was stirred overnight. Concentrated sulphuric acid (25 mL) was slowly added to glycerol previously taken in a 500 mL capacity beaker. The latter was placed on a hot plate magnetic stirrer. The temperature of the resulting mixture was then gradually increased from a temperature of 25 ^{o}C up to 180 ^{o}C. The foaming was ceased after 20 minutes. The resulting black mass was cooled to ambient temperature and washed with distilled water until the washings were neutral (pH around 7). The carbon thus obtained was dried in an oven at 120 ^{o}C and further activated using KOH. The activated carbon thus produced was designated as GBC_{S1}.

3.3.2 SDS activated glycerol based carbon

The process of synthesis was carried out by first mixing SDS solution (8 mM) and glycerol (~ 8 mL). The mixture was kept for stirring overnight using magnetic stirrer. Later concentrated H_2SO_4 was added dropwise into the above mixture. The temperature was then gradually raised to 180 ^{o}C and was maintained till foaming was ceased. The resulting product was washed till the filtrate shows a neutral pH. It was dried and further activated using $ZnCl_2$ as an activating agent. The activated carbon obtained was designated as GBC_{S2}.

3.4 Characterization of the surfactant activated glycerol based carbons

3.4.1 Structural properties of GBC_{S1} and GBC_{S2} – XRD and Raman studies

The X-ray diffractograms of GBC_{S1} and GBC_{S2} are given in Fig. 3.8. The two characteristics peaks of activated carbon centered at 2θ value of ~24^o and ~43^o were also observed for the samples. These peaks are indexed respectively to (002) and (100) reflections and are representative of turbostratic carbon structure [35]. Such broad diffraction peaks in XRD pattern at around 24^o and 43^o suggest better alignment of carbon layers and well ordered structure [18]. The interlayer spacing d_{002} calculated using Bragg's equation for GBC_{S1} and GBC_{S2} are 0.37 nm and 0.35 nm respectively. The peak indexed to (100) reflection is comparatively sharper and broader in GBC_{S2}.

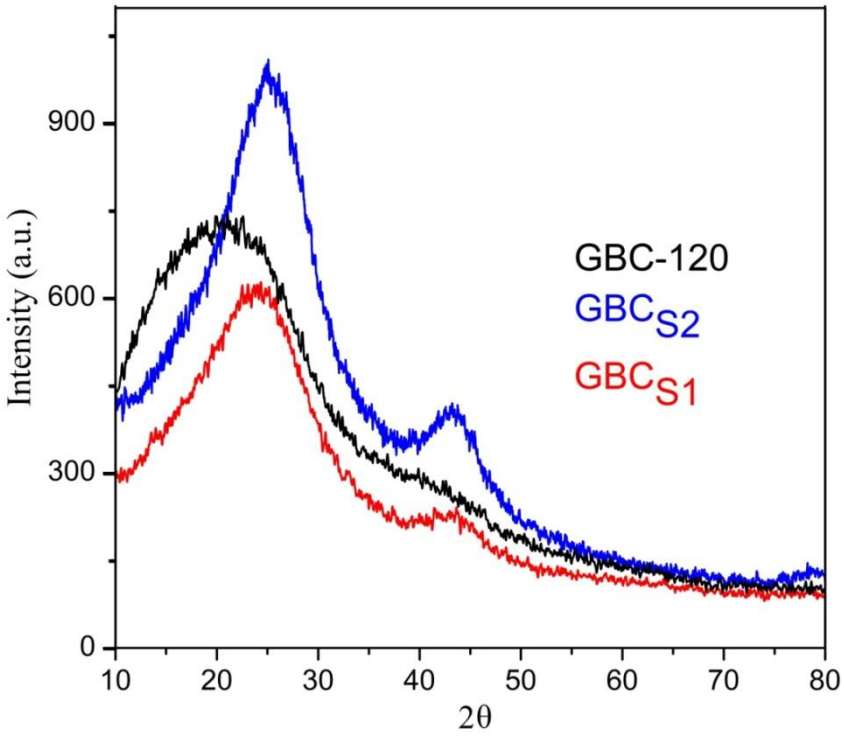

Fig. 3.8: X-ray diffraction patterns of the glycerol based carbons GBC_{S1} andGBC_{S2}.

The Raman spectra displayed in Fig 3.9 show the characteristic D and G bands at around 1294 cm^{-1} and 1596 cm^{-1} respectively. The corresponding value of R for GBC_{S1} is 1.11 and for GBC_{S2} is 1.09. This indicates more ordered structure of these carbons as

compared to GBC_K and GBC_Z which were synthesized without use of surfactants. As given in table 3.1 their R values were 1.15 and 1.21. For pure graphite oxide the value of R is less than 1. Crystallite size L_a along a-axis is calculated using formula L_a = 4.4/R. The L_a values obtained for GBC_{S1} is 3.95 nm and for GBC_{S2} is 4.03 nm, which are larger than those obtained for GBC_K and GBC_Z.

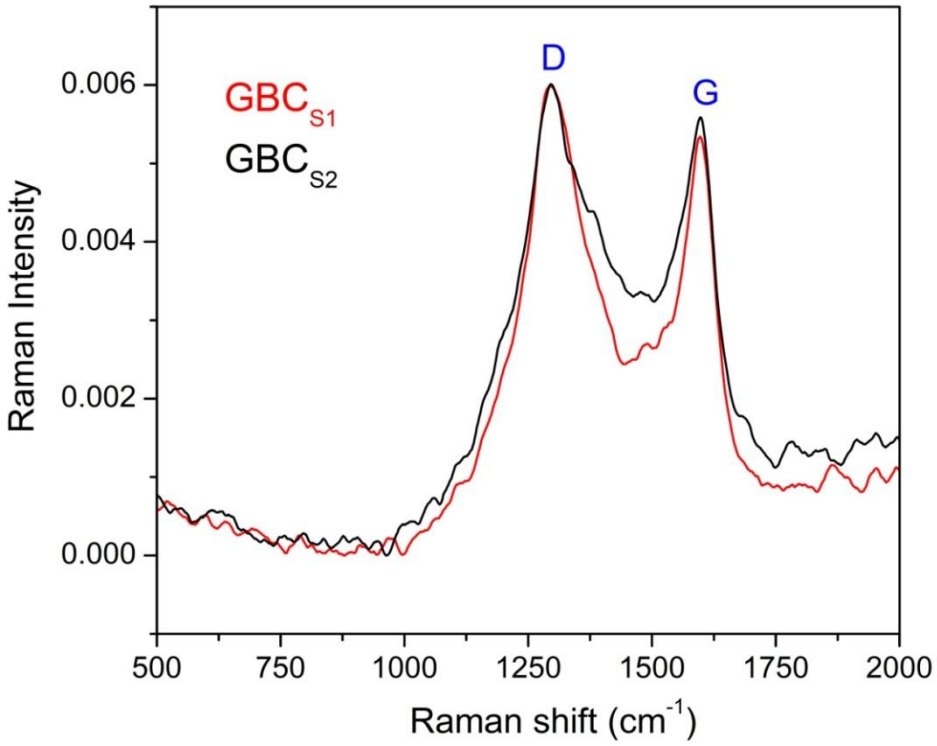

Fig. 3.9: Raman spectra of glycerol based carbons GBC_{S1} and GBC_{S2}.

3.4.2 Surface functional groups on GBC_{S1} and GBC_{S2} - FTIR spectra

Infrared spectra of GBC_{S1} and GBC_{S2} are shown in Fig. 3.10. Various characteristic peaks were observed and have been assigned to specific functionalities as reported in literature. Among the major peaks observed in GBC_{S1}, peak centered at 3451 cm^{-1} is very sharp and intense and is associated with –OH stretch indicating the presence of surface hydroxyl groups. The peak at ~2100 cm^{-1} is equally sharp and is due to

increased order in graphitization in the carbon structure. The intense band at 1078 cm^{-1} is attributable to SO_3H. The band centered around 1732 cm^{-1} is due to C=O vibrations. The band centered around 1578 cm^{-1} is associated with quinone groups [36]. Infrared spectra of GBC_{S2} as shown in Fig. 3.10 (b) shows intense band at 2100 cm^{-1} and this peak overshadows the intensity of other peaks. This suggests that GBC_{S2} possesses higher degree of ordered graphitization. The band at 3441 cm^{-1} is sharp and intense indicating presence of surface hydroxyl groups. Table 3.1 gives some of the IR assignment of functional groups on glycerol based carbon surface.

An important feature of the IR spectra of these samples is the relative intensity of the bands at 1070 cm^{-1} and the band at ~2100 cm^{-1}. These bands are associated with SO_3H groups and increased graphitization respectively. The intensity of SO_3H band in GBC_{S2} is much less in relation to the 2100 cm^{-1} band. On the contrary the intensity of SO_3H band in GBC_{S1} is very high and relatively larger than its 2100 cm^{-1} band. This suggests that in GBC_{S2} the decreased sulphur content (or SO_3H) is associated with greater formation of ordered graphitic carbon structures.

The SEM/EDS analysis presented below confirms the observations.

Carbon sample	**At % of the elements**			
	C	O	S	K
GBC_{S1}	87.07	10.47	2.44	0.02
GBC_{S2}	95.85	2.30	1.85	--

The sulphur content in GBC_{S2} is much less (1.85 %) compared to 2.44 % in GBC_{S1}. Further there was enhancement in carbon content of GBC_{S2} as compared to that of GBC_{S1}.

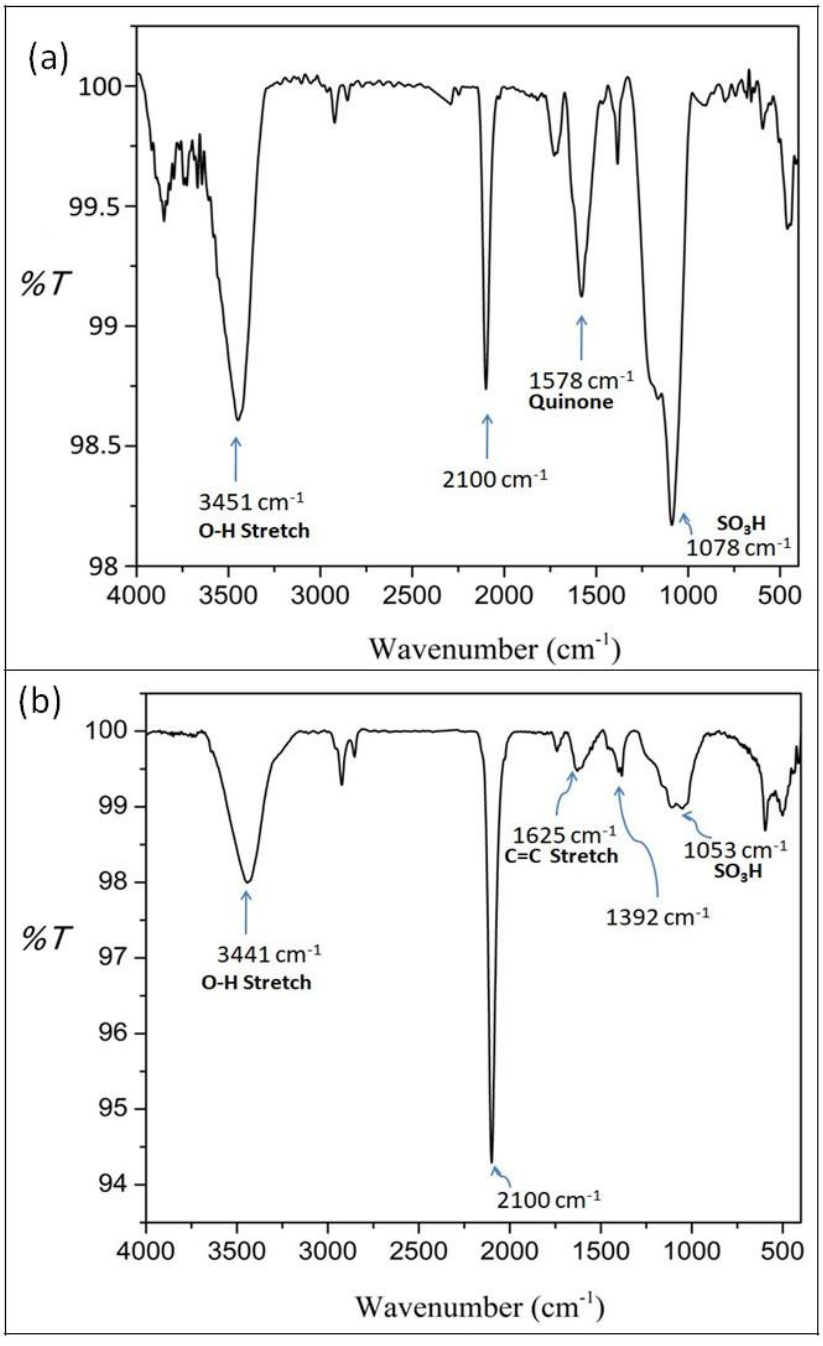

Fig. 3.10: Infrared spectra of glycerol based carbons (a) GBC_{S1} and (b) GBC_{S2}.

3.4.3 Textural properties of glycerol based carbons GBC_{S1} and GBC_{S2} – BET sorptometry and SEM analysis

N_2 adsorption desorption isotherms and corresponding pore size distribution profiles (BJH) obtained for the glycerol based carbons GBC_{S1} and GBC_{S2} are shown in Fig 3.11. The adsorption isotherms of both these samples are essentially of Type I and analogous to that of GBC_Z described in the previous section. However as expected for a Type I isotherm, there is no complete saturation in a small region beyond $P/P_o \sim 0.8$ upto 1. Hence the final phase of the isotherm profiles appears like in Type II. The non-existence of plateau is representative of monolayer-multilayer adsorption with condensation taking place only at a relative pressure of 1. Such isotherms are known to be observed in case of open and stable surfaces and are also seen in the microporous materials [37]. Puziy et al [38] observed such isotherm for calgon carbon with pore structure consisting of both micropores and mesopores.

Most of the activated carbons are highly microporous and investigating the micropore size distribution and assessment of total micropore volume still remains a problem. N_2 adsorption is regarded as only the first step for characterizing microporous carbon. Similar isotherm profile was observed for microporous carbon cloth JF517 [39]. Both GBC_{S1} and GBC_{S2} showed distinct hysteresis loop of type H4 in the P/P_o region of 0.5-1.0. This is indicative of the presence of micro and mesopores. The specific surface area, total pore volume and a average pore size obtained from N_2 adsorption desorption isotherm are summarized in Table 3.5.

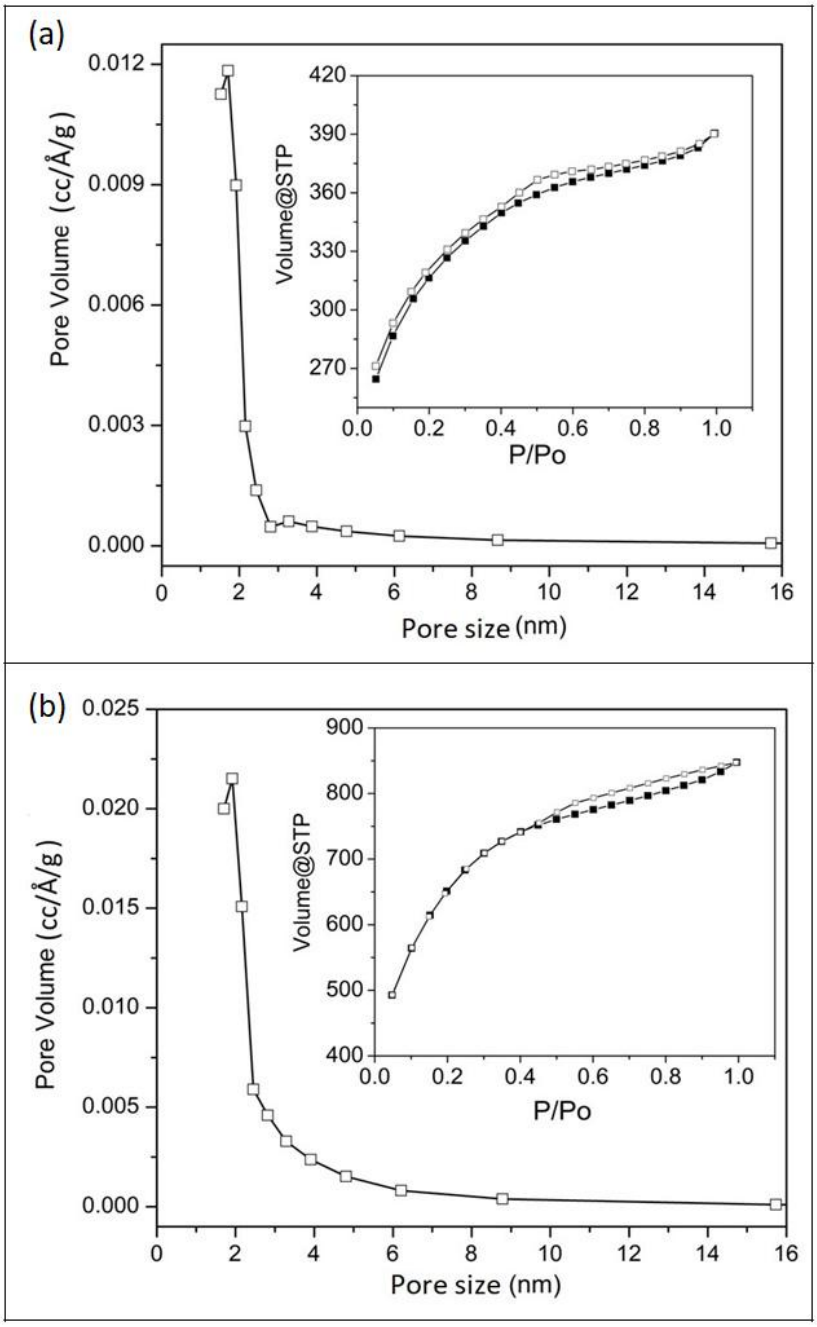

Fig. 3.11: Pore size distribution (BJH) and N_2 adsorption desorption isotherms of carbons (a) GBC_{S1} and (b) GBC_{S2}

Table 3.5: Textural properties obtained from BET analysis of glycerol based carbons GBC_{S1} and GBC_{S2}.

Sample	**S_{BET} ($m^2\ g^{-1}$)**	**V_{Total} ($cm^3\ g^{-1}$)**	**$V_{Micropore}$ ($cm^3\ g^{-1}$)**	**$V_{Mesopore}$ ($cm^3\ g^{-1}$)**	**Average pore radius (nm)**
GBC_{S1}	1069	0.60	0.40	0.13	1.12
GBC_{S2}	2289	1.31	0.72	0.54	1.14
GBC_Z	1577	1.23	0.77	0.50	1.12

For comparison the values of GBC_Z are also shown in Table 3.5. All the samples not only showed similar shaped adsorption profiles; there average pore radius were also similar having a value of around 1.12 nm. It is interesting to note that unlike GBC_{S1}; the pore volume of GBC_{S2} and GBC_Z was similar and so too their micropore and mesopore volumes. It may be recalled that of GBC_{S2} and GBC_Z were $ZnCl_2$ activated samples. The only difference was incase of GBC_{S2}, the surfactant SDS was used along with glycerol. Thus the presence of surfactant SDS caused higher pore volume as well as provided much larger surface area.

The surface morphology of glycerol based carbons GBC_{S1} and GBC_{S2} was examined from SEM analysis at different magnification. Fig.3.12 shows SEM images taken at a magnification of 60000 X. A highly porous surface was observed in case of both the carbons.

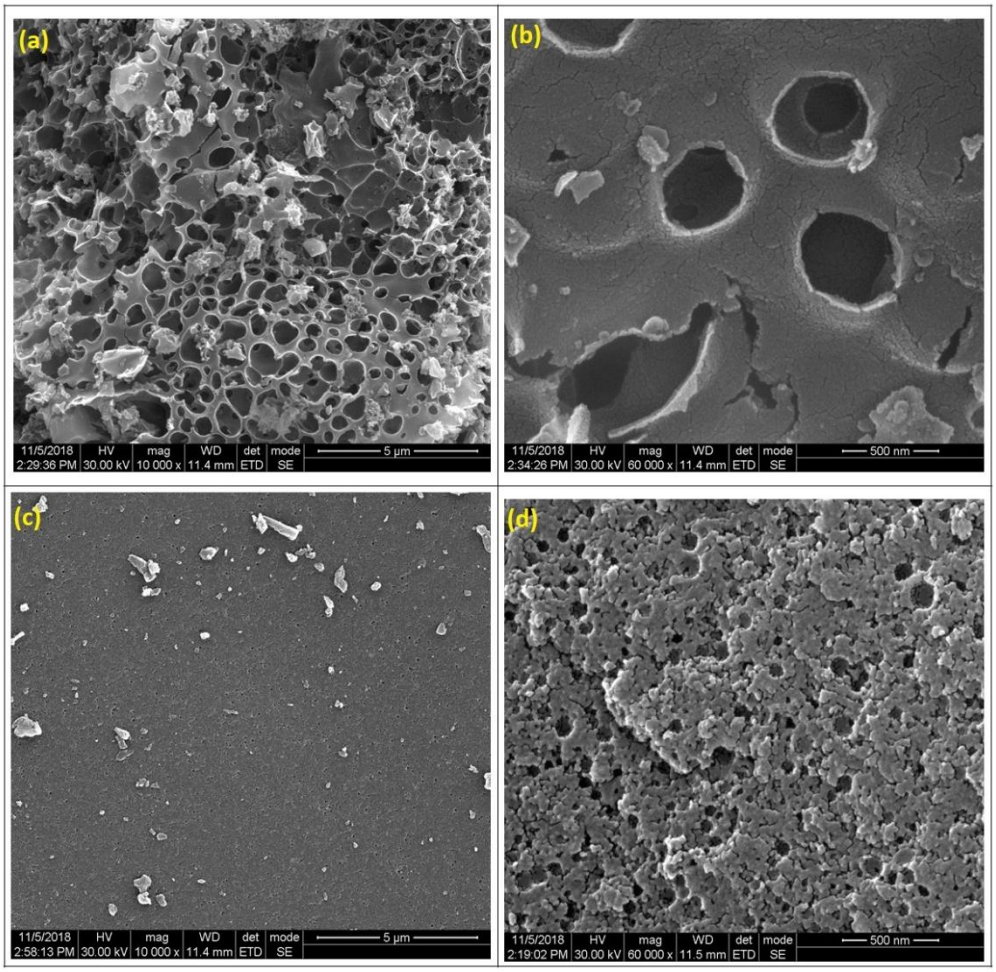

Fig. 3.12: SEM images of GBC_{S1} at a magnification of (a) 10000x, (b) 60000x and GBC_{S2} at a magnification of (c) 10000x (d) 60000x.

3.5 Adsorption of methylene blue on glycerol based carbons (GBC_K, GBC_Z, GBC_{S1} and GBC_{S2})

The synthesized glycerol based activated carbons were found to possess large surface area and enhanced porosity. Their adsorption ability was investigated by using methylene blue as model adsorbent. Fig. 3.13 shows a comparative adsorption behavior of these carbons. The corresponding extent of adsorption is presented below.

Carbon type	**Activation method**	**Adsorption (mg g^{-1})**		**Surface area**
		After 3 hours	After 20 hours	
GBC_K	KOH activation of GBC-120	1180	1700	1653
GBC_Z	$ZnCl_2$ activation of GBC-120	1290	2400	1577
GBC_{S1}	CTAB + KOH	850	1000	1069
GBC_{S2}	SDS + $ZnCl_2$	1380	1600	2289

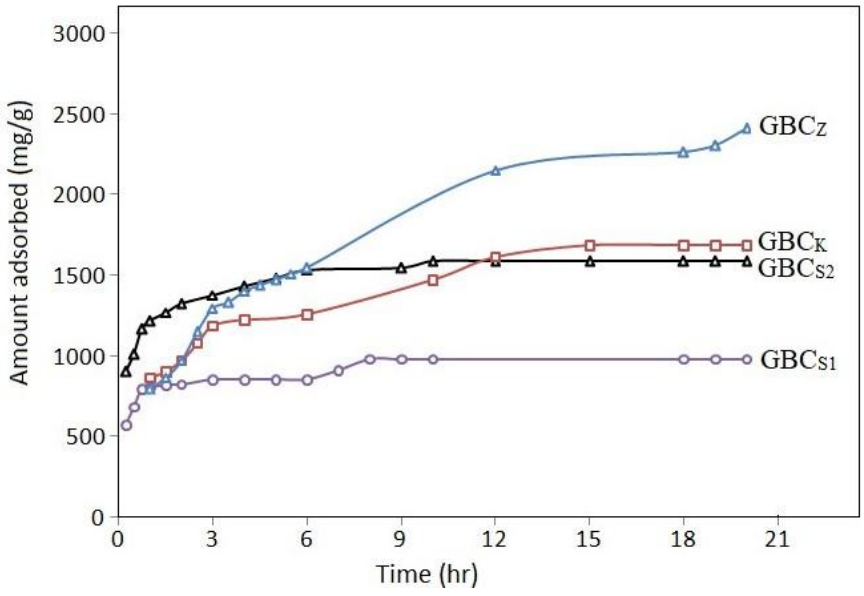

Fig.3.13: Comparative kinetic plots of adsorption of methylene blue on glycerol based carbon samples. (Volume of adsorbate: 200 mL, Dosage of adsorbent: 20 mg, Temperature: 299 K, Contact time: 20 hours, Initial concentration = 50 µg mL).

In chapter II, the adsorption behavior of the un-activated sample GBC-120 was reported [10]. It showed high adsorption capacity of 1050 mg g^{-1}. All the activated samples reported here showed similar or much higher adsorption. At the end of 3 hours, the high surface area carbons showed higher adsorption. The GBC_{S2} carbon which has highest surface area showed rapid initial adsorption with a value of ~ 1400 mg g^{-1} within 3 hours. At this time the adsorption with the relatively low surface area carbons was much slower and the adsorption was significantly less. All the carbons generally showed equilibrium adsorption after 12 hours. Further equilibriation did not have much effect on extent of adsorption except for GBC_Z. It showed gradually rising adsorption and reached unusually high value of 2400 mg g^{-1}. It is attributed to relatively higher concentration of SO_3H as evident from their infrared spectra vis a vis higher S/O ratio. Adsorption of methylene blue on the carbons was thus influenced by interplay of factors such as surface area, porosity and surface functionalities.

3.6 General adsorption behavior of the activated carbons GBC_K and GBC_Z

GBC_Z showed highest adsorption for methylene blue. So the details adsorption study of activated glycerol based carbon GBC_K and GBC_Z was carried out.

3.6.1 Experimental

3.6.1.1 Effect of initial pH

To investigate the effect of pH on adsorption of methylene blue on GBC_K and GBC_Z. 2 mg of each was added to two conical flask of 250 mL capacity containing 100 mL of methylene blue solution (25 μg/mL). pH of the solution was adjusted in the range 2-10 using NaOH or HCl solution. Adsorption data was recorded after two hours.

3.6.1.2 Adsorption kinetics and determination of equilibration time

Time required to establish equilibrium between the adsorbed methylene blue on carbon and the amount of methylene blue in solution was investigated. 200 mL of methylene blue solution of concentration 50 μg/mL was kept for equilibration with 20 mg of carbon sample. pH of the solution was adjusted to 6. The progress was monitored by taking 1.0 mL of solution at different time intervals until equilibrium was recorded. The data obtained was then fitted in different kinetic models.

3.6.1.3 Adsorption Isotherm

To determine the adsorption isotherm of GBC_K and GBC_Z, different initial concentrations of methylene blue solution (10-50 mg/L) were equilibriated with ~ 2 mg of GBC_K and GBC_Z carbons. The pH of all the solutions was adjusted to optimum value

of 6. All the solutions were equilibrated at a fixed equilibration time of 20 hours. The adsorption data obtained was then fitted in different adsorption isotherm models.

3.6.2 Results and discussion

3.6.2.1 Effect of initial pH on adsorption efficiency

Effect of solution pH on adsorption behavior is primarily studied to know the optimum pH for adsorption on particular adsorbent. GBC_K and GBC_Z show a maximum adsorption capacity of 66% and 70% respectively at a pH of around 6 (Fig. 3.14). On increasing the pH further in the alkaline range adsorption was observed to drop significantly. Thus all the further studies was carried out with pH of the solutions adjusted to 6±0.2.

3.6.2.2 Effect of contact time and adsorption equilibrium

Adsorption-time behavior of GBC_K and GBC_Z was investigated by monitoring the amount of methylene blue adsorbed at definite time intervals (Fig. 3.13). Initial adsorption pattern was linear with respect to time up to 3 hours with maximum adsorption capacity of 1185 and 1290 mg/g for GBC_K and GBC_Z respectively. Later for GBC_K, adsorption slows down by reaching equilibrium value of 1686 mg/g whereas for GBC_Z, noticeably large adsorption is seen after the initial adsorption stage and it reached a high adsorption capacity of 2471 mg g^{-1}.

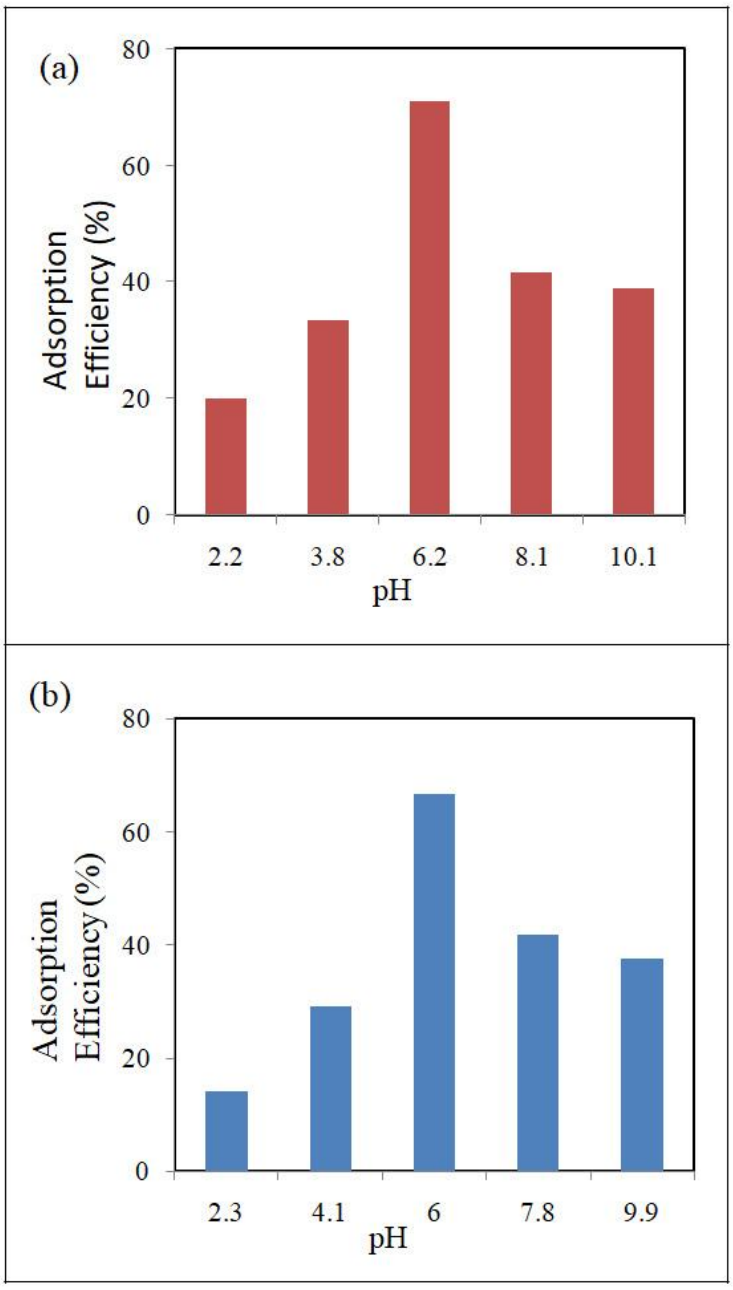

Fig. 3.14: Adsorption efficiency of (a) GBC_K and (b) GBC_Z carbon at different initial pH values.

3.6.2.3 Adsorption isotherms

From the general adsorption isotherm profiles presented in Fig.3.15, Freundlich isotherm tends to fit better for entire range of concentration in case of GBC_K as well as for GBC_Z. Langmuir adsorption is often a representative of most adsorption behavior on

activated carbon materials. It involves rapid increase in adsorption with increase in concentration, and finally lead to a plateau region as the surface adsorption sites are saturated with adsorbate molecules. The Freundlich adsorption isotherm is mainly indicative of formation of multilayer beyond saturation.

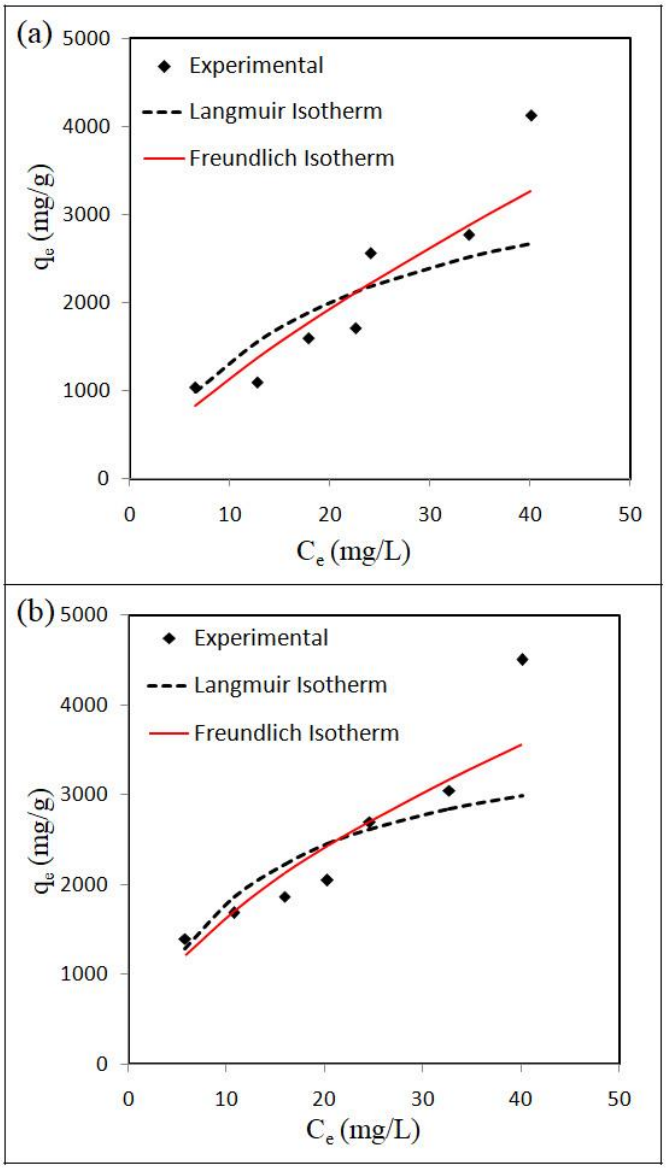

Fig. 3.15: General adsorption isotherm profiles for the glycerol based carbons (a) GBC_K and (b) GBC_Z.

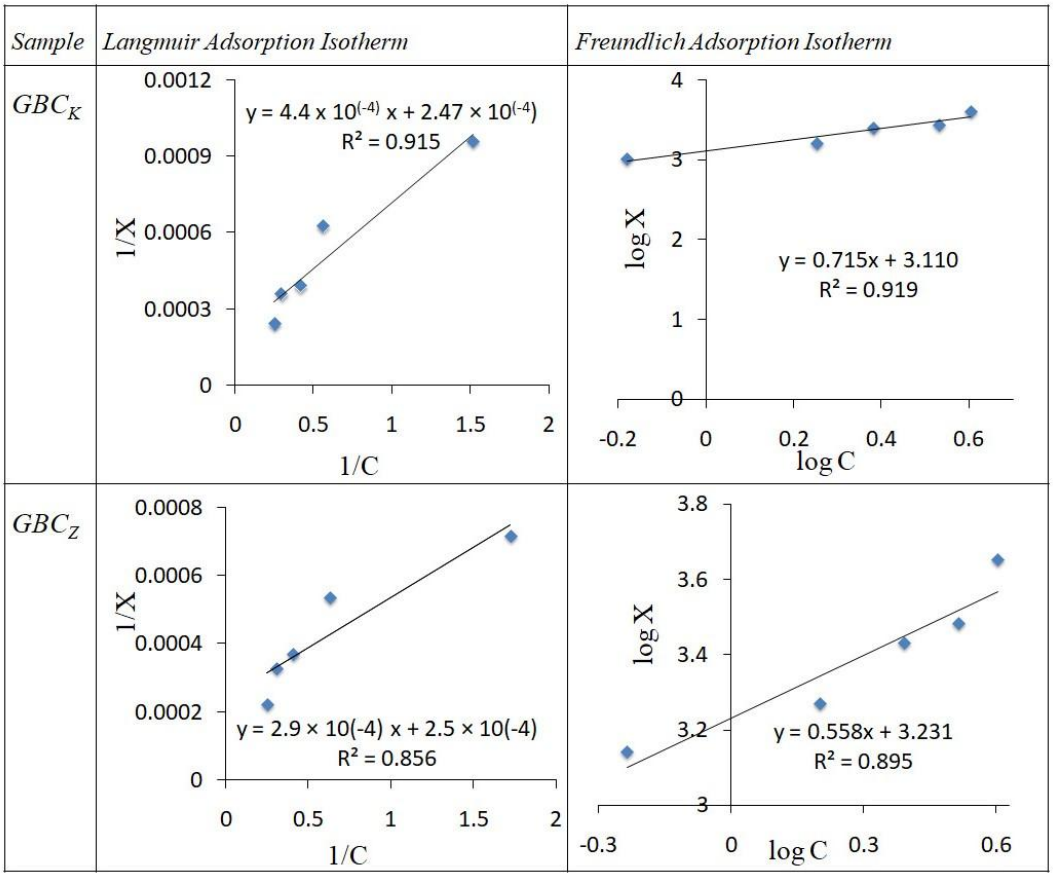

Fig 3.16: Langmuir isotherm and Freundlich isotherm for adsorption of Methylene blue on GBC_K and GBC_Z.

Table 3.6: Values of Langmuir adsorption isotherm and Freundlich adsorption isotherm parameters during adsorption of methylene blue on activated glycerol based carbons GBC_K and GBC_Z.

Sample	**Langmuir isotherm**		**Freundlich isotherm**	
GBC_K	X_m (mg/g)	4048	k (mg/g)	1288
	K (L/mg)	0.558	1/n	0.715
	R^2	0.915	R^2	0.919
GBC_Z	X_m (mg/g)	4000	k (mg/g)	1702
	K (L/mg)	0.862	1/n	0.558
	R^2	0.856	R^2	0.895

As can be seen from Fig. 3.16 the data of adsorption of methylene blue on GBC_K and GBC_Z fitted well for Langmuir isotherm with R^2 value of ~ 0.9. However the value of X_m i.e. the maximum adsorption capacity obtained from the Langmuir plot was too high compared to observed value of ~2400 mg g^{-1}. Thus it suggests that at higher concentration adsorption doesn't follow Langmuir isotherm. The K value is a Langmuir adsorption constant and it is related to energy of adsorption. The calculated K for GBC_K and GBC_Z are less than 1 suggesting Van der Waals type of adsorption. It may be seen from Fig. 3.15, the experimental points beyond 30 mg L^{-1} suggest multilayer formation indicative of Freundlich adsorption behavior. The data was also fitting for Freundlich isotherm model with R^2 value of ~0.9. The parameter 1/n obtained from Freundlich isotherm model is a measure of intensity of adsorption and it ranges from 0 - 1. The values of 1/n obtained in the present case were ~0.5 – 0.7 within this range. The maximum calculated adsorption obtained for GBC_K and GBC_Z were 1288 mg g^{-1} and 1702 mg g^{-1} respectively. In case of GBC_K the maximum adsorption capacity observed from experiment (Fig. 3.13) was ~1700 mg g^{-1}. It thus matches well with that obtained from Freundlich model suggesting that GBC_K show better fit for Freundlich adsorption isotherm at entire concentration range. Similarly the experimental value for GBC_Z at the end of 4 hours of adsorption was ~ 1300 mg g^{-1}. This value is close to calculated value (1288 mg g^{-1}) obtained from Freundlich model. Thus for GBC_Z the Freundlich adsorption isotherm was not applicable in the entire concentration range. It is attributed to its comparatively wider pore radii distribution as compared to GBC_K.

3.6.2.4 *Kinetics of Adsorption*

The pseudo first-order and pseudo second-order kinetic models were employed to understand kinetics of the adsorption process by adapting the following linear equations. Fig. 3.17 gives kinetic plots for adsorption of methylene blue on GBC_K and GBC_Z.

The coefficient of determination (R^2) obtained from best fit points, did not show significant difference when adsorption data was fitted in pseudo first-order model for both the samples. The values were ~ 0.95 and 0.93. But R^2 value obtained for pseudo second order kinetic model was close to 1. Also, the value of 'q_e observed' obtained from pseudo second order kinetics model (2500 mg g^{-1} for GBC_Z and 1666 mg g^{-1} for GBC_K) was quite close to 'q_e calculated' (2471 mg g^{-1} for GBC_Z and 1685 mg g^{-1} for GBC_K). Thus the kinetic model analysis confirm the observed high initial rate of adsorption of the cationic dye in the glycerol based carbons investigated.

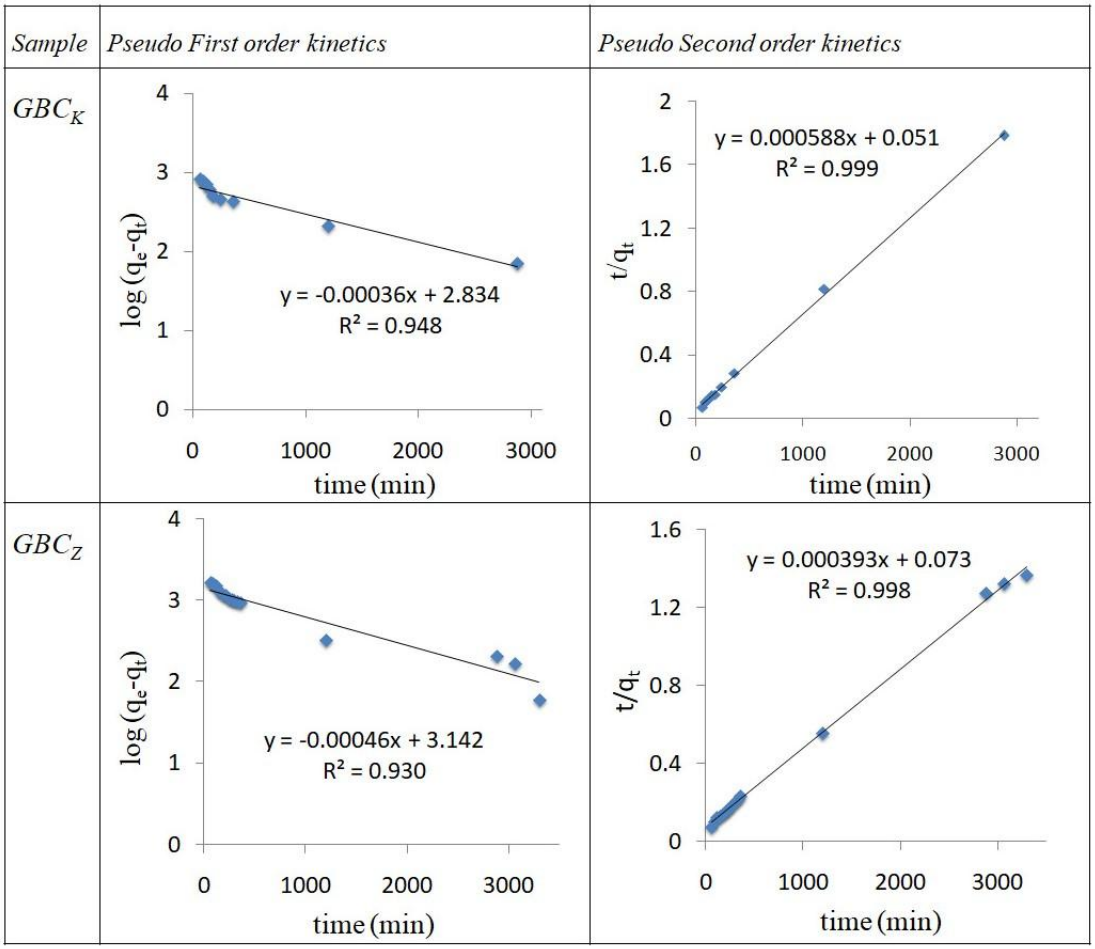

Fig. 3.17: Pseudo first and second order kinetic plots for adsorption of methylene blue on GBC_K and GBC_Z.

Table 3.7: Kinetic parameters obtained from application of Pseudo First order and second order kinetic models.

Sample	Pseudo First order kinetic model			Pseudo Second order kinetic model		
	R^2	K_1 (min^{-1})	q_e (mg g^{-1})	R^2	K_2 (g mg^{-1} min^{-1})	q_e (mg g^{-1})
GBC_K	0.948	$8.3 \times 10^{(-4)}$	682	0.999	$7.0 \times 10^{(-6)}$	1685
GBC_Z	0.930	$8 \times 10^{(-4)}$	1386	0.998	$2.2 \times 10^{(-6)}$	2500

*q_e calculated values for GBC_K and GBC_Z are 1685 and 2471 mg g^{-1} respectively.

Summary & Conclusions

(i) Activated glycerol based carbons (GBC_K and GBC_Z) were prepared by using KOH and $ZnCl_2$ as chemical activating agents. The mixture of un-activated glycerol based carbon GBC-120 and chemical activating agents were heated at 800 ^oC in N_2 atmosphere.

(ii) Surfactant mediated activation of glycerol based carbon using CTAB and SDS surfactants were carried out and were further chemically activated as in for GBC_K and GBC_Z. The resultant carbons were denoted as GBC_{S1} and GBC_{S2}.

(iii) Synthesized glycerol based carbons GBC_K, GBC_Z, GBC_{S1} and GBC_{S2} showed characteristic peaks at ~ 24^o and ~ 43^o. An additional peak at 2θ ~14^o observed was due to formation of oxidized graphitic surface.

(iv) From Infra red spectral analysis it was observed that the C=C band intensity at 1625 cm^{-1} in GBC_K was greatly increased suggesting enhanced aromatization following activation. The peak at 2100 cm^{-1} was observed indicating enhanced graphitization. The Raman spectra of these carbons showed two distinct peaks at Raman shift values of 1296 cm^{-1} and 1596 cm^{-1} and are known as D and G bands respectively.

(v) BET analysis showed that activation resulted in large enhancement in surface area as well as evolution of pores in the carbon structure with a relatively large pore volume. Thus the surface area and pore volume before activation was 21 $m^2\ g^{-1}$ and 0.06 $cm^3\ g^{-1}$. These values became as high as 2290 $m^2\ g^{-1}$ and 1.31 $cm^3\ g^{-1}$ for GBC_{S2}; the carbon obtained using SDS surfactant. Glycerol based carbon activated using KOH is found to be largely mesoporous and $ZnCl_2$ activation is observed to induce microporosity in the carbon.

(vi) Maximum adsorption capacity of ~2400 mg g^{-1} is shown by the $ZnCl_2$ activated

carbon GBC_Z for adsorption of methylene at pH of 6. Adsorption efficiency increased with increase in solution pH from 2-6. The GBC_{S2} showed less adsorption in spite of its much larger surface area in comparison to GBC_Z due to partial loss of SO_3H functionalities.

(vii) The adsorption data could be fitted in Freundlich adsorption isotherm over entire concentration range. Adsorption kinetics studies display better fit for pseudo second order kinetic for adsorption of methylene blue on GBC_K and GBC_Z adsorbents.

References

[1] M. Ruiz-Fernández, M. Alexandre-Franco, C. Fernández-González, V. Gómez-Serrano, *Development of activated carbon from vine shoots by physical and chemical activation method. Some insight into activation mechanisms,* Adsorption 17 (2011) 621-629.

[2] F. Kraehenbuehl, H. F. Stoeckli, A. Addoun, P. Ehrburger, J. B. Donnet, *The use of immersion calorimetry in the determination of micropore distribution of carbons in the course of activation,* Carbon 24 (1986) 483-488.

[3] T. Kawano, M. Kubota, M. S. Onyango, F. Watanbe, H. Matsuda, *Preparation of activated carbon from petroleum coke by KOH chemical activation for adsorption heat pump,* Appl. Therm. Engg. 28 (2008) 865-871.

[4] J. Hayashi, A. Kazehaya, K. Muroyama, A. P. Watkinson, *Preparation of activated carbon from lignin by chemical activation,* Carbon 38 (2000) 1873-1878.

[5] L. Xian-Fa, Q. Xu, Y. Fu, G. Qing-Xiang, *Preparation and characterization of activated carbon from Kraft Lignin via KOH activation,* Environ. Prog. Sustain Energy 33 (2014) 519-526.

[6] S. E. Abechi, C. E. Gimba, A. Uzairu, Y. A. Dallatu, *Preparation and characterization of activated carbon from palm kernel shell by chemical activation,* Res. J. Chem. Sci. 3 (2013) 54-61.

[7] A. Ahmadpour, D. D. Do, *The preparation of activated carbon from Macadamia nutshell by chemical activation,* Carbon 35 (1997) 1723-1732.

[8] T. S. Hui, M. A. A. Zaini, *Potassium hydroxide activation of activated carbon: a commentary,* Carbon Lett. 16 (2015) 275-280.

[9] B. Buczek, *Preparation of Active carbon by additional activation with potassium*

hydroxide and characterization of their properties, Adv. Mater. Sci. Eng. (2016) Article ID 5819208, 4 pages.

[10] A. A. Narvekar, J. B. Fernandes, S. G. Tilve, *Adsorption behavior of methylene blue on glycerol based carbon materials,* J. Env. Chem. Eng. 6 (2018) 1714-1725.

[11] S. Álvarez-Torrellas, R. S. Ribeiro, H. T. Gomes, G. Ovejero, J. García, *Removal of antibiotic compounds by adsorption using glycerol based carbon materials,* Chem. Eng. J. 296 (2016) 277-288.

[12] B. L. A. Prabhavathi Devi, K. N. Gangadhar, P. S. Sai Prasad, B. Jagannadh, R. B. N. Prasad, *A Glycerol-based carbon catalysts for the preparation of biodiesel*, ChemSusChem 2 (2009) 617-620.

[13] K. Ramesh, S. N. Murthy, K. Karnakar, K. H. Reddy, Y. V. D. Nageswar, M. Vijay, B. L. A. Prabhavathi Devi, R. B. N. Prasad, *A mild and expeditious synthesis of amides from aldehydes using bioglycerol based carbon as a recyclable catalyst*, Tetrahedron Lett. 53 (2012) 2636-2638.

[14] K. N. Gangadhar, M. Vijay, R. B. N. Prasad, B. L. A. Prabhavathi Devi, *Glycerol-based carbon-SO_3H catalyzed benign synthetic protocol for the acetylation of alcohols, phenols and amines under solvent-free conditions,* Green and Sust. Chem. 3 (2013) 122-128.

[15] C. Ummadisetti, B. N. P. Rachapudi, B. L. A. Prabhavathi Devi, *Glycerol-based SO_3H-carbon catalyst: A green recyclable catalyst for the chemoselective synthesis of pentaerythritol diacetals,* Eur. J. Chem. 5 (2014) 536-540.

[16] R. S. Ribeiro, A. M. T. Silva, M. T. Pinho, J. L. Figueiredo, J. L. Faria, H. T. Gomesa *Development of glycerol-based metal-free carbon materials for environmental catalytic applications,* Catal. Today 240 (2015) 61-66.

[17] S. Drewniak, R. Muzyka, A. Stolarczyk, T. Pustelny, M. Kotyczka-Morańska, M. Setkiewicz, *Studies of reduced graphene oxide and graphite oxide in the aspect of their possible application in gas sensors,* Sensors 16 (2016) 103-118.

[18] T. Yang, A. C. Lua, *Textural and chemical properties of zinc chloride activated carbons prepared from pistachio-nut shells,* Mater. Chem. Phys. 100 (2006) 438-444.

[19] G. Lota, P. Krawczyk, K. Lota, A. Sierczyńska, L. Kolanowski, M. Baraniak, T. Buchwald, *The application of activated carbon modified by ozone treatment for energy storage,* J. Solid State Electrochem. 20 (2016) 2857-2864.

[20] L. Bokobza, B. Jean-Luc, M. Couzi, *Raman spectra of carbon-based materials (from graphite to carbon black) and of some silicone composites,* C-*Journal of Carbon Research* 1 (2015) 77-94.

[21] A. A. Dubale, S. Wei-Nieu, A. G. Tamirat, P. Chun-Jern, B. A. Aragaw, C. Hong-Ming, C. Ching-Hsiang, H. Bing-Joe, *The synergetic effect of graphene on Cu_2O nanowires arrays as a highly efficient hydrogen evolution photocathode in water splitting,* J. Mater. Chem. A 2 (2014) 18383-18397.

[22] I. Childres, L. A. Jauregui, W. Park, H. Cao, Y. P. Chem, *Raman spectroscopy of graphene and related materials. New Development in photon and Materials Research,* Nova Science Publishers, Inc.; UK ed. Edition**.** (2013).

[23] J. L. Figueiredo, M. F. R. Pereira, M/ M. A. Freitas, J. J. M. Orfao, *Modification of the surface chemistry of activated carbons,* Carbon 37 (1999) 1379-1389.

[24] F. Rodriguez-Reinoso, M. Molina-Sabio, *Textural and chemical characterization of microporous carbons,* Adv. Colloid Interface Sci. 76-77 (1998) 271-294.

[25] S. Biniak, G. Szymanski, J. Siedlewski, A. Swiatkowski, *The characterization of*

activated carbons with oxygen and nitrogen surface groups, Carbon 35 (1997) 1799-1810.

[26] M. T. Izquierdo, B. Rubio, C. Mayoral, J. M. Andre's, *Modifications to the surface chemistry of low-rank coal-based carbon catalysts to improve flue gas nitric oxide removal,* Appl. Catal. B Environ. 33 (2001) 315-324.

[27] G. S. Szymanski, Z. Karpinski, S. Biniak, A. Swiatkowski, *The effect of the gradual thermal decomposition of surface oxygen species on the chemical and catalytic properties of oxidized activated carbon,* Carbon 40 (2002) 2627-2639.

[28] C. A. Okoli, O. D. Onukwuli, C. F. Okey-Onyesolu, C. C. Okoye, *Adsorptive removal of dyes from synthetic waste water using activated carbon from tamarind seed,* Eur. Sci. J. 11 (2015) 1857-7881.

[29] G. Gourdin, M. Foster, D. Qu*, Carbon surface functionalities and SEI formation during Li intercalation,* Carbon 92 (2015) 193-244.

[30] R. Chen, L. Li, Z. Liu, M. Lu, C. Wang, H. Li, W. Ma, S. Wang, *Preparation and characterization of activated carbons from tobacco stem by chemical activation,*J. Air Waste Manage. 67 (2017) 713-724.

[31] M. S. Shafeeyan, W. M. A. W. Daud, A. Houshmand, A. Shamiri, *A review on surface modification of activated carbon for carbon dioxide,* J. Anal. Appl. Pyrol. 89 (2010) 143-151.

[32] M. Gonçalves, R. Rodrigues, T. S. Galhardo, W. A. Carvalho, *Highly selective acetalization of glycerol with acetone to solketal over acidic carbon-based catalysts from biodiesel waste,* Fuel 181 (2016) 46-54.

[33] Y. Ma, *Comparison of activated carbons prepared from wheat straw via $ZnCl_2$ and KOH activation,* Waste biomass valori. 8 (2017) 549-559.

[34] F. Rouquerol, J. Rouquerol, K. S. W. Sing, P. Llewellyn, G. Maurin, *Adsorption by Porous Powders and Porous Solids: Principles, Methodology and Applications,* second edition, Elseviers; AP 2014

[35] P. Devarly, Y. Kartika, N. Indraswati, S. Ismadji, *Activated carbon from jackfruit peel waste by H_3PO_4 chemical activation: pore structure and surface chemistry characterization,* Chem. Eng. J. 140 (2008) 32-42.

[36] W. Shen, Z. Li, Y. Liu, *Surface chemical functional groups modification of porous carbon,* Recent Patents on chemical Engineering, 1 (2008) 27-40.

[37] S. J. Gregg, K. S. W. Sing, *Adsorption, Surface area and Porosity*, 2nd Edition, Academic Press, New York, 1982.

[38] A. M. Puziy, O. I. Poddubnaya, A. Martinez-Alonso, F. Suarez-Garcia, J. M. D. Tascon, *Synthetic carbon activated with phosphoric acid III. Carbons prepared in air,* Carbon 41 (2003) 1181-1191.

[39] F. Rouquerol, J. Rouquerol, K. Sing, *Adsorption by powders and porous solids: Principles, methodology and applications,* Academic Press, U K, 1999. ISBN 012-598920-2.

CHAPTER IV

SYNTHESIS AND CHARACTERIZATION

OF Fe-Mn OXIDES AND Mn OMS-2

Introduction

Transition metal oxides are among the attractive class of solids due to their remarkable properties such as adsorbents, catalysts, magnetic materials, energy storage materials etc. These properties are mainly related to presence of electrons in the outermost d-orbitals of metal ion. They possesses ionic, covalent or metallic bonding and can also form ternary oxides like spinel, perovskite etc. Transition metal oxides possess wide range of magnetic properties such as having magnetic behaviors like paramagnetism, diamagnetism, ferrimagnetisms, ferromagnetism and anti-ferromagnetism. With respect to their electrical conductivity, large numbers of these oxides are semiconductors. Some of transition metal oxides show phase transition from one type of crystal structure to another and such transitions are accompanied with change in electronic and magnetic properties. Several transition metal oxides show broad range of non-stoichiometry which influence their physical properties and chemical reactivity. This deviation in stoichiometry can lead to either increase in density by interstitial arrangement in the lattice or decrease in density creating vacancies [1]. Doping another metal ion in such oxides would thus show prominent change in its properties.

Pure and doped oxides of 3d transition metals like Fe, Cu, Mn, Zn, Ni, Co etc are widely studied. The present work is focused on synthesis of Fe-Mn oxides such as α-Fe_2O_3 (pure and Mn doped) and α-MnO_2 (pure and Fe doped) and to find their applicability in adsorption, catalysis and electrochemical behavior either alone or as a component of composites with the synthesized carbons. The prepared oxides were characterized by instrumental techniques like TG-DTA, FT-IR, XRD, BET analysis, TEM, VSM and ICP-AES analysis.

4.1. α-Fe_2O_3

Among various polymorphic forms of ferric oxide, the most abundant forms, α-Fe_2O_3 (hematite) and γ-Fe_2O_3 (maghemite) are most widely investigated [2, 3]. The former having advantage of higher stability while the latter, even though it is a metastable form, is often more desired owing to its high saturation magnetization, ~ 40-80 emu g^{-1}. The magnetism varies upon the methods of synthesis. Further, α-Fe_2O_3 is antiferromagnetic below Morin temperature (260 K) and shows a very weak ferromagnetic behavior (< 1 emu g^{-1}) between 260 K and the Neel temperature (950 K). The enhancement in magnetic behavior is also seen following divalent transition metal ion doping such as Mn^{2+}, Cu^{2+} etc. [4]. The various properties and applications of α-Fe_2O_3 have been recently reviewed [5]. The present investigation deals with a co-precipitation synthesis approach to obtain a ferromagnetic α-Fe_2O_3 by Mn^{2+} doping. The synthesis parameters such as temperature of calcinations etc, are aided through TG-DTA analysis of its Fe-Mn oxide precursor. The Mn^{2+} doped α-Fe_2O_3 thus obtained, showed enhanced catalytic and photo-Fenton activity in addition to its ferromagnetic behavior.

4.1.1 Investigation towards synthesis of doped α-Fe_2O_3

In a typical synthesis, 0.05 mole of $MnCl_2.4H_2O$ and 0.1 mole of $FeCl_3$ (anhydrous), were mixed in 100 mL of distilled water. The resulting solution was added dropwise into NaOH (0.80 moles) solution under constant stirring. The brownish black suspension thus obtained, was kept for digestion for 3 hours. It was then filtered and washed till the filtrate was free of chloride and dried at 100 ^oC for 5 hours. This 'as prepared' sample (designated as MF1) was divided into several portions for further treatment at various elevated temperatures such as 200 ^oC, 450 ^oC, 600 ^oC and 750 ^oC.

For convenience the samples thus obtained, were labelled as MF2, MF4, MF6 and MF7 respectively. (The simplified codes were indicative of M for Mn, F for Fe and the numerals 1, 2, 4, 6 or 7 were used to represent the first numeral of the temperatures used for thermal treatments). The Mn doped α-Fe_2O_3 was formed at around 600 ^oC.

Pure α-Fe_2O_3 was synthesized by similar method wherein 0.1 mole of $FeCl_3$ solution was added drop wise to 0.8 mole of NaOH solution kept on a magnetic stirrer. It was further washed, dried at 100 ^oC and a part of it was further calcined at 600 ^oC in air for 2 hours. These products were labeled as F1 and F6 respectively.

4.1.2 Thermal and XRD analysis of the Fe-Mn oxides

Fig 4.1 gives TG-DTA profile of the 'as prepared' Fe-Mn oxide material (MF1) recorded in air from ambient temperature up to 1000 ^oC. It showed rapid mass loss upto about 180 ^oC, which was mainly due to loss of physisorbed and hydrogen bonded water. There was no further significant mass loss upto 1000 ^oC. However, examination of the corresponding DTA profile revealed a broad exothermic peak in the above temperature range with a maximum at ~ 600 ^oC. This suggested occurrence of some structural transformation around this temperature. Hence in modified synthesis, the 'as prepared' sample MF1 was further investigated by heat treatment in air at 600 ^oC and 750 ^oC for 2 hours. The resulting products were designated as MF6 and MF7 respectively. It may be noted that the corresponding sample F1 (prepared without Mn) also shows an exothermic profile in a narrower temperature range with a maximum at around 800 ^oC. This underlines that crucial role Mn plays in the structural transformation of Fe-Mn oxide. The samples MF1, MF6 and MF7 were further characterized by XRD as shown in Fig. 4.2.

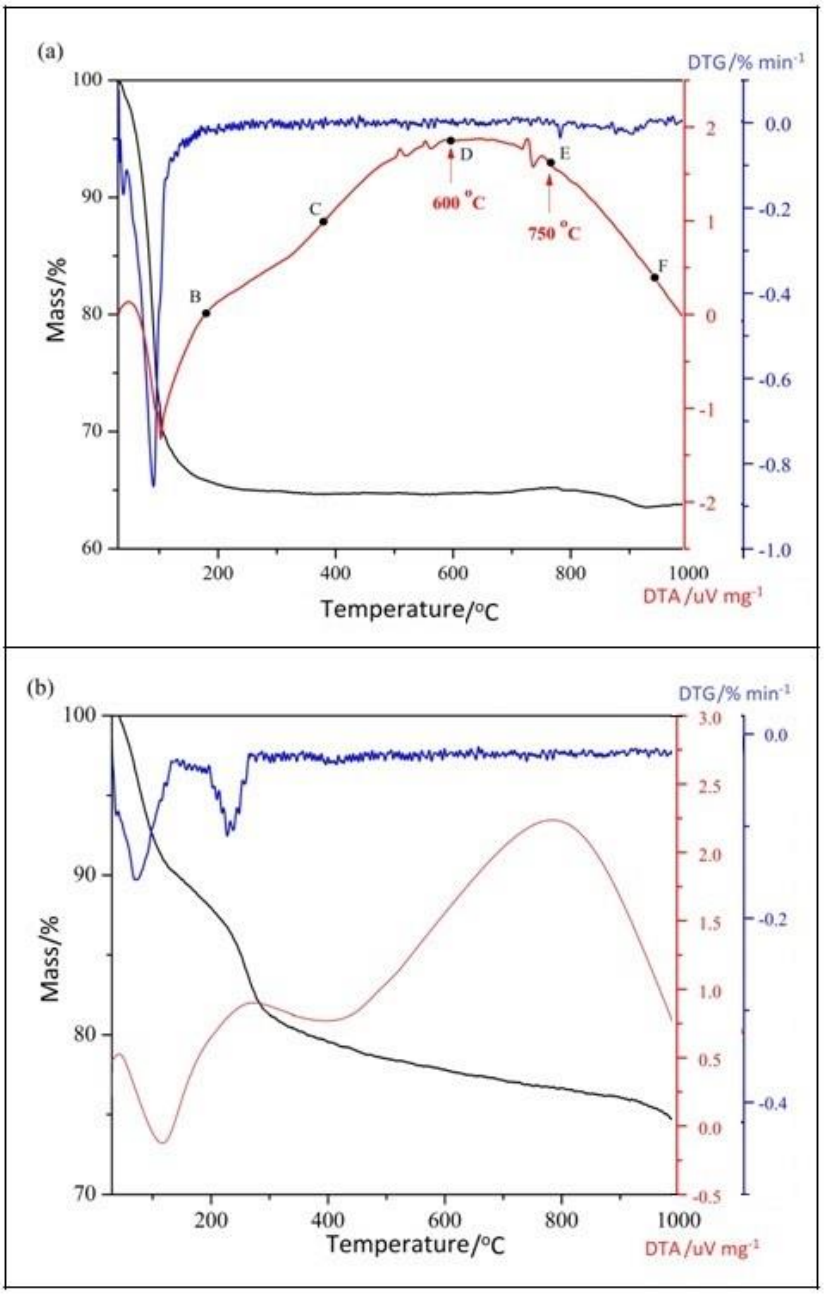

Fig. 4.1: (a) TG-DTA-DTG curves of the synthesized Fe-Mn oxide (MF1) obtained in air atmosphere in the temperature range of 30 °C to 1000 °C. (b) corresponding thermal analysis profiles of iron oxide sample (F1)

For comparison, the sample F1 was prepared in the same way as MF1, but without the presence of Mn. It is seen from Fig. 4.2 (b) that the undoped iron oxide (F1) showed a relatively amorphous pattern with peaks characteristic of α-FeOOH phase (JCPDS card number 29-0713). On the other hand the diffraction peaks in the 'as prepared' material

MF1 were observed at 2θ values of 30.20, 35.45, 43.22, 53.59, 62.65 degree corresponding to Miller indices (220), (311), (400), (422), and (440), reminiscent of cubic $MnFe_2O_4$ phase (JCPDS Card. 10-0319) [6].

Thus, MF1 was essentially an amorphous manganese ferrite in which the 100 intensity peak was observed at 2θ value ~ 35. In addition three other peaks were also observed at 2θ ~ 22, 34 and 36, which were characteristic peaks due to α-FeOOH as mentioned earlier. Thus MF1 is in fact a mixed phase due to $MnFe_2O_4$ + FeOOH.

However the XRD profile of the heat-treated sample at 600 ^oC (MF6) exhibited a characteristic diffraction pattern for α-Fe_2O_3 phase (JCPDS card 33-0664) [5]. In MF6 there is also presence of a small peak at 2θ ~ 35 due to presence of some residual Mn ferrite phase. Thus, XRD analysis confirm that the amorphous Fe-Mn mixed oxide following heat treatment beyond 600 ^oC gets transformed to Mn doped α-Fe_2O_3 phase. Thus MF6 is essentially an α-Fe_2O_3 with a trace of $MnFe_2O_4$. When the sample was further heated to 750 ^oC (MF7), no significant change in the XRD pattern was observed, but the XRD peaks became sharper indicating better crystallization of the α-Fe_2O_3 phase. Also the characteristic peak due to $MnFe_2O_4$ at 2θ ~35, completely disappears as temperature was raised to 750 ^oC, thus indicating formation of pure α-Fe_2O_3 phase at this temperature.

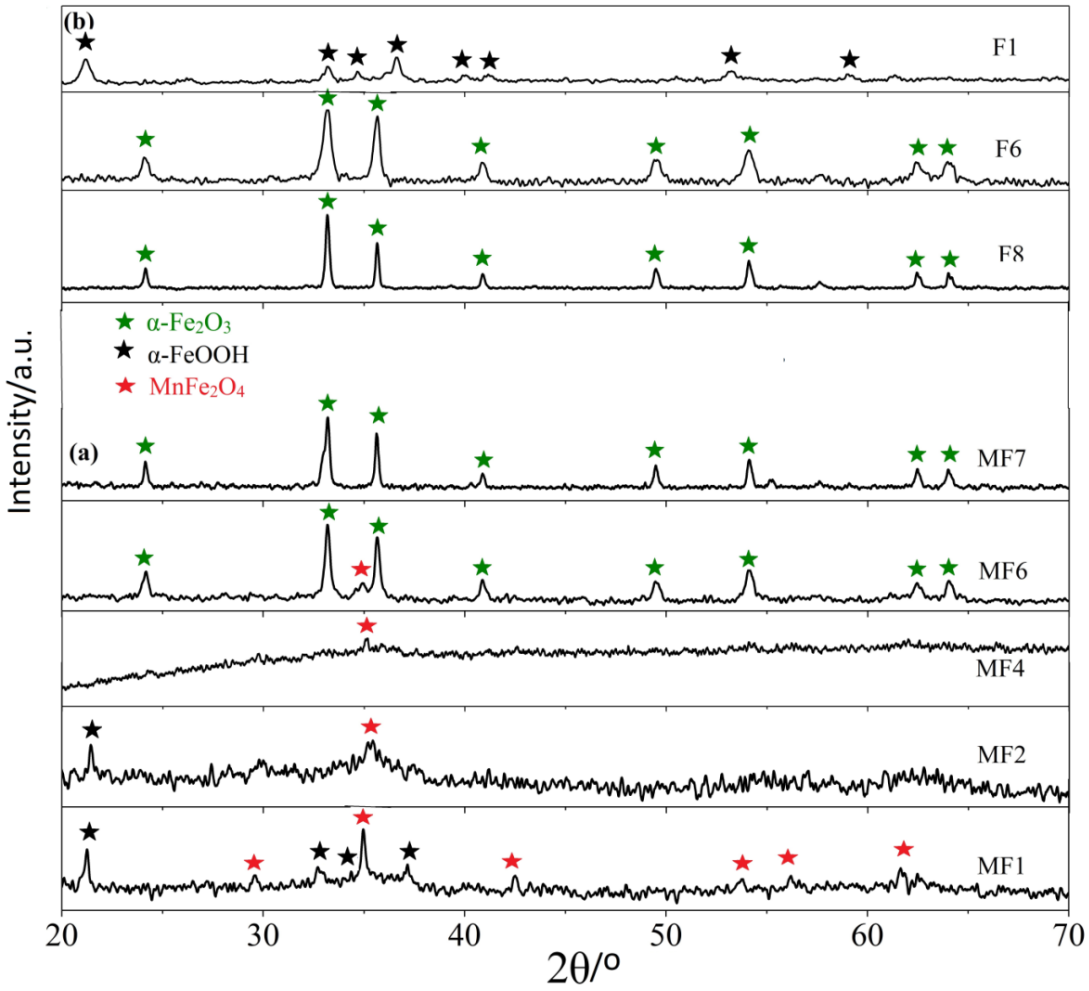

Fig. 4.2: X-ray powder diffraction pattern of Fe-Mn oxides (a) as Fe-Mn oxide mixed phase (MF1) gets transformed to MF7 which is Mn doped α-Fe_2O_3 (b) synthesized iron oxides in absence of Mn wherein α-FeOOH (F1) gets transformed to α-Fe_2O_3 (F6 and F8).

4.1.3 TEM in relation to XRD analysis

Fig. 4.3 gives the TEM images of the pure and Mn doped iron oxide samples. The details of TEM characteristics and XRD analysis are summarized in Table 4.1.

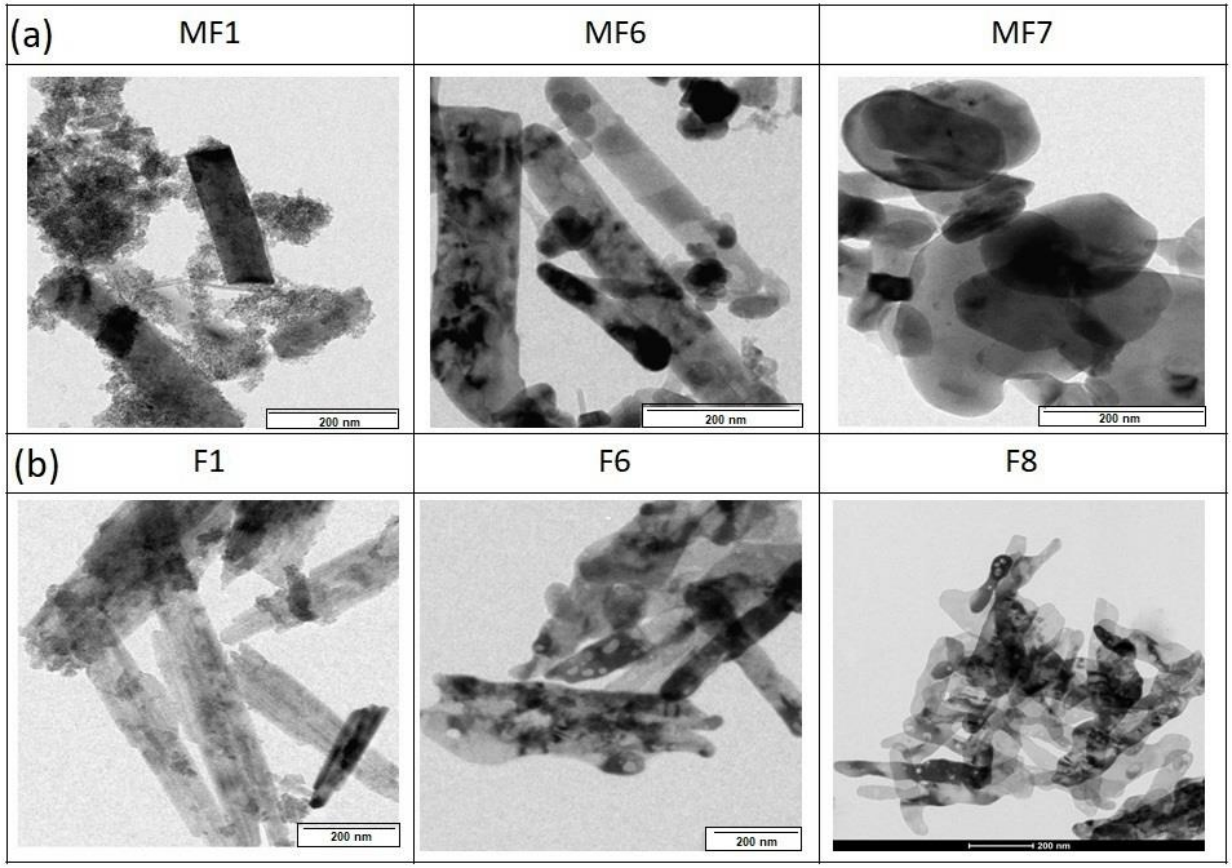

Fig. 4.3: (a) TEM images of the Mn containing iron oxide samples. MF1 was a mixed oxide obtained by co-precipitation from Fe(III) and Mn(II) salts followed by drying the product at 100 ^{o}C. MF6 was obtained by calcination of MF1 at 600 ^{o}C. MF7 was prepared by heating MF1 in air at 750 ^{o}C. (b) The iron oxide F1 was prepared by precipitation from Fe(III) salt, and drying at 100 ^{o}C. F6 was obtained by calcination of F1 at 600 ^{o}C. F8 was prepared by heating F1 in air at 800 ^{o}C.

Table 4.1: Synthesis, XRD and TEM characteristics of the Fe-Mn oxide samples

Code *	Temp of thermal treatment of MF1 or F1 /°C	Oxide phases	Scherrer crystallite sizes /nm	TEM shapes	Average TEM particle size /nm			Density	
					length	width	Aspect Ratio	XRD density /g cm^{-3}	Tap density /g cm^{-3}
	(a) Fe-Mn oxides								
MF1	100	α-FeOOH + $MnFe_2O_4$	22.4	nanorods in diffuse cloud	240	70	3.4	4.9	0.91
MF6	600	α-Fe_2O_3 + $MnFe_2O_4$ (trace)	28.1	nanorods	450	75	6.0	7.1	1.13
MF7	750	Mn^{2+}(α-Fe_2O_3)	25.2	wide oblong	200	140	1.4	7.1	1.33
	(b) iron oxides without Mn								
F1	100	α-FeOOH	18.9	nanorods	550	55	10.0	6.4	0.60
F6	600	α-Fe_2O_3	19.5	nanorods	500	70	7.1	5.2	0.58
F8	800	α-Fe_2O_3	28.6	nanorods	400	85	4.7	5.2	0.63

It is shown above from XRD analysis that F1 is α-FeOOH phase. The TEM image of F1 indicates that it is formed as a cluster of nanorods. However when synthesis was carried out in presence of Mn^{2+} to obtain MF1, a mixed phase of α-FeOOH and $MnFe_2O_4$ was observed. The TEM image of MF1 supports this observation wherein α-FeOOH component was present as nanorods embedded in a diffuse cloud like dispersion due to particles of the amorphous manganese ferrite. Further, when MF1 was heat treated at 600 ^oC to obtain MF6, a structural transformation occurred and the amorphous ferrite phase as well as the α-FeOOH got transformed into α-Fe_2O_3 having a trace of $MnFe_2O_4$. The TEM image of MF6 revealed better resolved nanorods of the α-Fe_2O_3 phase and the manganese ferrite cloud getting almost vanished. It is clear from Fig. 4.3 (a) or from the particle dimensions presented in Table 4.1, that the length of nanorods increased from 240 nm to 450 nm in MF6 and its aspect ratio was nearly double, from 3.4 to 6.0. Further the TEM image of MF7 which is Mn^{2+} doped α-Fe_2O_3, shows disappearance of nanorods and the particles acquired wide oblong shapes with the width of nanoparticles getting doubled from ~ 70 nm to 140 nm. This is associated with the doping of Mn^{2+} into the structure of α-Fe_2O_3. On the other hand, the undoped iron oxides α-Fe_2O_3 (F6 or F8) continue to be nanorods as in Fig. 4.3 (b).

4.1.4 Transformation of Fe-Mn oxide in Mn-doped α-Fe_2O_3.

To understand the transformation of the mixed phase sample MF1 into α-Fe_2O_3 at 600 ^oC, two additional samples were synthesized by thermal treatment of MF1 at 200 and 450 ^oC. This corresponds to the temperatures around the region BC in the DTA profile (Fig. 4.1). The resulting samples designated as MF2 and MF4 were further characterized by XRD. Their XRD profiles are also presented in Fig. 4.2. It is seen from

the profile of MF2 in Fig. 4.2 (a) that most of the peaks disappeared and the XRD profile was largely amorphous. The main peaks of α-FeOOH at about 2θ ~22 and that of $MnFe_2O_4$ around 2θ ~35 were greatly diminished in intensity. At 450 ^oC, as evident in the XRD profile of MF4, the peaks due to α-FeOOH completely disappeared and only a trace of $MnFe_2O_4$ peak was present. Further comparisons of XRD profiles of the MF1 to MF7 samples in Fig. 4.2 (a) indicate disappearance of peaks due to $MnFe_2O_4$ especially in the 2θ region between 30 - 40^o. This is accompanied by appearance of peaks due to α-Fe_2O_3. This structural transformation is summarized in Scheme 4.1.

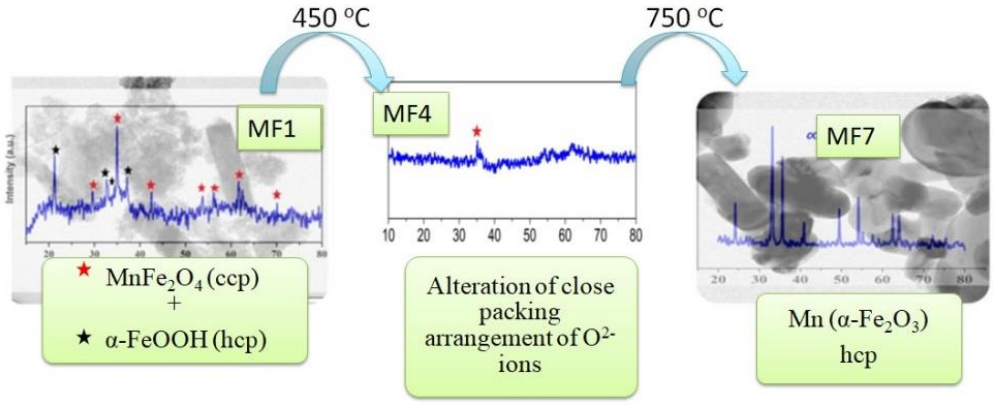

Scheme 4.1: Structural transformation of the 'as prepared' sample MF1 into a Mn^{2+} doped α-Fe_2O_3 (MF7); ccp and hcp in the illustration is indicative of structures formed by cubic and hexagonal close packing of O^{2-} ions respectively.

Bulk manganese ferrite $MnFe_2O_4$ is known to have chemical composition close to normal spinel (fcc close packed structure) with about 20 % of Mn^{2+} present in the octahedral sites, exchanging places with the Fe^{3+} going into tetrahedral sites as in $[\,Mn_{0.8}^{2+} \cdot Fe_{0.2}^{3+}\,]_t\ [\,Mn_{0.2}^{2+} \cdot Fe_{1.8}^{3+}\,]_{oct}\ O_4$. On the other hand, α-$Fe_2O_3$ is a hematite structure with ⅓ vacant octahedral sites in its hcp structure of O^{2-} ions. When $MnFe_2O_4$ component of MF1 or MF6 gets homogenized into MF7 to form a pure α-Fe_2O_3 phase, it has to occur via a rearrangement of oxygen ion close packing from ccp to hcp type.

During the process, Mn^{2+} ions would diffuse into the available vacant sites resulting into formation of Mn^{2+} doped α-Fe_2O_3. Such diffusion of Mn^{2+} ions was also proposed during calcination of a sol-gel synthesized manganese ferrite [7].

4.1.5 Surface area and porosity

To understand the surface properties, the synthesized materials were characterized by BET measurements. The surface area and pore characteristics obtained from adsorption-desorption isotherms (Fig. 4.4) are presented in Table 4.2. It is seen that the 'as prepared' samples F1 and MF1 showed large surface areas in the range 150 – 180 $m^2 g^{-1}$. They showed type II b adsorption isotherm profiles [8, 9] with well defined hysteresis loops (similar to H4 type) in the P/Po range of 0.4 to 1.0. This indicates presence of mesopores with no well defined pore structure. The corresponding heat treated samples F6 as well as the Mn^{2+} doped α-Fe_2O_3 sample MF6, showed much lower surface areas ~ 20 – 30 $m^2 g^{-1}$. Their adsorption-desorption profiles, indicated very low N_2 adsorption. They were of type III with small hysteresis loop (type H3) in the P/P_o range of 0.8 - 1.0. The low surface area and porosity of MF6 and MF7, is attributed to its high density achieved due to filling of the voids by Mn^{2+} doping during the thermal transformation. This is in agreement with an earlier result that higher temperatures induce migration of Mn^{2+} ions from tetrahedral sites into octahedral sites [7, 10]. Further, from pore size distribution plots (insets in Fig. 4.4b), it is observed that both pure α-Fe_2O_3 (F6) and Mn^{2+} doped α-Fe_2O_3 (MF6) are mesoporous in nature. However in MF6, maximum percentages of pores were ranging from 2.5 – 6 nm with average pore radius being 2.8 nm. On the other hand, the range in F6 is wider, i.e. pore size ranges from 2 – 30 nm with average pore radius being 16 nm. As a result, F6 showed larger pore volume of

0.20 cm^3 g^{-1} as compared to Mn^{2+} containing α-Fe_2O_3 which showed a pore volume of < 0.07cm^3g^{-1}.

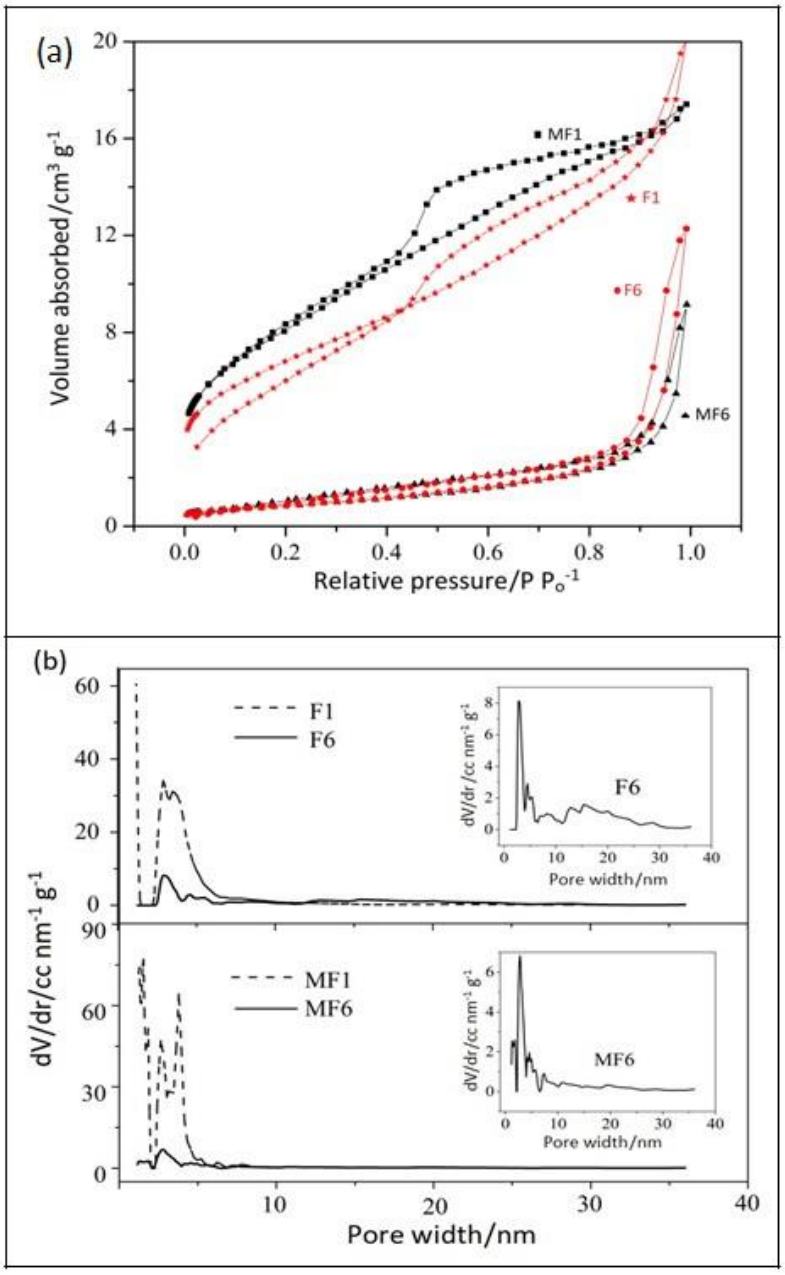

Fig. 4.4: (a) N_2 adsorption desorption isotherms and pore size distribution profiles of the synthesized samples**.** (b) Pore size distribution plots of the synthesized samples where MF1 is (α-FeOOH+ $MnFe_2O_4$); MF6 is Mn^{2+}(α-Fe_2O_3) ; F1 is α-FeOOH and F6 is undoped α-Fe_2O_3

Table 4.2: Synthesis and catalytic activity of the samples in relation to surface area, porosity and magnetic characteristics.

Code	Oxide phases	Surface area /$m^2 g^{-1}$	Pore size /nm	Pore volume /$cm^3 g^{-1}$	Magnetisation characteristics			Catalytic activity in terms of volume of O_2 evolved after 4 minutes of H_2O_2 decomposition reaction /mL	
					Ms /emu g^{-1}	M_R /emu g^{-1}	H_C /Oe	Sunlight	Dark
MF1	$MnFe_2O_4$ + α-FeOOH	177	3.8	0.20	12.7	0.83	146	24.0	20
MF6	α-Fe_2O_3 + $MnFe_2O_{4(trace)}$	19	2.8	0.07	8.4	0.16	10.4	12.6	10.5
MF7	Mn^{2+}(α-Fe_2O_3)	21	1.9	0.03	7.9	0.07	9.6	**25.0**	19.4
F1	α-FeOOH	159	3.8	0.23	10.0	–	--	2.7	0.0
F6	α-Fe_2O_3	32	16	0.20	0.68	0.02	568	6.0	1.5

4.1.6 Magnetic behavior

The magnetic characteristics of the samples are presented in Fig. 4.5 and Table 4.2. It can be seen from the figure that the 'as synthesized' Fe-Mn oxide sample (MF1) was ferromagnetic having saturation magnetization of 12.7 emu g^{-1}. When it was transformed to Mn^{2+} doped α-Fe_2O_3 (MF6 or MF7), the ferromagnetic behavior was slightly less (~ 8 emu g^{-1}). However the undoped α-Fe_2O_3 did not show such ferromagnetic behavior.

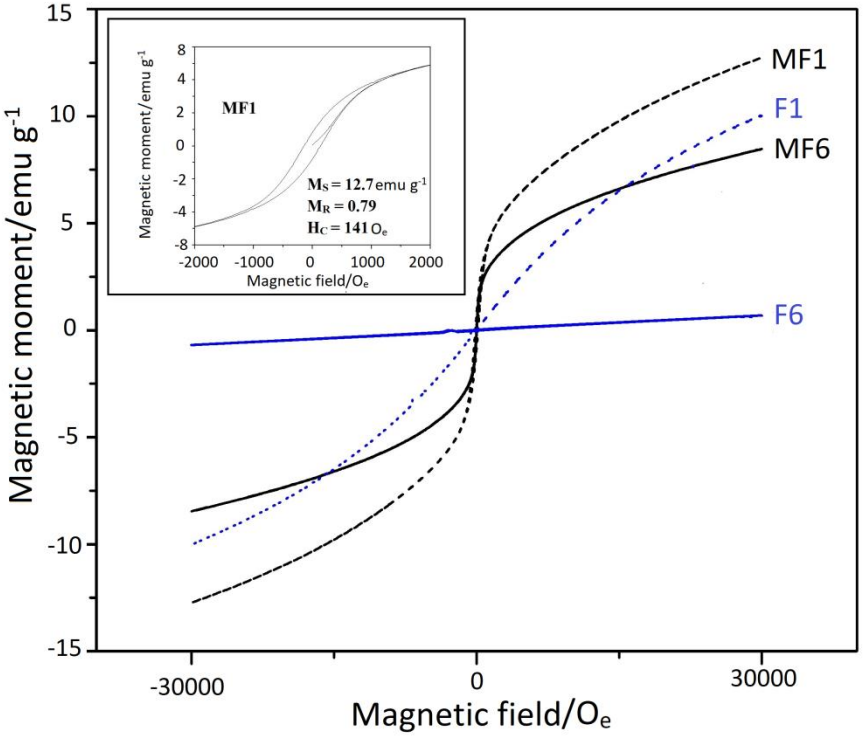

Fig. 4.5: Room temperature magnetization curves of the synthesized Fe-Mn and iron oxide samples where MF1 is (α-FeOOH+ $MnFe_2O_4$); MF6 or MF7 were Mn^{2+}(α-Fe_2O_3) ; F1 is α-FeOOH and F6 is undoped α-Fe_2O_3

4.1.7 Catalytic activity

The catalytic activity of the samples was investigated for their ability to decompose hydrogen peroxide. The reaction was carried out in alkaline medium both in presence and absence of sunlight as iron oxides are known to decompose H_2O_2 through Fenton or photo-Fenton process. This reaction is relevant to advance oxidation processes [11]. The relative catalytic activity is evident from the activity profiles presented in Fig. 4.6.

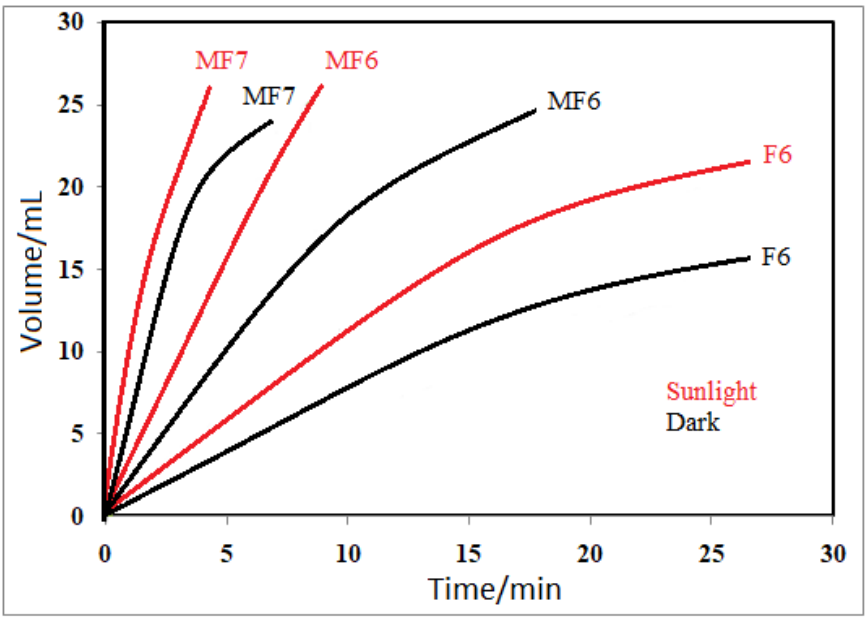

Fig. 4.6: Catalytic activity of the Mn doped α-Fe_2O_3 samples MF6 and MF7 in relation to the corresponding undoped iron oxide, for decomposition of H_2O_2 in presence and absence of sunlight. where MF6 or MF7 were Mn^{2+}(α-Fe_2O_3) and F6 is undoped α-Fe_2O_3

It can be seen from the Fig. 4.6 that all the samples show significant catalytic activity. The doped sample MF7 or Mn^{2+}(α-Fe_2O_3) was most active as compared to the corresponding undoped sample F6. Fe^{3+} ion is known to decompose hydrogen peroxide [12], as per reaction (1) in scheme 4.2. In alkaline medium, the ferric ion from the surface of Fe_2O_3(s) catalyst interacts with H_2O_2 resulting in formation of Fe^{2+} as shown in the reaction (2). The reduction of ferric ion is accompanied by evolution of O_2. The Fe^{2+} species generated as per equation (2) causes further decomposition of H_2O_2 through

intermediate formation of HO^* and HO_2^* species as illustrated in the above scheme. Presence of Mn^{2+} in the structure would further enhance the rate of O_2 evolution due to similar reactions occurring in presence of the Mn^{2+}/Mn^{3+} redox couple.

$$Fe^{3+} + \tfrac{1}{2} H_2O_2 \longrightarrow Fe^{2+} + H^+ + \tfrac{1}{2} O_2 \quad (1)$$

$$Fe^{3+} + \tfrac{1}{2} H_2O_2 + OH^- \longrightarrow Fe^{2+} + H_2O + \tfrac{1}{2} O_2 \quad (2)$$

$$(Fe^{3+} + e^- \longrightarrow Fe^{2+} \text{ and } \tfrac{1}{2} H_2O_2 - e^- + OH^- \longrightarrow H_2O + \tfrac{1}{2} O_2)$$

$$Fe^{2+} + H_2O_2 \longrightarrow Fe^{3+} + OH^- + HO^* \quad (3)$$

$$HO^* + H_2O_2 \longrightarrow H_2O + HO_2^* \quad (4)$$

$$HO_2^* + Fe^{3+} \longrightarrow Fe^{2+} + O_2 + H^+ \quad (5)$$

Considering the equations (2), (3), (4) & (5), we can write

$$H_2O_2 \xrightarrow{Fe_2O_3(s)} H_2O + \tfrac{1}{2} O_2 \quad (6)$$

Scheme 4.2 Mechanism of decomposition of hydrogen peroxide

Thus it is seen that the Mn^{2+} (α-Fe_2O_3) is much more reactive than the pure or undoped α-Fe_2O_3. When the reaction was studied in presence of sunlight, the reactivity increased further due to photo Fenton effect wherein the generated conduction band electrons would produce additional reactive intermediates (Fe^{2+} and OH^*). Thus the Mn^{2+} doped α-Fe_2O_3 sample synthesized in this work was ferromagnetic with high catalytic activity.

4.2 α-MnO_2 (OMS-2) and Fe-OMS-2

Manganese octahedral molecular sieve materials with [MnO_6] octahedra are widely studied as they are economical and eco-friendly materials. These octahedra are linked via corner or edges leading to different structural features of manganese dioxides. Due to their porous structures, ion exchange ability and acid-base properties they find applications in batteries, catalysis and other chemical processes [13-14]. Xiao et al. [14] studied different metal cation doped manganese oxide OMS-2 materials and it was observed that OMS-2 have comparatively lower surface area and pore volume but higher thermal stability than doped OMS-2. Thus doping with Ce and Sn metal ions showed enhancement in thermal stability and supercapacitance behavior of OMS-2 [15, 16]

In present investigation, pure and Fe doped OMS-2 were synthesized by $KMnO_4$ oxidation of $MnSO_4$. These samples were further characterized by Infrared spectroscopy, X-ray diffraction, ICP-AES analysis, TG-DTA, BET analysis and TEM. Their activity towards electrocatalytic oxidation of methanol and ethanol was investigated and was also studied for their capacitance application.

4.2.1 Synthesis of OMS-2 and Fe-OMS-2

Mn OMS-2 was synthesized by following an earlier procedure [17]. Thus hot 0.37 M $KMnO_4$ solution was added drop wise to 0.52 M $MnSO_4$ solution containing 3 mL of conc. HNO_3 by stirring the solution continuously on a magnetic stirrer. Then the mixture was constantly agitated and refluxed for 24 hrs on a rotamantle by maintaining the temperature to 90 ^oC. The residue of MnO_2 was extracted in hot water after cooling

to room temperature, then filtered and washed till neutral pH. The product was dried overnight at 120^{o}C.

Similarly Fe^{+3} doped OMS-2 samples were prepared by adding calculated quantities of ferric nitrate to $MnSO_4$ solution. Thus OMS-2 samples containing 0.3, 2.5 and 3.5 % Fe respectively were prepared.

4.2.2 Characterization

Synthesized OMS-2 and Fe-OMS-2 samples were first examined using ICP-AES analysis to determine % metal present in the final product. The results are presented in Table 4.3.

Table 4.3: % Fe and % Mn in Fe doped OMS-2 obtained from ICP-AES analysis.

Sample code	**% Fe**	**% Mn**
0.3 % Fe-OMS-2	0.29	60.2
2.5 % Fe-OMS-2	2.53	57.5
3.5 % Fe-OMS-2	3.49	44.1

Fig. 4.7 gives the TG-DTA profile of OMS-2. The major mass losses in the temperature range of 35− 800 °C were observed. (i) The mass loss between 35 – 250 ^{o}C is associated with loss of physisorbed and hydrogen bonded water and (ii) between 250 – 570 ^{o}C is due to loss of lattice oxygen in the form of gaseous molecules from the surface. The mass loss of about 4 % between 580 and 660 °C is caused by evolution of structural oxygen associated with chemical decomposition. This loss in oxygen is accompanied with reduction of Mn from +4 to +3 oxidation state. This was due to transformation of α-MnO_2 phase to Mn_2O_3 [17]. Thus over this temperature range OMS-2 tunnel structure

become unstable and at temperature above 650 ^{o}C, Mn_2O_3 gets transformed to Mn_3O_4 by further loss of lattice oxygen [18].

Further the TG profiles of Fe-OMS-2 are presented in Fig. 4.8 and their mass loss values are given in Table 4.4. It is seen that Fe doped OMS-2 samples show similar thermal behavior as that of undoped OMS-2. However, % mass loss for 0.3% Fe doped OMS-2 was half (~ 5%) in comparison to that of OMS-2 (~ 10%) in the temperature range of 35 to 570 ^{o}C. Similarly for 2.5 % Fe-OMS-2 the % mass loss was ~ 4.5 %. Thus, thermal stability of OMS-2 increased with Fe doping upto 2.5 %. But as % Fe dopant was further increased from 2.5 to 3.5 %, decrease in thermal stability was observed with increase in % mass loss of ~ 12 %.

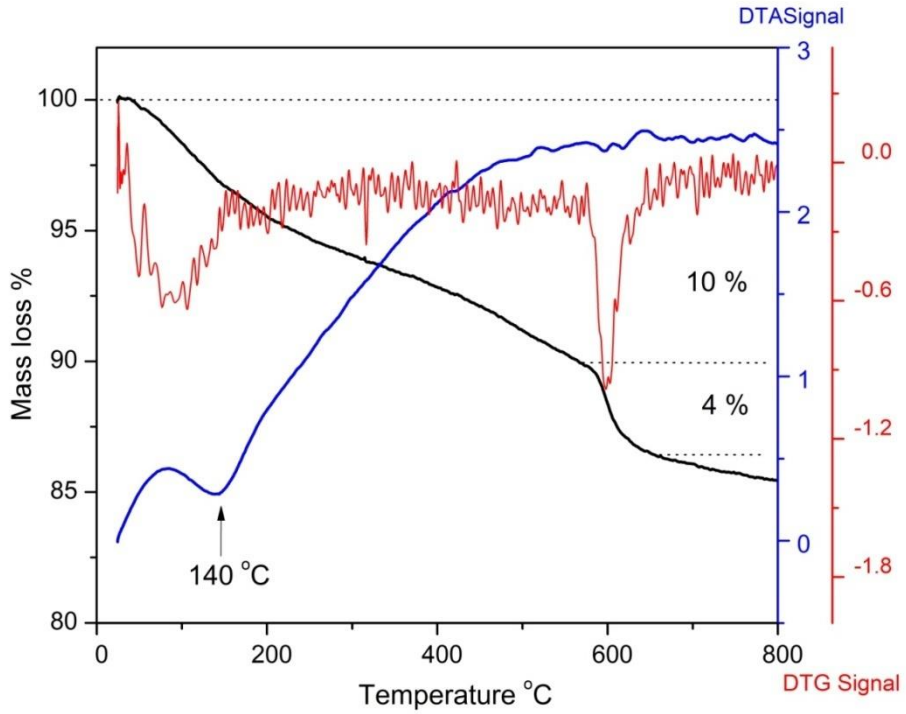

Fig. 4.7: TG-DTA profile of OMS-2 in oxygen atmosphere.

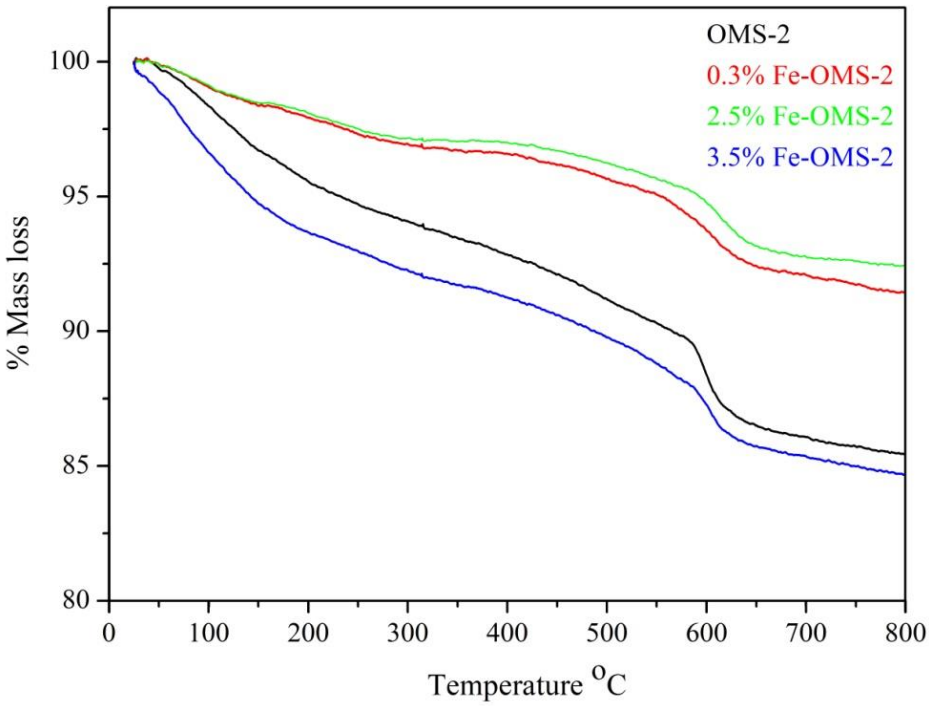

Fig. 4.8: TG profile of OMS-2 and Fe-OMS-2 in oxygen atmosphere.

Table 4.4: Thermal analysis of pure and Fe doped OMS-2 samples.

Sample	**% mass loss**			Phase transition temperature from DTG signal (°C)
	100 – 250 °C	**250 – 570 °C**	**570 – 800 °C**	
OMS-2	5	5	5	595
0.3 % Fe-OMS-2	3	2	4	601
2.5 % Fe-OMS-2	3	1.5	3.5	597
3.5 % Fe-OMS-2	8	4	3.5	601

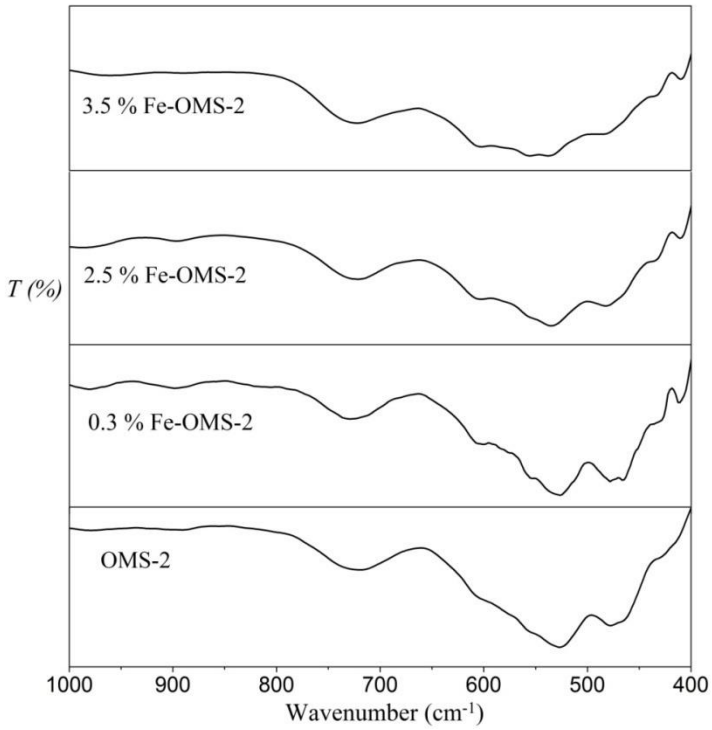

Fig 4.9: Infrared spectra of OMS-2 and Fe doped OMS-2.

Fig 4.9 displays IR spectra of synthesized OMS-2 and Fe-OMS-2 materials. The intense absorption band due to Mn-O lattice vibrations in the octahedra usually appears between 400-800 cm^{-1}. OMS-2 shows three peaks in this range at about 721, 521, and 474 cm^{-1}. The band at about 721 cm^{-1} is characteristic absorption due to O-Mn-O bond vibration [19, 20]. Peaks at 521 and 474 cm^{-1} are attributed to stretching modes of Mn-O bond in the octahedra [21, 22]. Fe doped OMS-2 also shows characteristic peaks due to vibrations of Mn-O bond. But as % Fe dopant increases from 0.3 to 3.5 %, the peak at ~474 cm^{-1} was observed to decrease in intensity.

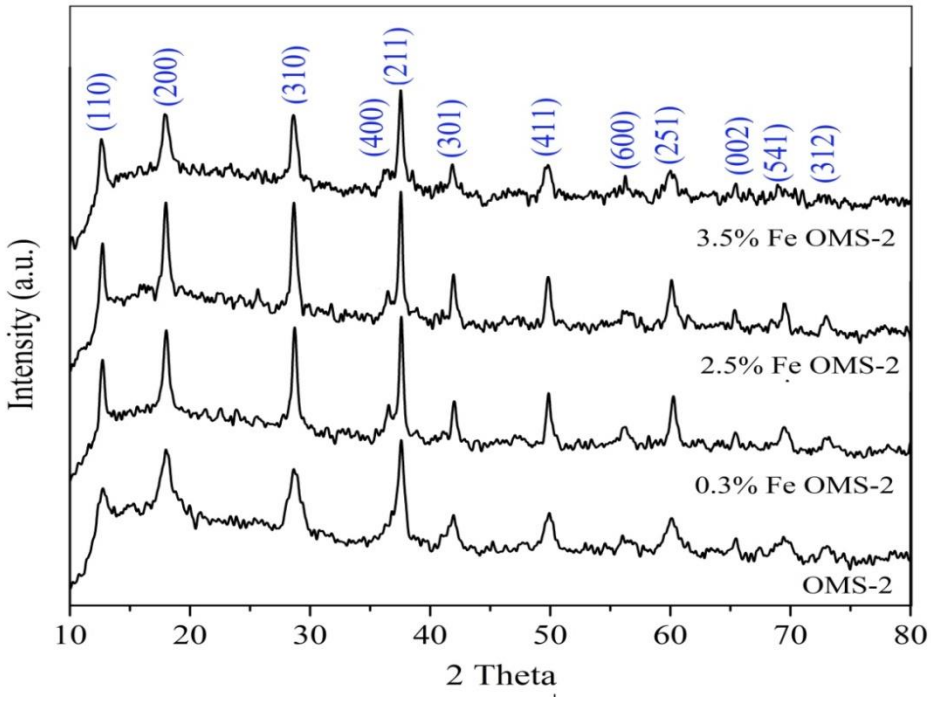

Fig. 4.10: X-ray diffraction patterns of undoped OMS-2 and Fe doped OMS-2.

XRD patterns were recorded for these samples in the 2θ range of 10°−80°. All the peaks in the X-ray diffraction pattern (Fig. 4.10) of undoped and doped OMS-2 samples could be indexed to α-MnO_2 phase. The 100 intensity peak in all the samples were observed at 2θ ~ 37.52 and is attributed to (211) plane of α-MnO_2 (JCPDS No: 44-0141) [23, 24]. For Fe doped OMS-2 the XRD peaks become sharper indicating increase in particle size. Thus, it can be concluded that small percent of Fe doping in α-MnO_2 does not alter its structure but can affect the crystallinity and particle size. Similar observation was made by Hui et al. [25] for their study on Fe doped manganese oxides. However the XRD pattern of 3.5 % Fe-OMS-2 appeared diffuse and the 100 intensity peak shifted to 2θ ~ 37.50.

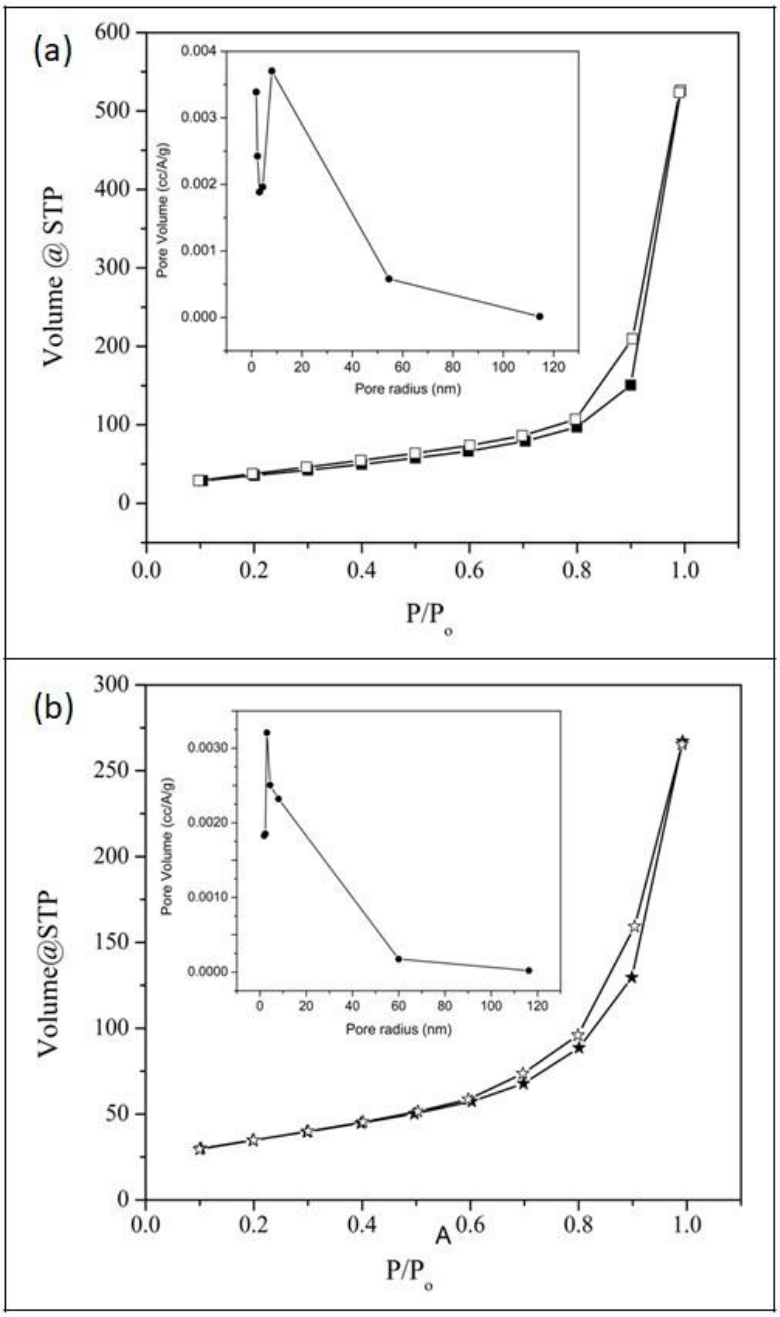

Fig. 4.11: N_2 adsorption desorption and pore size distribution profiles (inset) of (a) OMS-2 (b) 0.3% Fe-OMS-2.

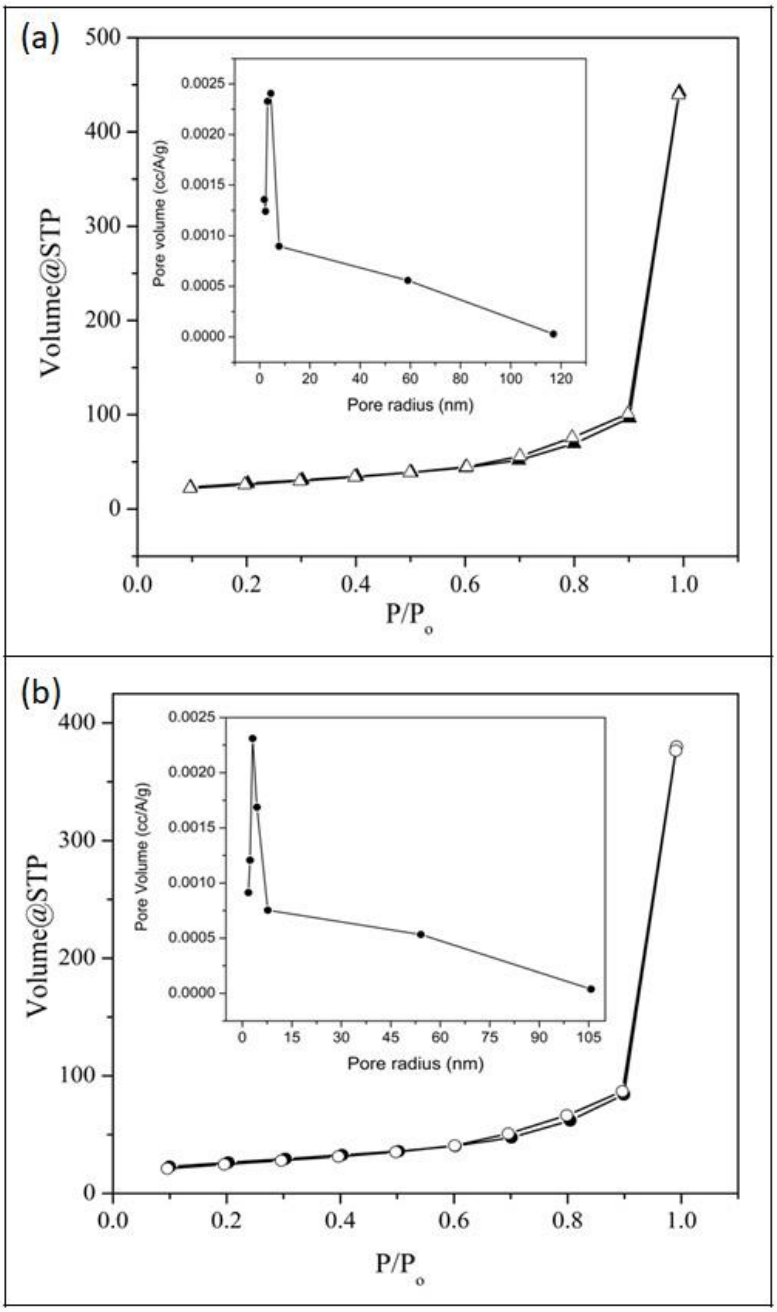

Fig. 4.12: N_2 adsorption desorption and pore size distribution profiles (inset) of (a) 2.5% Fe-OMS-2 (b) 3.5% Fe-OMS-2.

Table 4.5: The estimated values of surface area, porosity and Scherrer crystallite sizes of OMS-2 and Fe doped OMS-2.

Sample	**Surface area ($m^2 g^{-1}$)**	**Pore volume ($cm^3 g^{-1}$)**	**Pore radius (nm)**	**Scherrer crystallite sizes (nm)**
OMS-2	137	0.80	8.0	8.1
0.3 % Fe doped OMS-2	123	0.40	3.0	16.2
2.5 % Fe doped OMS-2	94	0.67	4.4	16.3
3.5 % Fe doped OMS-2	90	0.57	3.1	10.5

Fig. 4.11 and 4.12 gives N_2 adsorption desorption isotherms and pore size distribution profiles of OMS-2 and Fe doped OMS-2. Isotherms observed for OMS-2 as well as Fe-OMS-2 can be classified as type III isotherm with very narrow hysteresis loops in the relative pressure ranges of P/Po ~ 0.3-0.4 for OMS-2 which is indicative of the presence of mesopores in the material. However when compared to OMS-2, Fe doped OMS-2 shows lower adsorption at high relative pressure of 1 and the hysteresis loop is in very narrow range of 0.6-0.9 of P/Po. The BET surface area obtained for 0.3 % Fe doped OMS-2 materials was comparatively less than pure OMS-2. Further with increase in % Fe dopant to 3.5 % the surface area considerably decreased to ~ 90 $m^2 g^{-1}$ from a value of 137 $m^2 g^{-1}$ for pure OMS-2. Fe doping also leads to decrease in total pore volume to half that of undoped OMS-2. Also pore size decreases from 8 nm (OMS-2) to 3-4 nm (Fe doped OMS-2). Pore size distribution profile shows that large volume is contributed by mesopores in the range of 2-30 nm in OMS-2 whereas for Fe doped OMS-2 with 2.5% and 3.5 % Fe, maximum mesopore volume is due to smaller mesopores having radius of less than 10 nm. TEM images (Fig. 4.13) revealed rod shaped structures for

OMS-2. On the other hand the Fe doping resulted in increase in width of the rods leading to narrow oblong shaped particles.

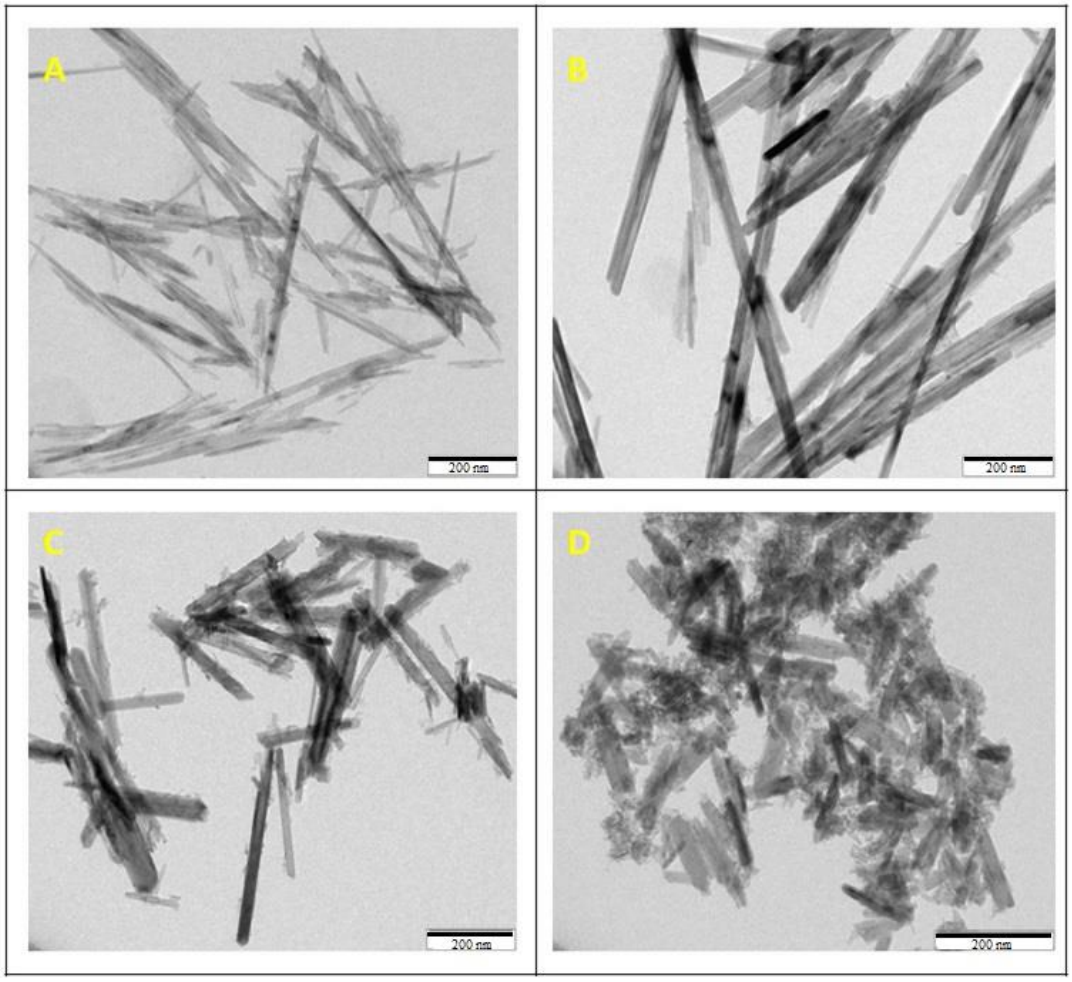

Fig.4.13: TEM images of (A) OMS-2 (B) 0.3% Fe-OMS-2 (C) 2.5% Fe-OMS-2 (D) 3.5% Fe-OMS-2.

Summary & Conclusions

- Mn^{2+} doped ferromagnetic α-Fe_2O_3 nanoparticles having saturation magnetization around 8 emu g^{-1}, have been synthesized by an economical and eco-friendly co-precipitation route. The synthesis involved addition of Fe(II) and Mn(II) chlorides in a molar ratio of 2:1 to an aqueous solution of alkali and the resulting precursor MF1 was dried and characterized by TG-DTA and XRD.
- The investigation revealed that the synthesized precursor was a mixed phase of (α-FeOOH + $MnFe_2O_4$) which when calcined beyond 600 ^oC, got transformed into Mn^{2+}(α-Fe_2O_3) nanorods and particles with wide oblong shapes. The corresponding iron oxide synthesized without Mn produced only nanorods having no such ferromagnetic character (Ms ~ 0.8 emu g^{-1}).
- The Mn^{2+}(α-Fe_2O_3) nanoparticles showed high catalytic activity towards decomposition of H_2O_2 and the catalyst being ferromagnetic, could be easily recovered using an external magnet. The activity was further enhanced when the catalytic reaction was carried out in presence of sunlight due to photo-Fenton process.
- OMS-2 (α-MnO_2) and Fe doped OMS-2 was synthesized by $KMnO_4$ oxidation of $MnSO_4$ method.
- Fe doping resulted in decrease in surface area of OMS-2 along with reduced pore volume and pore sizes giving rise to smaller mesopores. X-ray diffraction patterns of Fe-OMS-2 did not alter much as compared to pure OMS-2. TEM images revealed rod shaped structures for OMS-2. On the other hand Fe doping resulted in increase in width of rods leading to narrow oblong shaped particles.

References

[1] C. N. Rao, G. V. Subha Rao, *Transition metal oxides: crystal chemistry, phase transition and related aspects*, Washington 1974.

[2] R. A. Bepari, P. Bharali, B. K. Das, *Controlled synthesis of α- and γ-Fe_2O_3 nanoparticles via thermolysis of PVA gels and studies on α-Fe_2O_3 catalyzed styrene*, J Saudi Chem. Soc. 21 (2017) 170-178.

[3] S. Sakurai, A. Namai, K. Hashimoto, S. Ohkoshi, *First Observation of Phase Transformation of All Four Fe_2O_3 Phases (γ → ε → β → α-Phase)*, J. Am. Chem. Soc. 51 (2009) 18299-303.

[4] S. I. Ramya, C. K. Mahadevan, *Preparation and structural, optical, magnetic, and electrical characterization of $Mn^{2+}/Co^{2+}/Cu^{2+}$ doped hematite nanocrystals*, J. Solid State Chem. 211 (2014) 37-50.

[5] D. A. Wheeler, G. Wang G, Y. Ling, Y. Li, J. Z. Zhang, *Nanostructured hematite: synthesis, characterization, charge carrier dynamics and photoelectrochemical properties*, Energy Environ. Sci. 5 (2012) 6682-6702.

[6] A. Mirzaei, K. Janghorban, B. Hashemi, S. R. Hosseini, M. Bonyani, S. G. Leonardi, A. Bonavita, G. Neri, *Synthesis and characterization of mesoporous α-Fe_2O_3 nanoparticles and investigation of electrical properties of fabricated thick films*, Process Appl. Ceram. 10 (2016) 209-217.

[7] J. Li, H. Yuan, G. Li, Y. Liu, J. Leng, *Cation distribution dependence of magnetic properties of sol-gel prepared $MnFe_2O_4$ spinel ferrite nanoparticles*, J Magn. Magn. Mater. 322 (2010) 3396-400.

[8] M. M. L. Ribeiro Carrott, *Physisorption of Gases by Solids: Fundamentals, Theories and Methods for the Textural Characterisation of Catalysts*. J. L. Figueiredo, M. M.

Pereira, J. Faria, Eds. *Catalysis From Theory to Application - an Integrated Course.* Coimbra; (2008) 83-105.

[9] Rouquerol F, Rouquerol J, Sing KSW, Llewellyn P, Maurin G. *Adsorption by Porous Powders and Porous Solids: Principles, Methodology and Applications*, 2nd ed. Elseviers; AP 2014.

[10] L. Zhang, Y. Wu, *Sol-Gel Synthesized Magnetic $MnFe_2O_4$ Spinel Ferrite Nanoparticles as Novel Catalyst for Oxidative Degradation of Methyl Orange*, J. Nanomater. (2013).

[11] C. Wang, H. Liu, Z. Sun, *Heterogeneous Photo-Fenton Reaction Catalyzed by Nanosized Iron Oxides for Water Treatment*, Int. J. Photoenergy. (2012) http://dx.doi.org/10.1155/2012/801694

[12] Y-H. Jo, Y. W. Chung, S-H. Do, *Simple preparation of Mn-Fe_2O_3 composite: Identification and evaluation as an activator in Fenton like oxidation*, 2nd Ann. Int. Conf. (SEES 2013) http://doi: 10.5176/2251-189X_SEES13.23.

[13] T. D. Xiao, Bokhimi, M. Benaissa, R. Pérez, P. R. Strutt, M. J. Yacamán, *Microstructural Characteristics of Chemically Processed Manganese Oxide Nanofibres*, Acta mater. 45 (1997) 1685-1693.

[14] C. Xiao, Y-F. Shen, S. L. Suib, C. L. O'Young, *Characterization of Manganese Oxide Octahedral Molecular Sieve (M-OMS-2) Materials with Different Metal Cation Dopants*, Chem. Mater. 14 (2002) 940-948.

[15] E. Hapeshi, C. R. Theocharis, *Preparation and Characterization of a Cerium (IV)-incorporated Manganese Oxide OMS-2. Effect of Cerium(IV) Template on Octahedral Molecular Sieves of Manganese Oxide and Characterization of*

Manganese Oxide Molecular Sieves with Cerium(IV) as Dopant, Adsorption Science & Technology 26 (2008) 789 – 801.

[16] M. Sun, F. Ye, B. Lan, L. Yu, X. Cheng, S. Liu, X. Zhang, *One-step Hydrothermal Synthesis of Sn-doped OMS-2 and Their Electrochemical Performance*, Int. J. Electrochem. Sci., 7 (2012) 9278 – 9289.

[17] Roberto N. DeGuzman, Yan-Fei Shen, Edward J. Neth, Steven L. Suib, Chi-Lin O'Young, Steven Levine, John M. Newsam, *Synthesis and Characterization of Octahedral Molecular Sieves (OMS-2) having the Hollandite Structure*, Chem. Mater. 6 (1994) 815-821.

[18] D. Y. Shen, X. Sithambaram, S. Gomez, S. Kumar, R. Crisostomo, V.M.B. Suib, S.L. Aindow, *Synthesis and Catalytic Activity of Cryptomelane-Type Manganese Dioxide Nanomaterials Produced by a Novel Solvent-Free Method*, M. Chem. Mater. **17** (2005) 5382-5389.

[19] S. Maiti, A. Pramanik, S Mahanty, *Interconnected Network of MnO_2 Nanowires with a "Cocoonlike", Morphology: Redox Couple-Mediated Performance Enhancement in Symmetric Aqueous Supercapacitor*, ACS Appl. Mater. Interfaces 6 (2014) 10754−10762.

[20] C. M. Julien, M. Massot, C. Poinsignon, *Lattice vibrations of Manganese oxides: Part I. Periodic structures*, Spectrochim. Acta, Part A 60 (2004) 689-700.

[21] W. Yao, H Zhou, Y. Lu, *Synthesis and property of novel MnO_2@polypyrrole coaxial nanotubes as electrode materials for supercapacitors*, J. Power Sources, 241(2013) 359 – 366.

[22] L. C. Zhang, Z. H. Liu, X. H. Tang, J. F. Wang, K Ooi, *Synthesis and characterization of β-MnO_2 single crystals with novel tetragonal morphology*, Mater. Res. Bull. 42 (2007) 1432-1439.

[23] R. Poonguzhali, N. Shanmugam, R. Gobi, A. Senthilkumar, G. Viruthagiri, N. Kannadasan, *Effect of Fe doping on the electrochemical capacitor behavior of MnO_2 nanocrystals*, J. Power Sources 293 (2015) 790-798.

[24] R Patrice, L. Dupont, L. Aldon, J. C. Jumas, E. Wang, J. M. Tarascon, *Structural and Electrochemical Properties of Newly Synthesized Fe-Substituted MnO_2 Samples*, Chem. Mater. 16 (2004) 2772-2782.

[25] J. Hui, D. Yuping, L. Zhuo, Z. Jia, L. Shunhua, *Influence of Fe doping on the microstructure and electromagnetic performance of manganese oxides*, Physica B 407 (2012) 971–977.

CHAPTER V

ELECTROCHEMICAL PROPERTIES OF GLYCEROL BASED CARBONS AND THEIR NANOCOMPOSITES

5.1: Supercapacitance

5.2: Electrocatalytic oxidation of methanol

5.3: Electrocatalytic oxidation of ethanol

General introduction

Carbons are important materials in energy research in the area of supercapacitors and electrocatalytic supports in fuel cells. In this investigation carbons with high surface area are produced from glycerol; the latter being available in abundance as a byproduct of transesterification reaction during biodiesel production process in the industry.

H_2-O_2 fuel cells use H_2 as fuel and are more efficient than batteries or fossil fuel power stations. However, transportation cost, energy loss during transportation and hydrogen storage are some of the issues that need to be faced when employing H_2-O_2 fuel cells. Direct methanol fuel cells are interesting as methanol as a fuel has advantages over other fuels due to ease of storage and transportation. The electrocatalysis is relatively simple due to absence of C-C bond as compared to higher alcohols like ethanol and propanol. In spite of its substantial capability one of the downside of the direct alcohol fuel cells is use of precious metals like Pt as electrocatalyst. Pt alone shows a very high activity for methanol oxidation but it has a poor tolerance for CO. This led to the development of bimetallic catalysts with the second metal used should be more oxophilic than Pt. Currently the most promising fuel cell catalyst is Pt-Ru/C (where C is carbon support with high surface area)

Further carbon materials are largely investigated for supercapacitor electrode materials as they possess good electrical conductivity and high surface area. They are used for energy storage such as in supercapacitor- battery/fuel cell hybrid systems.

Therefore the present investigation is undertaken to evaluate supercapacitance and electrocatalytic activity of glycerol based carbons. Also MnO_2 and its composites with glycerol based carbons are screened for capacitance under similar experimental conditions. Glycerol based carbons are also examined for its activity as electrocatalytic

support in methanol/ethanol fuel cells. In this investigation Ru on glycerol based carbon is synthesized and examined for its activity towards methanol/ethanol electro-oxidation in combination with commercially available 10% Pt/C and previously synthesized α-MnO_2 (OMS-2).

5.1 Supercapacitance behavior of glycerol based carbons and its composites

Development in the area of electronic devices is influenced by energy sources of high energy density and power density. In this context, supercapacitors seemed propitious as it has numerous applications in energy storage systems in addition to electronic devices. Commercial carbon based supercapacitors have low energy density issues [1-3]. Among other candidates explored for supercapacitor electrode materials, metal oxides have gained increasing attention. Specifically transition metals oxides are favorable for capacitor application as these metals exhibit variable oxidation states and so their oxides have capability of storing energy via chemical redox mechanism. However, research shows that the major problem with employing metal oxides in capacitors is their low electrical conductivity. Considering these issues, supercapacitor research was further extended to developing a good composite material comprising of carbon and metal oxides. It was observed that composites of various carbons with metal oxides like MnO_2, RuO_2, Fe_2O_3 exhibited improved capacitance behavior.

5.1.1 In the present work following synthesized materials are investigated for their capacitance (synthesis described in chapter III and chapter IV)

i. Activated glycerol based carbons

   GBC_K: KOH activated carbon

   GBC_Z: $ZnCl_2$ activated carbon

   GBC-800: It is obtained from carbonized glycerol GBC-120 and heated to 800 ^oC in N_2 atmosphere

ii. Surfactant modified glycerol based carbons

   GBC_{S1}: Glycerol based carbon synthesized using CTAB surfactant

   GBC_{S2}: Glycerol based carbon synthesized using SDS surfactant

iii. Commercial carbons

   CNT and VulcanXC-72R

iv. Metal oxides

   α - MnO_2 also known as OMS-2 and Fe doped OMS-2

5.1.2 Capacitance measurement

The capacitance of the samples was determined by cyclic voltammetry (CV). The measurements were carried out at various scan rates ranging from 2 to 100 mV/sec using CH electrochemical instrument (Instrument Model: CHI6107D). Aqueous Ag/AgCl/KCl (0.1M) was used as a reference electrode and Pt wire as a counter electrode. The working electrode was prepared by first making an ink of carbon using Nafion solution. The ink was then applied to the glassy carbon surface which was initially cleaned using alumina powder. The electrode was then allowed to dry overnight at ambient temperature. The electrolyte used was 0.5 M Na_2SO_4.

The capacitance (C) which is mainly charge storage capacity of the material is a quantitative property expressed by equation:

$$C = I \div (a \times v) \qquad (1)$$

Where I is the average current in ampere, v is scan rate in V s^{-1} and a is geometrical area of glassy carbon electrode used (0.071 cm^2).

5.1.3 Results and discussion

(a) Capacitance of Glycerol Based Carbons

In the present work, capacitance behavior of some standard carbons was investigated (SWCNT, VulcanXC72R and acetylene black), along with synthesized glycerol based carbons, OMS-2 and glycerol based carbon-OMS-2 composites.

Fig. 5.1 and 5.2 gives cyclic voltammograms of the glycerol based carbons while the profiles of commercially available carbons are presented in Fig. 5.3. The corresponding capacitance values at a scan rate of 2 mV s^{-1} are presented in Table 5.1 in relation to their surface area and porosity characteristics. It can be seen from the Table that generally all the glycerol based carbons show capacitance in the range of 100 – 650 mF cm^{-2}. This value is much higher than the capacitance of the commercial carbons wherein the Vulcan XC-72R and CNT showed values of only 5.2 and 31 mF cm^{-2} respectively.

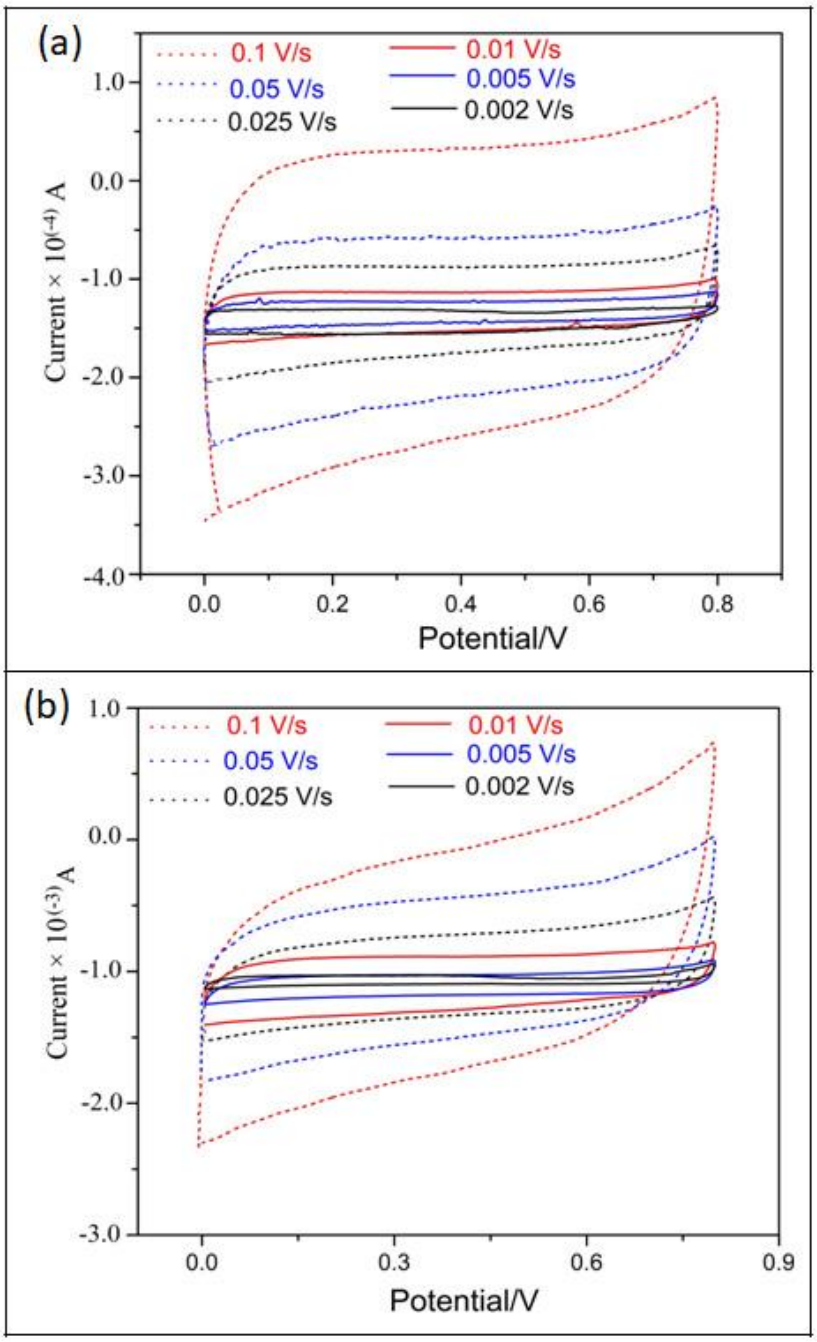

Fig. 5.1: Cyclic voltammetry profiles of carbons at different scan rate recorded in 0.5 M Na_2SO_4 (a) GBC_K (b) GBC_Z at different scan rates.

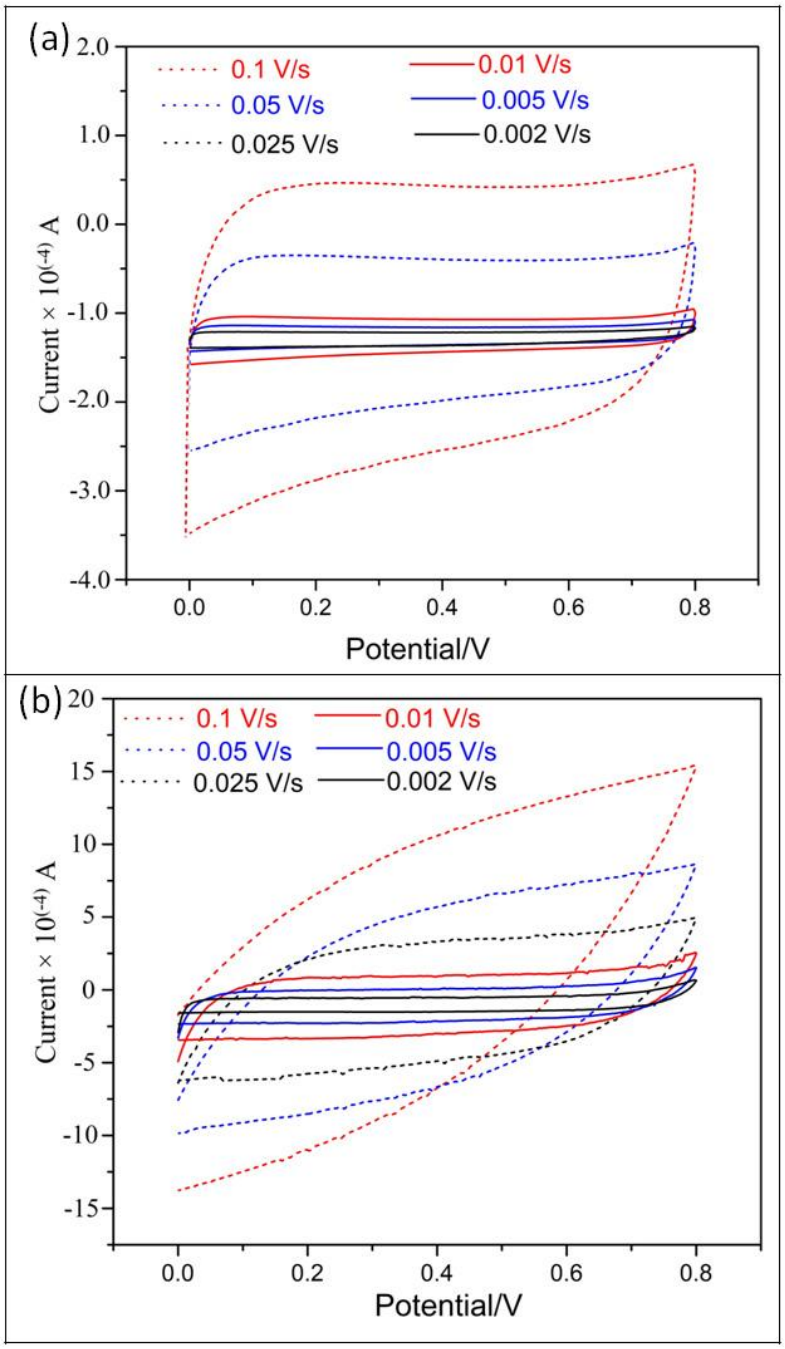

Fig. 5.2: Cyclic voltammetry profiles of glycerol based carbons at different scan rate recorded in 0.5 M Na_2SO_4 (a) GBC_{S1} (synthesized using surfactant CTAB) (b) GBC_{S2} (synthesized using surfactant SDS).

Capacitance offered by carbons is normally influenced by combined effect of the following three factors

i) Structural properties like surface area and pore size distribution

ii) Micropore volume

iii) Surface functionalities like hydroxyl groups are also known to enhance the capacitance through a redox mechanism leading to additional pseudocapacitance [4-5].

The redox reaction in presence of –OH group can be represented as:

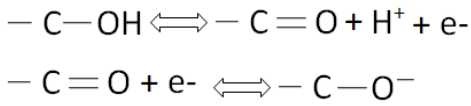

Infrared spectra of glycerol based carbons showed existence of several functionalities on its surface (Fig. 2.3 and Fig. 3.4). Moreover it was noted that specifically micropores can enhance the specific capacitance when the size of electrolyte ion is in micropore range (< 2 nm) [6]. It is generally the interplay of the factors of surface area and micropore volumes that determine the magnitude of capacitance among the glycerol based carbons (GBC^s). Thus from Table 5.1, it can be seen that GBC_{S2} have highest accessible surface area and large pore volume among the GBC^s. It thus offers higher capacitance of 640 mF cm^{-2} as compared to the other glycerol based carbons examined. Further, the surface functionalities of the glycerol based carbons makes them hydrophilic. In the aqueous electrolyte therefore they facilitate diffusion of the ions and consequently enhance the capacitance.

In comparison to GBC_{S2}; the sample GBC_Z has lower capacitance (500 mF cm^{-2}). GBC_{S2} and GBC_Z have almost similar micropore volumes ~ 0.70 cm^3 but GBC_Z possesses comparatively lower surface area and thus lower charge storage ability. GBC_K

on the other hand shows even much lower capacitance (~ 220 mF cm^{-2}). It has similar surface area as GBC_Z but much lower micropore volume (~ 0.43 cm^3 g^{-1}) which is approximately half that of GBC_Z. Among GBC^s, GBC_{S1} showed low specific capacitance ~ 104 mF cm^{-2}. It is due to the combined effect of its lowest surface area and pore volumes. To confirm the effects of surface area, porosity and surface functional groups, the sample GBC-800 was synthesized. As mentioned earlier it was obtained by thermal treatment of GBC-120 at 800 ^oC to defunctionalize most of its surface. Fig. 2.3 gives comparative IR spectra of GBC-120 and GBC-800. It is seen that in GBC-800, the intensity of most functional groups is greatly reduced. It is also clear from Table 5.1 that its surface area and porosity is greatly diminished with very less micropore volume of 0.08 cm^3 g^{-1}. As expected its specific capacitance is lowest (~1.3 mF cm^{-2}). Thus surface area and micropore volume affects to a large extent the capacitance property of the carbon material.

Table 5.1: Surface characteristics and capacitance (mF cm^{-2}) of carbon materials

Sample	**S_{BET} (m^2 g^{-1})**	**V_{Total} (cm^3 g^{-1})**	**$V_{Micropore}$ (cm^3 g^{-1})**	**$V_{Mesopore}$ (cm^3 g^{-1})**	**Capacitance (mF cm^{-2})**
GBC_{S2}	2289	1.31	0.72	0.54	640
GBC_Z	1577	1.23	0.77	0.50	500
GBC_K	1653	1.76	0.43	1.20	220
GBC_{S1}	1069	0.60	0.40	0.13	104
GBC-800	425	0.22	0.18	0.01	1.3
VulcanXC72R	306	0.36	0.08	0.21	5.2
SWCNT	2431	3.98	0.43	2.80	31

Similarly Vulcan XC72R presented very low capacitance of 5.2 mF cm^{-2}. This is due to its very low accessible surface area and negligible micropore volume of 0.08 cm^3 g^{-1}. However in case of SWCNT the capacitance is quite low (~31 mF cm^{-2}) inspite of the fact that its surface area is very high (2289 m^2 g^{-1}) and micropore volume is 0.43 cm^3 g^{-1}. This is due to its lower micropore volume and absence of surface functionalities in comparison to GBC^s. Fig. 5.4 gives a plot of capacitance as a function of scan rate. It can be seen from the figure that capacitance decreases with increase in the scan rate from 2 to 100 mV s^{-1}.

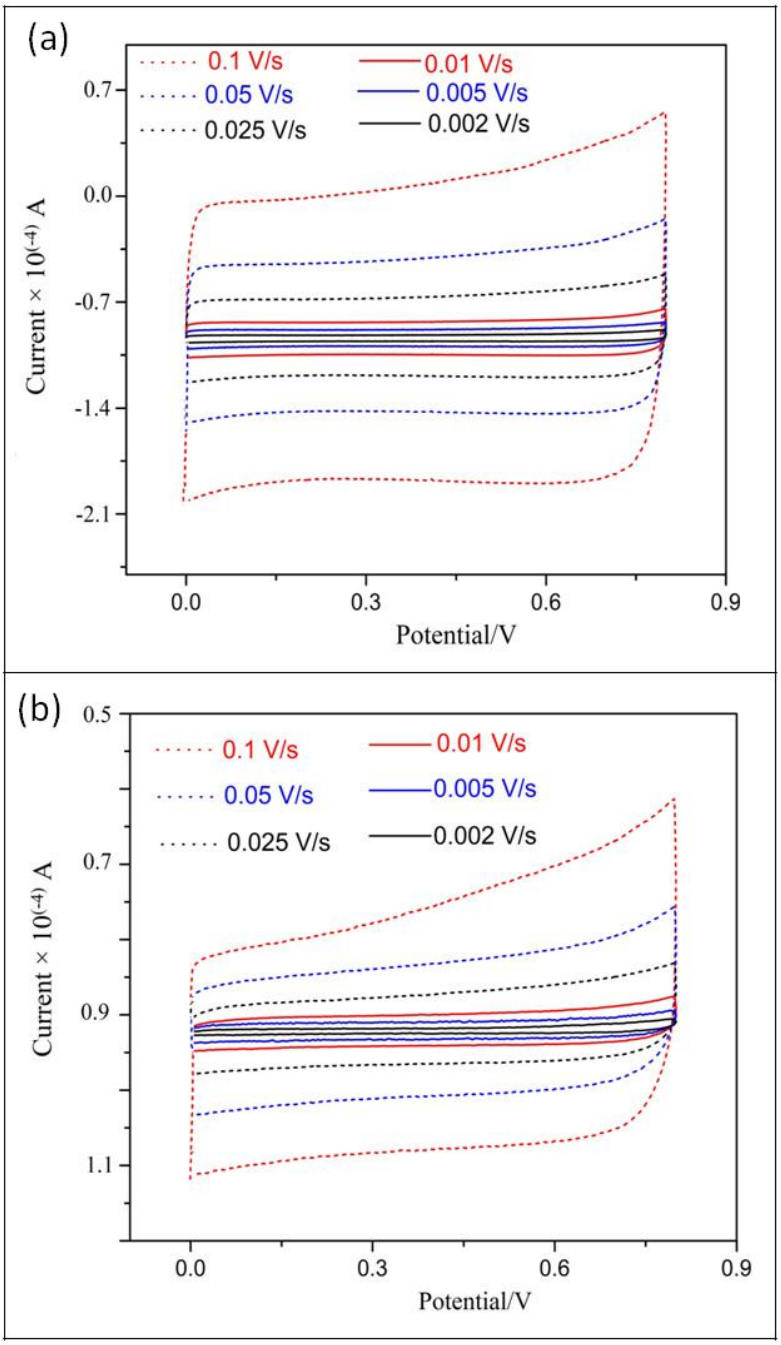

Fig. 5.3: Cyclic voltammetry profiles of commercially available carbons at different scan rates recorded in 0.5 M Na_2SO_4 (a) SWCNT (b) VulcanXC72R.

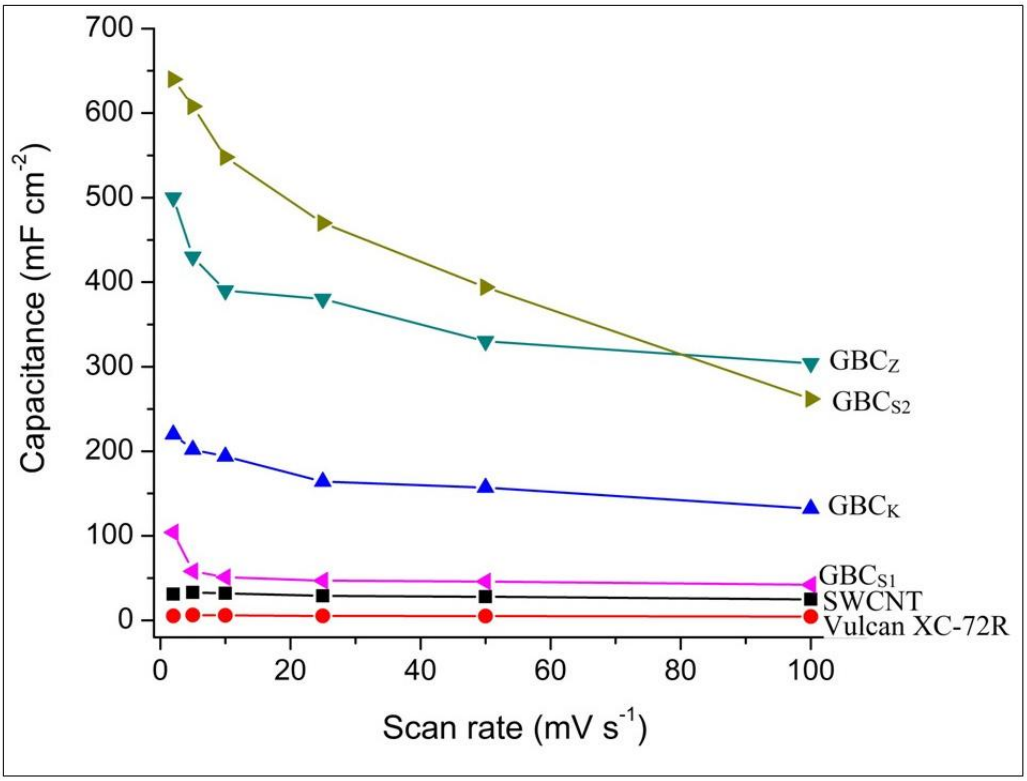

Fig. 5.4: Plot of capacitance as a function of scan rate.

(b) Capacitance of OMS-2 and Fe-OMS-2

Among different transition metal oxides examined for capacitance, RuO_2 is known to exhibit high charge storage capacity with exceptional cyclability as well [7]. At the same time RuO_2 is known to be too costly and toxic. MnO_2 on the other hand is a promising pseudocapacitance material which is also non toxic and also affordable. The present investigation concerns with determination of capacitance of OMS-2 form of MnO_2 and Fe doped OMS-2 and its composites with the synthesized glycerol based carbons. Fig. 5.5 gives cyclic voltammograms of OMS-2 and Fe doped OMS-2 in 0.5 M Na_2SO_4 at a scan rate of 2 mV s^{-1}. Table 5.2 gives the corresponding capacitance values in relation to their surface areas.

The pure or undoped OMS-2 possesses higher surface area of ~137 m^2 g^{-1}. The presence of Fe^{3+} in OMS-2 caused decrease in surface area. As the Fe concentration increased the surface area was observed to progressively decrease. There was a correlation between capacitance and surface area of the metal oxides examined. Undoped sample with higher surface area showed higher capacitance.

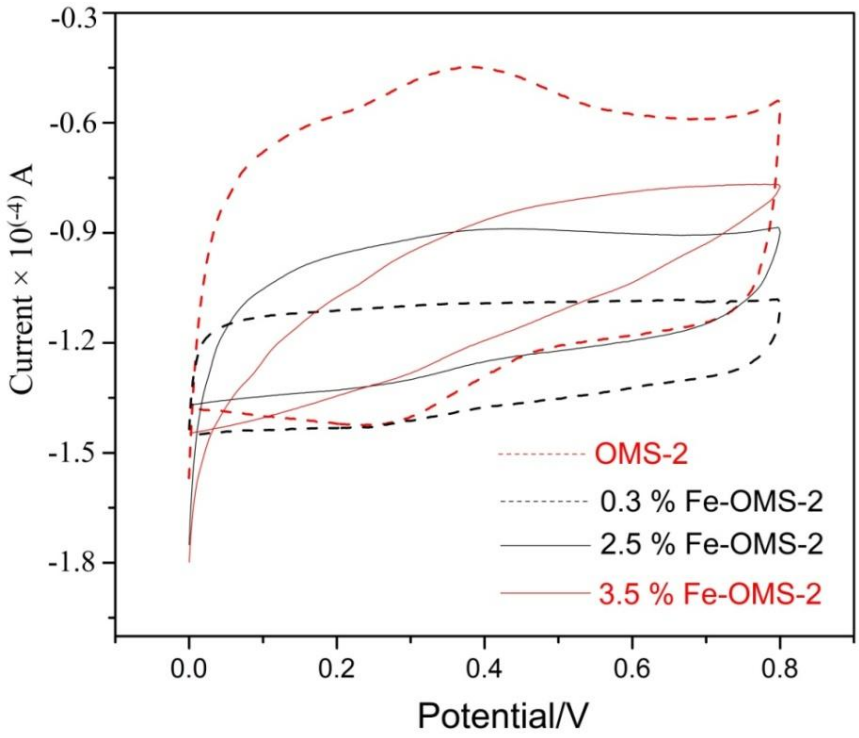

Fig. 5.5: Cyclic voltammograms of OMS-2 and Fe-OMS-2 in 0.5 M Na_2SO_4 at a scan rate of 2 mV s^{-1}.

Table 5.2: BET surface area and Specific capacitance of OMS-2 and Fe doped OMS-2.

Sample	**S_{BET} (m^2 g^{-1})**	**Capacitance (mF cm^{-2})**
OMS-2	137	280
0.3 % Fe-OMS-2	123	260
2.5 % Fe-OMS-2	94	245
3.5 % Fe-OMS-2	90	190

(c) Capacitance of the GBC-OMS-2 composites

As seen in Table 5.1, the GBCs showed higher capacitance than the commercial carbons. The high capacitance values > 500 mF cm^{-2} were shown by GBC_{S2} and GBC_Z. This capacitance is EDLC or electrical double layer capacitance. It is known that EDLC can be enhanced when coupled with pseudocapacitance; the latter being provided by transition metal oxides having variable reversible oxidation state during charge discharge process. Hence the composite was prepared using OMS-2 which is in fact a polymorphic form of MnO_2 known as α-MnO_2. Its reversible oxidation states are Mn^{3+} and Mn^{4+}. GBC_Z having a high capacitance value of 500 mF cm^{-2} was chosen for initial optimization of the ratio of the two components GBC_Z and OMS-2. Individually their capacitance values were 500 mF cm^{-2} and 180 mF cm^{-2} respectively. A suitable composition of the two was expected to give an enhanced effect.

A series of composites were prepared as follows

Components	Ratio of the components (OMS-2 and GBCz)			
OMS-2 (%)	50	70	80	90
GBC_Z (%)	50	30	20	10
Capacitance of the GBC_Z-OMS-2 composite (mF cm^{-2})	164	108	82	52

It was seen that as percentage of OMS-2 was increased in the composite from 50 % to 90 % its capacitance performance lowers and it dropped from 164 mF cm^{-2} to 52 mF cm^{-2}. This must be due to blocking of accessible sites of GBC_Z by OMS-2. It was thus observed that the capacitance of the composites has dropped to low values. Not only OMS-2 did not enhance the capacitance, it was observed to be detrimental in the chosen composition range.

Further optimization was carried out using much lower quantities of OMS-2 as shown below

Components	Ratio of the components (OMS-2 and GBCz)			
OMS-2 (%)	0.5	1.0	2.0	3.0
GBC_Z (%)	99.5	99	98	97
Capacitance of the GBC_Z-OMS-2 composite (mF cm^{-2})	620	675	325	223

Thus 1 % OMS-2 in the composite gave optimum capacitance of 675 mF cm^{-2}. It was thus clear that capacitance enhancement occurs when OMS-2 is in a very low proportion. Best results were obtained when proportion of OMS-2 was ~ 1%. The CV profiles of some of the composites are given in Fig. 5.6 and the results of optimization are summarized in Fig. 5.7. The ratio of 1:99 for OMS-2:GBC^s composite thus offer higher capacitance compared to all other ratios examined. The conductive matrix provided by carbon for OMS-2 in the composite helps to improve the conductivity of the overall composites. But excess surface functional groups could lower the conductivity of the carbon.

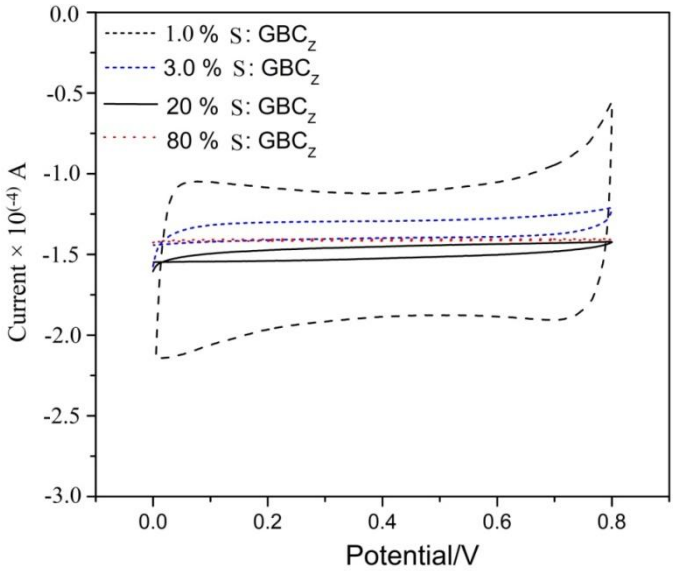

Fig. 5.6: Cyclic voltammetry profile of OMS-2 and GBC_Z composites at a scan rate of 2 mV s^{-1}.

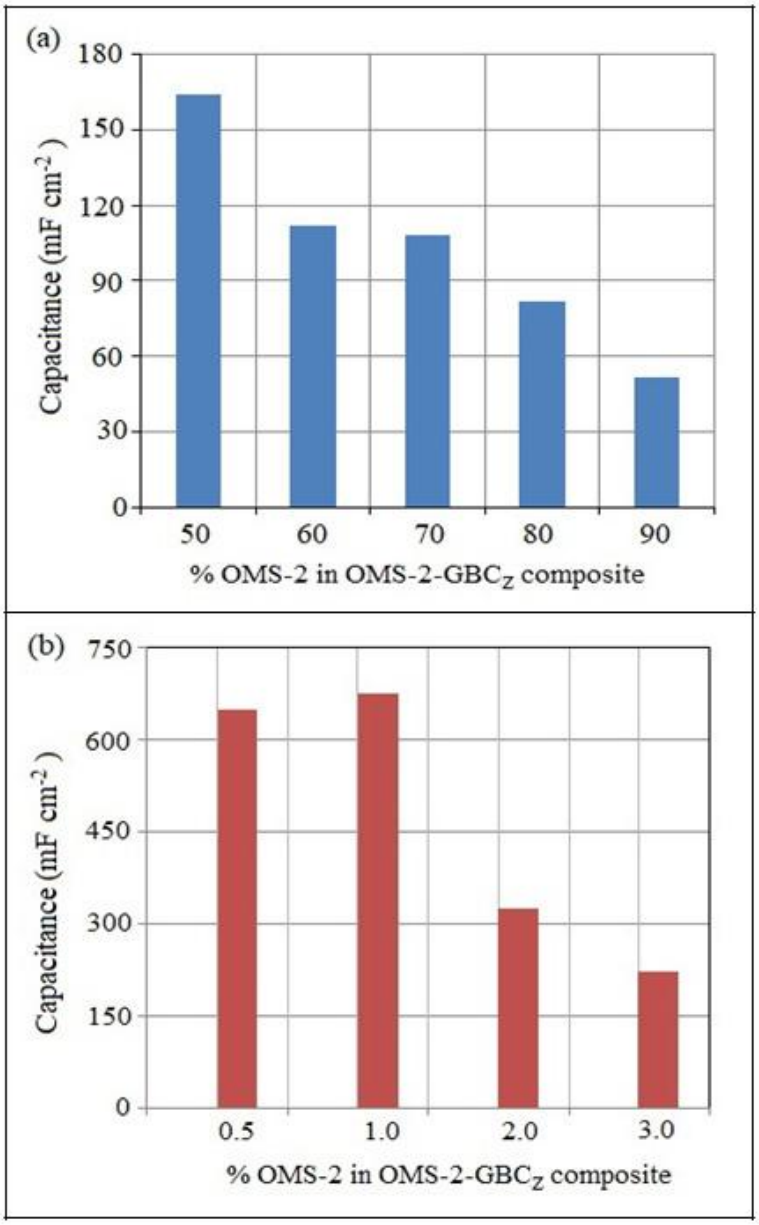

Fig. 5.7: Plot of capacitance versus % OMS-2 in OMS-2-GBC_Z composites.

(a) decrease in capacitance as % MnO2 increase

(b) determination of optimum composition to get maximum capacitance for the composite.

Similar results were obtained for other GBC-OMS-2 composites as shown in Table 5.3.

Table 5.3: Enhancement in capacitance of the GBC carbons when made into a composite with 1% OMS-2.

Carbon sample	**GBC_{S2}**	**GBC_{Z}**	**GBC_{K}**	**GBC_{S1}**
Capacitance (mF cm^{-2})	640	500	220	104
Capacitance of composites with 1% OMS-2 (mF cm^{-2})	1320	675	300	280

*Capacitance of OMS-2 alone is 280 mF cm^{-2}.

Thus an use of mere 1 % OMS-2 resulted in large capacitance particularly when the carbons were GBC_{S2} and GBC_{S1}. The capacitance value of 1320 mF cm^{-2} for the composite GBC_{S2}-OMS-2 was remarkably high. This synergistic interaction is believed to be due to cooperative redox behavior of surface functional groups and reversible conversion of Mn^{4+} to Mn^{3+} and back to Mn^{4+} during charge-discharge process. This is in addition to the electrical double layer capacitance of the carbons.

5.2 ELECTROCATALYSIS OF METHANOL OXIDATION REACTION (MOR)

Fuel cells are expected to significantly mitigate demand for fossil fuels. In order for this to materialize it is important that the research shall focus on making fuel cells economical. Pt on carbon (Pt_C) is a well known electro-catalyst used in fuel cells at it shows very high activity. Research shows that Ru together with Pt shows excellent activity towards alcohol oxidation reaction. In addition to different bimetallic or trimetallic catalyst combinations, various carbon materials as catalyst supports are also explored for their catalytic activity. The type and nature of carbon material employed, has a remarkable influence on electrocatalytic activity.

The present investigation deals with

i. Synthesis of Ru metal catalyst supported on glycerol based carbons Ru-GBC^s
ii. Preparation of bimetallic catalysts Pt_C-Ru(GBC^s)
iii. Preparation of bi and tri components catalysts using OMS-2
iv. Evaluation of the synthesized catalysts for electro-oxidation of methanol.

5.2.1 Experimental details

Two techniques namely cyclic voltammetry and Tafel Polarisation were employed to evaluate activity of the catalysts and their composites.

i. Cyclic voltammetry was performed using CH instrument (Instrument Model: CHI6107D). In a three electrode assembly, Pt wire was used as a counter electrode and Ag/AgCl as reference electrode. The working electrode was prepared by loading of the catalysts on glassy carbon. The ink of the catalyst under study was first prepared as follows: 60 mg of catalyst component or 30-30

mg of each two components or 20-20-20 mg each of three components were intimately mixed in presence of required amount of isopropyl alcohol. Then a few drops of Nafion solution were added to form a homogenous mixture (Nafion solution was ~5% in a mixture of lower aliphatic alcohols and water). The ink was then applied to glassy carbon surface which was previously polished using alumina powder. The electrode was then allowed to dry overnight at room temperature. The tests were carried out in 0.5 M H_2SO_4 and 1 M ethanol or methanol as the case may be.

ii. Tafel polarization studies were carried out in a separate three electrode assembly. The reference electrode used was saturated calomel electrode (SCE having potential 0.242 Volts v/s SHE) and Pt was a counter electrode. The working electrode was prepared by applying the catalyst ink to Toray carbon paper of 1 cm × 1 cm dimension. The ink was prepared by first dispersing the catalyst powder in isopropanol for few minutes followed by addition of Nafion solution. The electrolyte was 0.5 M H_2SO_4 and 1 M methanol or ethanol.

Synthesis of 5 % Ru on glycerol based carbons and their characterization

$RuCl_3.xH_2O$ is used as a Ru metal source and glycerol based carbons as a support material for preparation of Ru/GBC catalysts. 1 g of carbon support was dispersed in an aqueous solution of Ru (III) ions. Ru (III) solution was prepared by dissolving 0.13 g of $RuCl_3.xH_2O$ in H_2O. Slurry was obtained by stirring the above solution for ~1 h. The KOH solution was used as stabilizing agent with OH^-/Ru molar ratio of 8 [9]. 0.15 M $NaBH_4$ was added dropwise to the above mixture under continuous stirring. The final product was filtered and washed till the filtrate was neutral and then dried at 70 ^oC.

5 % Ru on VulcanXC72R was also synthesized under similar condition.

The percent Ru in the synthesized Ru_C samples were ~ 3% obtained from ICP-AES technique for % metal determination. Prepared Ru/Cs were further characterized by XRD, BET surface area and SEM. X-ray diffraction patterns are presented in Fig. 5.8.

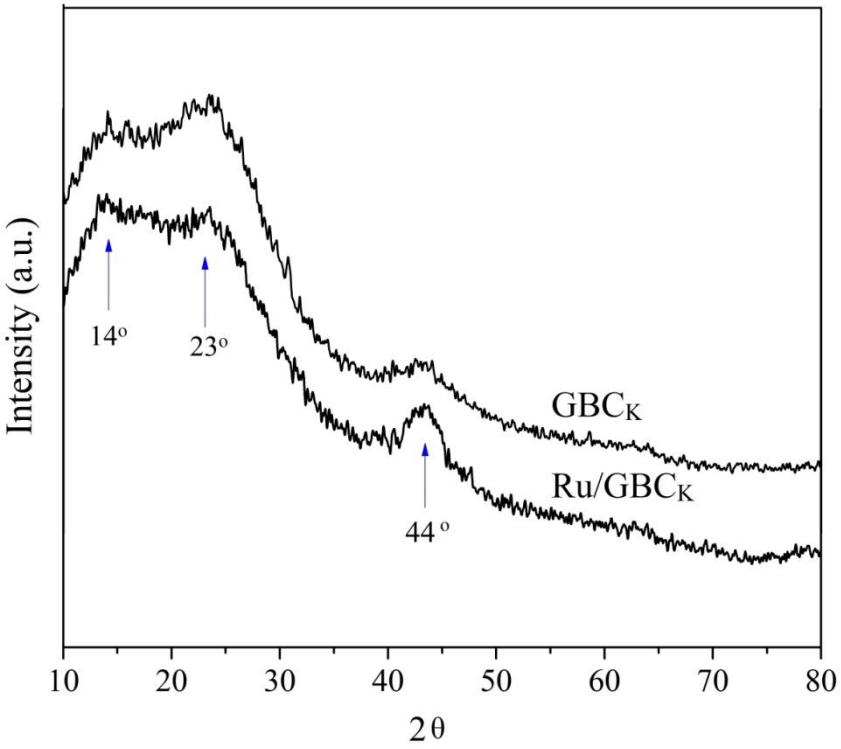

Fig. 5.8: X-ray diffraction patterns of GBC_K and $Ru_{GBCK.}$

Fig. 5.8 displays powder XRD pattern of the GBC_K and Ru/GBC_K catalyst. XRD pattern of GBC_K has been earlier discussed in Chapter 3. Accordingly the peaks centered at ~ 14^o and 23^o in the 2θ region of 10^o – 30^o were assigned to activated carbon GBC_K. In addition to these reflection planes, the peak at ~ 43^o is also related to reflections from (100) planes in carbon structure. In comparison to GBC_K, Ru/GBC_K shows very sharp peak at ~ 44^o as the peak is also associated with Ru (PDF-2, Card 00-006-0663, ICCD, 2004) [10-11].

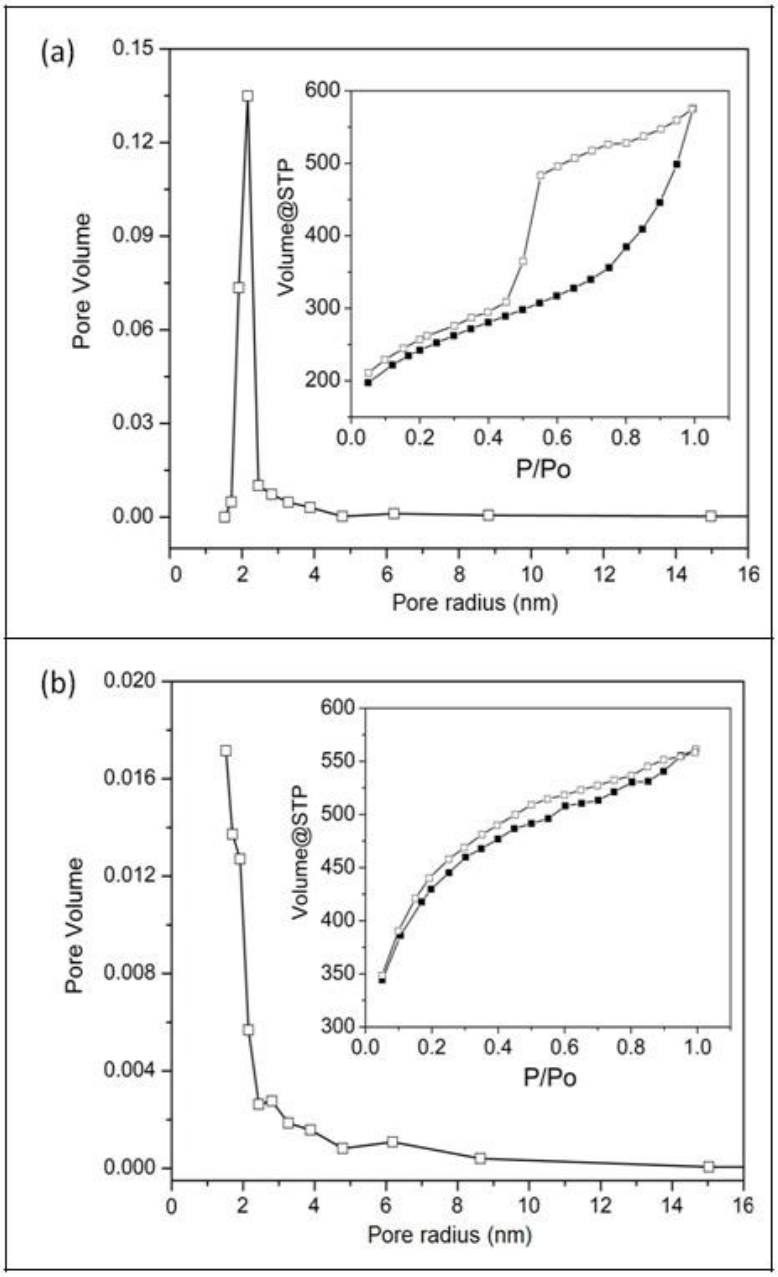

Fig. 5.9: N_2 adsorption desorption isotherm and pore size distribution profiles (a) Ru/GBC_K (b) Ru/GBC_Z

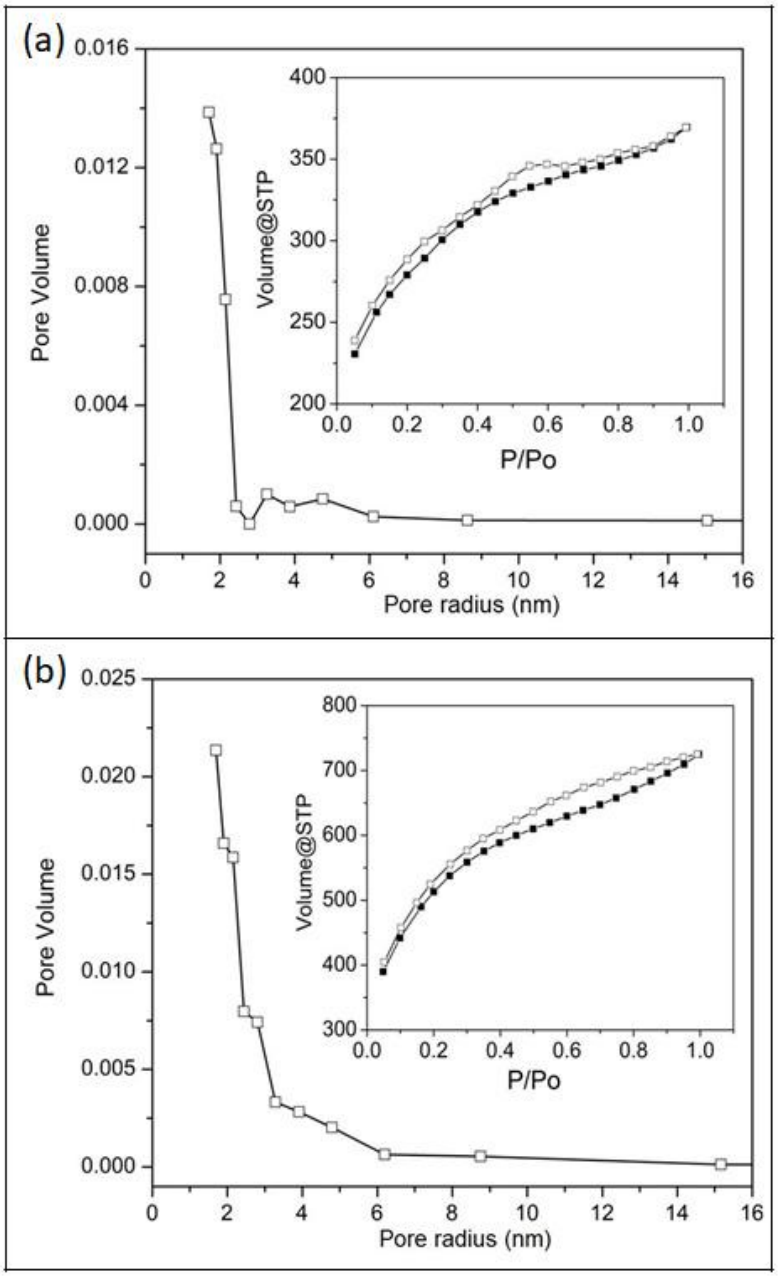

Fig. 5.10: N_2 adsorption desorption isotherm and pore size distribution profiles (a) Ru/GBC_{S1} (b) Ru/GBC_{S2}.

Table 5.4 Surface area, porosity data of synthesized Ru/GBCs samples.

Sr. No.	Catalysts	Surface area ($m^2 g^{-1}$)	Pore volume ($cm^3 g^{-1}$)	Average pore size (nm)
1	GBC_K	1653	1.76	2.13
	Ru-GBC_K	869	0.89	2.05
2	GBC_Z	1577	0.96	1.67
	Ru-GBC_Z	1150	0.80	1.12
3	GBC_{S1}	1069	0.60	1.13
	Ru-GBC_{S1}	1017	0.57	1.14
4	GBC_{S2}	2289	1.31	1.14
	Ru-GBC_{S2}	1856	1.12	1.21

Fig. 5.9 and 5.10 gives N_2 adsorption desorption profiles of GBC carbons following modification with Ru. The corresponding profiles of unmodified GBCs were earlier presented in Fig. 3.6 and Fig. 3.11. A comparison of Fig 5.9 and Fig 5.10 with Fig 3.6 and Fig. 3.11 would suggest no significant alteration in overall shapes of the profiles in presence of Ru. N_2 adsorption desorption profiles closely resemble in shape with the respective activated glycerol carbons. However the volume of maximum gas adsorbed by the samples at high relative pressures P/P_o decreases in the Ru-GBC samples. Table 5.4 highlights decrease in surface area following Ru insertion. Relatively lower surface area was observed after insertion of Ru in GBC_K, which is indicative of incorporation of Ru in the carbon. Thus the surface area decreases considerably from 1653 $m^2 g^{-1}$ for pure or unmodified GBC_K to 869 $m^2 g^{-1}$ for Ru/GBC_K. SEM images of Ru/GBC_K, Ru/GBC_Z, Ru/GBC_{S1} and Ru/GBC_{S2} are given in Fig. 5.11.

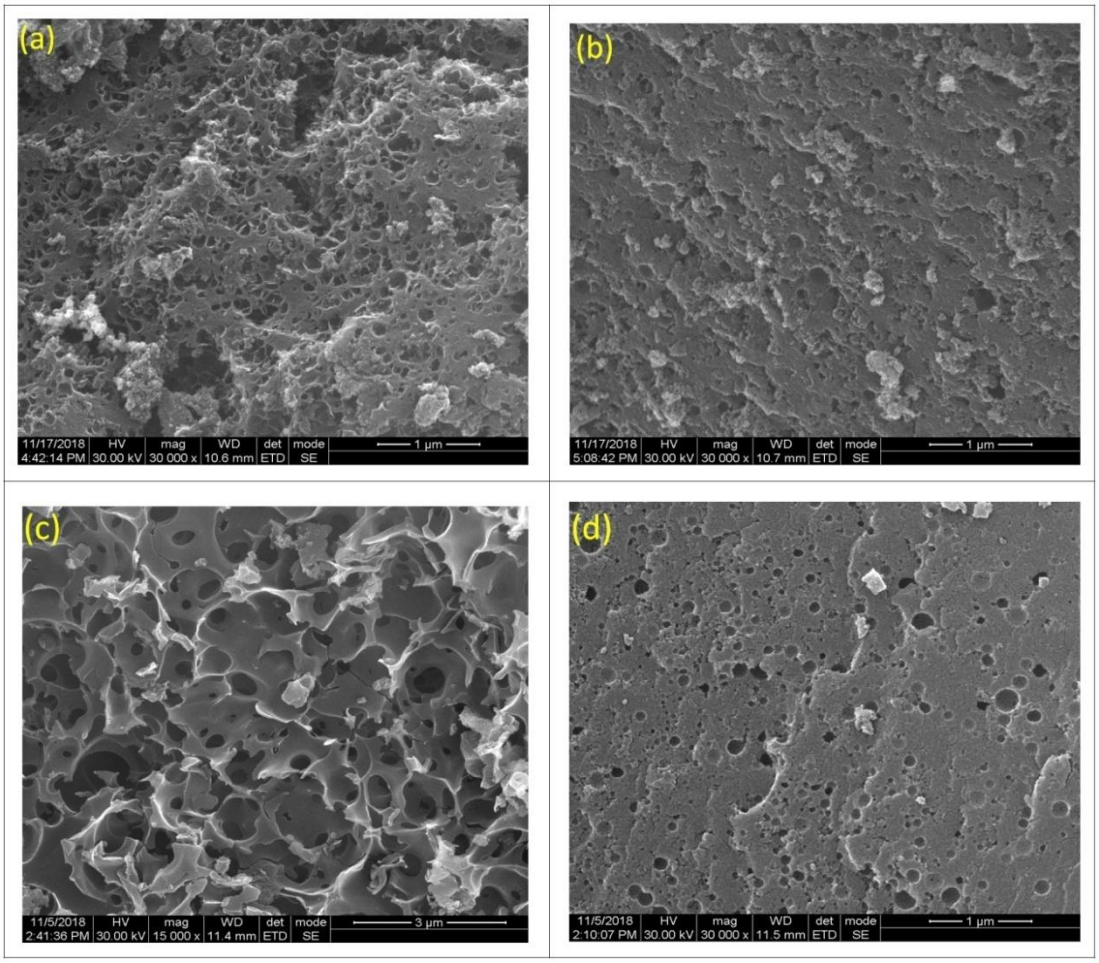

Fig. 5.11: FE-SEM (a) Ru/GBC_K (b) Ru/GBC_Z (c) Ru/GBC_{S1} (d) Ru/GBC_{S2}.

5.2.2 Results and discussion

Electrocatalytic activity of Ru supported carbons for MOR

Fig. 5.12 displays comparative Tafel plots for Ru/C samples for methanol oxidation reaction carried out in acidic medium. Activity of the catalysts is extracted from the Tafel plots and expressed in terms of i_{100} i. e. current produced at an overpotential of 100 mV. These values are presented in Table 5.5 in relation to $Ru_{VulcanXC72R}$ and Ru_C. $Ru_{VulcanXC72R}$ was prepared to compare the activity of the glycerol based carbons with a standard carbon support. Similarly commercially available Ru_C obtained from Arora

Matthey, Kolkata (India) was also studied. Ru_{GBCK} showed a significantly higher activity as compared to other Ru supported carbons like GBC_Z, GBC_{S1} and GBC_{S2}.

Thus a current of 430 µA was observed with Ru_{GBCK} as compared to current values in the range 50 – 100 µA for the other carbons including Vulcan XC72R. Although less it was comparable to the other commercial carbon Ru_C. Thus GBC_K carbon produced in this work by a simple synthesis procedure could be an effective and economical alternative support for electrocatalysts in fuel cells. This enhanced activity with GBC_K could be related to its structural properties. GBC_K possesses high mesopore volume (Table 5.1) in comparison to other GBCs. Its mesopore volume was 1.20 $cm^3\ g^{-1}$ which was much higher as compared to values < 0.54 $cm^3\ g^{-1}$ for other carbon samples, thus investigated for methanol electro-oxidation reaction. Thus GBC_K behaves as a more favorable support for alcohol electro-oxidation. Its suitability can be related to the ease of mass transfer ascribed to the specific structure of mesoporous carbon supports [12-13]. Additionally the presence of oxygen functionalities on the carbon surface also contribute to better diffusion of methanol via mesopores as they provide superior wettability in aqueous electrolyte in comparison to non-functionalized carbon supports. Thus Carmo et al. [14-15] concluded that HNO_3/H_2SO_4 oxidized carbon VulcanXC72R showed enhanced activity for methanol oxidation.

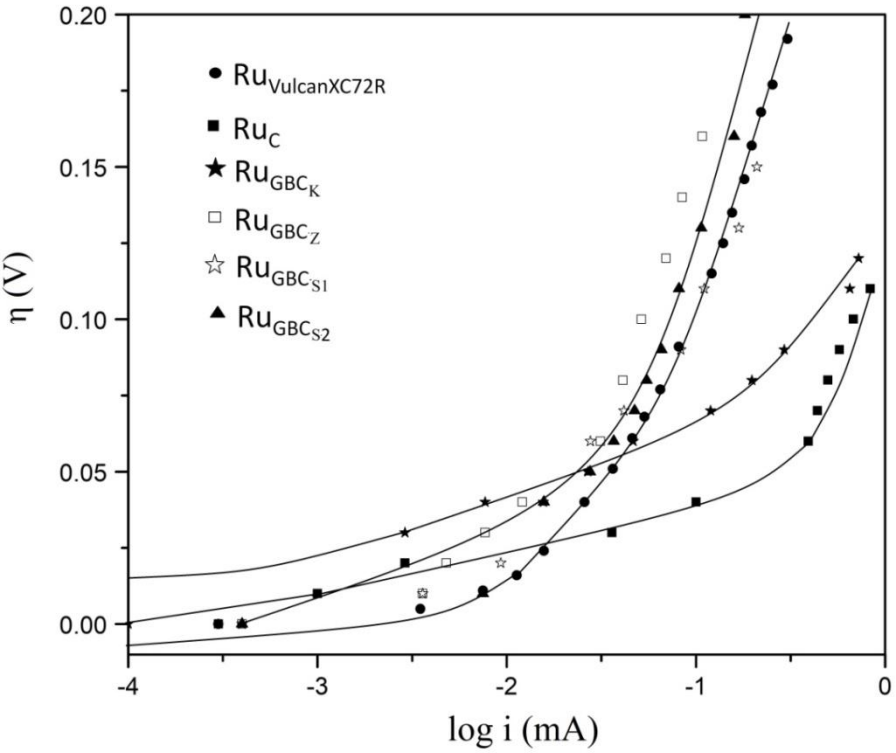

Fig. 5.12: Tafel polarization studies for methanol oxidation reaction in 0.5 M H_2SO_4 on GBC supported Ruthenium catalyst.

Table 5.5: Current produced i_{100} in μ amps, at overpotential of 100 millivolts for Ru/Cs and its composites with Pt/C catalysts.

Catalyst	**i_{100} (μA)**		**Catalyst**	**i_{100} (μA)**
$Ru_{VulcanXC72R}$	94		Pt_C	450
Ru_C (commercial sample)	661		$Pt_C – Ru_C$	830
Ru_{GBCK}	430		Pt_C - Ru_{GBCK}	925
Ru_{GBCZ}	50		$Pt_C – Ru_{GBCZ}$	830
Ru_{GBCS1}	94		$Pt_C – Ru_{GBCS1}$	45
Ru_{GBCS2}	73		$Pt_C – Ru_{GBCS2}$	570

Electrocatalytic activity of bimetallic catalysts

The bimetallic PtRu catalyst is known to be efficient catalyst for methanol electro-oxidation. It is due to better hydrophilicity of Ru as compared to Pt. Commercially available 10 % Pt/C (obtained from Sigma Aldrich) was initially checked for its electrocatalytic activity for methanol oxidation. It showed a significant activity by producing a current of 450 µ amps. Hence it was chosen to obtain bimetallic catalyst with the synthesized Ru/GBCs. Thus composite catalysts were prepared by homogenizing 10 % Pt_C with the synthesized Ru/GBCs in 1:1 ratio.

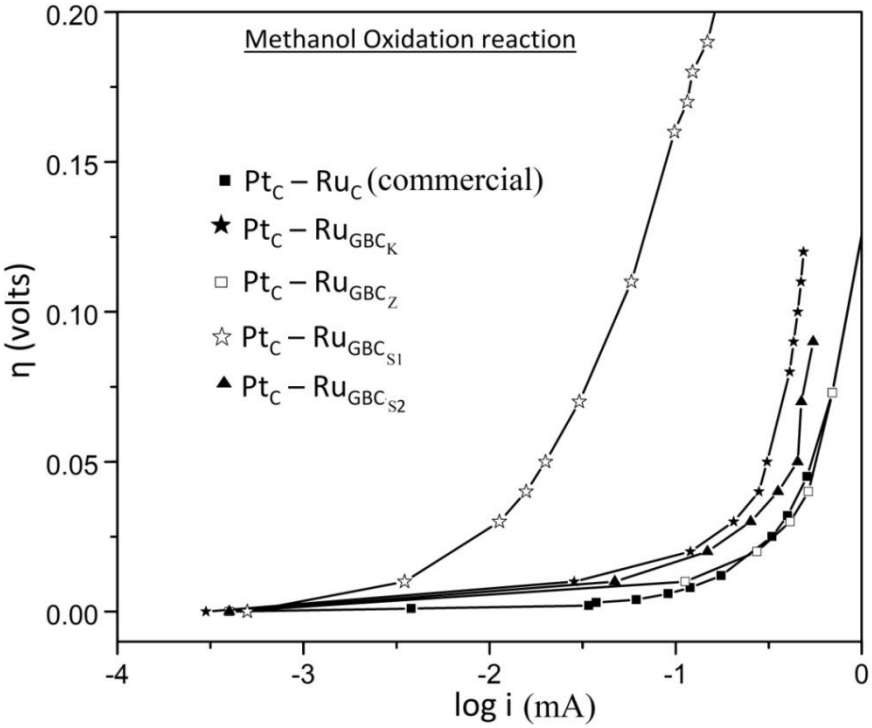

Fig. 5.13: Tafel plots of bimetallic composites studied for methanol electro-oxidation reaction in 0.5 M H_2SO_4.

From the i_{100} values derived from Fig. 5.13 (Table 5.5) it can be observed that the bimetallic catalysts studied showed improved catalytic activity compared to the individual catalysts, due to synergistic interaction of the two components used. Thus better results were obtained with the Pt/C and Ru/GBC_K combination. It can be seen that

a current of 925 µ amps produced by this catalyst with GBC_K was significantly higher as compared to the bimetallic catalysts prepared using other GBC supports. This once again underlines the importance of the glycerol based carbon support GBC_K prepared in this investigation and highlights its suitability as a promising alternative support in electrocatalytic oxidation of methanol.

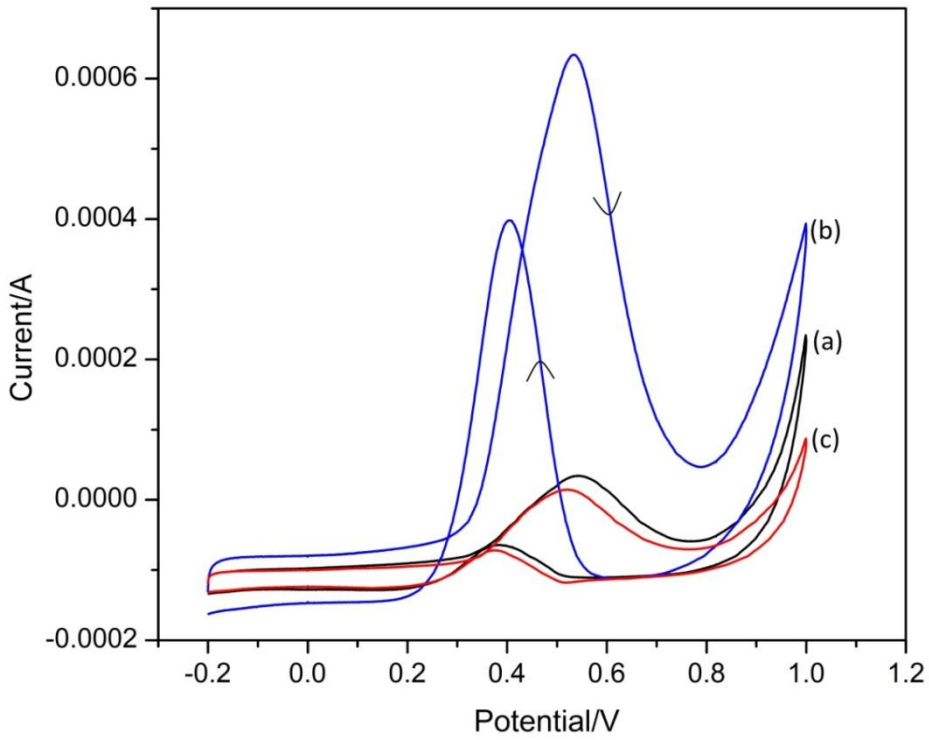

Fig. 5.14: The cyclic voltammetry profiles of the bimetallic catalyst composites in 0.5 M H_2SO_4 solution and 1 M methanol at a scan rate of 2 mV s^{-1}. (a) Pt_C - Ru_C (b) Pt_C - Ru_{GBCK} (c) Pt_C - Ru_{GBCZ} electrodes.

Table 5.6: Parameters from cyclic voltammograms of methanol electro-oxidation reaction on the bimetallic catalysts investigated.

Catalysts	**Peak potentials**		**Current values**		I_f / I_b
	forward scan E_f (V)	reverse scan E_b (V)	$I_f \times 10^{(-4)}$ (A)	$I_b \times 10^{(-4)}$ (A)	
Pt_C-Ru_C	0.54	0.38	0.34	0.65	0.52
Pt_C-Ru_{GBCK}	0.53	0.40	6.34	3.98	1.59
Pt_C-Ru_{GBCZ}	0.52	0.37	0.14	0.72	0.19

Cyclic voltammetry (CV) also provides a simple method to evaluate relative electrocatalytic activity of the samples. In the forward (or +ve going scan) methanol undergoes oxidation at the electrocatalysts surface forming intermediates. The forward current thus observed is I_f. In the reverse scan, methanolic residues which did not desorbs from the catalyst surface get reoxidised and generate the observed current I_b. The catalyst efficiency can thus be represented as I_f/I_b. A good electrocatalysts is the one in which $I_f >> I_b$. Further, the potential at which methanol is oxidized is also crucial. A good electrocatalyst induces oxidation of methanol at less +ve potential, implying more facile oxidation of methanol. CV profiles for methanol oxidation reaction in 0.5 M H_2SO_4 solution are presented in Fig. 5.14. The parameters extracted from these profiles are summarized in Table 5.6.

The CV for Pt_C - Ru_C (commercial sample) shows methanol oxidation peak in forward scan at 0.54 V and reverse peak is observed at 0.38 V which is mainly due to oxidation of intermediate species adsorbed on the surface of the catalysts during the forward methanol oxidation reaction. In forward scan Pt_C-Ru_{GBC} composites also show both the peaks due to methanol oxidation process. Comparatively methanol oxidation by Pt_C-Ru_{GBCZ} and Pt_C-Ru_{GBCK} catalysts occur at lower potentials than the commercial sample composite. Thus GBC catalysts can be considered good supports for noble metal catalysts in methanol oxidation reaction.

The peak current density in the forward scan serves as benchmark for the catalytic activity of Pt nanoparticles during methanol dehydrogenation. The peak current density on Pt_C – Ru_{GBCK} was enhanced compared with Pt_C – Ru_C indicating GBC_K as a good support for noble metal catalysts. Thus the eak current density of the synthesized electrocatalyst Pt_C – Ru_{GBCK} was 18.5 times that on Pt_C – Ru_C which has both

commercial catalyst components. The overall catalytic efficiency depends on the values of I_f/I_b. Thus the bimetallic catalyst Pt_C-Ru_{GBCK} which shows I_f/I_b value of 1.59 is three times higher than the corresponding value show by the catalyst Pt_C-Ru_C whose value was merely 0.52 (Table 5.6). The Pt-Ru catalyst synthesized in this work using GBCs generally showed significantly higher activity for electro-oxidation of methanol.

5.3 ELECTROCATALYSIS OF ETHANOL OXIDATION REACTION (EOR)

Alcohols like methanol and ethanol with power densities close to 6 or 8 k Wh kg^{-1} [17] are considered the most appropriate fuels for direct alcohol fuel cells ($DAFC^s$). However the efficiency and cost of these fuel cells are largely influenced by the activity and stability of the electrocatalysts used. Though costly, noble metal catalysts continue to be more effective and have therefore been investigated extensively by aiming to reduce the quantities used. Metal nanoparticle carbon supported catalysts are believed to be the most promising materials for efficient and stable catalysis in fuel cells. In the present work, Pt-Ru-Mn(OMS-2)/C catalyst composition is investigated for anodic oxidation reaction of ethanol.

The activity of Ru and Pt-Ru catalysts supported on various carbons

(a) Tafel polarization studies

The Ru catalysts supported on GBCs were investigated for electro-oxidation of ethanol. Fig. 5.15 gives various Tafel plots. The corresponding current values extracted from these plots at an overpotential of 100 mV are presented in Table 5.7.

All the Ruthenium-GBC^s showed significant activity for EOR. They showed currents in the range 50 – 175 µ amps. In comparison, the Ru modified commercial carbon sample $Ru_{Vulcan\ XC72R}$ showed very poor activity (current of merely 17 µ amps) towards electro-oxidation of ethanol. This improved effect for Ru/GBCs is attributed to the interplay of several favorable factors such as higher surface area, well developed pore structure and surface oxygen functionalities present in glycerol based carbons.

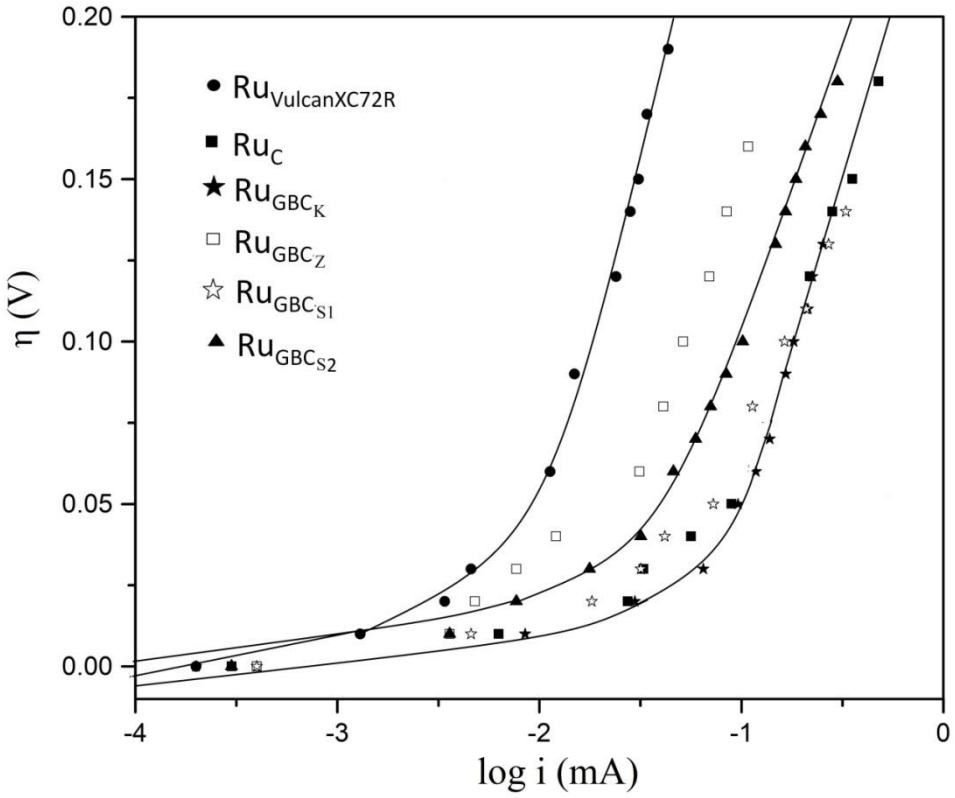

Fig. 5.15: Tafel polarization studies for ethanol oxidation reaction using Ru on various samples in acidic medium.

Table 5.7: Current produced in μ amps, at overpotential of 100 mV for different catalysts for ethanol oxidation reaction.

Carbon supported Ru metal catalyst	Electrocatalytic activity i_{100} (μ A)		Pt-Ru bimetallic catalysts	Electrocatalytic activity i_{100} (μ A)
Ru_C	170		$Pt_C – Ru_C$	340
$Ru_{VulcanXC72R}$	17		Pt_C - Ru_{GBCK}	532
Ru_{GBCK}	175		$Pt_C – Ru_{GBCZ}$	225
Ru_{GBCZ}	50		$Pt_C – Ru_{GBCS1}$	160
Ru_{GBCS1}	160		$Pt_C – Ru_{GBCS2}$	100
Ru_{GBCS2}	100			

* $\mathbf{i_{100}}$ for Pt_C is 8 μA

The Ru_{GBCK} catalyst in particular continues to show superior performance than the other catalysts. It was earlier seen (Table 5.5) that Ru_{GBCK} also had higher activity for MOR among the GBCs. Thus for ethanol oxidation on Ru_{GBCK}, a current of 175 µ amps was observed which increased to 532 µ amps when combined in the bimetallic catalyst Pt_C-Ru_{GBCK}. The other bimetallic catalysts showed much lower activity with currents less than 350 µ amps.

In glycerol based carbons like GBC_Z, GBC_{S1} and GBC_{S2} maximum pore volume is contributed by micropores (Table 5.1). Therefore their efficiency decreases as micropores are too small and create diffusion limitation during electro-oxidation of alcohol. Conversely the presence of larger mesopores would facilitate diffusion pathways for the reaction intermediates. Thus if we compare porosity of the similar surface area samples GBC_K (~1650 $m^2\ g^{-1}$) and GBC_Z (~1580 $m^2\ g^{-1}$), the corresponding mesopore volumes were 1.20 and 0.50 $cm^3\ g^{-1}$. Accordingly, their currents observed during EOR were 175 and 50 µ amps under the same experimental condition. These results underline the importance of surface area and mesoporosity of the carbon supports for the electrocatalysis.

(b) Cyclic voltammetry studies

Fig. 5.16 gives cyclic voltammogram for ethanol oxidation when Pt and Pt-Ru bimetallic catalysts were used. It can be seen that the Pt catalyst apparently shows much higher currents at potentials -0.09 V and 1.2 V as compared to Pt-Ru catalyst. It also shows a small current at a´ and a peak c´ in the reverse scan. The peaks at -0.09 V and 1.2 V are due to hydrogen and oxygen evolution associated with decomposition of water. Thus the Pt catalyst was very effective in water electrolysis. It was not as effective for ethanol electro-oxidation as evident from the small current produced at a´. on the other hand, the Pt-Ru catalyst didn't show any significant currents at x and y, thus implying the relative inactivity of the bimetallic catalyst for water decomposition. However this catalyst showed significantly well resolved peaks at the potentials at 'a' and 'b' in the forward scan and 'c' in the reverse scan. These peaks are due to ethanol oxidation, thus implying superior activity of Pt-Ru bimetallic catalysts for ethanol oxidation. This result is in agreement with Tafel polarization results wherein relative i_{100} current value for Pt_C and Pt_C-Ru_{GBCK} catalysts were 8 and 532 μ amps respectively.

Fig. 5.17 shows amplified version of CV profile of Pt_C-Ru_{GBCK} for the sake of comparison with Pt_C-Ru_C bimetallic catalysts prepared using commercial Ruthenium catalyst. It can be seen that the ethanol oxidation peaks 'a' and 'b' were not well resolved and were observed at lower potentials between 0.30 – 0.50 volt. On the other hand the bimetallic catalyst prepared from the synthesized Ru catalyst i. e. Pt_C-Ru_{GBCK} showed peaks at relatively higher potentials with much larger currents. These results are also in agreement with Tafel polarization studies, wherein i_{100} currents for Pt_C-Ru_C and Pt_C-Ru_{GBCK} were 340 and 532 μ amps respectively as shown in Table 5.7. Thus the

synthesized Ru_{GBCK} catalyst gave superior performance as compared to the corresponding commercial catalyst.

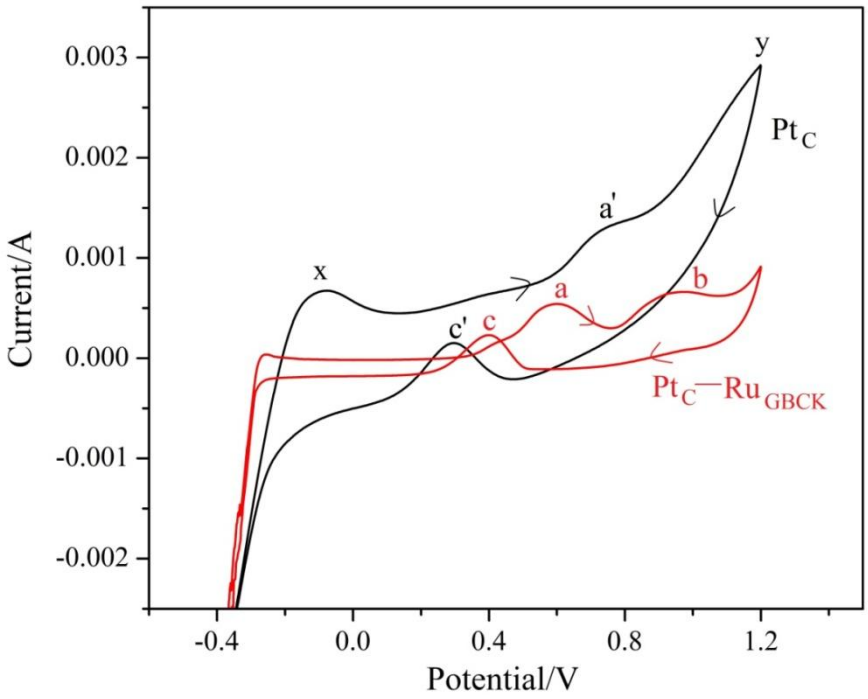

Fig. 5.16: The CV profiles of Pt_C and Pt_C - Ru_{GBCK} electrodes in 0.5 M H_2SO_4 solution and 1 M ethanol at a scan rate of 2 mV s^{-1}.

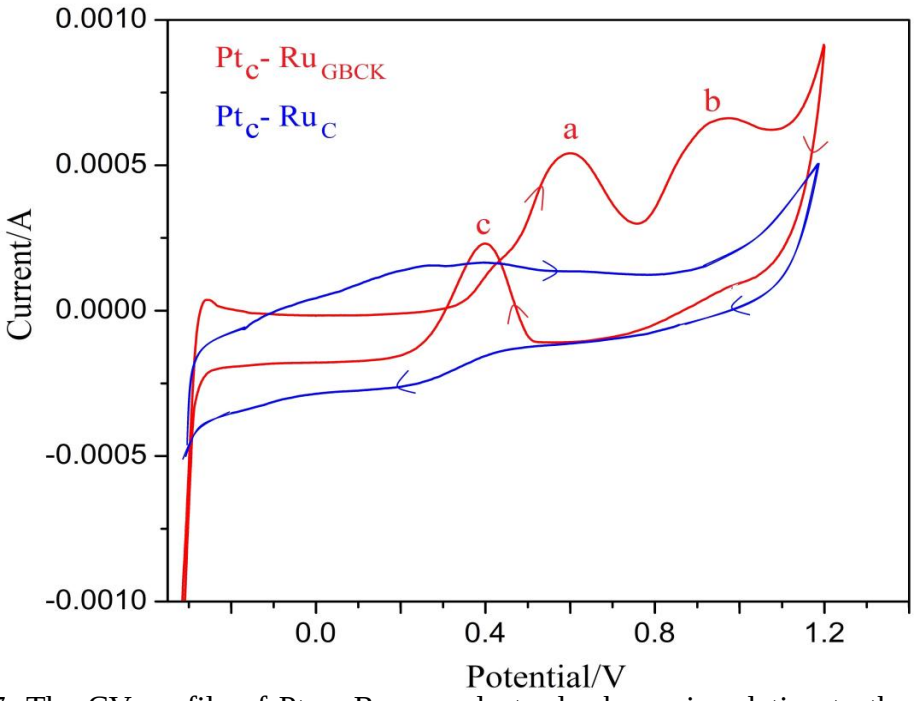

Fig. 5.17: The CV profile of Pt_C - Ru_{GBCK} electrode shown in relation to the Pt_C-Ru_C electrocatalyst in 0.5 M H_2SO_4 solution and 1 M ethanol at a scan rate of 2 mV s^{-1}.

Activity of the catalysts in presence of Mn OMS-2

Ethanol electro-oxidation using Mn OMS-2 as a component of the catalyst composite was investigated further. Catalysts tested were two and three component systems such as

i Ru_C –S

ii Ru_{GBCK} -S

iii Pt_C-Ru_C-S

iv Pt_C-Ru_{GBCK}-S

v Pt_C-Ru_{GBCS2}-S

Where S is the abbreviation used for Mn OMS-2, Ru_C is a commercially available Ruthenium metal catalyst on carbon, Ru_{GBCK} and Ru_{GBCS2} are the synthesized Ruthenium catalysts supported on GBC_K and GBC_{S2}.

The Tafel plots obtained using these catalysts are presented in Fig 5.18 and 5.19 and the corresponding currents are given in Table 5.8.

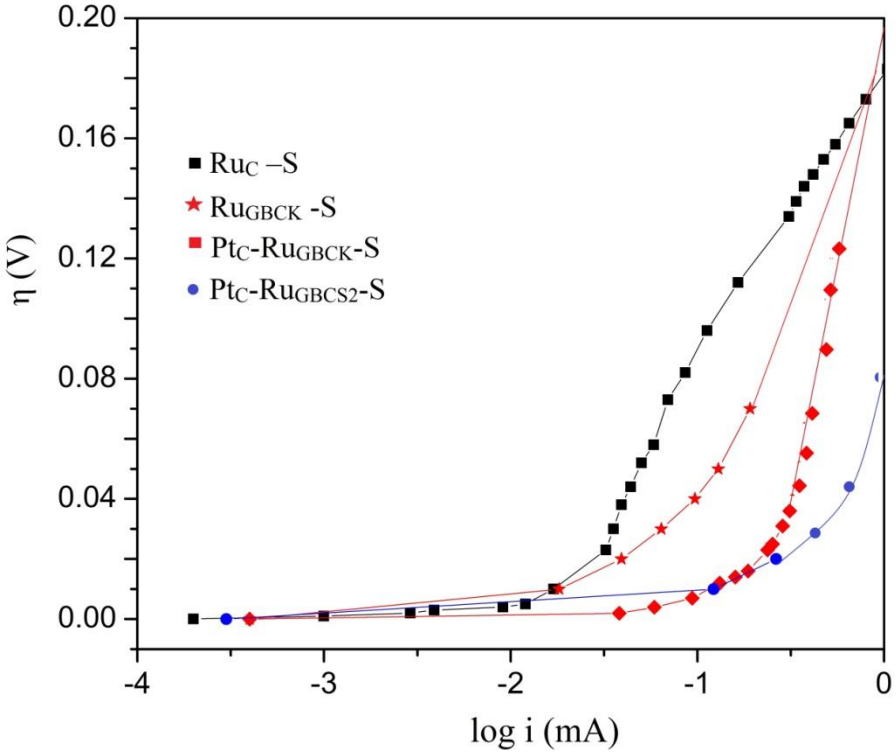

Figure 5.18: Tafel plots for ethanol electro-oxidation on the synthesized composite catalysts.

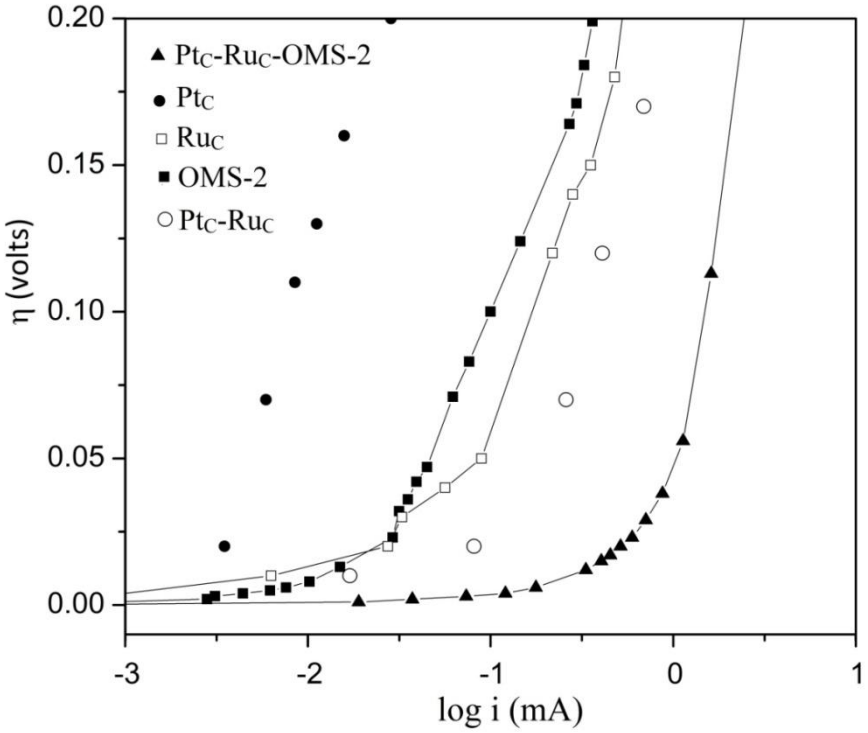

Figure 5.19: Tafel plots of different catalysts for ethanol oxidation; the electrolyte was 1M ethanol and 0.5 M H_2SO_4.

Table 5.8: Current produced i_{100} in µ amps, at overpotential of 100 millivolts for various catalysts composition.

Catalyst	i_o (µA cm^{-2})	Tafel slopes	Anodic transfer coefficient (α_a)
Pt_C	8.0	163	0.37
Ru_C	171	175	0.34
Pt_C-Ru_C	340	182	0.33
Pt_C-Ru_{GBCK}	532	151	0.39
Pt_C-Ru_C-OMS-2	1508	466	0.13
Pt_C-Ru_{GBCK}-OMS-2	340	84	0.70
Pt_C-Ru_{GBCS2}-OMS-2	735	31	1.9
OMS-2	101	275	0.22

Among the various composites thus studied using Pt_C, Ru_C and OMS-2, significant catalytic activity was observed for Pt_C-Ru_C-OMS-2 tri-component catalyst. It showed the highest current of 1508 µ amps while the other tri component catalysts showed much less currents which were approximately in the range of 100 – 800 µ amps. Therefore the activity of this tri component catalyst was further investigated.

The catalysts and their composites were first characterized by X-ray diffraction patterns

Fig. 5.20 displays the powder XRD pattern in relation to its individual components. The commercial Ru_C shows a sharp peak at about 2θ value of 26^o and a small peak at 21^o. These diffraction peaks are associated with the carbon material used as support. The peak due to Ru metal is observed at 2θ ~ 43^o as evident in the figure. It is attributed to Ru (002) plane [10]. Further Pt/C catalyst exhibits diffraction peaks due to (111), (200) and (220) planes at 2θ values of 39.9◦, 46.55◦ and 67.85◦, respectively. These are the characteristic peaks for Pt nanomaterial with face-centered cubic structure (JCPDS No.

04-0802) [21]. In addition to that there exist a broad peak at 2θ of ~ 25^{o} and is attributed to carbon support of the Pt_C. Further the intensity of the peak due to Pt at 2θ value of 40^{o} is significantly decreased in the composite catalyst Pt_C-Ru_C-OMS-2. Also the diffraction peaks of the individual components in the composites are comparatively weaker. The Scherrer particle sizes of Pt were 2.12, 0.27 and 0.24 nm for Pt_C, Pt_C-Ru_C and Pt_C-Ru_C-OMS-2 respectively. The apparent decrease I particle sizes of Pt NP^{s} could be due to presence of greater dispersion of Pt or increase in Pt-Pt distances in the composites. The peaks due to OMS-2 (MnO_2) appear at 2θ values of 12.78^{o}, 17.98^{o}, 28.65^{o}, 37.68^{o}, 41.91^{o}, 49.96^{o}, 55.98^{o}, 60^{o} and 65.43^{o} corresponding to (110), (200), (310), (211), (301), (411), (521), (600) and (002) respectively. They compare well with JCPDS file 20-908 for Mn OMS-2. Thus the XRD patterns of the tricomponent catalyst Pt_C-Ru_C-OMS-2 was a homogenous blend of the three individual components. Fig. 5.19 shows Tafel plots using this catalyst as well as the plots obtained using individual components. Table 5.8 also gives the values of Tafel slopes and Transfer coefficients. The values of Tafel slopes for individual components were in the range 160-185 mV dec^{-1}. However the tricomponents composite catalyst Pt_C-Ru_C-OMS-2 showed a very high Tafel slope of 466 mV dec^{-1} beyond an overpotential of around 40 mV. In general increased slope indicate existence of diffusion limitation for adsorbed intermediates and additional energy may be needed for the reaction to progress [18, 22].

From Table 5.9 it is evident that Tafel slopes greatly increase in presence of metal oxides, particularly when SnO_2 was used in combination with a palladium metal catalyst. Hence the unusually high Tafel slope of 466 mV dec^{-1} when the metal oxide OMS-2 is used in the present investigation imply a different mechanistic pathway during EOR.

Table 5.9: Tafel slopes reported in literature for EOR [17, 18].

Catalysts	Pd/C	Pd-MnO_2/C	Pd-SnO_2/C	Pd-NiO/C	Pt-Ru/C + SnO_2	Pt-Ru/C + TiO_2
Tafel slopes (mV/dec)	155	193	308	190	186	192

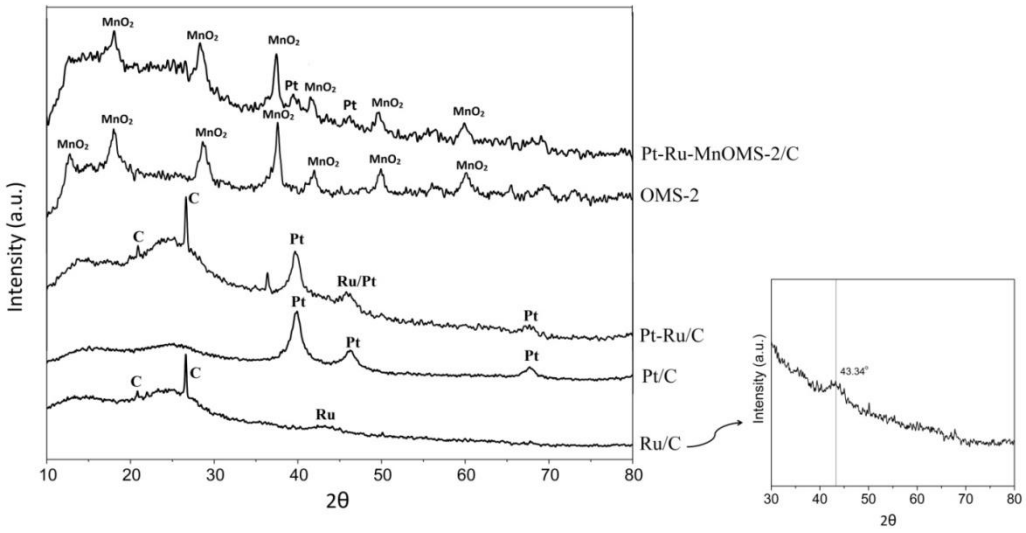

Fig. 5.20: XRD pattern of Pt/C, Ru/C, Mn OMS-2 and the composite Pt-Ru-MnOMS-2/C.

In alcohols like methanol and ethanol, electro-oxidation is known to be a multistep reaction (as presented earlier in chapter I). It thus start with cleavage of O-H bond or C_α-H bond giving CH_3CH_2O or CH_3CHOH type species which get further oxidized to acetaldehyde (CH_3CHO) or acetyl (CH_3CO) etc. intermediates. They get adsorbed on the catalyst surface at low potential range. The above ethanolic intermediates can get further dehydrogenated followed by C-C bond cleavage resulting in formation of CO_{ads} species. Metal-CO bond is known to be very strong due to back donation of electrons from metal antibonding orbital to –CO. This can lead to blocking of active catalyst site making it less active. Further dissociative adsorption of water molecule lead to the surface –OH species such as Pt-OH or Ru-OH. The –OH species which gets readily

formed on surface of metal like Ru forming Ru-OH_{ads}, brings about the oxidation of CO to CO_2.

It is known from previous studies [23] that OMS-2 is an active catalyst for MOR wherein methanol dehydrogenates on OMS-2 to form adsorbed S---CO_{ads}; the latter eventually desorbs as CO_2 by taking up lattice oxygen O^{2-}. However EOR activity of OMS-2 is observed to be quite low (Table 5.8). In fact all the individual components Pt_C, Ru_C, OMS-2 or Pt_C-Ru_C showed very low current in the range of about 10-350 μ amps. However as mentioned above, the composite catalyst formed from them showed a synergistic effect with an unusually large current of 1508 μ amps. On the other, the catalysts showed a low anodic transfer coefficient of 0.13. This showed that EOR activity is promoted without much input of outside electrical energy. Thus electron transfer could occur through participation of lattice oxygen O^{2-}.

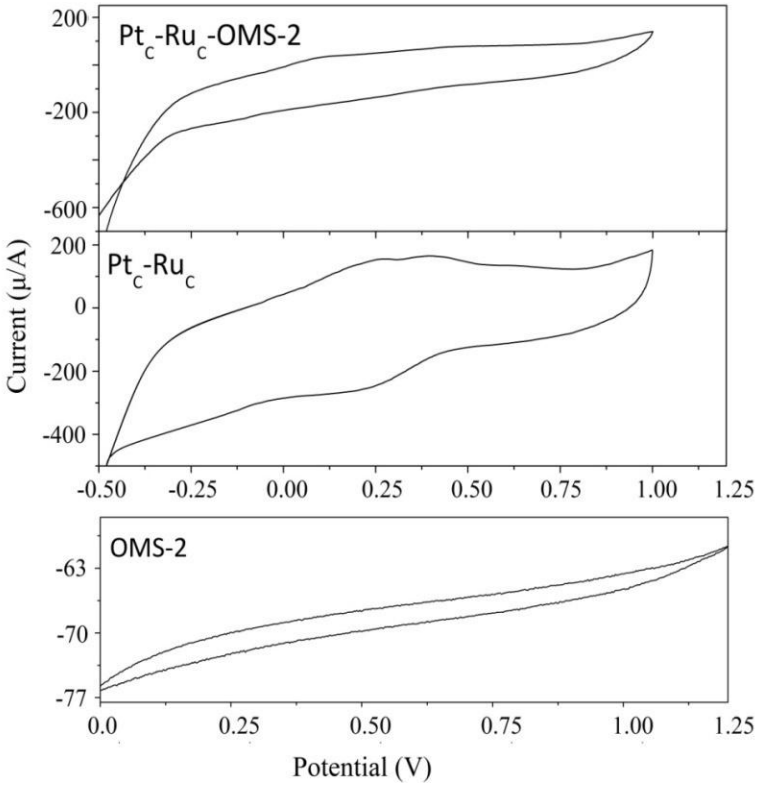

Figure 5.21: Cyclic voltammogram for ethanol oxidation reaction in 0.5M H_2SO_4 for Pt_C-Ru_C-Mn-OMS-2 in relation to OMS-2 and Pt_C-Ru_C catalysts. (*The catalysts use to make the composites were Ru_C and Pt_C. In a single component catalyst the mass of the catalyst was 10 mg. In the bimetallic catalyst Pt and Ru were 1:1 ratio for mass of 10 mg. In tri-component catalyst Pt, Ru and OMS-2 were in mass ratio of 1:1:1).*

Fig. 5.21 shows the CV profile of this catalyst. The profile doesn't show the conventional peaks a, b or c as seen in Pt-Ru bimetallic catalyst as was observed in Fig. 5.17. This confirms the hypothesis of alternate pathway followed for ethanol oxidation reaction in the presence of OMS-2 via possible intervention of lattice oxygen.

Summary & Conclusions

1. Synthesized glycerol based carbons were studied for the electrochemical applications like
   (i) capacitance
   (ii) electrocatalyst support for oxidation of methanol and ethanol in fuel cells.
2. Capacitance behavior was investigated using cyclic voltammetry technique in 0.5 M Na_2SO_4.
   (i) For the four GBCs that were investigated the following results were observed for the capacitance.

   $GBC_{S2} > GBC_Z > GBC_K > GBC_{S1}$

   The capacitance was found to increase with
   - Surface area
   - Microporous nature
   - Presence of oxygenated functional groups

   (ii) Undoped MnO_2 showed capacitance of 280 mF cm^{-2} and it decreased upon Fe doping. This is because Fe doping lowers the surface area of the doped MnO_2.
   (iii) Composites were prepared by blending together GBC^s with 1 % OMS-2. The resulting capacitance was significantly increased. Thus when a composite of GBC_{S2} was prepared with OMS-2, there was a synergistic increase in capacitance from 640 mF cm^{-2} to 1320 mF cm^{-2}.

3. Electrocatalytic oxidation of methanol was investigated on Ruthenium catalyst supported on glycerol based carbons and compared with Ruthenium catalysts supported on commercial carbons.

   (i) Among the catalysts tested, Ru supported on GBCK showed highest electrocatalytic activity. It follows order

   $Ru_C > Ru_{GBCK} > Ru_{GBCS2} > Ru_{GBCZ}$

   (ii) When bimetallic catalysts were prepared with commercial Pt catalyst the activity followed the order

   $Pt_C\text{-}Ru_{GBCK} > Pt_C\text{-}Ru_{GBCZ} \approx Pt_C\text{-}Ru_C > Pt_C\text{-}Ru_{GBCS2}$

Thus the GBCs synthesized in the present investigation were generally better electrocatalytic support material for oxidation of methanol.

4. A tri-component nanocomposite prepared from Pt_C, Ru_C and OMS-2 exhibited higher electrocatalytic performance for ethanol oxidation.

References

[1] A. Borenstein, O. Hanna, R. Attias, S. Luski, T. Brousse, D. Aurbach, *Carbon-based composite materials for supercapacitor electrodes : a review,* J. Mater. Chem. A, 5 (2017) 12653 – 12672.

[2] X. Li, B. Wei, *Supercapacitors based on nanostructured carbon,* Nano. Energy 2 (2013) 159 – 173.

[3] J. R. Rani, R. Thangavel, S-I. Oh, Y. S. Lee, J-H. Jang, *An Ultra-High-Energy Density Supercapacitor; Fabrication Based on Thiol-functionalized Graphene Oxide Scrolls,* Nanomaterials 9 (2019) 148-159.

[4] P. Ragupathy, H. N. Vasan, N. Munichandraiah, *Synthesis and characterization of nano-MnO_2 for electrochemical supercapacitor studies,* J. Electrochem. Soc., 155 (2008) 34 – 40.

[5] J. M. Miller, B. Dunn, *Deposition of Ruthenium Nanoparticles on Carbon Aerogels for High Energy Density Supercapacitor Electrodes,* J. Electrochem. Soc., 144 (1997) 309 - 311.

[6] R. Heimböckel, F. Hoffmann, M. Fröba, *Insights into the influence of the pore size and surface area of activated carbons on the energy storage of electric double layer capacitors with a new potentially universally applicable capacitor mode,* Phys. Chem. Chem. Phys. 21 (2019) 3122-3133.

[7] J. P. Zheng, P. J. Cygan, T. R. Jow, *Hydrous ruthenium oxide as an electrode material for electrochemical capacitors,* J. Electrochem. Soc., 142 (1995) 2699 - 2703.

[8] C. Ramirez-Castro, O. Crosnier, L. Athou¨el, R. Retoux, D. B´elanger, T. Broussea, *Electrochemical Performance of Carbon/MnO_2 Nanocomposites Prepared via*

Molecular Bridging as Supercapacitor Electrode Materials, J. Electrochem. Soc., 162 (2015) 5179 - 5184.

[9] M. C. Lima dos Santos, R. M. Dutra, V. A. Ribeiro, E. V. Spinacé, A. O. Neto, *Preparation of PtRu/C Electrocatalysts by borohydride reduction for Methanol Oxidation in Acidic and Alkaline Medium,* Int. J. Electrochem. Sci., 12 (2017) 3549 – 3560.

[10] A. M. Ruppert, M. Jędrzejczyk, O. Sneka-Płatek, N. Keller, A. S. Dumon, C. Michel, P. Sautetc, J. Grams, *Ru catalysts for levulinic acid hydrogenation with formic acid as a hydrogen source,* Green Chem**.**, 18 (2016) 2014-2028.

[11] M. Hilgendorff, K. Diesner, H. Schulenburg, P. Bogdanoff , M. Bron, S. Fiechter *Preparation Strategies towards Selective Ru-Based Oxygen Reduction Catalysts for Direct Methanol Fuel Cells,* J. New. Mat. Electrochem. Systems. 5 (2002) 71 – 81.

[12] J. Zeng, C. Francia, M. A. Dumitrescu, A. H. A. M. Videla, V. S. Ijeri, S. Specchia, P. Spinelli, *Electrochemical Performance of Pt-Based Catalysts Supported on Different Ordered Mesoporous Carbons (Pt/OMCs) for Oxygen Reduction Reaction,* Ind. Eng. Chem. Res. 51 (2012) 7500 - 7509.

[13] S. Songa, Y. Liangb, Z. Li, Y. Wanga, R. Fub, D. Wub, P. Tsiakaras, *Effect of pore morphology of mesoporous carbons on the electrocatalytic activity of Pt nanoparticles for fuel cell reactions,* Appl. Catal B 98 (2010) 132–137.

[14] M. Carmo, M. Linardi, J. G. R. Poco, *Characterization of nitric acid functionalized carbon black and its evaluation as electrocatalyst support for direct methanol fuel cell applications,* Appl. Catal. A-Gen 355 (2009) 132–138.

[15] M. Carmo, M. Brandalise, A. O. Neto, E. V. Spinace, A. D. Taylor, M. Linardi, J. G. R. Poço *Enhanced activity observed for sulfuric acid and chlorosulfuric acid*

functionalized carbon black as PtRu and PtSn electrocatalyst support for DMFC and DEFC applications, Int. J. Hydrogen energy 36 (2011) 14659 – 4667.

[16] T. G. H. Nguyen, T. V. A. Pham, T. X. Phuong, T. X. B. Lam, V. M. Tran, T. P. T. Nguyen, *Nano-Pt/C electrocatalysts: synthesis and activity for alcohol oxidation*, Adv. Nat. Sci.: Nanosci. Nanotechnol 4 (2013) 035008.

[17] R. M. Abdel Hameed, *Enhanced ethanol electro-oxidation reaction on carbon supported Pd-metal oxide electrocatalysts*, J. Colloid and Interface Sci. 505 (2017) 230–240.

[18] S. C. Zignani, V Baglio, D. Sebastián, S. Siracusano, A.S. Aricò, *Enhancing ethanol oxidation rate at PtRu electro-catalysts using metal-oxide additives*, Electrochim. Acta 191 (2016) 183-191.

[19] V. Comignani, J. M. Sieben, M. E. Brigante, M. M.E. Duarte, *Carbon supported Pt-NiO nanoparticles for ethanol electro-oxidation in acid media,* J. Power Sources 278 (2015) 119-127.

[20] R. N. DeGuzman, Y-F. Shen, E. J. Neth, S. L. Suib, C-L. O'Young, S. Levine, J. M. Newsam, *Synthesis and Characterization of Octahedral Molecular Sieves (OMS-2) Having the Hollandite Structure,* Chem. Mater. 6 (1994) 815-821.

[21] H. Wang, S. Ji, W. Wang, V. Linkov, S. Pasupathi, R. Wang, *Pt decorated PdFe/C: Extremely High Electrocatalytic Activity for Methanol Oxidation,* Int. J. Electrochem. Sci., 7 (2012) 3390 – 3398.

[22] A. S. Aricoá, E. Modica, I. Ferrara, V. Antonucci, *CO and CO/H_2 electrooxidation on carbon supported Pt-Ru catalyst in phosphotungstic acid ($H_3PW_{12}O_{40}$) electrolyte,* J. Appl. Electrochem 28 (1998) 881-887.

[23] J. S. Rebello, P.V. Samant, J. L. Figueiredo, J. B. Fernandes, *Enhanced electrocatalytic activity of carbon- supported MnO_x/Ru catalysts for methanol oxidation in fuel cells,* J. Power Sources 153 (2006) 36-40.

LIST OF PUBLICATIONS

1. A. A. Narvekar, J. B. Fernandes, S. G. Tilve, Adsorption behavior of methylene blue on glycerol based carbon materials, J. Environ. Chem. Eng., 6 (2018) 1714 – 1725. https://doi.org/10.1016/j.jece.2018.02.016

2. A. A. Narvekar, S. G. Tilve, J. B. Fernandes, Transformation of a Fe-Mn oxide into a ferromagnetic α-Fe_2O_3, J. Therm. Anal. Calorim., https://doi.org/10.1007/s10973-019-09142-3.

Presented papers/posters at the following conferences

1. National seminar on Advanced materials for renewable energy and sustainable environment (*AMRESE-2020*), PG and Cluster Research Centre, Department of Chemistry, Government College of Arts, Science and Commerce, Khandola, Marcela-Goa on January 31st – 1st February 2020.
2. Two days workshop on Material science, Goa University, University of Coimbra and University of Porto on 18th – 19th November 2019.
3. Seminar on Advancement in Science and Technology, Department of Chemistry and Physics, Government College of Arts, Science and Commerce, Khandola, Marcela-Goa on 9th February 2019.
4. Conference on Electrochemistry in Advanced Materials, Corrosion and Radiopharmaceuticals (*CEAMCR 2018*), Indian Society of Electroanalytical Chemistry at DAE Convention Centre, BARC, Mumbai on January 15th – 17th February 2018.

5. 2[1st] Workshop and Symposium on Thermal Analysis (*THERMANS 2018*), Indian Thermal Analysis Society, Mumbai and Goa University, Goa on 1st – 2nd January 2018.

3. International Conference on Electrochemical Science and Technology (*ICONEST 2017*), Electrochemical Society of India and Department of Inorganic and Physical Chemistry Indian Institute of Science at J.N. Tata Auditorium, Indian Institute of Science, Bangalore, 10th -12th August 2017. *(A. A. Narvekar, J. B. Fernandes, S. G. Tilve, Relative catalytic behaviour of Pt/Ru/C/MnOMS-2 nanocomposite towards methanol And ethanol electro-oxidation in acidic and alkaline medium, ICONEST-2nd International Conference on Electrochemical Science and Technology, PP-Eng-50, Aug. 10-12, 2017, I.I.Sc. Bengaluru, India)*

6. New Frontiers in Chemistry-from Fundamentals to Applications-II (*NFCFA-2017*), Department of Chemistry, BITS Pilani K.K. Birla Goa Campus on 28th – 29th January 2017.
7. 6th International Science Congress (*ISC-2016*), International Science Community Association (Registered under Ministry of Corporate Affairs, Government of India) in collaboration with Hutatma Rajguru Mahavidyalaya, Pune, Maharashtra, India on 8th – 9th December 2016.
8. National level symposium on "Material Characterization and Manufacturing (*MCM-2016*), Department Of mechanical engineering, Padre Conceicao College of Engineering and Department of Physics, Goa University at Goa University on 18th – 19th August 2016.

9. New Frontiers in Chemistry-from Fundamentals to Applications (*NFCFA-2015*), Department of Chemistry, BITS Pilani K.K. Birla Goa Campus on 18^{th} – 19^{th} December 2015.
10. International Conference on Green Chemistry Catalysis, Energy and Environment (*ICGC 2015*) Department of chemistry, Goa University, Goa on 22^{nd} – 24^{th} January 2015.
11. International Conference on Electrochemical Science and Technology (*ICONEST 2014*) organized by Electrochemical Society of India at Indian Institute Of Science, Bengaluru on 7^{th} – 9^{th} August 2014.

Journal of Environmental Chemical Engineering 6 (2018) 1714–1725

Contents lists available at ScienceDirect

Journal of Environmental Chemical Engineering

journal homepage: www.elsevier.com/locate/jece

Adsorption behavior of methylene blue on glycerol based carbon materials

Apurva A. Narvekar, J.B. Fernandes*, S.G. Tilve

Department of Chemistry, Taleigao Plateau, Goa University, Goa, 403206, India

ARTICLE INFO

Keywords:
Glycerol
Sulphonyl
Adsorption
Kinetics
Methylene blue

ABSTRACT

In the present investigation a glycerol based carbon was synthesized by partial carbonization of glycerol using concentrated H_2SO_4 in the molar ratio 1:4. The carbonized material was further treated at 120 °C and 350 °C to obtain the carbons GBC-120 and GBC-350 respectively. The samples were characterized by XRD, ir, thermal analysis (TG-DTG-DTA), pzc measurements; SEM and BET surface area analysis. The TGA showed a gradual weight loss up to about 800 °C. The adsorption studies were carried out using methylene blue as a model adsorbate. The BET surface area of GBC-120 and GBC-350 were determined to be 21 and 464 $m^2 g^{-1}$. The GBC-120 gave maximum adsorption capacity with nearly 100% dye removal efficiency using 8 10 milligrams of the adsorbent powder, when the dye concentration was 25 $\mu g\, mL^{-1}$. It showed Type I adsorption isotherm profile at lower concentration range and the data could be readily fitted into Langmuir adsorption model. At higher concentration the adsorption data showed a better fit for Frumkin adsorption model. The adsorption generally increased with temperature and showed a favorable free energy change. The GBC-350 showed comparatively less adsorption and but the data could also be fitted in Langmuir adsorption profile. Investigation of adsorption kinetics revealed better fit with pseudo second order kinetic model for both GBC-120 and GBC-350. GBC-120 due to presence of SO_3H surface functionality showed a high adsorption capacity ~1050 $mg\, g^{-1}$ which is significantly higher than the literature values.

1. Introduction

There is a continuing interest in developing newer methods of synthesis of carbon materials as adsorbents and catalysts. In recent times, increasing attention is given to develop functionalized carbon materials that could both act as excellent catalysts and also have improved adsorption characteristics [1]. Carbon catalysts with acid functionalities are finding increasing use in organic transformations. A glycerol based carbon (GBC) was recently synthesized by partial carbonization of glycerol using sulfuric acid. This carbon was found to be an effective solid acid catalyst in organic transformations including chemo selective synthesis [2–5]. This was due to the presence of acidic functionalities such as SO_3H on its surface. Thus the GBC carbon was found to be advantageous over other carbon catalysts owing to its ease of synthesis, efficiency and comparative stability.

On the other hand activated carbons obtained from different natural sources including nutshells, wood, coconut husk etc. often need appropriate chemical or physical activation in order to get efficient activity. However glycerol as a carbon source is readily available as a byproduct of biodiesel production industry and is thus cost effective. In addition to being used as a catalyst, a glycerol based carbon was also recently synthesized for adsorptive removal of antibiotics from their aqueous solutions [6,7].

Apart from being used as adsorbents and catalysts, carbons are also required as supports for noble metal catalysts such as electrocatalysts in fuel cell reactions. The catalysts used in fuel cells are often platinised carbons such as Pt-C or Pt-Ru/C etc. These carbon supports need to be very pure carbon materials free from any metallic impurities as well as free from any residual chloride or sulphur. Since glycerol is readily available in a pure form, it is amenable towards appropriate synthesis of pure carbon materials of desired properties. Depending upon synthesis conditions, it should also be possible to use glycerol as a raw material to synthesize pure microporous carbon or mesoporous carbon with desired surface functionalities. A series of investigations would thus be required to selectively develop various forms of carbon starting from glycerol as a raw material and then tailor its properties to make it useful either as an adsorbent or as a catalyst or as a catalyst support or having combination of these characteristics. In the present investigation, a glycerol based carbon is synthesized and examined for its adsorption behavior towards removal of methylene blue. The knowledge gained here is expected to be a background information when further studies are undertaken in development of suitable glycerol based carbon materials. Since methylene blue is also a well known pollutant associated with effluents from textile industry, the present investigation

* Corresponding author.
E-mail address: julio@unigoa.ac.in (J.B. Fernandes).

https://doi.org/10.1016/j.jece.2018.02.016
Received 24 October 2017; Received in revised form 8 February 2018; Accepted 11 February 2018
Available online 16 February 2018

Table 1
Review of some adsorption and kinetic models.

Sr. No.	Adsorption Isotherm	Parameters and their significance
1	Langmuir adsorption isotherm $x = \frac{x_m K c}{1 + Kc}$ $\frac{1}{x} = \frac{1}{x_m K} \cdot \frac{1}{c} + \frac{1}{x_m}$	x = Amount of methylene blue adsorbed per unit mass of carbon (mg g^{-1}). x_m = Maximum adsorption capacity with complete monolayer coverage on the surface of carbon (mg g^{-1}). c = Concentration of methylene blue in the solution which is in equilibrium with the carbon. K = Langmuir adsorption constant which is related to energy of adsorption
2	Freundlich adsorption isotherm $x = kc\frac{1}{n}$ $\log x = \log k + \frac{1}{n}\log c$	k = Freundlich adsorption constant which is indicative of maximum adsorption capacity. 1/n = Measure of intensity of adsorption. (1/n = 0 − 1)
3	Frumkin adsorption isotherm $\frac{\theta}{(1-\theta)} e^{-2\alpha\theta} = \frac{\beta}{55.55} c$ $\log\left(\frac{\theta}{(1-\theta)c}\right) = \log\frac{\beta}{55.55} + \frac{2\alpha\theta}{2.303}$ *Where* $\theta = \frac{M}{M_{ads}}$	α = adsorbate interaction parameter β = Adsorption-desorption equilibrium constant. θ = Amount of adsorbate adsorbed at equilibrium. M = Concentration of the dye adsorbed at equilibrium. M_{ads} = Maximum amount of dye adsorbed at equilibrium.

	Kinetic models (expressions in linear form)	Parameters and their significance
1.	Pseudo first order kinetic model $\log(q_e - q_t) = \log q_e - \frac{K_1}{2.303} t$	K_1 and K_2 are first and second order rate constants.
2.	Pseudo second order kinetic model $\frac{t}{q_t} = \frac{t}{q_e} + \frac{1}{K_2 q_e^2}$	q_e is the amounts of dye adsorbed at equilibrium and q_t is the amounts of dye adsorbed at time t.

will throw light not only on surface characteristics of the glycerol based carbon but also on its efficacy in mitigating pollutants by adsorption.

The activated carbons play a crucial role in mitigating pollutants such as dyes, pharmaceuticals, surfactants, heavy metal ions etc. by adsorption from industrial waste waters [8–12].

The dyeing process in the textile industry leads to release of approximately 10–15% dyes into the environment. The effluents from these industries thus carry a large number of dyes and other additives which are added during the coloring process [13]. Due to their high water solubility they get readily transferred through water bodies. They may also undergo degradation to form products that are highly toxic [14]. Thus removal of dyes from the water bodies is important as they are harmful for living beings. A widely used cationic dye in different industries is methylene blue which is known to be carcinogenic.

Adsorption by activated carbons is an important process for removal of pollutants particularly dyes and metal ions from industrial waste waters. Adsorption is a very effective separation technique in terms of initial cost, simplicity of design, ease of operation and insensitive to toxic substances. It is a tertiary technology during waste water treatment for adsorption of micropollutants, as well as to remove colour and odor [15]. The efficiency of removal by adsorption from solution depends upon the nature of dyes (cationic or anionic dyes), pH of adsorbate solution, pzc of the adsorbent and its surface functionalities, as well as surface area and porosity of the adsorbent. The use of different adsorbents like clay, silica materials, zeolite and activated carbons for removal of methylene blue (MB) has been extensively studied and is recently reviewed [16]. A variety of adsorbents have been designed depending upon the type of adsorbates to be removed. Activated carbons are generally more effective adsorbents for removal of high molecular weight compounds particularly those with low water solubility. However activated carbons with surface functionalities are efficient for adsorbing a wider range of organic pollutants such as dyes and pharmaceuticals.

Zhang et al., [17] have examined the comparative adsorption of two cationic dyes (Rhodamine B and Methylene blue) by milled sugarcane bagasse which gave an adsorption capacity of 31 mg g^{-1}. Similarly Xiong et al., [18] studied the adsorption of methylene blue on titanate nanotubes and maximum adsorption capacity of 133 mg g^{-1} was reported. Among all the described adsorbents in literature, the ability of activated carbons is eminent for adsorption of dyes due to its ease of availability and economic feasibility. It is one of the most widely used adsorbent as compared to all other materials. Adsorption of methylene blue onto activated carbon produced from steam activated bituminous coal was reported with maximum adsorption capacity of 580 mg g^{-1} at equilibrium [19]. Further, adsorption from aqueous solutions onto carbon nanotubes was also studied wherein monolayer adsorption capacity of 132 mg g^{-1} was observed [20]. Recently a high adsorption capacity for methylene blue (714 mg g^{-1}) was reported when birnessite type manganese dioxide in presence of diatomite, was used as an adsorbent for the removal of MB in alkaline solution (pH 11). It was however not considered favorable for regeneration and reuse [21]. The microwave-induced H_2SO_4 treated activated carbon obtained from rice agricultural wastes was also used for methylene blue sorption and maximum adsorption capacity of 62.5 mg g^{-1} at initial pH of 7 is reported [22]. In general carbon materials obtained from various biomass sources showed adsorption capacity of methylene blue in the range 100–600 mg g^{-1} [23–30].

The nature of interaction between the adsorbate molecules and the adsorbent can be understood from the adsorption isotherms. An adsorption isotherm is a plot which relates the amount of substance adsorbed to the equilibrium concentration of the adsorbate molecules in the solution at a specified temperature. The amount adsorbed depends on the nature of adsorbate and adsorbent which in turn affect the shape of adsorption isotherm profile. The data is usually investigated in terms of different adsorption isotherm models which include, Langmuir, Freundlich, Frumkin adsorption isotherms. These are considered in the present investigation. The Langmuir Isotherm assumes that adsorption is of monolayer and all the active sites on the adsorbent surface are equivalent in energy. Freundlich adsorption isotherm explains the multilayer adsorption behavior. For understanding interaction between adsorbed molecules, the applicability of Frumkin adsorption isotherm is generally investigated. The description of adsorption isotherms and kinetic models [31–36] used in this work are briefly summarized in Table 1.

2. Experimental

2.1. Chemicals and materials

Glycerol (GR) was purchased from Molychem (India), Sulphuric acid (AR) was obtained from RUNA (India), Methylene blue (dye content > 96.0%.) was purchased from S D Fine-Chem Limited (India). Double distilled water was used during the adsorption studies.

2.2. Synthesis and characterization of glycerol based carbon

The sulphonated glycerol based carbon was synthesized by dehydration of glycerol using sulphuric acid in the molar ratio (*1*: *4*) [2,6]. Thus 25 mL (Density = 1.84 g mL^{-1}) of sulphuric acid was added drop wise to 10 g of glycerol under continuous stirring over a period of 25 min (approximately at the rate of 1 mL min^{-1}). During the process, glycerol was taken in a 500 mL beaker and kept on hot plate magnetic stirrer. The sulphuric acid was added from an overhead reservoir. As the temperature was increased from ambient temperature to 180 °C, the clear solution gradually became a brown viscous mass. The temperature of the product was continued to be maintained at 180 °C for another 20 min until the evolution of the gases was completed. The black mass was then filtered and washed with hot water until the washings were neutral. The product was designated as GBC-120. The yield of GBC-120 (carbon-SO_3H) was 0.467 g per gram of glycerol used. The details of preparing GBC-120 and GBC-350 are summarized in Scheme 1.

2.3. Characterization

The carbon samples were characterized by XRD on a Rigaku Ultima IV diffractometer using Cu-Kα radiation of wavelength of 1.5419 Å. Thermal analysis was carried out using TG-DTA analyzer (NETZSCH STA 409 PC) in N_2 atmosphere at a heating rate of 10 °C min^{-1}. The infrared spectra were recorded in KBr dispersion, using Shimadzu IR Prestige-21 FTIR spectrophotometer from 4000 to 400 cm^{-1}. The surface area was obtained by multipoint BET method and BJH pore size distribution analysis using Quantachrome® ASiQwin™ – Automated Gas Sorption system. The morphology of carbon samples was determined with environmental scanning electron microscope (Ouanta FEG 250). To determine pHpzc of the carbon samples, various solutions having pH values ranging from 2 to 10 were prepared. The pH values were adjusted by drop wise addition of HCl (0.02 M) or NaOH (0.02 M)–50 mL solutions of 0.01 M NaCl. 0.15 g of carbon was then added to each of these solutions, which were then stirred for 24 h. The final pH of the solutions was then measured. A graph of final pH v/s initial pH was plotted and the pHpzc was obtained from the intersection point.

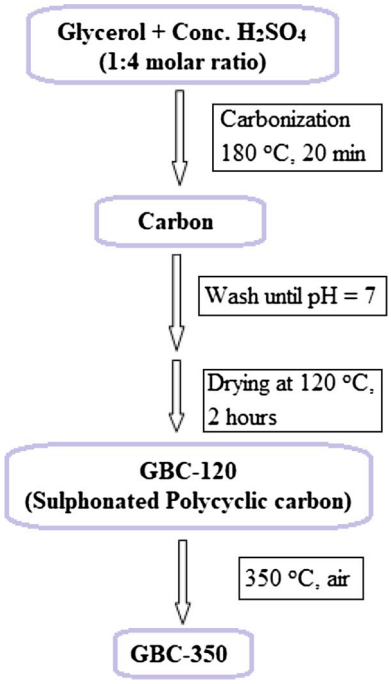

Scheme 1. Flow chart for synthesis of the glycerol based carbons (GBC-120 and GBC-350).

2.4. Adsorption

2.4.1. Effect of adsorbent dosage

2, 4, 6, 8, 10 mg of GBC-120 were each taken in conical flasks containing 100 mL of 5 μg mL^{-1} solution of methylene blue. The adsorption was carried out at pH 4.7. The flasks were kept for shaking overnight (~15 h) and the amount adsorbed in each case was determined.

2.4.2. Effect of initial methylene blue concentration

The dye concentration were varied from 10 to 50 μg mL^{-1}. The adsorption was carried out using 2 mg of GBC-120. The adsorption was allowed to take place overnight (~15 h). The adsorption was carried out at pH 4.7.

2.4.3. Effect of initial pH

2 mg of GBC-120 was contacted with 50 mL of 50 μg mL^{-1} of methylene blue at different pH (2.6-9.6). The flasks were kept for shaking for 2 h and then the amount of methylene blue adsorbed was determined.

2.4.4. Effect of contact time and determination of adsorption equilibrium

The time required to establish equilibrium between the concentration of methylene blue adsorbed and its concentration in the solution was determined. Thus 20 mg of the previously dried carbon sample was added to known concentration (50 μg mL^{-1}) of methylene blue (pH = 7). The progress of adsorption was monitored by taking out 1.0 mL aliquots of the solution at various predetermined time intervals until the equilibrium is reached. The data was interpreted in terms of relevant kinetic models.

2.4.5. Adsorption isotherms

The adsorption isotherms of GBC-120 and GBC-350 carbons were determined at ambient temperature by equilibriating various concentrations of methylene blue with a know amount of the carbons (~ 2 mg). All the solutions were allowed to equilibriate at 25 °C at predetermined equilibriation times. The equilibrium concentrations were calculated by measuring the absorbance of methylene blue solution in each case. The data was then fitted in various adsorption isotherm and kinetic models.

3. Results and discussion

3.1. Characterization techniques

3.1.1. XRD and thermal analysis

The synthesized glycerol based carbon was characterized by XRD, thermal analysis and infra-red spectroscopy. Fig. 1 gives the XRD profiles of the samples GBC-120 and GBC-350.

Both the samples showed the expected two broad peaks at 2θ around 20–24° and 43° which correspond to reflection planes of (002) and (100) respectively [37]. It was observed that the peak at 43° was diffuse for the as prepared GBC-120 sample, due to its comparatively amorphous nature.

Fig. 2 gives thermal analysis profiles of GBC-120 carried out in N_2 atmosphere. The TGA profile (Fig. 2a) shows an initial weight loss of ~ 16.4% up to 108 °C, due to loss of physisorbed and hydrogen

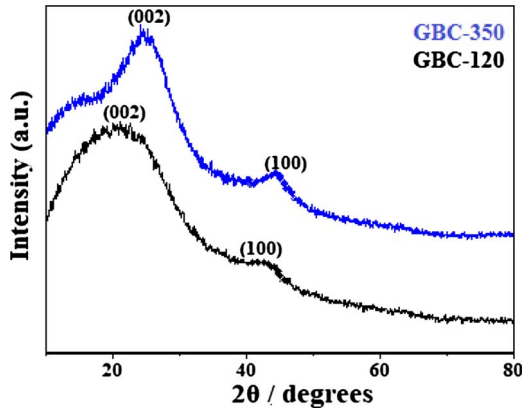

Fig. 1. XRD profiles of the glycerol based carbons obtained by treatment of the as prepared carbons at 120 °C and 350 °C using Cu-Kα radiation of wavelength of 1.5419 Å.

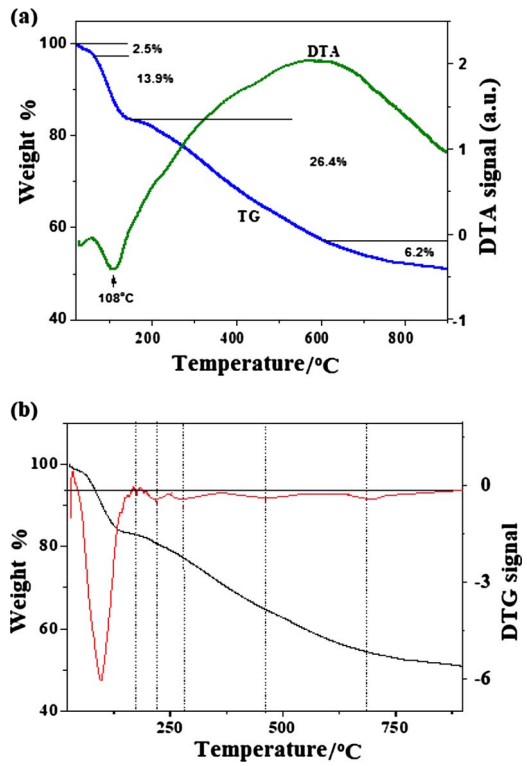

Fig. 2. (a) TG-DTA plot of GBC-120 in nitrogen atmosphere and (b) Comparison of TG/DTG profiles (N_2 atmosphere, heating rate of 10 °C min^{-1}).

bonded water. Further weight loss continues till about 800 °C due to gradual loss of the surface functional groups. The DTA shows a broad endothermic profile in this temperature range with a maximum around 600 °C. This suggested that the loss of surface functionalities was accompanied with structural rearrangement, resulting in development of porosity in the carbon structure. It can be seen from Fig. 2(b) that the TG-DTG profile of GBC-120 exhibits a broad weight loss between 180 and 700 °C. This broad range shows three distinct regions. The peak at 220 °C is considered as characteristic for decomposition of $-SO_3H$ and −COOH groups. A large broad peak between 280 and 460 °C is due to decomposition of lactones and phenolic groups. And the similar broad peak from 460 to 700 °C is due to decomposition of carbonyl group. These results are in agreement with a recent report on a similarly prepared carbon based catalyst [38].

3.1.2. Infrared spectral analysis

Fig. 3 gives the infrared spectra of GBC-120 carbon and the spectra

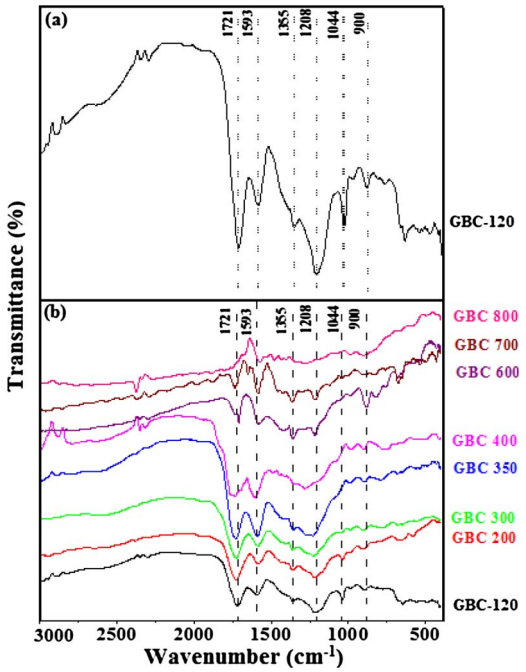

Fig. 3. Infrared spectra of GBC carbons (a) spectrum of GBC-120 (b) spectra of various GBC carbons heat treated between 200 and 800 °C (using KBr dispersion).

recorded after subjecting it to various heat treatments between 200 and 800 °C.

The glycerol based carbon which is known to have $-SO_3H$ groups attached to polycyclic cluster of graphitic rings, shows characteristic absorptions in the infrared region of 1720–900 cm^{-1} [39–43]. The corresponding assignments are given in Table 2.

From Fig. 3b, it can be observed that when GBC-120 was heated at varying temperatures above 120 °C, the intensity of $-SO_3H$ peak at 1044 cm^{-1} decrease. This peak vanished by 300 °C while the other peaks at 1208 cm^{-1} and 1355 cm^{-1} which are also due to $-SO_3H$ functionality were still + present. Thus the thermal treatment at 300 °C resulted in partial decomposition of $-SO_3H$ due to dehydroxylation of the adjacent sulphonyl groups. The other peaks at 1593 and 1721 cm^{-1} were due to C=C and C=O groups respectively. The carbonyl peak is a composite peak due to −CHO and −COOH and in agreement with the ir spectra reported earlier [44]. A −CHO functionality was expected as it is known that glycerol in presence of sulphuric acid decomposed via an acrolein type intermediate which has a −CHO group [45]. The peak at 1721 cm^{-1} was present till 700 °C. It eventually disappeared for the GBC-800 sample when the carbonyl functionalities were finally decomposed. This is supported by the evidence from the thermal analysis profile (Fig. 2) that decomposition of the surface functionalities gets completed around 800 °C.

3.1.3. Surface area, porosity and SEM

Fig. 4 gives the N_2 adsorption desorption isotherms along with pore size distribution profiles for GBC-120 and GBC-350. A clear hysteresis

Table 2
The assignments corresponding to different frequencies observed in the infra-red spectra of glycerol based carbons.

Frequencies cm^{-1}	Functional groups
1721	C O stretch of COOH and carbonyl group
1593	C C stretch of graphitic rings
1355	O S O stretch of $-SO_3H$
1208	(i) Symmetric S O stretch (ii) C−OH stretching of phenolic group
1044	Asymmetric stretching of SO_3H

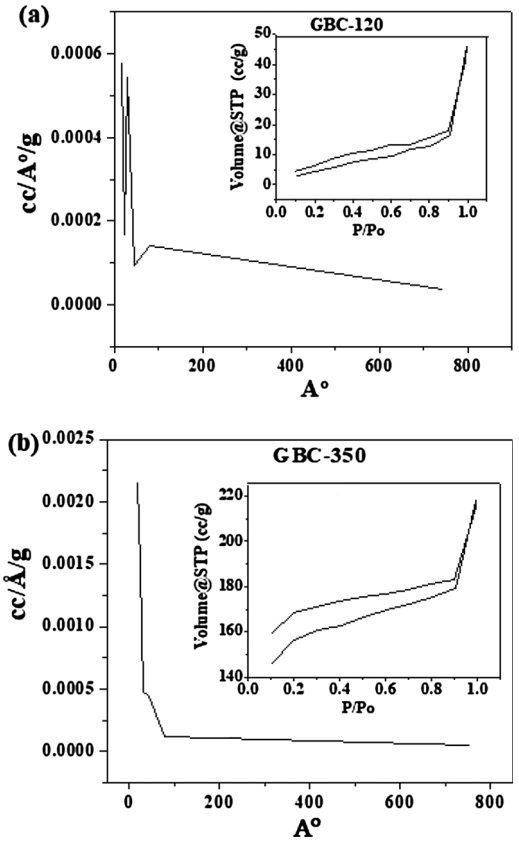

Fig. 4. Pore size distribution and N_2 adsorption-desorption isotherm (inset) for the carbon samples (a) GBC-120 and (b) GBC-350.

Table 3
The values of surface area, pore volume and pore size of GBC-120 and GBC-350 from BET analysis.

Sample	Surface Area ($m^2 g^{-1}$)	Pore volume ($cc\,g^{-1}$)	Pore radius (Å)	SEM/EDAX Analysis Wt (%) of the elements		
				C	O	S
GBC-120	21.00	0.06	18.38	82.45	15.82	1.74
GBC-350	464.00	0.10	18.27	87.55	12.09	0.36

loop was observed for both the samples. The surface area and porosity values are presented in Table 3 along with SEM data.

It can be seen from Table 3 that GBC-120 with its associated SO_3H functionalities showed a relatively small surface area of about $21\,m^2\,g^{-1}$. On the other hand GBC-350 showed much larger surface area of $464\,m^2\,g^{-1}$. This suggested that the partial decomposition of SO_3H greatly enhances the surface area of the carbon due to greater dispersion of the GBC-350 particles. This is supported by the respective SEM images (Fig. 5) wherein GBC-120 shows larger agglomerates as compared to GBC-350. Further, the increased surface area of GBC-350 exposes its surface porosity resulting in its having much larger pore volume. Thus the pore volume of GBC-350 was $0.099\,cm^3\,g^{-1}$ as compared to $0.065\,cm^3\,g^{-1}$ for GBC-120 even though both the samples have similar pore radii of around 18.3 Å.

3.2. General adsorption behaviour

The adsorption studies were carried out to investigate the influence of SO_3H groups on the carbon surfaces. The removal efficiency of the methylene blue dye from the solution was calculated using the relation

$$Removal(\%) = \frac{C_i - C_e}{C_i} \times 100 \tag{3.1}$$

and equilibrium adsorption was determined using the equation:

$$q_e = \frac{C_i - C_e}{W} \times V \tag{3.2}$$

C_i and C_e are the initial and equilibrium concentrations of the dye in $\mu g\,mL^{-1}$ respectively, W is the weight of carbon in g and V is volume of the dye solution in litres.

3.2.1. Effect of adsorbent dosage

The effect of adsorbent dosage was studied by taking methylene blue solution of $25\,\mu g\,mL^{-1}$. 100 mL aliquots of the above solution were equilibrated by stirring with varying quantities of the adsorbents for 15 h. The resulting adsorption behavior is shown in Fig. 6. It can be seen that the relative percent removal of the dye gradually increased and the adsorption efficiency was nearly 100% with 8–10 mg of the carbon. The adsorption capacity or q_e thus obtained using equation 3.2 was around $300\,mg\,g^{-1}$ of the carbon. This investigation was carried out at pH 4.7. This was the unadjusted pH value was observed when GBC-120 carbon was stirred in methylene blue solution. Further studies were carried out to investigate the effect of pH on probable enhancement in adsorption.

3.2.2. Effect of initial pH

2 mg of GBC-120 carbon was stirred for 2 h with 50 mL of methylene blue solution having concentration of $50\,\mu g\,mL^{-1}$. The pH of the solutions were adjusted in the range 2.6–9.6 using either HCl or NaOH. Fig. 7 shows the percent efficiency of methylene blue at various pH values. It can be seen from Fig. 7 that there is low adsorption efficiency at lower pH values and the adsorption tends towards maximum in the pH range 7–9. Therefore the subsequent adsorption studies were carried out at pH around 7.

The adsorption capacity at pH 7 using Equation (3.2) was $428\,mg\,g^{-1}$.

3.2.2.1. Adsorption following regeneration. GBC-120 was regenerated by treatment with small amount of concentrated H_2SO_4. Further, 10 mg of the regenerated carbon was treated with 20 mL of methylene blue solution of concentration $50\,\mu g\,mL^{-1}$and the pH was adjusted to 7. The adsorption was carried out for 2 h using the original and regenerated carbons. The amount adsorbed in both the cases was found to be around $419\,mg\,g^{-1}$. Thus GBC-120 carbon could be easily regenerated and reused.

3.2.3. Effect of initial methylene blue concentration

Adsorption studies were carried out by equilibriating 2 mg of GBC-120 carbon using 100 mL methylene blue solution having initial concentrations of 10, 20, 30, 40, $50\,\mu g\,mL^{-1}$. The pH of each solution was adjusted to 7. The results are presented in Fig. 8. It can be seen from the figure that the mass of 2 mg carbon could completely remove methylene blue solution from its initial concentration of $10\,\mu g\,mL^{-1}$. This was equivalent to an adsorption capacity of $500\,mg\,g^{-1}$.

3.2.4. Effect of contact time and determination of adsorption equilibrium

The adsorption was studied by equilibriating 20 mg of carbon with methylene blue solution of concentration $50\,\mu g\,mL^{-1}$. The adsorption was studied in two separate experiments in which the pH of the methylene blue solution was 4.7 and 7.0 respectively. The adsorption was carried out for about 15–20 h until no further adsorption occurred as evident from constant absorbance of the supernatant solution. The resulting adsorption time profiles are given in Fig. 9.

At pH 4.7, the amount adsorbed gradually increased and became maximum (about $300\,mg\,g^{-1}$) after about 13 h. It is seen in the previous section that adsorption increases with pH. Hence adsorption

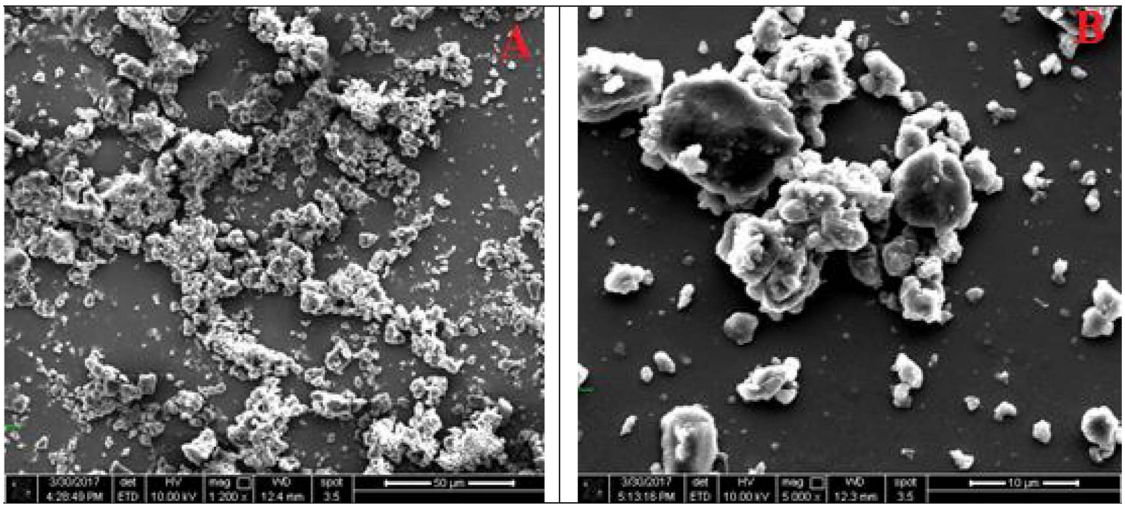

Fig. 5. SEM images of (A) GBC-120 (B) GBC-350.

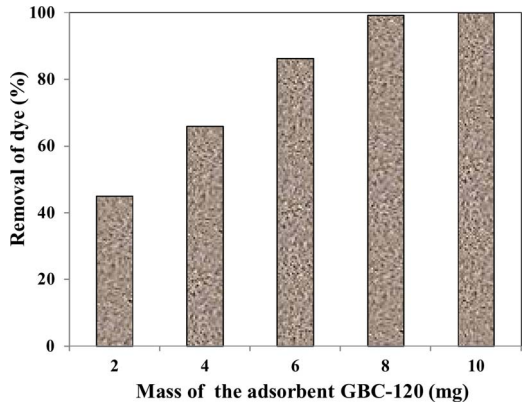

Fig. 6. Effect of amount of adsorbent on adsorption efficiency Volume of adsorbate: 100 mL, Temperature: 298 K, Contact time: 15 h, Initial Conc: 25 μg mL^{-1}.

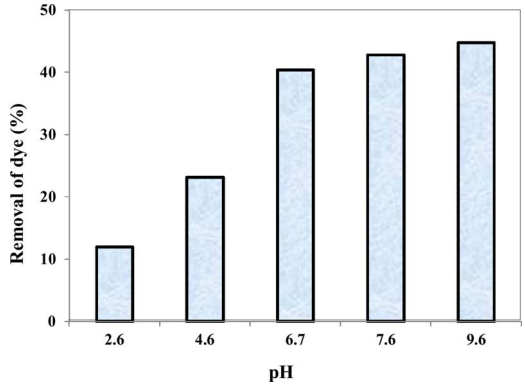

Fig. 7. Relative adsorption efficiency of GBC-120 carbon at different pH values Volume of adsorbate: 50 mL, Dosage of adsorbent: 2 mg, Temperature: 298 K, Contact time: 2 h, Initial Conc: 50 μg mL^{-1}.

equilibrium-time profile was also investigated at pH 7.0. It was seen that adsorption increased at relatively faster rate and equilibrium was reached within 7 h. The amount adsorbed under this condition reached a high value of about 1050 mg g^{-1}. This is noteworthy since the recent literature suggest that maximum adsorption capacity of methylene blue on activated carbon is up to about 580 mg g^{-1}. This high adsorption capacity of GBC-120 is due to its SO_3H functionality. It is shown that when surface functional groups are affected by thermal treatment at 350 °C the adsorption capacity significantly drops to 130 mg g^{-1}.

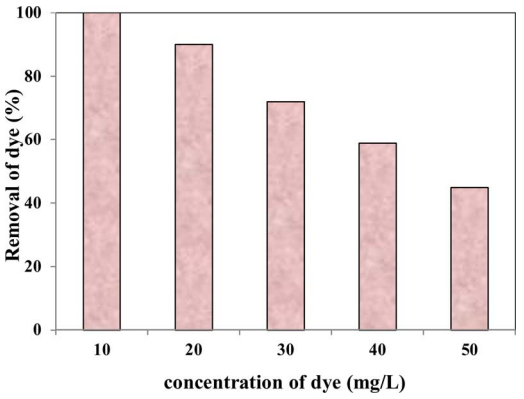

Fig. 8. Effect of intial concentration of methylene blue on adsorption efficiency Volume of adsorbate: 100 mL, Dosage of adsorbent: 2 mg, pH of the solution: 7.0, Temperature: 298 K, Contact time: 15 h.

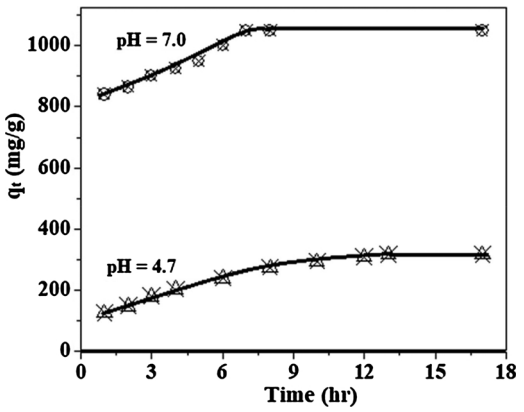

Fig. 9. Kinetic plots obtained when GBC-120 carbon samples were equilibrated with methylene blue solution at pH = 4.7 and 7.0. (q_t is the amounts of dye adsorbed at various time interval t) Volume of adsorbate: 200 mL, Dosage of adsorbent: 2 mg, Temperature: 298 K, Contact time: 15–20 h, Initial concentration = 50 μg mL.

3.3. Adsorption isotherms

An adsorption isotherm is a plot of amount of substance adsorbed per unit mass of adsorbent as a function of various equilibrium concentrations at a specified temperature. Typically an adsorption isotherm falls in one of the six specified categories [46]. Accordingly the plots are classified into Type I, Type II etc. The nature of these plots

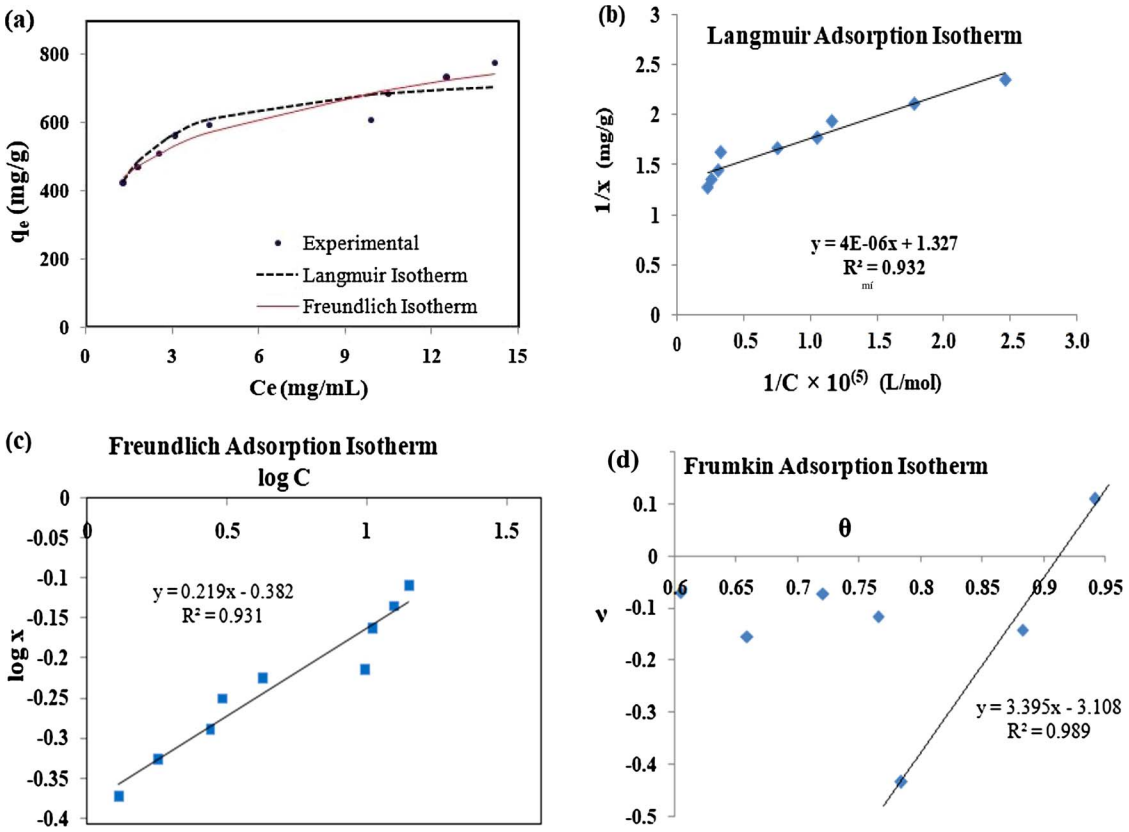

Fig. 10. (a) General adsorption Isotherm and (b-d) Applicability of various adsorption models for adsorption of methylene blue on GBC-120 at 25 °C and pH = 7.

depends on nature of adsorbate and adsorbent. Further the adsorption is influenced by the surface area, porosity and nature of surface functionalities of the adsorbent. Various mathematical expressions are available to describe the nature of adsorption as described in Table 1. Typical adsorption behavior involves Langmuir adsorption. It corresponds to rapid rise in adsorption as concentration increases, and ends up with a plateau region due to saturation of surface adsorption sites. The Freundlich adsorption isotherm extends to further adsorption beyond saturation due to formation of multilayers.

Fig. 10(a) gives the general adsorption isotherm profile observed in this work for adsorption of MB on GBC-120. It showed Type I adsorption behavior in the lower concentration range. Such a behavior is expected for Langmuir adsorption isotherm. However at higher concentration above 10 μg mL^{-1} of the adsorbate, adsorption suddenly increased suggesting an overall Freundlich type of adsorption behavior.

The general adsorption behavior represented above in Fig. 10(a), the experimental points can be fitted in one or more mathematical descriptions of adsorption isotherm models such as those reviewed in Table 1. Fig. 10 (b-d) gives corresponding plots. The data extracted from these plots is presented in Table 4.

It is clear from Fig. 10(b) that the data fitted well for Langmuir adsorption isotherm with coefficient of determination R^2 value of 0.93 and value of Xm obtained from the graph was close to the observed value around 750 mg g^{-1}. The low value of Langmuir adsorption constant K is indicative of predominantly Van der Waals type of adsorption. On the other hand Freundlich adsorption 1/n was about 0.22.1/n which represents intensity of adsorption usually have values between 0 and 1. From the q_e versus C plot (Fig. 10(a)) it is seen that the overall fit is better for Freundlich adsorption isotherm across the full concentration range studied.

However it is seen from Fig. 10(d) that the Frumkin adsorption isotherm fits the experimental data well at higher concentration with coefficient of determination R^2 value of 0.99 with a positive interaction parameter α having a value of 3.9 μg mL^{-1}. This is due to multiple adhesive interactions between the surface SO_3H groups and MB molecules as well as the cohesive attractive interaction between the adsorbed MB multilayers. Evidence for such interactions during adsorption of MB on smectites was reported earlier [47]. Further the high value of α equal to 3.9 is also indicative of lateral interaction between the adsorbate molecules in adjacent layers resulting in greater tendency for desorption or breakdown of the multilayers. This is supported by negative value of β. The various adsorption mechanisms are summarised in Fig. 11.

Table 4
Values of various adsorption isotherm parameters during adsorption of methylene blue on GBC-120.

Volume of adsorbate: 100 mL, Dosage of adsorbent: 2 mg, pH of the solution: 7.0, Temperature: 298 K, Contact time: 15 h

Langmuir		Freundlich		Frumkin	
X_m (mg/g)	754.00	k (mg/g)	415.00	α (μg/mL)	3.90
K (L/mg)	1.00	1/n	0.22	β (μg/mL)	−172.00
R^2 (Linear)	0.93	R^2 (Linear)	0.93	R^2	0.99
R^2 (Non Linear)	0.84	R^2 (Non Linear)	0.97	–	–

3.4. Thermodynamic studies

The evaluation of thermodynamic parameters following adsorption studies have been recently reviewed [50–53]. Thus the free energy change for the adsorption process and the corresponding Langmuir adsorption constant K_L can be shown to be related by the equation [48,50]

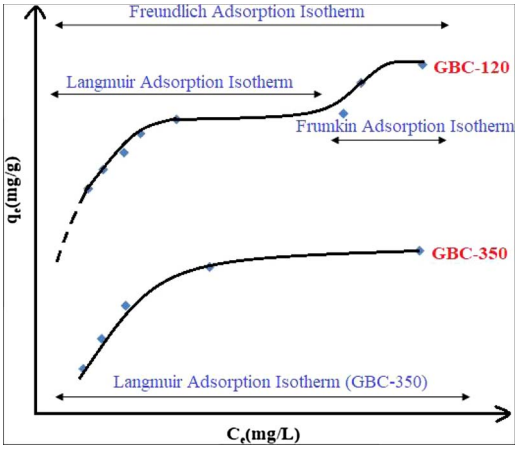

Fig. 11. Summary of the adsorption mechanism discussed in the Section 3.3.

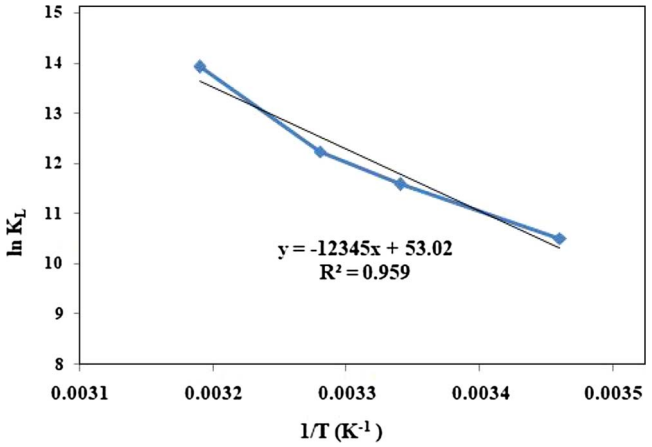

Fig. 12. Plot of ln K_L v/s 1/T for adsorption of methylene blue on GBC-120 at various temperatures between 289 and 323 K.

$$\Delta G^o = -RTlnK_L \tag{3.3}$$

The Langmuir isotherm with the following form has been commonly used for description of adsorption data at equilibrium [50]

$$q_e = q_{max}\ \frac{C_e K_L}{C_e K_L + 1} \tag{3.4}$$

in which q_e and q_{max} are the adsorption capacity of adsorbent at equilibrium (mg g^{-1}) and its maximum value, C_e, is the equilibrium concentration of adsorbate in solution (moles L^{-1}),

K_L can be calculated using the Eq. (3.4) [50]:

$$K_L \frac{\theta_e}{(1-\theta_e)C_e} \quad \text{where} \quad \theta_e = \frac{q_e}{q_{max}} \tag{3.5}$$

Since $\Delta G^o = \Delta H^o - T\Delta S^o$, it follows that the enthalpy of activation and entropy of activation can be evaluated by using the equation

$$lnK_L = -\frac{\Delta H^o}{R}\frac{1}{T} + \frac{\Delta S^o}{R} \tag{3.6}$$

Where R is the universal gas constant (8.314 J mol^{-1} K^{-1}) and T is temperature in Kelvin at which adsorption is carried out. Fig. 12 gives a plot of ln K_L v/s 1/T from which the activation parameters are calculated and are given in Table 5.

It is clear from these values that the free energy change becomes progressively more negative suggesting increasing spontaneity in adsorption as the temperature was increased from 289 K to 323 K. The enthalpy of activation for the adsorption process as calculated from the ln K v/s 1/T plot, was 102 KJ mol^{-1}. This confirmed that the formation of the activated complex during adsorption is an endothermic process.

3.5. Adsorption behavior of GBC-350

GBC-350 is formed by partial decomposition of SO_3H groups from GBC-120. When GBC-350 was stirred in methylene blue solution its pH remained close to 6.5. Fig. 13(a–d) gives the general adsorption isotherm profile and its applicability to various adsorption isotherm models. It showed comparatively low adsorption (~130 mg g^{-1}) which was about 10 times less than that observed for GBC-120.

It can be seen from Fig. 13(a) that there was initial rapid rise in adsorption. This was followed by decrease in adsorption till there was saturation of adsorption. Such a behavior is generally observed during monolayer formation. As expected the Langmuir adsorption model fitted the data more appropriately with R^2 value of 0.95 as compared when other adsorption models, Freundlich and Frumkin were used wherein the R^2 values were found to be generally less than 0.9.

Fig. 14 describes the comparative adsorption behavior of GBC-120 and GBC-350.

It can be seen from the above Figure that GBC-120 showed rapid adsorption in the beginning till it reached equilibrium at the end of 7 h. On the other hand, GBC-350, although showed much lower adsorption, its initial rate of adsorption was much higher as evident from the initial slope of 61 mg g^{-1} h^{-1} as compared to GBC-120 whose initial slope was only 28 mg g^{-1} h^{-1}. The higher equilibrium adsorption of 1050 mg g^{-1} on GBC-120 was due to presence of large amount of $-SO_3H$ as compared to GBC-350, where some surface functionalities were lost upon the thermal treatment.

The adsorption in GBC-350 was to a large extent completed after about 5 h. However complete equilibriation was not reached as there was very small amount of adsorption which occurred very slowly in the time interval of 5–17 h. Hence in GBC-350, it can be considered as a two stage adsorption process (i) initial equilibrium due to high surface area (ii) the second slow equilibrium, due to tendency of MB to diffuse into the micropores that were developed in the sample after heating it at 350 °C as discussed earlier in 3.1. Accordingly, to evaluate the kinetic parameters, the GBC-350 sample is referred to as GBC-350(I) and GBC-350(II). The corresponding adsorption profile is shown resolved in Fig. 14 (inset)

Further GBC-120 showed relatively low pzc value of 2.0 as compared to that of GBC-350 (3.5). Therefore it is expected that the cationic dye MB will be preferentially adsorbed on GBC-120 having large number of highly acidic sulphonyl groups generally in a dissociated

Table 5
Evaluation of thermodynamic parameters during adsorption of methylene blue on GBC-120 at various temperatures.

Volume of adsorbate: 100 mL, Dosage of adsorbent: 2 mg, pH of the solution: 7.0, Contact time: 2 h

T (K)	q_e (mg g^{-1})	C_e (μg mL^{-1})	θ_e	K_L (L mg^{-1})	K_L (L mol^{-1}) × 10^5	ln K_L	1/T × 10^3	ΔG (KJ mol^{-1})	ΔH° (KJ mol^{-1})	ΔS° (KJ mol^{-1})
289	265.40	11.70	0.57	0.12	0.37	10.51	3.46	−26.05	102.00	0.44
299	338.00	8.10	0.73	0.33	1.08	11.58	3.34	−28.70		
304	372.20	6.40	0.80	0.65	2.07	12.24	3.28	−30.33		
313	427.80	3.60	0.92	3.48	11.1	13.92	3.19	−34.49		
323	461.90	1.90	1.00	–	–	–	3.09	–		

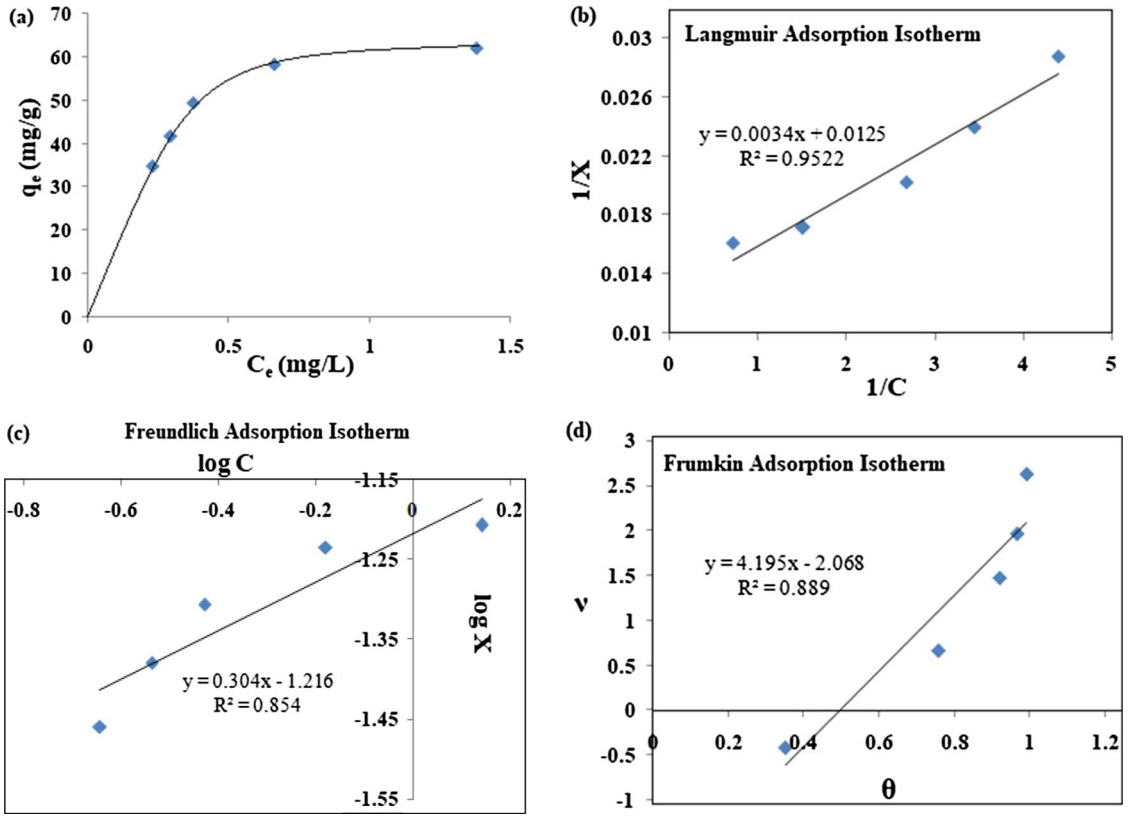

Fig. 13. (a) General adsorption Isotherm and (b-d) Applicability of various adsorption models for adsorption of methylene blue on GBC-350 at 25 °C.

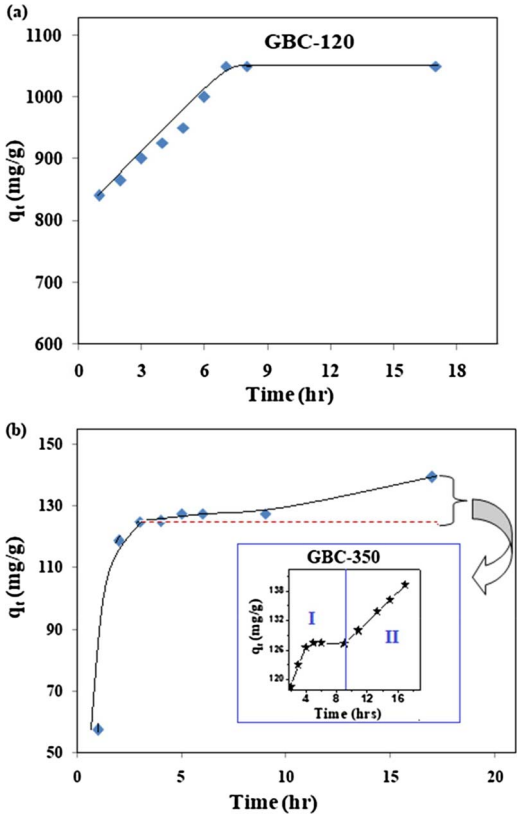

Fig. 14. Comparative investigation of adsorption-time behavior of the glycerol based carbons at 25 °C (a) GBC-120 and (b) GBC-350.

form. The high adsorption in GBC-120 is due to hydrogen bonding between H of $-SO_3H$ functionality on GBC-120 surface and N of the methylene blue dye. A similar hydrogen bonded interaction was proposed during adsorption of methylene blue on iron oxide surface [49]. Further enhanced adsorption is also due to interaction of the cationic dye with the dissociated sulphonyl groups.

3.6. Kinetics of adsorption

The adsorption process from solution generally involves diffusion of the dyes (i) from the bulk solution to near the surface of the adsorbent followed by (ii) diffusion at the boundary layer.

The boundary layer is composed of the surface functionalities of the adsorbent and the pre-adsorbed layer of the adsorbate (MB) as well as the layer of water dipoles. Therefore the boundary layer can offer resistance to diffusion of the adsorbate before the actual adsorption interaction occurs on the available surface sites. (iii) The adsorbate molecules may further diffuse inside the pores of the adsorbent depending upon the nature of adsorbate, adsorbent and equilibriation time [20].

The kinetic data obtained on the GBC samples in the present investigation (Fig. 14) was then fitted in thr first and second order kinetic models (Table 1).

3.6.1. Applicability of pseudo first and pseudo second order kinetic models for GBC-120 and GBC-350

Fig. 15. gives the pseudo first and pseudo second order kinetic plots for GBC-120, GBC-350(I) and GBC-350(II). The resulting kinetic parameters are summarized in Table 7.

It can be seen from the R^2 values that the GBC-120 (Table 6) showed a relatively better fit for pseudo second order kinetics. This is confirmed by the fact that the value of q_e observed is more closer to the calculated value for all the initial concentrations. On the other hand for GBC-350(I), the R^2 values as well as the observed and calculated q_e values differed widely, 29 and 130 mg g^{-1} respectively for pseudo second

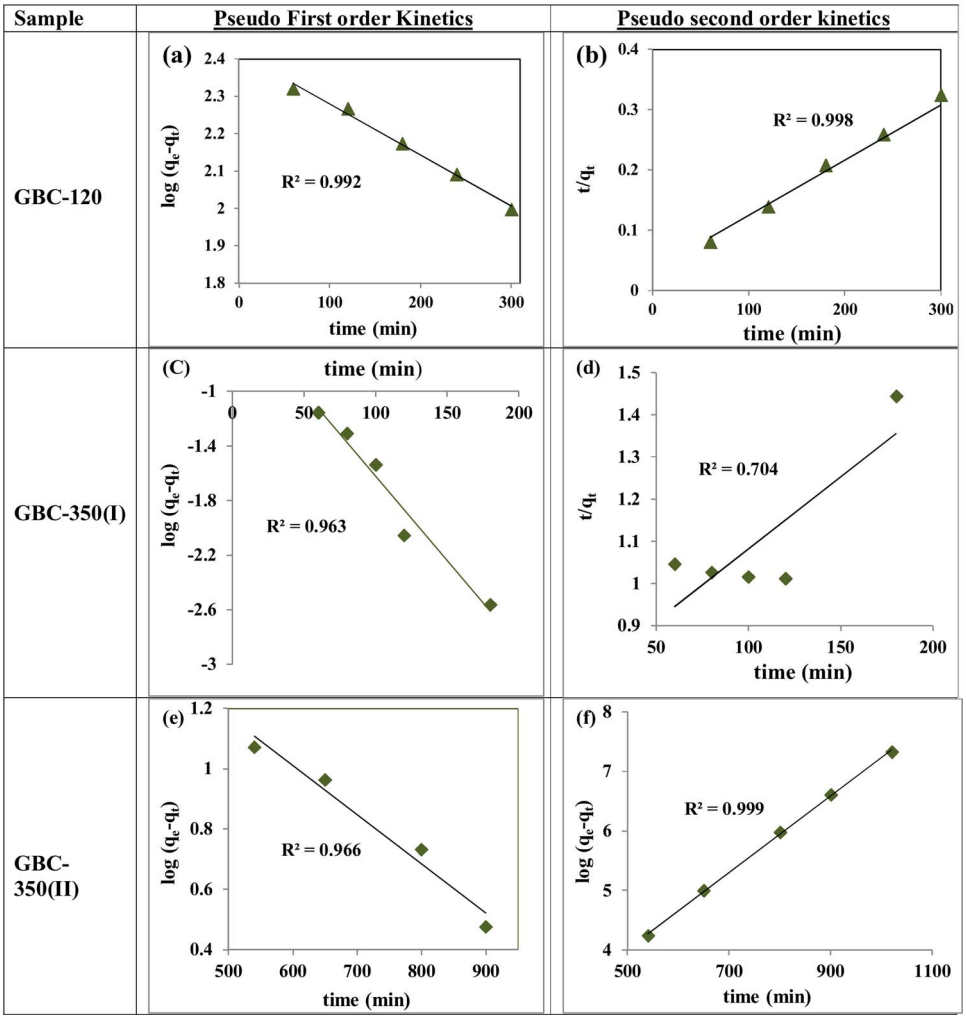

Fig. 15. Application of pseudo first and pseudo second order kinetic models during equilibriation of methylene blue on the GBC samples. GBC-350(I) is initial stage of adsorption and GBC-350(II) is second stage of adsorption.

Table 6
Kinetic parameters obtained from application of pseudo first and pseudo second order kinetic models for adsorption of MB on GBC carbons initial concentration of 50 μg $mL^{-1.}$

Samples	pseudo first order kinetic model			pseudo second order kinetic model			q_e calculated (mg g^{-1})
	R^2	K_1 (min^{-1})	q_e observed (mg g^{-1})	R^2	K_2 (g mg^{-1} min^{-1})	q_e observed (mg g^{-1})	
GBC-120	0.91	0.0046	385	0.99	$4.17*10^{(-5)}$	865	1050
GBC-350 I	0.96	0.0286	408	0.70	$1.56 \times 10^{(-5)}$	029	130
GBC-350 II	0.97	0.0036	098	0.99	$5.14 \times 10^{(-5)}$	156	139

order kinetic model. Thus the adsorption process did not follow first as well as pseudo second order kinetics. However GBC-350(II) showed a good fit for pseudo second order adsorption process ($R^2 = 0.999$) as the observed and calculated values of q_e (156 and 139 mg g^{-1}) were quite close. The investigation of the kinetic data was further extended to some of the other well-known kinetic models.

4. Conclusions

A glycerol based carbon (GBC) was synthesized by partial carbonization of glycerol using con H_2SO_4 in the molar ratio 1:4. The carbonized material was further treated at 120 °C and 350 °C to obtain the carbons GBC-120 and GBC-350 respectively.

The samples were characterized by XRD, ir, thermal analysis (TG-DTG-DTA) and pzc measurements. The TGA showed a gradual weight loss up to about 800 °C. The ir spectra of the GBC-120 showed characteristic absorptions due to $-SO_3H$ groups. The ir spectra were also recorded of GBC samples heat treated at various higher temperatures. All the peaks due to surface functionalities were eventually disappeared for the GBC-800 sample, in agreement with thermal analysis wherein the decomposition was complete around this temperature (800 °C). The BET surface area of GBC-120 was 21 m^2 g^{-1} while GBC-350 showed much larger surface area of about 464 m^2 g^{-1}.

The adsorption studies were carried out using methylene blue as a model adsorbate. The GBC-120 gave maximum adsorption capacity of 1050 mg g^{-1}. The adsorption efficiency was observed to be dependent on initial concentration of the dye. There was nearly 100% dye removal efficiency using 8–10 milligrams of the adsorbent powder, when the dye concentration was 25 μg mL^{-1}.

The GBC-120 showed Type-I adsorption isotherm profile at lower concentration range which obeyed conventional Langmuir adsorption isotherm models. However at higher equilibrium concentration above

10 μg mL^{-1}, the data fits better in Frumkin adsorption model with R^2 value of 0.989 due to large interaction between the adsorbate molecules. The adsorption generally increased with temperature and showed a favorable free energy change.

The GBC-350 showed comparatively less adsorption in spite of its much larger surface area due to loss of SO_3H functionalities. The adsorption data could be fitted in Langmuir adsorption isotherm profile. Investigation of adsorption kinetics revealed better fit with pseudo second order kinetic model for GBC-120 while GBC-350 showed a unique two stage adsorption profile and the data could be better fitted into pseudo second order kinetic model.

This investigation is expected to be an important contribution for further development of glycerol based carbon as an adsorbent, catalyst as well as catalysts support such as in electrocatalysis related to fuel cell where very pure carbon is necessary.

Acknowledgment

We acknowledge University Grant Commission New-Delhi for BSR fellowship F.No.25-1/2014-15 (BSR)/7-09/2007(BSR) to A. A. N.

Appendix A. Supplementary data

Supplementary data associated with this article can be found, in the online version, at https://doi.org/10.1016/j.jece.2018.02.016.

References

[1] K.V. Raghavan, B.M. Reddy (Eds.), Industrial Catalysis and Separations: Innovations for Process Intensification, CRC Press, 2014.
[2] B.L.A. Prabhavathi Devi, K.N. Gangadhar, P.S. Sai Prasad, B. Jagannadh, R.B.N. Prasad, A glycerol-based carbon catalysts for the preparation of biodiesel, ChemsusChem 2 (2009) 617–620.
[3] K. Ramesh, S.N. Murthy, K. Karnakar, K.H. Reddy, Y.V.D. Nageswar, M. Vijay, B.L.A. Prabhavathi Devi, R.B.N. Prasad, A mild and expeditious synthesis of amides from aldehydes using bio-glycerol-based carbon as a recyclable catalyst, Tetrahedron Lett. 53 (2012) 2636–2638.
[4] K.N. Gangadhar, M. Vijay, R.B.N. Prasad, B.L.A. Prabhavathi Devi, Glycerol-based carbon-SO_3H catalyzed benign synthetic protocol for the acetylation of alcohols, phenols and amines under solvent-free conditions, Green Sust. Chem. 3 (2013) 122–128.
[5] C. Ummadisetti, B.N.P. Rachapudi, B.L.A. Prabhavathi Devi, Glycerol-based SO_3H-Carbon Catalyst: a green recyclable catalyst for the chemoselective synthesis of pentaerythritoldiacetals, Eur. J. Chem. 5 (2014) 536–540.
[6] R.S. Ribeiro, A.M.T. Silva, M.T. Pinho, J.L. Figueiredo, J.L. Faria, H.T. Gomesa, Development of glycerol-based metal-free carbon materials for environmental catalytic applications, Catal. Today 240 (2015) 61–66.
[7] S. Álvarez-Torrellas, R.S. Ribeiro, H.T. Gomes, G. Ovejero, J. García, Removal of antibiotic compounds by adsorption using glycerol-based carbon materials, Chem. Eng. J. 296 (2016) 277–288.
[8] Tawfik A. Saleh, Ihsan Budi Rachman, Shaikh A. Ali, Tailoring hydrophobic branch in polyzwitterionic resin for simultaneous capturing of Hg(II) and methylene blue with response surface optimization, Sci. Rep. (2017) 1–15, http://dx.doi.org/10.1038/s41598-017-04624-6 7:4573.
[9] Tawfik A. Saleh, Nanocomposites of carbon nanotubes/silica nanoparticles and their use for adsorption of Pb(II): from surface properties to sorption mechanism, Desalin. Water Treat. (2015) 1–15.
[10] Tawfik A. Saleh, Mercury sorption by silica/carbon nanotubes and silica/activated carbon: a comparison study, J. Water Supply: Res. Technol.-AQUA (2015) 892–903.
[11] Tawfik A. Saleh, Mustafa Tuzen, Ahmet Sari, Magnetic activated carbon loaded with tungsten oxide nanoparticles for aluminum removal from waters, J. Environ. Chem. Eng. 5 (2017) 2853–2860.
[12] Tawfik A. Saleh, Ahmet Sari, Mustafa Tuzen, Optimization of parameters with experimental design for the adsorption of mercury using polyethylenimine modified-activated carbon, J. Environ. Chem. Eng. 5 (2017) 1079–1088.
[13] B.S. Padhi, Ratna, Pollution due to synthetic dyes toxicity & carcinogenicity studies and remediation, Int. J. Environ. Sci. 3 (2012) 940–955.
[14] E. Rindle, W.J. Troll, Metabolic reduction of benzidine azo dyes to benzidine in the Rhesus monkey, J. Natl. Cancer Inst. 55 (1975) 181–182.
[15] M.A.M. Saleh, D.K. Mahmoud, W.A.W.A. Karim, A. Idris, Cationic and anionic dye adsorption by agricultural solid wastes: a comprehensive review, Desalination 280 (2011) 1–13.
[16] M.A. Mohammed, A. Shitu, A. Ibrahim, Removal of methylene blue using low cost adsorbent: a review, Res. J. Chem. Sci. 4 (2014) 91–102.
[17] Z. Zhang, I.M. O'Hara, G.A. Kent, W.O.S. Doherty, Comparative study on adsorption of two cationic dyes by milled sugarcane bagasse, Ind. Crops Prod. 42 (2013) 41–49.
[18] L. Xiong, Y. Yang, J. Mai, W. Sun, C. Zhang, D. Wei, Q. Chen, J. Ni, Adsorption behavior of methylene blue onto titanate nanotubes, Chem. Eng. J. 156 (2009) 313–320.
[19] E.N. El Qada, S.J. Allen, G.M. Walker, Adsorption of Methylene Blue onto activated carbon produced from steam activated bituminous coal: a study of equilibrium adsorption isotherm, Chem. Eng. J. 124 (2006) 103–110.
[20] Z. Shahryari, A.S. Goharrizi, M. Azadi, Experimental study of methylene blue adsorption from aqueous solution on to carbon nanotubes, Int. J. Water Res. Environ. Eng. 2 (2010) 16–28.
[21] Yu X Zhang, X.D. Hao, F. Li, Z.P. Diao, Z.Y. Guo, J. Li, pH-dependent degradation of methylene blue via rational-designed MnO_2 nanosheet-decorated diatomites, Ind. Eng. Chem. Res. 53 (2014) 6966–6977.
[22] Somaye Mashhadi, Hamedreza Javadian, Maryam Ghasemi, Tawfik A. Saleh, Vinod Kumar Gupta, Microwave-induced H_2SO_4 activation of activated carbon derived from rice agricultural wastes for sorption of methylene blue from aqueous solution, Desalin. Water Treat. (2016) 1–14.
[23] A.A. Spagnoli, D.A. Giannakoudakis, S. Bashkova, Adsorption of methylene blue on cashew nut shell based carbons activated with zinc chloride: the role of surface and structural parameters, J. Mol. Liquids 229 (2017) 465–471.
[24] B.H. Hameed, A.T.M. Din, A.L. Ahmad, Adsorption of methylene blue onto bamboo-based activated carbon: kinetics and equilibrium studies, J. Hazard. Mater. 141 (2007) 819–825.
[25] B.H. Hameed, A.L. Ahmad, K.N.A. Latiff, Adsorption of basic dye (methylene blue) onto activated carbon prepared from rattan sawdust, Dyes Pigm. 75 (2007) 143–149.
[26] S. Valliammai, Y. Subbareddy, K.S. Nagaraja, B. Jeyaraj, Removal of methylene blue by activated carbon of Vigna mungo L and Paspalum scobiculatum:equilibrium, kinetic and thermodynamic studies, Indian J. Chem. Technol. 24 (2017) 134–144.
[27] O. Üner, Ü. Geçgel, Y. Bayrak, Adsorption of methylene blue by an efficient activated carbon prepared from *Citrullus lanatus* rind: kinetic, isotherm, thermodynamic, and mechanism analysis, Water Air Soil Pollut. (2016) 227–247.
[28] N. Kannan, M.M. Sundaram, The kinetics and mechanism of methylene blue adsorption on commercial activated carbon (CAC) and indigenously prepared activated, Dyes Pigm. 51 (2001) 25–40.
[29] Ü. Geçgel, G. Özcan, G.Ç. Gürpınar, Removal of methylene blue from aqueous solution by activated carbon prepared from Pea Shells (Pisum sativum), J. Chem. 2013 (2013), http://dx.doi.org/10.1155/2013/614083.
[30] A.H. Jawad, 1R.A. Rashid, M.A.M. Ishak, L.D. Wilson, Adsorption of methylene blue onto activated carbon developed from biomass waste by H_2SO_4 activation: kinetic, equilibrium and thermodynamic studies, Desalin. Water Treat. 57 (2016) 25194–25206.
[31] J.H. Potgieter, Adsorption of methylene blue on activated carbon, J. Chem. Educ. 68 (1991) 349–350.
[32] M. Santhi, P.E. Kumar, Adsorption of basic dye, methylene blue by a novel activated carbon prepared from Typha Angustata, Chem. Sci. Trans. 4 (2015) 389–400.
[33] S.M. Yakout, E. Elsherif, Batch kinetics, isotherm and thermodynamics studies of adsorption of strontium from aqueous solution into low cost rice-straw based carbons, Carbon –Sci. Technol. 14 (2010) 144–153.
[34] Y. Önal, Kinetics of adsorption of dyes from aqueous solutions using activated carbon prepared from the waste apricot, J. Hazard. Mater. B 137 (2006) 1719–1728.
[35] V. Srivastava, P. Maydannik, Y.C. Sharma, M. Sillanppa, Synthesis and applications of polypyrrole coated tenorite nanoparticles (PPy@TN) for the removal of anionic food dye 'tartrazine' and divalent metallic ions viz Pb(II), Cd(II) Zn(II), Co(II), Mn (II) from synthetic wastewater, RSC Adv. 5 (2015) 80829–80846.
[36] Y. Li, Q. Du, X. Wang, P. Zhang, D. Wang, Z. Wang, Y. Xia, Removal of Lead from aqueous solution by activated carbon prepared from Entermorpha Prolifera by zinc chloride activation, J. Hazard. Mater. 183 (2010) 583–589.
[37] L. Wang, X. Li, J. Ma, Q. Wu, X. Duan, N. Non-activated, S-co-doped biochar derived from banana with superior capacitive properties, Sustain. Energy 2 (2014) 39–43.
[38] M. Gonçalves, R. Rodrigues, T.S. Galhardo, W.A. Carvalho, Highly selective acetalization of glycerol with acetone to solketal over acidic carbon-based catalysts from biodiesel waste, Fuel 181 (2016) 46–54.
[39] J.L. Figueiredo, M.F.R. Pereira, M.M.A. Freitas, J.J.M. Órfão, Modification of surface chemistry of activated carbon, Carbon 37 (1999) 1379–1389.
[40] R. Fareghi-Alamdari, M. Golestanzadeh, N. Zekri, Z. Mavedatpoor, Multi SO_3H supported on carbon nanotubes: a practical, reusable, and regioselective catalysts for the tert-butylation of p-cresol under solvent-free conditions, J. Iran. Chem. Soc. 12 (2015) 12537–12549.
[41] P.A. Russo, M.M. Antunes, P. Neves, P.V. Wiper, E. Fazio, F. Neri, F. Barreca, L. Mafra, M. Pillinger, N. Pinna, A.A. Valente, Mesoporous carbon?silica solid acid catalysts for producing useful bio-products within the sugar-platform of biorefineries, Green Chem. 16 (2014) 4292–4305.
[42] H. Guo, Y. Lian, L. Yan, X. Qi, R.L. Smith, Cellulose-derived superparamagnetic carbonaceous solid acid catalyst for cellulose hydrolysis in an ionic liquid or aqueous reaction system, Green Chem. 15 (2013) 2167–2174.
[43] J. Wang, W. Xu, J. Ren, X. Liu, G. Lu, Y. Wang, Efficient catalytic conversion of fructose into hydroxyethylfurfural by a novel carbon based solid acid, Green Chem. 13 (2011) 2678–2681.
[44] L. Na, Z. Jian, Z. Qing-Fang, Quantitative and qualitative analyses of oxygen-containing surface functional groups on activated carbon, Chem. J. Chin. Univ. 3 (2012) 548–554.
[45] H. Park, Y.S. Yun, T.Y. Kim, K.R. Lee, J. Baek, J. Yi, Kinetics of the dehydration of glycerol over acid catalysts with an investigation of deactivation mechanism by coke, Appl. Catal. B 176–177 (2015) 1–10.

[46] S. Brunauer, L.S. Deming, W.S. Deming, E. Teller, Classification of adsorption isotherms, J. Am. Chem. Soc. 62 (1940).
[47] J. Bujdák, M. Janek, J. Madeiová, P. Komadel, Methylene blue interaction with reduced-charged smectites, Clays Clay Miner. 49 (2001) 244–254.
[48] A.S. Özcan, A. Özcan, Adsorption of acid dyes from aqueous solutions onto acid-activated bentonite, J. Colloid Interface Sci. 276 (2004) 39–46.
[49] F. Li, X. Wu, S. Ma, Z. Xu, W. Liu, F. Liu, Adsorption and desorption mechanism of methylene blue removal with iron-oxide coated porous ceramic filter, J. Water Resour. Prot. 1 (2009) 1–57.
[50] Yu Liu,, Is the free energy change of adsorption correctly calculated? J. Chem. Eng. Data 54 (2009) 1981–1985.
[51] Yu Liu, Ya-Juan Liu, Review Biosorption isotherms, kinetics and thermodynamics, Sep. Purif. Technol. 61 (2008) 229–242.
[52] Hui Xu Yu Liu, Equilibrium, thermodynamics and mechanisms of Ni^{2+} biosorption by aerobic granules, Biochem. Eng. J. 35 (2007) 174–182.
[53] E.C. Lima, M.A. Adebayo, F.M. Machado, Kinetics and equilibrium models of adsorption, in: C.P. Bergmann, F.M. Machado (Eds.), Carbon Nanomaterials as Adsorbents for Environmental and Biological Applications, Springer, 2015, pp. 33–69 (ISBN 978-3-319-1887-4, Chapter 3).

Transformation of a Fe–Mn oxide into a ferromagnetic α-Fe_2O_3

Apurva A. Narvekar, S. G. Tilve & J. B. Fernandes

Journal of Thermal Analysis and Calorimetry
An International Forum for Thermal Studies

ISSN 1388-6150

J Therm Anal Calorim
DOI 10.1007/s10973-019-09142-3

Springer

Journal of Thermal Analysis and Calorimetry
https://doi.org/10.1007/s10973-019-09142-3

Transformation of a Fe–Mn oxide into a ferromagnetic α-Fe_2O_3

Apurva A. Narvekar[1] · S. G. Tilve[1] · J. B. Fernandes[1]

Received: 4 July 2019 / Accepted: 1 December 2019

Abstract
The present investigation concerns synthesis of a ferromagnetic Mn^{2+}-doped α-Fe_2O_3 following a co-precipitation method. Thus, an aqueous solution containing Fe^{3+} and Mn^{2+} ions in a molar ratio of 2:1 was precipitated as hydroxides and then dried at 100 °C. The product was characterized by XRD, TEM and TG–DTA. XRD and TEM analysis revealed that the 'as-prepared' material was largely 'amorphous' containing mixed-phase nanoparticles of α-FeOOH and $MnFe_2O_4$. The TG showed mass loss up to 250 °C while the DTA profile exhibited a broad exothermic peak in the temperature range ~ 300–800 °C, suggesting structural transformation. Additional phases were also synthesized by calcination of the initial product, at various temperatures, which were 200 °C, 450 °C, 600 °C and 750 °C. It was observed that in the temperature interval 600–750 °C, the material was transformed to Mn^{2+}-doped α-Fe_2O_3 nanorods and nanoparticles having wide oblong shapes. The results were compared with pure α-Fe_2O_3 which was similarly synthesized without the presence of Mn^{2+}. It was observed that unlike pure α-Fe_2O_3 which was antiferromagnetic, the Mn^{2+}(α-Fe_2O_3) sample was ferromagnetic and showed much higher catalytic activity toward decomposition of hydrogen peroxide. The catalytic decomposition of H_2O_2 could be explained on the basis of Fenton and photo-Fenton effects.

Keywords α-FeOOH · TG–DTA · Ferromagnetic · Mn^{2+} doped · α-Fe_2O_3 · Fenton effect

Introduction

Iron oxides continue to evoke considerable interest due to their technological importance in several areas as well as because of their ease of availability and generally low-cost synthesis. They are attractive as they possess tunable properties such as optical, electrical, magnetic, electrochemical and catalytic. They become particularly relevant owing to non-toxicity, biocompatibility, chemical inertness, environmentally friendly nature [1]. The range of magnetic as well as electrical properties owned by transition metal oxides is significant. Among various polymorphic forms of ferric oxide, the most abundant forms, α-Fe_2O_3 (hematite) and γ-Fe_2O_3 (maghemite), are most widely investigated [2, 3]. The former is having advantage of higher stability while the latter, even though it is a metastable form, is often more desired owing to its high saturation magnetization which is often in the range 40–80 emu g^{-1}. The magnetism varies upon the methods of synthesis. Further, α-Fe_2O_3 is antiferromagnetic below Morin temperature (260 K) and shows a very weak ferromagnetic behavior (< 1 emu g^{-1}) between 260 K and the Neel temperature (950 K). The enhancement in magnetic behavior is also seen following divalent transition metal ion doping such as Mn^{2+} and Cu^{2+} [4]. Various properties and applications of α-Fe_2O_3 have been recently reviewed [5].

Further, enhancement in one or more properties is often achieved by employing suitable synthetic strategies and/or preparing doped metal oxides [8–10]. Several methods have also been adopted for synthesis of iron–manganese oxides and manganese ferrites to obtain materials of higher magnetism and catalytic activity [2–7]. Yuping et al. reported formation of a mixture of α-Fe_2O_3 and $MnFe_2O_4$ phases produced from a Fe–Mn containing slurry whose magnetic properties could be of interest as catalysts or as catalyst support material [11]. Iron–manganese mixed oxide catalysts were also studied for catalytic combustion of ethanol, and the catalytic activity was found to be greatly influenced by the Fe:Mn ratio of the mixed oxide formed [12] and several other catalytic processes [13, 14]. Fe(III) oxides are well known to show high activity for catalytic decomposition of H_2O_2 [15, 16], the activity being dependent on surface area

✉ S. G. Tilve
stilve@unigoa.ac.in

[1] School of Chemical Sciences, Goa University, Taleigao Plateau, Goa 403206, India

Published online: 11 December 2019

and particle sizes [17, 18]. Several synthetic strategies have been adopted to obtain hematite of high reactivity, such as surfactant-assisted synthesis [16], combustion synthesis [19, 20], sol–gel method [21, 22] and co-precipitation method [23]. These methods have to be chosen considering their cost-effectiveness and methods that would avoid or minimize emission of hazardous gases. The recent trend is to adopt simple aqueous solution methods of co-precipitation to obtain α-Fe_2O_3, as that affords better control over synthesis conditions, product morphology and particle sizes [23, 24].

The present investigation deals with a co-precipitation synthesis approach to obtain a ferromagnetic α-Fe_2O_3 by Mn^{2+} doping. The synthesis parameters such as temperature of calcinations are aided through TG–DTA analysis of its Fe–Mn oxide precursor. The Mn^{2+}-doped α-Fe_2O_3 thus obtained showed enhanced catalytic and photo-Fenton activity in addition to its ferromagnetic behavior.

Experimental

Synthesis

In a typical synthesis, 0.05 mol of $MnCl_2.4H_2O$ and 0.1 mol of $FeCl_3$ (anhydrous) were mixed in 100 mL of distilled water. The resulting solution was added dropwise into NaOH (0.80 mol) solution under constant stirring. The brownish black suspension thus obtained was kept for digestion for 3 h. It was then filtered and washed till the filtrate was free of chloride and dried at 100 °C for 5 h. This 'as-prepared' sample (designated as MF1) was divided into several portions for further treatment at various elevated temperatures such as 200 °C, 450 °C, 600 °C and 750 °C. For convenience, the samples thus obtained were labeled as MF2, MF4, MF6 and MF7, respectively. (The simplified codes were indicative of M for Mn and F for Fe, and the numerals 1, 2, 4, 6 or 7 were used to represent the first numeral of the temperatures used for thermal treatments.)

Pure α-Fe_2O_3 was synthesized by similar method wherein 0.1 mol of $FeCl_3$ solution was added dropwise to 0.8 mol of NaOH solution kept on a magnetic stirrer. It was further washed and dried at 100 °C, and a part of it was further calcined at 600 °C in air for 2 h. These products were labeled as F1 and F6, respectively.

Characterization

The characterization of the samples was carried out using various techniques. X-ray diffractometer (a Rigaku Ultima IV diffractometer) with Cu Kα radiation was used to determine phase structures of the samples. The magnetic properties of the samples were measured at 27 °C using a vibrating sample magnetometer (Quantachrome Versa Lab). Thermal analysis was carried out using TG–DTA analyzer (NETZSCH STA 409 PC) in oxygen atmosphere at the heating rate 10 °C min^{-1}. Scherrer density was calculated using formula $d = 8M/NV$ (M is molar mass, N is Avogadro's number and V is volume of the unit cell). In order to determine surface area and pore characteristics of the synthesized samples, Brunauer–Emmett–Teller (BET) isotherms were studied. The morphology of the samples was identified by TEM. The percentage of Mn and Fe was obtained from ICP-AES analysis, and the data were correlated with values obtained from chemical analysis. Thus, % Mn was determined by EDTA complexometric titration using thymolphthalexone indicator while % Fe was determined by colorimetry using KSCN. The catalytic activity of the samples was determined by their ability to decompose H_2O_2. Thus, 10 mg of the catalyst was stirred in 20 mL of 0.1 M KOH and 1 mL of 20 volume H_2O_2. The evolved gas was measured by exposing the solution to sunlight. The experiments were also repeated in the absence of sunlight. The catalytic activity of the synthesized samples was expressed in terms of volume of O_2 gas evolved in a given time interval.

Result and discussion

Synthesis, thermal and XRD analysis of the Fe–Mn oxides

As iron and manganese oxides or their mixed phases continue to evoke considerable attention over the years, the present investigation was undertaken to elucidate structural parameters of a typical iron–manganese oxide following a conventional synthesis. The starting molar composition was 2:1 for Fe:Mn. Thus, the metal salts were precipitated in alkaline medium and the resulting product was characterized by thermal analysis.

Figure 1 gives TG–DTA profile of the 'as-prepared' Fe–Mn oxide material (MF1) recorded in air from ambient temperature up to 1000 °C.

The TG profile of MF1 (Fig. 1a) showed rapid mass loss up to about 180 °C, which was mainly due to loss of physisorbed and hydrogen-bonded water. There was no significant further mass loss up to 1000 °C. However, examination of the corresponding DTA profile revealed a broad exothermic peak in the above temperature range with a maximum at ~600 °C. This suggested occurrence of some structural transformation around this temperature. Hence, in modified synthesis, the 'as-prepared' sample MF1 was further investigated by heat treatment in air at 600 °C and 750 °C for 2 h. The resulting products were designated as MF6 and MF7, respectively. It may be noted that the corresponding sample F1 (prepared without Mn) also shows an exothermic profile in a narrower temperature range with a maximum at

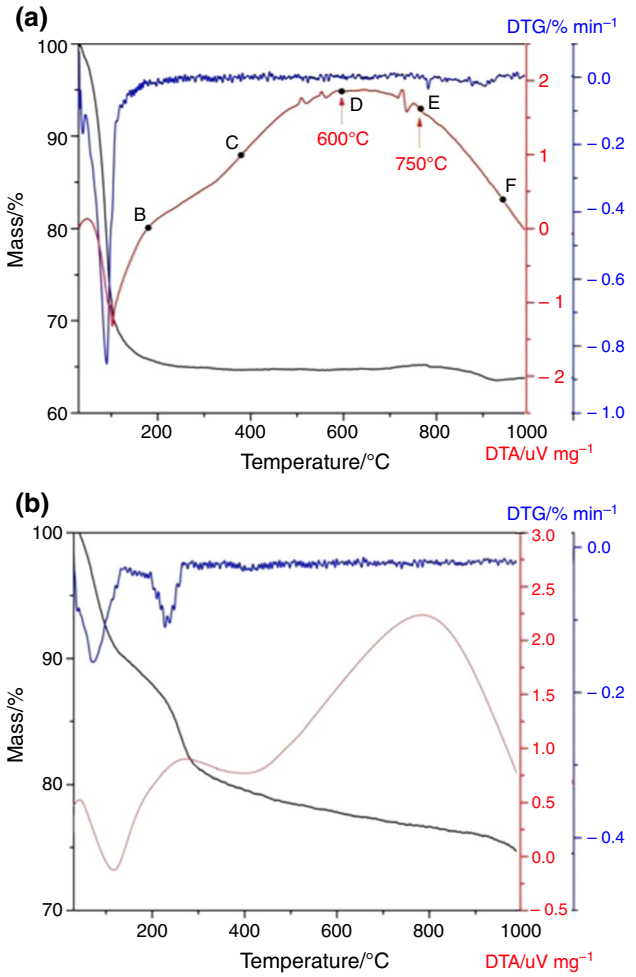

Fig. 1 **a** TG–DTA–DTG curves of the synthesized Fe–Mn oxide (MF1) obtained in air atmosphere in the temperature range of 30–1000 °C. **b** Corresponding thermal analysis profiles of iron oxide sample (F1)

around 800 °C. This underlines the crucial role Mn plays in the structural transformation of Fe–Mn oxide as elaborated below in 'TEM in relation to XRD analysis' and 'Transformation of Fe–Mn oxide in Mn-doped α-Fe_2O_3' sections.

The samples MF1, MF6 and MF7 were further characterized by XRD as shown in Fig. 2.

For comparison, the sample F1 was prepared in the same way as MF1, but without the presence of Mn. It is seen from Fig. 2b that the undoped iron oxide (F1) showed a relatively amorphous pattern with peak characteristic of α-FeOOH phase (JCPDS card number 29-0713). On the other hand, the diffraction peaks in the 'as-prepared' material MF1 were observed at 2θ values of 30.20, 35.45, 43.22, 53.59, 62.65 degree corresponding to Miller indices (220), (311), (400), (422) and (440), reminiscent of cubic $MnFe_2O_4$ phase (JCPDS Card. 10-0319) [1].

Thus, MF1 was essentially an amorphous manganese ferrite in which the 100 intensity peak was observed at 2θ value ~ 35. In addition, three other peaks were also observed at 2θ ~ 22, 34 and 36, which were characteristic peaks due to α-FeOOH as mentioned earlier. Thus, MF1 is in fact a mixed phase due to $MnFe_2O_4$ + FeOOH.

However, the XRD profile of the heat-treated sample at 600 °C (MF6) exhibited a characteristic diffraction pattern for α-Fe_2O_3 phase (JCPDS card 33-0664) [5]. In MF6, there is also the presence of a small peak at 2θ ~ 35 due to the presence of some residual Mn ferrite phase. Thus, XRD analysis confirms that the amorphous Fe–Mn mixed oxide following heat treatment beyond 600 °C gets transformed to Mn-doped α-Fe_2O_3 phase. Thus, MF6 is essentially an α-Fe_2O_3 with a trace of $MnFe_2O_4$. When the sample was further heated to 750 °C (MF7), no significant change in the XRD pattern was observed, but the XRD peaks became sharper indicating better crystallization of the α-Fe_2O_3 phase. Also the characteristic peak due to $MnFe_2O_4$ at 2θ ~ 35 completely disappears as temperature was raised to 750 °C, thus indicating formation of pure α-Fe_2O_3 phase at this temperature.

TEM in relation to XRD analysis

Figure 3 gives the TEM images of the pure and Mn-doped iron oxide samples.

The details of TEM characteristics and XRD analysis are summarized in Table 1.

It is shown above from XRD analysis that F1 is an α-FeOOH phase. The TEM image of F1 indicates that it is formed as a cluster of nanorods. However, when synthesis was carried out in the presence of Mn^{2+} to obtain MF1, a mixed phase of α-FeOOH and $MnFe_2O_4$ was observed. The TEM image of MF1 supports this observation wherein α-FeOOH component was present as nanorods embedded in a diffuse cloud-like dispersion due to particles of the amorphous manganese ferrite. Further, when MF1 was heat-treated at 600 °C to obtain MF6, a structural transformation occurred and the amorphous ferrite phase as well as the α-FeOOH got transformed into α-Fe_2O_3 having a trace of $MnFe_2O_4$. The TEM image of MF6 revealed better resolved nanorods of the α-Fe_2O_3 phase and the manganese ferrite cloud getting almost vanished. It is clear from Fig. 3a or from the particle dimensions presented in Table 1 that the length of nanorods increased from 240 to 450 nm in MF6 and its aspect ratio was nearly double, from 3.4 to 6.0. Further, the TEM image of MF7 which is Mn^{2+}-doped α-Fe_2O_3 shows disappearance of nanorods and the particles acquired wide oblong shapes with the width of nanoparticles getting doubled from ~ 70 to 140 nm. This is associated with the doping of Mn^{2+} into the structure of α-Fe_2O_3. On the other hand, the undoped iron oxides α-Fe_2O_3 (F6 or F8) continue to be nanorods as shown in Fig. 3b. It is also observed that the undoped iron oxide showed brighter and well-defined electron diffraction rings. However, electron diffraction

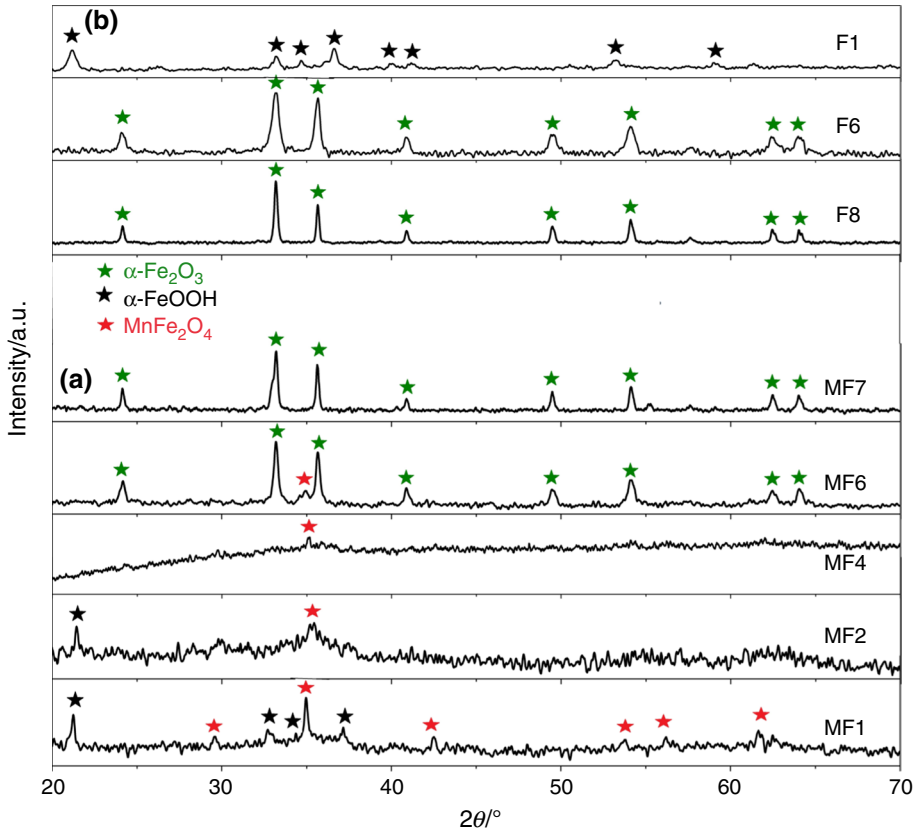

Fig. 2 X-ray powder diffraction pattern of Fe–Mn oxides (a) as Fe–Mn oxide mixed phase (MF1) gets transformed to MF7 which is Mn-doped α-Fe_2O_3, (b) synthesized iron oxides in the absence of Mn wherein α-FeOOH (F1) gets transformed to α-Fe_2O_3 (F6 and F8)

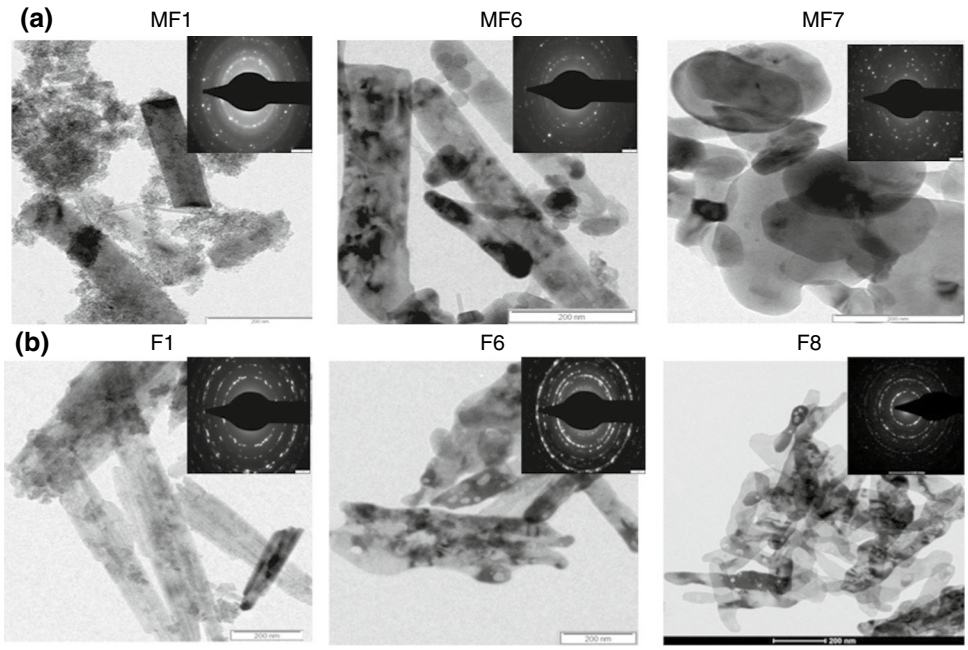

Fig. 3 **a** TEM images and electron diffraction pattern (inset) of the Mn containing iron oxide samples. MF1 was a mixed oxide obtained by co-precipitation from Fe(III) and Mn(II) salts followed by drying the product at 100 °C. MF6 was obtained by calcination of MF1 at 600 °C. MF7 was prepared by heating MF1 in air at 750 °C. **b** The iron oxide F1 was prepared by precipitation from Fe(III) salt and drying at 100 °C. F6 was obtained by calcination of F1 at 600 °C. F8 was prepared by heating F1 in air at 800 °C where MF1 is (α-FeOOH + $MnFe_2O_4$); MF6 or MF7 was Mn^{2+}(α-Fe_2O_3); F1 is α-FeOOH (goethite) and F6 and F8 were undoped α-Fe_2O_3

pattern in the presence of Mn is relatively diffused and less intense.

Transformation of Fe–Mn oxide in Mn-doped α-Fe_2O_3

To understand the transformation of the mixed-phase sample MF1 into α-Fe_2O_3 at 600 °C, two additional samples were

Table 1 Synthesis, XRD and TEM characteristics of the Fe–Mn oxide samples

Code[a]	Temp of thermal treatment of MF1 or F1/°C	Oxide phases	Scherrer crystallite sizes/nm	TEM shapes	Average TEM particle size/nm			Density	
					Length	Width	Aspect ratio	XRD density/g cm^{-3}	Tap density/g cm^{-3}
(a) Fe–Mn oxides									
MF1	100	α-FeOOH + $MnFe_2O_4$	22.4	Nanorods in diffuse cloud	240	70	3.4	4.9	0.91
MF6	600	α-Fe_2O_3 + $MnFe_2O_{4(trace)}$	28.1	Nanorods	450	75	6.0	7.1	1.13
MF7	750	Mn^{2+}(α-Fe_2O_3)	25.2	Wide oblong	200	140	1.4	7.1	1.33
(b) Iron oxides without Mn									
F1	100	α-FeOOH	18.9	Nanorods	550	55	10.0	6.4	0.60
F6	600	α-Fe_2O_3	19.5	Nanorods	500	70	7.1	5.2	0.58
F8	800	α-Fe_2O_3	28.6	Nanorods	400	85	4.7	5.2	0.63

[a]The simplified codes are indicative of M for Mn, F for Fe, and the numerals 1, 2, 4, 6, 7 or 8 were used for convenience, to represent the first numeral of the temperatures used for thermal treatments MF1 was obtained by co-precipitation from aqueous solution of Fe^{2+} and Mn^{2+} in molar ratio of 2:1 followed by thermal treatment at 100 °C. Samples MF2 and MF4 were also synthesized by calcinations of MF1 at 200 °C and 450 °C, respectively. F1 was similarly prepared but without the presence of Mn^{2+}

synthesized by thermal treatment of MF1 at 200 and 450 °C. This corresponds to the temperatures around the region BC in the DTA profile (Fig. 1). The resulting samples designated as MF2 and MF4 were further characterized by XRD. Their XRD profiles are also presented in Fig. 2. It is seen from the profile of MF2 in Fig. 2a that most of the peaks disappeared and the XRD profile was largely amorphous. The main peaks of α-FeOOH at about $2\theta \sim 22$ and those of $MnFe_2O_4$ around $2\theta \sim 35$ were greatly diminished in intensity. At 450 °C, as evident in the XRD profile of MF4, the peaks due to α-FeOOH completely disappeared and only a trace of $MnFe_2O_4$ peak was present. Further comparisons of XRD profiles of the MF1 to MF7 samples in Fig. 2a indicate disappearance of peaks due to $MnFe_2O_4$, especially in the 2θ region between 30° and 40°. This is accompanied by appearance of peaks due to α-Fe_2O_3. This structural transformation is summarized in Scheme 1.

Bulk manganese ferrite $MnFe_2O_4$ is known to have chemical composition close to normal spinel (fcc close packed structure) with about 20% of Mn^{2+} present in the octahedral sites, exchanging places with the Fe^{3+} going into tetrahedral sites as in $[Mn^{2+}_{0.8}{\cdot}Fe^{3+}_{0.2}]_t$ $[Mn^{2+}_{0.2}{\cdot}Fe^{3+}_{1.8}]_{oct}$ O_4. On the other hand, α-Fe_2O_3 is a hematite structure with 1/3 vacant octahedral sites in its hcp structure of O^{2-} ions. When $MnFe_2O_4$ component of MF1 or MF6 gets homogenized into MF7 to form a pure α-Fe_2O_3 phase, it has to occur via a rearrangement of oxygen ion close packing from ccp to hcp type. During the process, Mn^{2+} ions would diffuse into the available vacant sites resulting into formation of Mn^{2+}-doped α-Fe_2O_3. Such diffusion of Mn^{2+} ions was also proposed during calcinations of a sol–gel synthesized manganese ferrite [25].

Surface area and porosity

To understand the surface properties, the synthesized materials were characterized by BET measurements. The surface area and pore characteristics obtained from adsorption–desorption isotherms (Fig. 4) are presented in Table 2. It is seen that the 'as-prepared' samples F1 and MF1 showed large surface areas in the range 150–180 m^2 g^{-1}. They showed

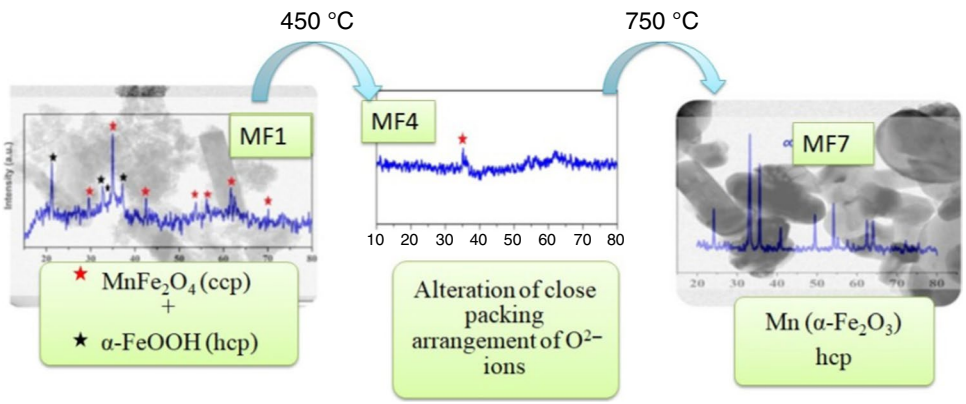

Scheme 1 Structural transformation of the 'as-prepared' sample MF1 into a Mn^{2+}-doped α-Fe_2O_3 (MF7); ccp and hcp in the illustration are indicative of structures formed by cubic and hexagonal close packing of O^{2-} ions, respectively

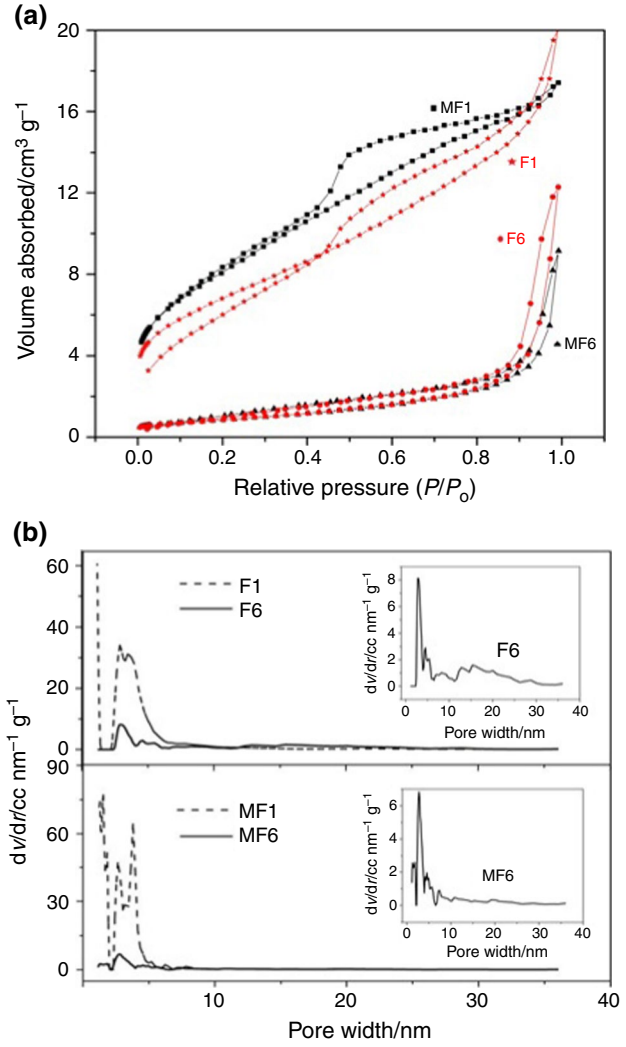

Fig. 4 **a** N_2 adsorption desorption isotherms and pore size distribution profiles of the synthesized samples. **b** Pore size distribution plots of the synthesized samples where MF1 is (α-FeOOH + $MnFe_2O_4$); MF6 is Mn^{2+}(α-Fe_2O_3); F1 is α-FeOOH and F6 is undoped α-Fe_2O_3

type II b adsorption isotherm profiles [26, 27] with well-defined hysteresis loops (similar to H4 type) in the P/P_o range of 0.4 to 1.0. This indicates the presence of mesopores with no well-defined pore structure. The corresponding heat-treated samples F6 as well as the Mn^{2+}-doped α-Fe_2O_3 sample MF6 showed much lower surface areas ~ 20–30 $m^2\ g^{-1}$. Their adsorption–desorption profiles indicated very low N_2 adsorption. They were of type III with small hysteresis loop (type H3) in the P/P_o range of 0.8–1.0. The low surface area and porosity of MF6 and MF7 are attributed to its high density achieved due to filling of the voids by Mn^{2+} doping during the thermal transformation. This is in agreement with an earlier result that higher temperatures induce migration of Mn^{2+} ions from tetrahedral sites into octahedral sites [25, 28]. Further, from pore size distribution plots (insets in Fig. 4b), it is observed that both pure α-Fe_2O_3 (F6) and Mn^{2+}-doped α-Fe_2O_3 (MF6) are mesoporous in nature. However, in MF6, maximum percentages of pores were ranging from 2.5 to 6 nm with average pore radius being 2.8 nm. On the other hand, the range in F6 is wider, i.e., pore size ranges from 2 to 30 nm with average pore radius being 16 nm. As a result, F6 showed larger pore volume of 0.20 $cm^3\ g^{-1}$ as compared to Mn^{2+} containing α-Fe_2O_3 which showed a pore volume of < 0.07 $cm^3 g^{-1}$.

Magnetic behavior and catalytic activity

The magnetic characteristics of the samples are presented in Fig. 5 and Table 2. It can be seen from the figure that the 'as-synthesized' Fe–Mn oxide sample (MF1) was ferromagnetic having saturation magnetization of 12.7 emu g^{-1}. When it was transformed to Mn^{2+}-doped α-Fe_2O_3 (MF6 or MF7), the ferromagnetic behavior was slightly less (~ 8 emu g^{-1}). However, the undoped α-Fe_2O_3 did not show such ferromagnetic behavior.

The catalytic activity of the samples was investigated for their ability to decompose hydrogen peroxide. The reaction was carried out in alkaline medium both in the presence

Table 2 Synthesis and catalytic activity of the samples in relation to surface area, porosity and magnetic characteristics

Code	Oxide phases	Surface area/$m^2\ g^{-1}$	Pore size/nm	Pore volume/$cm^3\ g^{-1}$	Magnetization characteristics			Catalytic activity in terms of volume of O_2 evolved after 4 min of H_2O_2 decomposition reaction/mL	
					M_s/emu g^{-1}	M_R/emu g^{-1}	H_C/Oe	Sunlight	Dark
MF1	$MnFe_2O_4$ + α-FeOOH	177	3.8	0.20	12.7	0.83	146	24.0	20
MF6	α-Fe_2O_3 + $MnFe_2O_{4(trace)}$	19	2.8	0.07	8.4	0.16	10.4	12.6	10.5
MF7	Mn^{2+}(α-Fe_2O_3)	21	1.9	0.03	7.9	0.07	9.6	25.0	19.4
F1	α-FeOOH	159	3.8	0.23	10.0	–	–	2.7	0.0
F6	α-Fe_2O_3	32	16	0.20	0.68	0.02	568	6.0	1.5

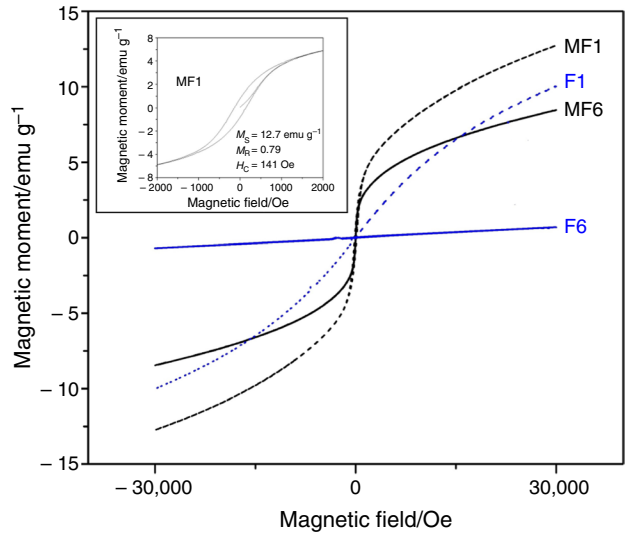

Fig. 5 Room temperature magnetization curves of the synthesized Fe–Mn and iron oxide samples where MF1 is (α-FeOOH + $MnFe_2O_4$); MF6 or MF7 was Mn^{2+}(α-Fe_2O_3); F1 is α-FeOOH and F6 is undoped α-Fe_2O_3

and in the absence of sunlight as iron oxides are known to decompose H_2O_2 through Fenton or photo-Fenton process. This reaction is relevant to advance oxidation processes [29]. The relative catalytic activity is evident from the activity profiles presented in Fig. 6.

It can be seen from the figure that all the samples show significant catalytic activity. The doped sample MF7 or Mn^{2+}(α-Fe_2O_3) was most active as compared to the corresponding undoped sample F6. Fe^{3+} ion is known to decompose hydrogen peroxide [15], as per reaction (1) in scheme 2. In alkaline medium, the ferric ion from the

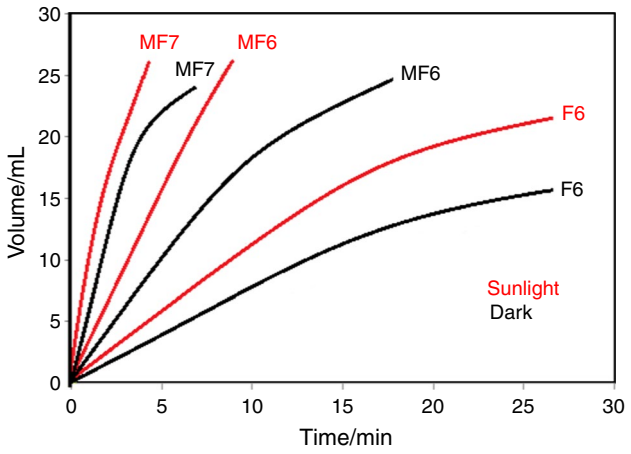

Fig. 6 Catalytic activity of the Mn-doped α-Fe_2O_3 samples MF6 and MF7 in relation to the corresponding undoped iron oxide, for decomposition of H_2O_2 in the presence and in the absence of sunlight where MF6 or MF7 was Mn^{2+}(α-Fe_2O_3) and F6 is undoped α-Fe_2O_3

$$Fe^{3+} + \tfrac{1}{2}\,H_2O_2 \longrightarrow Fe^{2+} + H^+ + \tfrac{1}{2}\,O_2 \quad (1)$$

$$Fe^{3+} + \tfrac{1}{2}\,H_2O_2 + OH^- \longrightarrow Fe^{2+} + H_2O + \tfrac{1}{2}\,O_2 \quad (2)$$

$$(Fe^{3+} + e^- \longrightarrow Fe^{2+} \text{ and } \tfrac{1}{2}\,H_2O_2 - e^- + OH^- \longrightarrow H_2O + \tfrac{1}{2}\,O_2)$$

$$Fe^{2+} + H_2O_2 \longrightarrow Fe^{3+} + OH^- + HO^* \quad (3)$$

$$HO^* + H_2O_2 \longrightarrow H_2O + HO_2{}^* \quad (4)$$

$$HO_2{}^* + Fe^{3+} \longrightarrow Fe^{2+} + O_2 + H^+ \quad (5)$$

Considering the equations (2), (3), (4) and (5), we can write

$$H_2O_2 \xrightarrow{Fe_2O_3(s)} H_2O + \tfrac{1}{2}\,O_2 \quad (6)$$

Scheme 2 Mechanism of decomposition of hydrogen peroxide

surface of Fe_2O_3(s) catalyst interacts with H_2O_2 resulting in the formation of Fe^{2+} as shown in the reaction (2). The reduction of ferric ion is accompanied by evolution of O_2. The Fe^{2+} species generated as per equation (2) causes further decomposition of H_2O_2 through intermediate formation of HO* and HO_2* species as illustrated in the above scheme. The presence of Mn^{2+} in the structure would further enhance the rate of O_2 evolution due to similar reactions occurring in the presence of the Mn^{2+}/Mn^{3+} redox couple.

In the present investigation, it is thus seen that the Mn^{2+} (α-Fe_2O_3) is much more reactive than the pure or undoped α-Fe_2O_3. When the reaction was studied in the presence of sunlight, the reactivity increased further due to photo-Fenton effect wherein the generated conduction band electrons would produce additional reactive intermediates (Fe^{2+} and OH*). Thus, the Mn^{2+}-doped α-Fe_2O_3 sample synthesized in this work was ferromagnetic with high catalytic activity.

Summary and conclusions

1. Mn^{2+}-doped ferromagnetic α-Fe_2O_3 nanoparticles having saturation magnetization around 8 emu g^{-1} have been synthesized by an economical and eco-friendly co-precipitation route. The synthesis involved addition of Fe(II) and Mn(II) chlorides in a molar ratio of 2:1 to an aqueous solution of alkali, and the resulting precursor MF1 was dried and characterized by TG–DTA and XRD.
2. The investigation revealed that the synthesized precursor was a mixed phase of (α-FeOOH + $MnFe_2O_4$) which when calcined beyond 600 °C got transformed into Mn^{2+}(α-Fe_2O_3) nanorods and particles with wide oblong shapes. The corresponding iron oxide synthe-

sized without Mn produced only nanorods having no such ferromagnetic character ($M_s \sim 0.8$ emu g^{-1}).

3. The $Mn^{2+}(\alpha\text{-}Fe_2O_3)$ nanoparticles showed high catalytic activity toward decomposition of H_2O_2, and the catalyst being ferromagnetic could be easily recovered. The activity was further enhanced when the catalytic reaction was carried out in the presence of sunlight due to photo-Fenton process.

Acknowledgements Authors are thankful to University Grant Commission, New Delhi, for BSR fellowship F.No.25-1/2014-15 (BSR)/7-09/2007(BSR) to A.A.N.

References

1. Mirzaei A, Janghorban K, Hashemi B, Hosseini SR, Bonyani M, Leonardi SG, Bonavita A, Neri G. Synthesis and characterization of mesoporous $\alpha\text{-}Fe_2O_3$ nanoparticles and investigation of electrical properties of fabricated thick films. Process Appl Ceram. 2016;10(4):209–17.
2. Bepari RA, Bharali P, Das BK. Controlled synthesis of α- and $\gamma\text{-}Fe_2O_3$ nanoparticles via thermolysis of PVA gels and studies on $\alpha\text{-}Fe_2O_3$ catalyzed styrene. J Saudi Chem Soc. 2017;21:170–8.
3. Sakurai S, Namai A, Hashimoto K, Ohkoshi S. First observation of phase transformation of all four Fe_2O_3 phases ($\gamma \rightarrow \varepsilon \rightarrow \beta \rightarrow \alpha$-phase). J Am Chem Soc. 2009;51:18299–303.
4. Ramya SI, Mahadevan CK. Preparation and structural, optical, magnetic, and electrical characterization of $Mn^{2+}/Co^{2+}/Cu^{2+}$ doped hematite nanocrystals. J Solid State Chem. 2014;211:37–50.
5. Wheeler DA, Wang G, Ling Y, Li Y, Zhang JZ. Nanostructured hematite: synthesis, characterization, charge carrier dynamics and photoelectrochemical properties. Energy Environ Sci. 2012;5:6682–702.
6. Deraz NM, Alarifi A. Controlled synthesis, physicochemical and magnetic properties of nanocrystalline and Mn ferrite system. Int J Electrochem Sci. 2012;7:5534–43.
7. Zipare K, Dhumal J, Bandgar S, Mathe V, Shahane G. Superparamagnetic manganese ferrite nanoparticles: synthesis and magnetic properties. J Nanosci Nanoeng. 2015;1:178–82.
8. Glasscock JA, Barnes PRF, Plumb IC, Savvides N. Enhancement of photoelectrochemical hydrogen production from hematite thin films by the introduction of Ti and Si. J Phys Chem C. 2007;111:16477–88.
9. Jang JH, Shin WJ, Han GB. A study on production of oxidant by decomposition of H_2O_2 on Mn based catalyst and no oxidation. J Ind Pollut Control. 2018;34:1811–7.
10. Liu X, Zhao C, Feng F, Yu F, Kang W, Shen Q. The controlled synthesis and improved electrochemical cyclability of Mn-doped $\alpha\text{-}Fe_2O_3$ hollow porous quadrangular prisms as lithium-ion battery anodes. RSC Adv. 2015;5:7604–10.
11. Feng Y, Fornell J, Zhang H, Solsona P, Baró MD, Suriñach S, Pellicer E, Sort J. Synthesis of $\alpha\text{-}Fe_2O_3$ and Fe-Mn oxide foams with highly tunable magnetic properties by the replication method from polyurethane templates. Materials. 2018;11:280–7.
12. Durán FG, Cadús LE, Barbero BP. Iron-manganese mixed oxide catalysts for ethanol combustion influence of the Fe: Mn atomic ratio and the calcination temperature. Lat Am Appl Res. 2012;42:217–21.
13. Herranz T, Rojas S, Ojeda M, Pérez-Alonsa FJ, Terreros P, Pirota K, Fierro JLG. Synthesis, structural features, and reactivity of Fe–Mn mixed oxides prepared by microemulsion. Chem Mater. 2006;18:2364–75.
14. Sun W, Li X, Zhao Q, Mu J, Chen J. Fe–Mn mixed oxide catalysts synthesized by one-step urea-precipitation method for the selective catalytic reduction of NO_x with NH_3 at low temperatures. Catal Lett. 2018;148:227–34.
15. Jo Y-H, Chung YW, Do S-H (2013) Simple preparation of Mn-Fe_2O_3 composite: identification and evaluation as an activator in Fenton like oxidation. In: 2nd annual international conference (SEES 2013). https://doi.org/10.5176/2251-189X_SEES13.23.
16. Hermanek M, Zboril R, Medrik I, Pechousek J, Gregor C. Catalytic efficiency of iron(III) oxides in decomposition of hydrogen peroxide: competition between the surface area and crystallinity of nanoparticles. J Am Chem Soc. 2007;129:10929–36.
17. Araujo FVF, Yokoyama L, Teixeira LAC, Campos JC. Heterogeneous Fenton process using the mineral hematite for discoloration of a reactive dye solution. Braz J Chem Eng. 2011;28:605–16.
18. Liu J, Wang B, Li Z, Wu Z, Zhu K, Zhuang J, Xi Q, Hou Y, Chen J, Cong M, Li J, Qian G, Lin Z. Photo-Fenton reaction and H_2O_2 enhanced photocatalytic activity of $\alpha\text{-}Fe_2O_3$ nanoparticles obtained by a simple decomposition route. J Alloys Compd. 2019;771:398–405.
19. Ianos R, Takulescu A, Pacurariu C, Lazau I. Solution combustion synthesis and characterization of magnetite nanopowders. J Am Ceram Soc. 2012;98:2236–40.
20. Mihoc G, Ianos R, Pacurariu C, Lazau I. Combustion synthesis of some iron oxides used as adsorbents for removal of phenol and p-chlorophenol from waste water. J Therm Anal Calorim. 2013;112:391–7.
21. Raja K, Jaculine MM, Jose M, Verma S, Prince AAM, Ilangovan K, Das SJ. Sol–gel synthesis and characterization of $\alpha\text{-}Fe_2O_3$ nanoparticles. Superlattice Microstruct. 2015;86:306–12.
22. Sundar S, Venkatachalam G, Kwon SJ. Sol-gel mediated greener synthesis of $\gamma\text{-}Fe_2O_3$ nanostructures for the selective and sensitive determination of uric acid and dopamine. Catalysts. 2018;10:10. https://doi.org/10.3390/catal8110512.
23. Lassoued A, Dkhil B, Gadri A, Ammar S. Control of the shape and size of iron oxide ($\alpha\text{-}Fe_2O_3$) nanoparticles synthesized through the chemical precipitation method. Results Phys. 2017;7:3007–15.
24. Mansour H, Bargougui R, Autret-Lambert C, Gadri A, Ammar S. Co-precipitation synthesis and characterization of tin-doped $\alpha\text{-}Fe_2O_3$ nanoparticles with enhanced photocatalytic activities. J Phys Chem Solids. 2018;114:1–7.
25. Li J, Yuan H, Li G, Liu Y, Leng J. Cation distribution dependence of magnetic properties of sol-gel prepared $MnFe_2O_4$ spinel ferrite nanoparticles. J Magn Magn Mater. 2010;322:3396–400.
26. Ribeiro Carrott MML. Physisorption of gases by solids: fundamentals, theories and methods for the textural characterisation of catalysts. In: Figueiredo JL, Pereira MM, Faria J, editors. Catalysis from theory to application—an integrated course. Coimbra; 2008. p. 83–105.
27. Rouquerol F, Rouquerol J, Sing KSW, Llewellyn P, Maurin G. Adsorption by porous powders and porous solids: principles, methodology and applications. 2nd ed. Amsterdam: Elseviers; 2014.
28. Zhang L, Wu Y. Sol-gel synthesized magnetic $MnFe_2O_4$ spinel ferrite nanoparticles as novel catalyst for oxidative degradation of methyl orange. J Nanomater. 2013. https://doi.org/10.1155/2013/640940.
29. Wang C, Liu H, Sun Z. Heterogeneous photo-fenton reaction catalyzed by nanosized iron oxides for water treatment. Int J Photoenergy. 2012. https://doi.org/10.1155/2012/801694.